CRITERIA OF DESIGN IMPROVEMENT OF SHAPED CHARGES USED AS OIL WELL PERFORATORS

A Thesis submitted to The University of Manchester for the degree of

Doctor of Philosophy

The Faculty of Engineering and Physical Sciences

2012

Tamer Abd Elazim Elshenawy

School of Mechanical, Aerospace and Civil Engineering

(This page is intentionally left blank)

TABLE OF CONTENTS

Word count: 59,473

LIST OF FIGURES

LIST OF TABLES

NOMENCLATURE

ACRONYMS

AD	Autodyn
API-RP	American petroleum institute research procedure
bcc	Body centred cubic
CD	Charge diameter
CSC	Conical shaped charge
CFE	Core fluid efficiency
cg	Coarse grain
DW	Detonation wave
ERA	Explosive reactive armour
EOS	Equation of state
EMP	Electromagnetic pulse
EFP	Explosive formed projectile
fcc	Face centred cubic
HERF	High energy rate fabrication
HB	Brinell hardness
HD	The dynamic hardness of the target material
HE	High explosive
HEAT	High explosive anti-tank
hcp	Hexagonal close packed
JWL	John-Wilkins-Lee equation of state of high explosives
J-C	Johnson-Cook constitutive model
K.E.	Kinetic energy
OWP	Oil well perforator
OFHC	Oxygen free high conductivity copper
OFEC	Oxygen free electrolytic copper
PER	Pugh-Eichelberger-Rostoker unsteady state jet theory
PM	Powder metallurgy
PURE	Perforating for ultimate reservoir exploitation
PVE	Pressure-volume-energy relation
QC	Quality control concrete target
Re	Reynold’s number
RHT	Riedel-Hiermaier-Thoma brittle material constitutive model
RA	Reduction of area
RHA	Rolled homogeneous armours
SOD	Stand-off distance
TOW	Tube launched optically tracked wire-guided missile
VO	Virtual origin
V&V	Validation and verification

NOTATION

A	Parameter in Held crater radius formula
A	Constant in explosive JWL equation of state
A	Failure surface constant
a	Tensile strain-rate factor
a	Hall-Petch constant
a	Biot's constant
B	Parameter in Held crater radius formula
B	Constant in explosive JWL equation of state
B_{max}	The target Brinell hardness beneath the penetrating projectile
B_{max}	Brinell hardness
B_o	Grunisen Gamma Constant in Mie-Grunisen equation of state
C_o	Shock velocity
C_L	Collapse velocity limit for coherency criteria
C	Explosive mass per unit area
c	Speed of light in vacuum
c	Sound wave velocity
D_a	Detonation wave speed
D	Projectile diameter
D	Compressive strain-rate factor
d_{jo}	Initial jet diameter
d	Grid spacing
d	Average grain size
E_t	Young's modulus
E	Gurney constant related to explosive
e_H	Initial Hugoniot energy
f_c	Compressive strength
g_i	The gap distance between two subsequent broken-up jet elements
g_o	Empirical constant in particulated jet penetration formulae
g_{ave}	The average gap distance between jet fragments
H_o	Height of interaction region between the jet and the target
H_D	Dynamic hardness of the target
I_{FG}	Shape index
I_{sp}	Specific impulse of the explosive

k_T	The body shape factor of the target in the Alekseevskii penetration model
k_j	The body shape factor of the jet in the Alekseevskii penetration model
k	Hall-Petch constant
k	Number of broken-up elements
L, l	Projectile length
M	Liner mass per unit area
m	Jet mass
m	Thermal softening exponent in Johnson-Cook model
m	Hardening exponent in Zerilli-Armstrong constitutive model
m_j	Jet mass
m_s	Slug mass
N	Failure surface exponent
P^*	Normalized pressure
P	Depth of penetration
P	Pressure
P_e	The elastic pressure of the brittle material
P_s	The fully compaction pressure
P_{CJ}	Chapman-Jouguet pressure of the explosive
P^-	Penetration in particulated jet
P_o	Penetration at zero stand-off distance
p_H	Initial Hugoniot pressure
Q_v	Explosion heat
R	Liner radius in jet radius formula
Re	Reynold's number
R_o	The explosive outer radius
R_I	The explosive inner radius
R_x	The radius of the stationary surface
R_t	The target strength factor defined in Tate model
r	Jet radius
r_1, r_1	Constants in explosive JWL equation of state
r_o	Initial radius of the jet
r_c	Crater radius
S	The distance between the VO and the target surface
s	Constant representing the slope in shock EOS
T	Temperature in Zerilli-Armstrong constitutive model

T_L	Liner thickness
T_H	Homologous temperature in Johnson-Cook model
T_L	Liner thickness
T_t	The thickness of the perforated target in VO penetration model
T_e	Explosive thickness
t	Current time
t_o	Detonation wave arrival time in Randers-Pehrson relation
t_o	Arrival time of the jet to the target surface
t_b	Breakup time of the jet
t_f	Final cratering time
U_D	Detonation velocity of the explosive
U	Penetration velocity
U	Shock velocity
u_p	Particle velocity in shock equation of state
V_j	Jet tip velocity
V_c	Jet cut-off velocity
V_o	Collapse velocity in jet formation theories
V_1	Stagnation velocity in jet formation theories
V_2	Flow velocity in jet formation theories
V_{tail}	Jet tail velocity
V_{min}	The minimum jet velocity for penetration
V_{PL}	Plastic particle velocity
Y	Yield strength
Y_p	The projectile strength factor defined in Tate model
Z_o	The effective jet length in virtual origin model
Z	The jet coordinate measured along the liner axis
z_o	The initial position of the jet element

GREEK SYMBOLS

α	Half cone angle
α	Porosity
α	Constant in the Haugstad breakup time equation
α	Constant in the Pack and Evan penetration formulae
β	Collapse angle in jet formation
β	Constant representing the jet spreading.

β_c	Critical collapse angle
δ	Deflection angle in jet formation
σ	Flow stress
σ_j	Jet dynamic yield strength
σ_{eff}	Effective stresses
σ_t	Compression strength of the target material
σ_y	Yield stress
$\dot{\varepsilon}$	Strain-rate
ε	Strain
ε	Explosive thickness
ε^*_p	Normalized effective plastic strain
ε_p	Effective plastic strain
γ	The square root of the ratio of the target to jet density
τ	Time constant in Randers-Pehrson relation
λ	Constant in the particulated jet penetration formula
μ	Viscosity coefficient
μ	Metal to explosive mass ratio
μ	Compressibility
φ	Plate bending angle ($\varphi=2\delta$)
π	Non-dimensional number
ω	Constant in the JWL equation of state of explosives
ψ	Constant depending on the velocity gradient
ν	The kinematic viscosity
Δt	Time step for finite difference calculations
ρ_j	Density of jet material
$\rho_{Exp.}$	Density of explosive material
ρ_l	Density of the liner material
ζ	The angle between the normal to the detonation wave front and the liner surface.

ABSTRACT

In addition to its various military applications, shaped charges have been used in oil industry as an oil well perforator (OWP) to connect oil and gas to their reservoirs. The collapse of the liner material under the explosive load produces a hypervelocity jet capable of achieving a deep penetration tunnel into the rock formation. The achieved penetration depends on the OWP design, which includes the geometry and the material of the explosive and the liner as well as the initiation mode and the casing of the shaped charge. The main purpose of this research is to assess the performance of OWP with different design aspects in terms of its penetration depth into concrete material.

This research employed the Autodyn finite difference code to model the behaviour of OWPs in the stages of liner collapse, jet formation and jet penetration. The design parameters of OWPs were studied quantitatively to identify the effect of each individual parameter on the jet characteristics and the jet penetration depth into concrete material according to the API-RP43 standard test configuration. In order to validate the Autodyn jetting analysis, this research compared the jetting simulation results of copper OWP liners with those obtained from flash x-ray measurements while the numerical jet penetration into the laminated concrete target was validated experimentally by the static firing of OWPs. Above-mentioned experiments were designed and performed in this project.
The validated hydrocode was implemented in this research to study the effects of the concrete target strength, the liner material and the liner shape on the jet penetration depth into concrete targets.

For the target strength, the traditional virtual origin (VO) penetration model was modified to include a strength reduction term based on Johnson's damage number and the effect of the underground confinement pressure using Drucker-Prager model. The VO analytical model is also implemented in the liner material study to account for the jet density reduction phenomena and its induced reduction of jet penetration capability. The jets obtained from machined copper and zirconium liners and from copper-tungsten powder liner all exhibited the density reduction phenomena. The modified VO model considers the non-uniform distribution of jet density based on the jet profile analysis using Autodyn and the experimental soft recovery for some tested liners. The results lead to a modified VO penetration model including the non-uniform jet density effect.

For zirconium liner material, numerical and analytical studies were conducted for different flow velocities and different collapse angles in order to determine the boundaries between the jetting and non-jetting phases and whether a coherent or a non-coherent jet will form. This study indicated that the suggested four different liner shapes (i.e. the conical, the biconical, the hemispherical and the bell) will produce coherent jet when the zirconium is used as OWP liner.

The validated Autodyn hydrocode is also used in this thesis to calculate the velocity difference between two neighbouring zirconium jet fragments. The velocity difference is related directly to the breakup time of an OWP jet, and thus, it is calculated for a range of zirconium liners with different liner wall thicknesses. The calculated values of velocity difference gave a clear insight for the breakup time formulae for zirconium jet in terms of the liner thickness and the charge diameter.

DECLARATION

I hereby declare that no portion of the work referred to in the thesis has been submitted in support of an application for another degree or qualification of this or any other university or other institute of learning.

Sign ……..

COPY RIGHT STATEMENT

I. The author of this thesis (including any appendices and/or schedules to this thesis) owns certain copyright or related rights in it (the "Copyright") and he has given The University of Manchester certain rights to use such Copyright, including for administrative purposes.

II. Copies of this thesis, either in full or in extracts and whether in hard or electronic copy, may be made only in accordance with the Copyright, Designs and Patents Act 1988 (as amended) and regulations issued under it or, where appropriate, in accordance with licensing agreements which the University has from time to time. This page must form part of any such copies made.

III. The ownership of certain Copyright, patents, designs, trade marks and other intellectual property (the "Intellectual Property") and any reproductions of copyright works in the thesis, for example graphs and tables ("Reproductions"), which may be described in this thesis, may not be owned by the author and may be owned by third parties. Such Intellectual Property and Reproductions cannot and must not be made available for use without the prior written permission of the owner of the relevant Intellectual Property and/or Reproductions.

IV. Further information on the conditions under which disclosure, publication and commercialisation of this thesis, the Copyright and any Intellectual Property and/or Reproductions described in it may take place is available in the University IP Policy (see http://www.campus.manchester.ac.uk/medialibrary/policies/ intellectual-property.pdf), in any relevant Thesis restriction declarations deposited in the University Library, The University Library's regulations (see http://www.manchester.ac.uk/library/aboutus/regulations) and in The University's policy on presentation of Theses.

DEDICATION

For my parents,

My dear father – Abd Elazim Elshenawy

My loving mother – Samia Elshenawy

and

My wife and children

ACKNOWLEDGEMENTS

First and foremost, I wish to give all the praise to Almighty Allah for giving me the strength and time to complete this research.

I wish to express my deepest gratitude to my supervisor, Dr Qingming Li, for his constant encouragement, inspiration, guidance, various helpful advices and comments on the thesis during this research. He provided me with all kinds of support during my PhD study.

I would like to express my gratitude to Dr Steve Burley for his assistance, support, helpful advices and time. My past and present colleagues in the research group have always been an unfailing source of comfort. I would like to thank all of them for their support and help.

Special thanks go to Charlie, Ambrose and Tom, the technical staffs of the Event Horizon Company and to Eric Palmer and technical staffs of COTEC for their help during my experimental field testing.

This study would not have been possible without the financial support of my sponsor, Technical Research Centre of the Egyptian Armed Forces.

My special gratitude goes to Dr. Abd Elhameed Mostafa, Dr. Gamal Abdo and Dr. Hussien Elwany for their moral support. Besides, I cannot forget Dr Mohamed Ismail and Prof. Ahmed Reyad for their tremendous effort in the beginning of my research career.

Finally, I would like to express my deepest gratitude to my wife, my son, my daughters, and my brothers for their unflinching support, encouragement and love. Without them, this would not have been possible.

Tamer Elshenawy

December, 2012

LIST OF PUBLICATIONS

T. Elshenawy, Q.M. Li, Parametric analysis of the penetration performance of shaped charges used as oil well perforators, 41st International ICT-Conference, Karlsruhe, Germany, June 29 – July 2, **2010**.

T. Elshenawy, Q.M. Li, Penetration performance of oil well perforators into rocks, The First International Conference of Protective Structures; ICPS, Manchester, **2010**.

T. Elshenawy, Q.M. Li, Perforator charge casing effect on the wave shape and jet characteristics, The 9th New Models and Hydrocodes for Shock Wave Processes, NMH Conference, Imperial College London, **2012**.

T. Elshenawy, Q.M. Li, Design of shaped charge as oil well perforator, 23rd International Congress of Theoretical and Applied Mechanics (ICTAM2012) XXIII ICTAM, Beijing, China, 19-24 August **2012**.

T. Elshenawy, Q.M. Li, Influences of target strength and confinement on the penetration depth of an oil well perforator, International Journal of Impact Engineering, **2012,** (in press).

T. Elshenawy, Q.M. Li, A Modified virtual origin model for shaped charge jet penetration with non-uniform density distribution, submitted to International Journal of Impact Engineering, August, **2012**.

T. Elshenawy, Q.M. Li, Performance of zirconium jet with different liner shapes, Submitted to International Journal of Mechanical Sciences, November, **2012**.

T. Elshenawy, Q.M. Li, Zirconium shaped charge jet breakup time, submitted to the Journal of Propellant, Explosives and Pyrotechnics, November, **2012**.

CHAPTER.1 INTRODUCTION

1.1 Research Background

In addition to its military applications such as anti-tank munitions and missile warhead, shaped charge has been used in civilian applications. For example, oil well perforator (OWP) based on shaped charge technology is used to connect the wellbore to the oil and gas reservoir by creating deep holes. When a shaped charge is detonated, it produces a hypervelocity jet with a tip velocity around 10km/s and a slug velocity around 2km/s. Due to the velocity gradient between its tip and slug, the jet stretches until its breakup. The hypervelocity stretching jet can produce a deep penetration into the target in front of the shaped charge jet. For the OWP application, the shaped charge jet penetrates multi-layered laminated targets.

The performance of the OWP in terms of its penetration depth for a given target depends mainly on the type and the amount of the explosive used, the liner geometry and liner material. Other parameters such as the charge confinement and the mode of initiation also have evident effects on the jet characteristics and its penetration capability. The penetration performance of an OWP is characterised by the static firing of the OWP against the standard laminated targets representing the geological medium, the gun carrier, the well steel wall and the wellbore fluid. The standard laminated target is steel/water/steel/concrete with respective thicknesses of 3.2/17.2/9.5/1000mm according to the American Petroleum Institute test section (API-RP43).

This thesis is aimed to identify the dominant parameters that influence the OWP jet formation and its penetration capability into concrete target with the assistance of the Autodyn hydrocode package. This hydrocode is validated by the experimental static firing of OWP against the standard test configurations in field tests and by measuring some designed liner aspects (e.g. velocity and breakup time) using flash x-ray facility. The suitability of Autodyn hydrocode for the simulation of shaped charge jet formation and penetration has also been demonstrated by many previous works.

Small diameter OWP (i.e. 36mm) is selected as a baseline in this study, while the design improvements include the liner material and its shape. The design of the liner material based on a range of new material candidates, such as zirconium and copper-tungsten

powder mixtures in addition to the traditional copper. The liner geometries include conical, hemispherical, bell and bi-conical shapes.

1.2 Originality of Research

The wide usages of shaped charges in the military and civilian sectors have demonstrated that the increase of penetration depth is one of the main objectives of the shaped charge designers. Thus, the penetration enhancement is one of the key issues to be resolved, and therefore, is the focus of this research.

The majority of existing research work on shaped charge penetration employed the assumption that the jet has a uniform density with the same value as that of the solid liner material, where the effects of the jet heating, compressibility and metallurgical changes are usually ignored. Zernow [1] is one of the few researchers who discussed the unexplained jet density reduction and density deficit phenomena, but he did not discuss the effect of density reduction on the penetration depth. Thus, the virtual origin penetration model introduced initially by Allison and Vitalli [2], where constant jet density was assumed, was modified in this research to account for the penetration decrease due to the density reduction phenomena. The influences of concrete strength and its underground confinement pressure on the penetration depth are also studied in this research where a modified Allison-Vitalli equation is proposed to include a target strength correction term.

On the other hand, Cowan and Holtzman [3] calculated flow velocities of jet elements and the corresponding collapse angles for some common liner materials except zirconium. These parameters are important because they give the different regions defined by jetting/non-jetting and coherent/non-coherent boundaries for a given shaped charge liner material. These regions were determined by analytical and numerical studies for the zirconium liner material in this study. The numerical modeling of the jet formation was presented to understand the features of jet formation in different regions for four zirconium liners of different shapes. The bell, hemispherical, conical and bi-conical liners were successfully designed and tested based on these analytical and numerical results.

Hirsh [4-5] suggested a unique way to determine the jet breakup time based on the maximum plastic particle velocity (or the velocity difference between neighbouring jet fragments) for shaped charge copper jet, which is a critical parameter to distinguish continuous and particulated jets that have significant influence on the jet penetration. This research calculated the plastic particle velocity for shaped charge jet of zirconium liners of different wall thicknesses. A simple analytical relation between the ratio of liner thickness

to charge diameter and the plastic particle velocity is introduced and used directly for the calculation of the breakup time of the zirconium jet, which demands huge computing cost if numerical approach is employed to obtain the plastic particle velocity over the entire range of liner thicknesses.

1.3 Objectives and methodology of research

The objectives of this study are

- To develop a modified virtual origin model with the considerations of the jet density reduction and the target strength enhancement due to the confinement pressure effect in order to improve the prediction of the jet penetration depth.

- To test the penetration performance of OWP using different liner materials.

- To investigate the conditions of jet formation and its coherency for different zirconium liner shapes.

- To present an independent formula for zirconium jet, by which the plastic particle velocity can be easily estimated and used to predict breakup time directly.

1.4 Thesis structure

Chapter 2 introduces shaped charge, the general parameters affecting its performance, the different liner materials and their manufacturing techniques.

Chapter 3 describes the shaped charge jet formation process, the jet breakup models and jet penetration models.

Chapter 4 introduces Autodyn hydrocode, equation of state (EOS) and material constitutive/strength models.

Chapter 5 presents a general parametric study including the validation and the verification of the codes used in this project.

Chapter 6 discusses the effects of concrete strength on the penetration reduction, in which four concrete targets with different strengths are tested for the identical OWP design.

Chapter 7 studies the liner shape effect on shaped charge jet performance for four different shapes of zirconium liners, i.e. the conical, bell, hemispherical and bi-conical

liner shapes. The theoretical calculations in this chapter include the jet formation and jet cohesion conditions for the zirconium liner material. The performances of the OWP with these zirconium liner shapes are verified against concrete targets.

Chapter 8 studies the liner material effect, including copper, zirconium and copper-tungsten un-sintered powder mixture liners. The effect of the jet density reduction phenomena on its penetration capability is discussed, in which the traditional virtual origin model was modified to account for the reduced penetration depth due to the jet density reduction.

Chapter 9 calculates the velocity difference between neighbouring zirconium jet fragments. Parameters of the Johnson-Cook constitutive equation are obtained for a range of strain, strain-rate and temperature, which are then used to calculate the characteristic plastic particle velocity and jet breakup time for zirconium jet.

The thesis is concluded in **Chapter 10** where the main findings from this research are presented together with recommendations for the future study in this field.

CHAPTER.2 LITERATURE REVIEW

2.1 Overview

2.1.1 Shaped charge phenomenology

The hollow charge is a cylinder of explosive with a hollow cavity in one end and a detonator at the opposite end. The hollow cavity causes the gaseous products formed from the detonation of explosive at the end of the cylinder to focus the energy of the detonation products. The focusing of the detonation products creates an intensive and localized force when it is directed against a target. This concentrated force is capable of creating a deeper cavity than a cylinder of explosive without a hollow cavity; even though more explosive is available in the latter case. This phenomenon is known in USA as Munroe effect, and in Europe as the Vonfoester or Neumann effect [6], as illustrated in Figure 2-1.

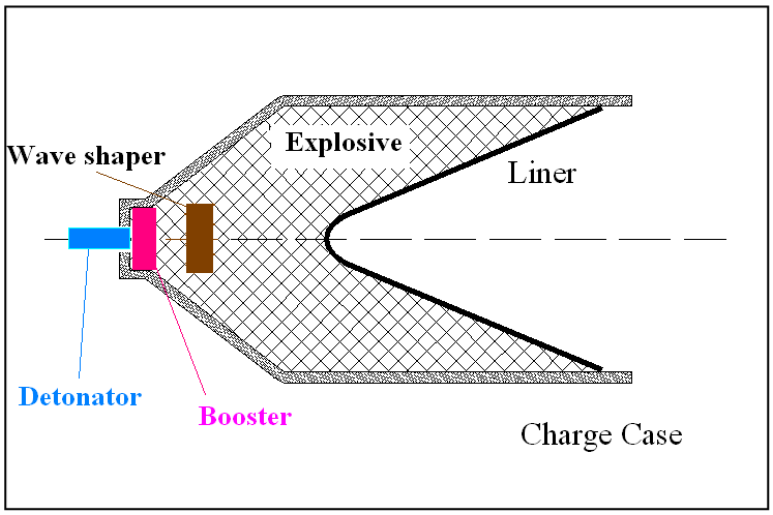

Figure 2-1 A schematic drawing of a shaped charge configuration.

If the hollow cavity is lined with a thin layer of ductile metal, glass, ceramic, or any solid, the liner may form a jet when the explosive charge is detonated.

After the detonation of a shaped charge, a spherical wave propagates outward from the point of initiation. The extremely high pressure resulting from the explosive detonation pushes out the liner material causing it to collide with other collapsed liner elements and form a hyper velocity jet with high strain-rate of the liner in the range of 10^4 to $10^7 s^{-1}$ [7]. Under this extremely high pressure, the succeeded jet will move with a tip velocity around

9 km/s, while the tail of the jet called a slug moves with a velocity around 2km/s as illustrated in Figure 2-2.

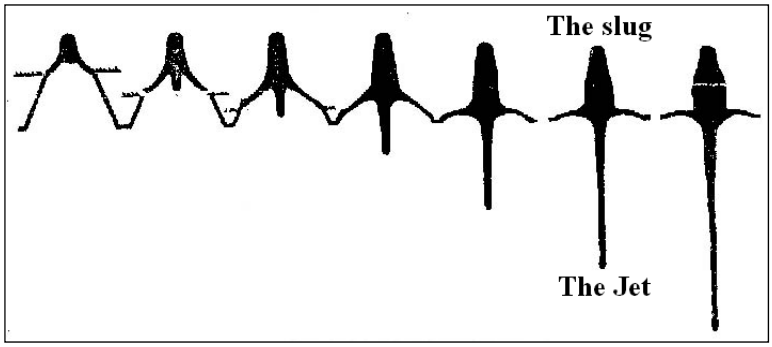

Figure 2-2 Collapse of the liner and the formation of the jet [6].

When this extremely energetic jet strikes a metal target at a distance from the shaped charge (i.e. stand-off distance), a deep cavity is formed, exceeding that caused by a hollow charge without liner [6], as illustrated in Figure 2-3.

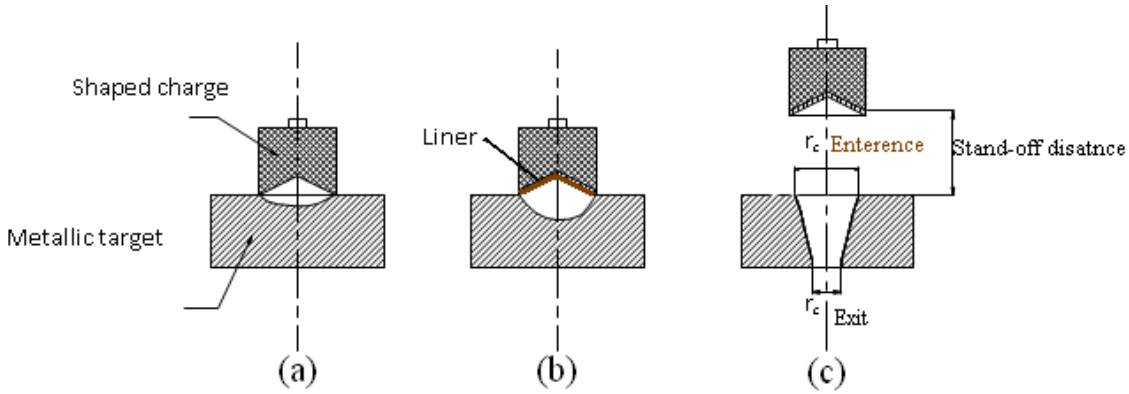

Figure 2-3 Different effects of shaped charge on target, (a) unlined cavity effect, (b) lined cavity effect, and (c) lined cavity with stand-off distance.

The cavity produced in the metal plate due to the jet-target interaction is not due to the thermal effect but due to the hydrodynamic flow of target material by extremely high pressure.

2.1.2 Shaped charge applications

2.1.2.1 Development of the shaped charge and its wide usage in military applications

Shaped charges are extremely useful for penetrating armours or piercing barriers in the field of military applications. It can be used as a part of torpedoes, missiles or particularly

as an anti-tank ammunition. Its military application started from World War II when the so-called hollow charge projectiles were proposed.

The effect of shaped charge with unlined cavity on metallic target was firstly recognized by Max Forester in 1883. This effect was also discovered by Charles Munroe in 1888 and by Neumann in 1910. The effect of shaped charge with unlined cavity was called the Munroe effect in the USA and UK and the Neumann effect in Germany [6]. Munroe used this device to print symbols on metal plates. Moreover, he discovered that placing the hollow charge at a distance from the target surface could increase the depth of crater in target [6].

The US army used the lined shaped charge invented by Mohaupt [6] to produce the first shaped charge grenades. Moreover, Mohaupt used his invention to produce rifle grenades and mortar bombs up to a calibre of 100 mm. After the end of World War II, UK started a development program of lined shaped charge, whereas USA produced the 2.26 in. high explosive anti-tank (HEAT) machine gun grenade and the 75 mm and 105 mm HEAT projectiles. Later, the machine gun round was modified to include a rocket motor and a shoulder launcher, which was named Bazooka. In 1941, the Bazooka was firstly used by UK in North Africa.

During the 1950's, tremendous efforts were done toward the understanding of the phenomenon associated with the shaped charge jet formation. Analytical models were developed to calculate the liner collapse characteristics and the penetration depth.

In 1973, when Manfred Held invented the explosive reactive armour, which can easily defeat the shaped charge jet, tandem warheads were developed to defeat modern armour. Each warhead consists of two shaped charges, placed one after the other. The idea was that the first jet would make the penetration easier for the second charge by initiating the high explosive or the reactive materials in the reactive armours or explosive reactive armour module (ERA) [8].

In 1990, new developments of shaped charges were performed regarding the type and the shape of liner material leading to the development of advanced warheads such as EFP (explosive formed projectiles) installed in rocket warhead TOW (Tube Launched Optically Tracked Wire Guided) missile.

Currently, shaped charge research continues in order to countermeasure the advanced armours. Studies that originated in the nineteenth century and developed in the twentieth

century still continue, notably, torpedo applications of shaped charge rounds, multi-staged or tandem warheads, long stand-off rounds, non-conical and non-copper liners, etc. Also, metallurgical and chemical aspects of the liner material as well as methods of liner fabrication remain important [6].

2.1.2.2 Civil applications of shaped charge

In addition to its wide usage in military fields, shaped charges can also be used in different civil fields such as:

- Oil industry as oil well perforator
- Explosive ordnance disposal
- Cautious blasting and demolishing works
- Break, crack or form holes in rocks
- Earthmover in large constructions (e.g. tunnels)
- Cutting of steel tubes and railways with large diameter and wall thickness [9]
- Explosive welding
- Generation of transient antennas to countermeasure the use of electromagnetic pulse (EMP) weapons [10].

2.1.3 Application of shaped charge in the oil field

2.1.3.1 Introduction

Oil well completion involves the drilling of a hole with the designated surface depth using pit cutting element, which crushes the rock efficiently as it rotates and initiates fluid out to loosen and carry out debris to the surface. When the hole reaches the designated depth, the logging information enables the oil company to determine if the well is a producer or not. If the well is characterized as a producer, a steel pipe is inserted back into the hole to ensure that it is still intact and circulate mud through it to test the casing. If everything tests positively, the pipe will be removed and the last casing pipe is inserted into the hole and cemented.

The perforating gun is lowered into the hole to the production depth using a thin metal cable called wireline and an electrical signal is sent down the wireline to fire the gun and ignite the explosive charges. These charges create holes through the cement, casing and formation connecting the well bore to the reservoir. To stimulate the flow of hydrocarbons, sometimes it is necessary to pump air, sand and fluids under high pressure through the perforations to increase the cracks in the formations. The remaining particles will hold the

cracks opened releasing the oil or gas. Once the pressure is released, the hydrocarbons are allowed to escape and flow into the well bore.

2.1.3.2 Description of the shaped charge used as perforator

In addition to its wide usage in anti-tank warheads and explosive disposal devices, shaped charge as oil well perforator (OWP), has been extensively used and developed in the field of oil extraction. In 1946, Mclemore [11] firstly used the shaped charge in the field of oil industry. According to Ref. [12], Rinehart et al revealed a design of shaped charge capable of perforating oil well casing, well bore fluid and tubing.

As the shaped charge detonates, the detonation energy liberated from the explosive charge detonation will collapse the metallic liner towards its axis to form a jet and a slug. The jet which represents about 20 % of the liner mass is moving in the front with a velocity ranging from 5000 to 10000 m/s, while the heavy tail representing about 80% of liner mass called the slug is moving with a velocity around 1000 m/s. Due to this velocity gradient between the jet tip and its slug, the jet length increases and its diameter decreases with both time and travelling distance. The jet under extremely high pressure behaves much like a fluid although it is still in its solid state. The produced jet is acting as a fluid due to severe plastic deformation by intensive shock loads from explosive detonation, rather than due to thermal melting although the temperature of explosion may exceeds 3000 or 4000^{o}C [13], [14].

The elongated jet has a very high kinetic energy and has the ability to create deep holes into different hard target materials. The shaped charge used in the oil completion referred to as OWP should perforate steel casing, wellbore fluid and cement to achieve a deep penetration depth into rock formation to connect oil and gas reservoirs to the wellbore.

Figure 2-4 presents a schematic drawing illustrating the fitting of the OWP inside the gun carrier, all centralized in the pipe tubing inside the rock formation.

The common features of the oil well perforators are:

- The stand-off distance is limited but a concave gap should be maintained in order to reduce the clogging with the wall of the casing [11].
- The shaped charge designed for rock penetration should cause both large penetration depth and large diameter hole.

- The OWP should be designed to withstand deep well pressures exceeding 150MPa [12]. The housing or casing of the shaped charge is made of pulverable material (Alumina Ceramic) having a very high compressive strength in order to resist the high pressure in the very deep wells for oil extraction and to create small fragments upon detonation of the OWP. Also, the charge casing design should consider the interference between the charge case fragments and the other perforators to avoid premature explosion.
- The selection of high explosive in the design of OWP should consider not only the explosive performance but also its sensitivity because the temperature of the downhole can be greater than 260^{o}C [11], which is close to the ignition temperatures of some high explosives.
- The main problem for the use of shaped charge as OWP is that the resultant useless slug can clog the aperture in the borehole; therefore, the oil productivity can be affected by this clog. To overcome this problem, research on powder metallurgy or powder pressing technique has been conducted in order to create a jet with high percentage of mass and low density porous slug from the pressed powder liner [15]. It has been shown that 30% of the clogged geological boreholes in the well production were caused by the heavy massive slugs, which is the main factor to affect the well productivity [15].

The most common type of gun perforator is the casing gun, in which all the perforators are fixed on a wireline and conveyed by steel tubing, which protects perforators from impact and isolating them from the well fluids [16]. Figure 2-4 illustrates the plan view of an OWP fitted inside the gun with the main elements of gun carrier.

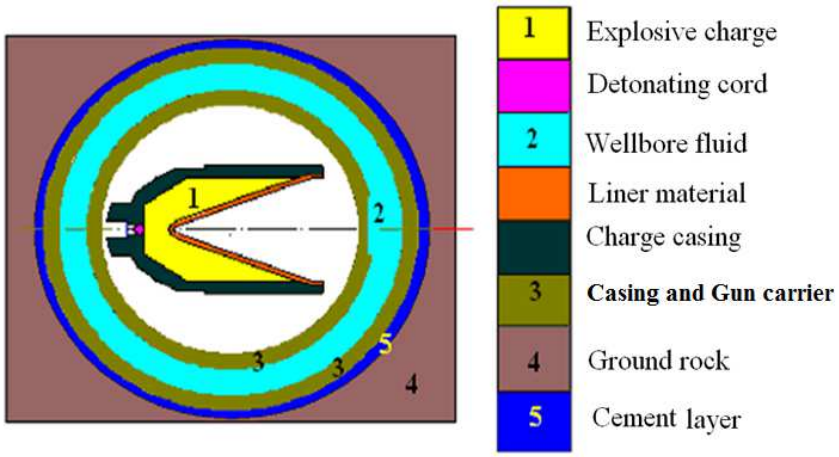

Figure 2-4 OWP fitted inside the gun carrier facing the cement and concrete materials.

Figure 2-5 represents a side view of down-hole gun perforator (i.e. the steel carrying the perforators), other elements and the detonating cord required for instantaneous detonation, as well as the well and the surroundings. The perforators are fixed inside the gun at constant angles in a top-view plane (Phasing). These perforators are held in a hollow steel carrier to protect them during operation. The thickness of the steel carrier is sufficient to protect the perforators from the downhole conditions of heat and pressure even at a thin scalloped area, through which the perforator is fired [17]. The cement layer is pumped into the annulus between the tube casing and the bearing rock in order to prevent contamination of the water around the well casing by the produced oil [17]. After the well is completed, the oil and the gas are allowed to travel up to the surface, stored and refined.

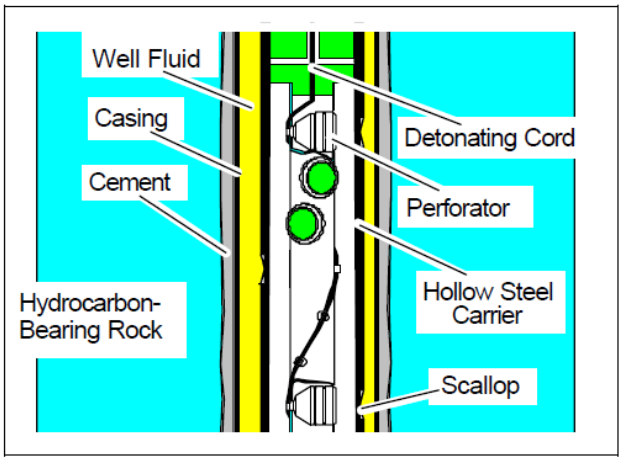

Figure 2-5 Schematic drawing of the location of down hole gun perforators, steel carrier, well fluid, well casing, cement layer, and hydrocarbon rock [17].

2.2 Factors affecting the shaped charge used as oil well perforators (OWP)

The shaped charge geometry design and the liner thickness are the most effective parameters governing the performance of an OWP [11]. Apart from its cone diameter; conical shaped charge (CSC) liner performance in terms of its breakup time is governed and controlled by the following factors [18]:

- The production method of the liner material,
- Quality of both the inner and outer surfaces of the copper liner,
- Purity and quality of the copper material,
- The adhesive material between copper and high explosive materials,
- The type of the high explosive, and

- The presence of air cavities in the liner material [19].

2.2.1 Stand-off distance

The shaped charge jet does not become fully formed until it has travelled a certain distance from the target. This distance is called the stand-off distance, which is proportional to the cone diameter. In general the optimum stand-off distance is between two and eight times that of the cone diameter depending on the cone diameter and the geometry [16]. A proper stand-off distance can increase the penetration depth by 50 % in comparison with zero stand-off distance [16]. Figure 2-6 illustrates the relation between the depth of penetration and the stand-off distance. If this stand-off distance is too large, the coherent unidirectional jet does not exist. Instead, tumbled, deflected and particulated columns of jet are observed.

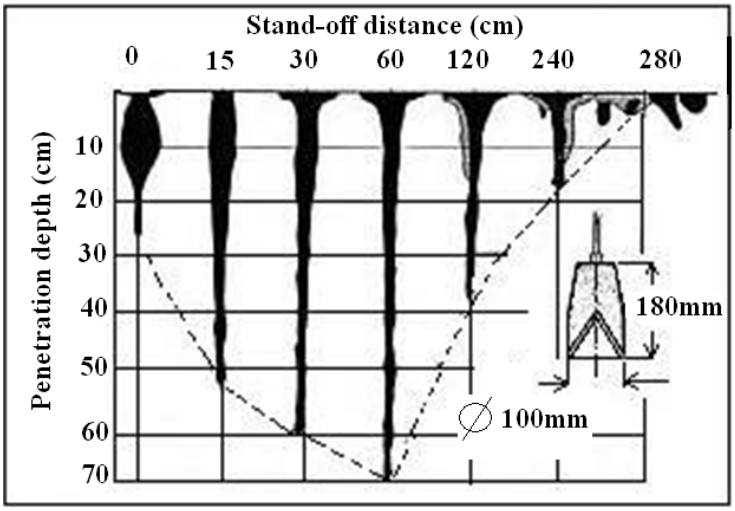

Figure 2-6 Depth of penetration versus stand-off [20].

Since the penetration depth depends on the length of the penetrator, the design of the shaped charges used in the oil industry should consider the limited clearance between the liner base of the shaped charge perforator and the casing wall. These perforators need to be fitted inside the casing of the gun leaving limited free space to allow the jet to stretch [11]. Thus, the achieved penetration depth may be lower than that of the shaped charges with suitable stand-off distances [16]. In a practical application, the stand-off distance between the liner base and the gun wall is about 1cm while the well bore fluid gap between the gun and the casing walls is about 2-2.5cm [11].

2.2.2 High explosive

Theoretically, more energetic explosive produces faster jet, greater jet kinetic energy and deeper penetration [6]. The energy obtained from the high explosive during its detonation is related to Gurney velocity of this explosive, which is the energy liberated from the high explosive and transformed into mechanical work imparted to the liner element. Gurney velocity increases with the detonation velocity and/or the detonation pressure of the explosive which leads to the increase of the jet tip velocity. As a result, the jet kinetic energy and its penetration potential into target will be enhanced.

Table 2-1 illustrates the explosive properties of some high explosives. It is expected that shaped charges filled with HMX, which has the highest Gurney velocity, will produce higher penetration depth, as shown by Tamer and Li [21].

Table 2-1 Explosive properties for some high explosives.

Parameter / H.E.	Density ρ (g/cm^3)	Detonation velocity (m/s)	Gurney velocity (m/s)	Explosion heat (kJ/kg)	Detonation pressure (GPa)	Ignition temp. (^oC)
HMX	1.891	9100	2960	5553	420	280
LX-14 (HMX/Estane) 95/4.5 %	1.835	8800	2800	5559	370	NA
RDX	1.730	8489	2870	4118	330	210
Cyclotol (RDX/TNT) 75/25	1.754	8250	2790	5245	320	NA
PETN	1.720	8142	2920	5770	220	202
TNT	1.600	6913	2390	3681	210	227

The Gurney velocity for Cyclotol was obtained from [22], while the ignition temperature was obtained from [23].

It is also known that the penetration depth of the shaped charge jet into concrete material increases with the increase in the amount of high explosive used in the shaped charge, which also causes the increase of the damage of the crushed region around the penetration path [24].

The selection of high explosive in the design of gun perforator is very important for both its performance and sensitivity issues. The temperature of the down-hole can be greater than 260^oC [11], which should be considered because it is close to the ignition

temperatures of some high explosives. Therefore, care should be taken in the design of the main explosive charge and the degree of casing confinement.

Another important issue related to the high explosive filling of the OWP is the manufacturing technique. The explosive density, the presence of air bubbles and cracks inside the explosive also affect the performance of OWP. The explosive should be pressed under vacuum to remove air bubbles and to increase its density, as shown by Renfre et al. [12]. Moreover, shaped charges used in military purposes should be checked by flash x-ray for air voids and cracks. Other parameters such as grain size and homogeneity of high explosives should also be considered [6]. Moreover, it has been claimed that the shaped charge warhead may be expected to perform much more effectively and efficiently when the filling explosive has a particle size less than 200μm [25].

2.2.3 Liner geometry

Liner is considered as the most critical element affecting the dynamic characteristics of the shaped charge jet and its penetration capability into target materials. There are many liner shapes, which could produce different jet charateristics. These shapes include conical, hemispherical, Tulip, trumpet (or bell shape) and bi-conical liners [6].

The liner shape determines the characteristic of the produced jet. For example, the conical liner produces deeper penetration with small hole diameter. On the other hand, the bell shape liners produce shallow depth penetration with greater hole diameter [11]. In general, the geometry of the cone is determined by the cone apex angle. If this angle is small, the jet is long, thin and more penetrative. As the cone angle widens, the jet becomes shorter, thicker, and less penetrative [11], as illustrated in Figure 2-7 and Figure 2-8.

Since the OWP performance is represented not only by the penetration depth but also the crater diameter, a balance must be established between the small cone angles which produce large penetration depth and the wide cone angles which produce large crater diameter. Figure 2-9 illustrates the relation between jet and slug velocities and liner cone angle.

Various improvements of the liner elements have been done in the past thirty years. In 1998, Davinson and Pratt [17] proved that modifying the liner shape design of shaped charge can increase the jet kinetic energy by 10% and hence can improve the penetration depth by 28%. The newly improved design includes the replacement of old conical liner of tapered (linearly increasing) thickness with a new bell-shaped one of variable thickness

maintaining the same explosive mass (39g) constant. Figure 2-10 illustrates the original and modified liner. The diameter of the baseline liner was 4.06 cm while the modified bell liner was 4.39 cm. The improvement of the liner design is attributed to the greater surface area of the improved bell shape which increases the absorption of the detonation energy, and in turn, increases the collapse velocity of the liner elements leading to the increase of the jet velocity. However, the increase in the collapse velocity attributes not only to the greater surface area in the bell shaped liner, but also to the greater space allowing the liner elements to accelerate than that of the conical baseline liner, as illustrated in Figure 2-10 [17].

In 2001, Lee [11] suggested a varied thickness liner of a hemisphere shape. The thicknesses were 1.41mm at the liner base and 0.52 mm at the apex section, which has a hole of 9.27mm diameter. The purpose of this design was to generate a double velocity gradient jet with a bulged section capable of creating small diameter hole in the well casing and big hole in the rock formation with maximum penetration depth in the rock layer.

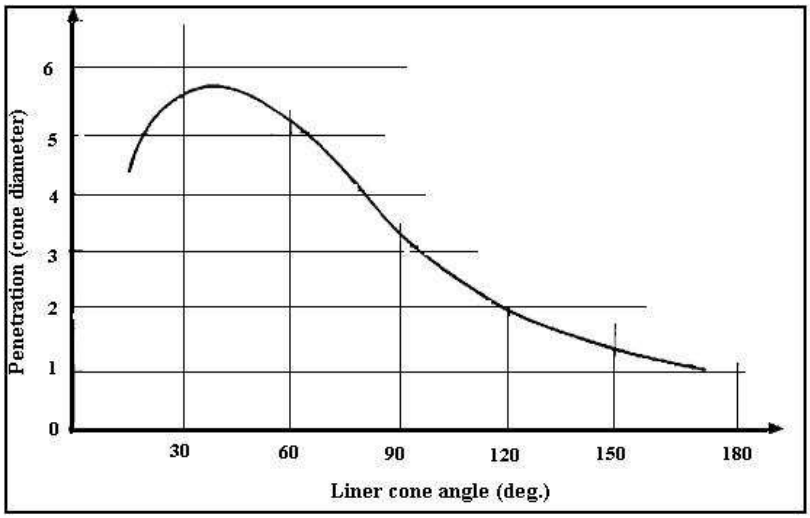

Figure 2-7 Penetration versus liner cone angle [26].

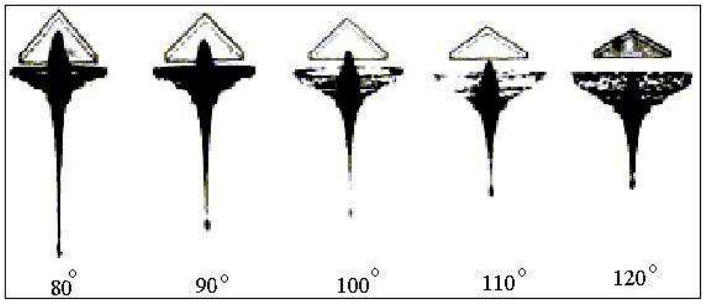

Figure 2-8 Shaped charge jet profile at different cone angle [6].

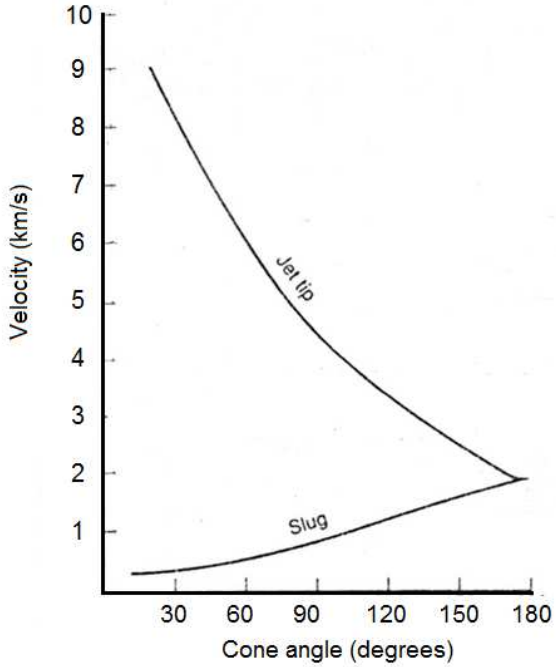

Figure 2-9 Jet and tail velocities as a function of cone angle [26].

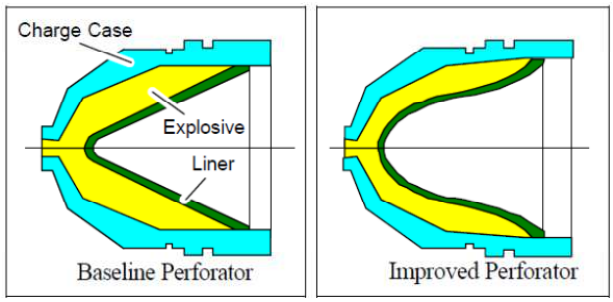

Figure 2-10 The original and modified liner shapes [17].

The optimum thickness of a liner has been shown experimentally to be about 2% of the cone diameter [26], [27]. In addition, divergent profile of varied thickness liner was designed according to desired jet characteristics. Renfre et al. [12] had performed an experimental testing of shaped charge of varied liner thickness, in which the liner thickness at the apex is 10-40% greater than that at the liner base. The thickness of the liner between the apex and the liner base is tapered smoothly. This shaped charge was tested against concrete target according to Standard API-RP43 (section II), where the resultant achieved penetration depth was 12 inches (4.5 times the charge diameter) and one inch in diameter.

2.2.4 Detonating wave form

The velocity, the length and the cohesion of the jet depend on the manner, in which the liner collapse, which is strongly influenced by the shape of the detonation wave (DW)

when it meets the liner. The DW travels inside the explosive in the form of hemispheres. The angle between the tangent to these hemispheres and the liner defines the value of the deflection angle, which has a great effect on the jet and the slug masses and velocities [28]. Moreover, it will determine the magnitude of the collapse angle, which is the key parameter to determine the jet formation. In general, a more cohesive jet is formed if a smaller angle is induced. This improvement can be achieved using a spacer (inert or active) in the explosive. This spacer is a barrier embedded in the explosive charge between the cavity and the rear initiation point in order to delay the DW. Such spacer has been referred by various researchers as wave-shaper, wave-former or explosive lense [26].

Figure 2-11 shows the plots of detonation wave of two conical shaped charges (CSC) indicating the shape of the DW as it meets the liner. The left shaped charge is without wave shaper, while the right one has a wave shaper of a spherical shape. Smaller incidence inclination angle is preferred for a shaped charge design improvement as it will increase the real collapse velocity of liner elements and therefore the jet element velocities will be increased. Further analysis of shaped charge jet formation will be discussed in detail in Chapter 3.

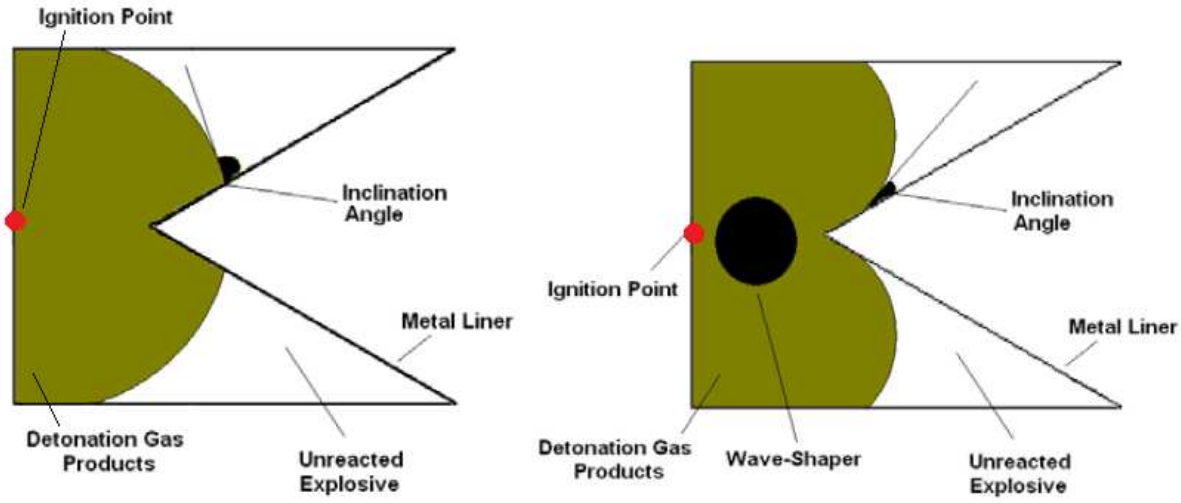

Figure 2-11 The shape of the DW travelling inside CSC explosive charges with and without wave shaper.

2.2.5 Symmetry

Any change in the shaped charge symmetry will produce a weak jet, in which curved path and radial velocity components are observed leading to the decrease of the penetration depth [29], [30].

2.2.6 Liner materials

2.2.6.1 Introduction

Recently, researchers have shown an increased interest in the different liner materials and their manufacturing techniques. Held [31] showed different materials that could be used as liners and their ranking according to the predicted penetration performance in terms of liner density and jet velocity, as illustrated in Table 2-2. In general, the characteristics of a good candidate material for shaped charge liner include [6]:

- High density
- High melt temperature
- High bulk speed of sound
- Fine grain and proper grain orientation
- Availability and cost
- Easiness of fabrication
- High dynamic strength and ductility

Table 2-2 Penetration potential ranking of the different liner materials [31].

Liner Material	Al	Ni	Cu	Mo	Ta	U	W
Density (g/cm^3)	2.7	8.8	8.9	10.0	16.6	18.5	19.4
Bulk sound speed (km/s)	5.4	4.4	4.3	4.9	2.4	2.5	4.0
$V_{jo,max}$ (km/s)	12.3	10.1	9.8	11.3	5.4	5.7	9.2
Jet performance $V_{jo,\max}\sqrt{\rho_j}$ $(kg/m)^{0.5}/s$	20.2	30.0	29.2	35.7	22.0	22.0	40.5
Ranking	7	3	4	2	6	5	1

Because tungsten has great density exceeding 19 g/cm^3, high melting point of 3410 ^oC, high sound speed and great ductility, it has been widely used in anti-armour technology as a shaped charge liner material [32]. However, the most commonly used liner material is copper. It flows easily to produce a coherent jet when it is deformed by the detonation wave. This copper material should be oxygen-free with high conductivity and low impurity according to ASTM standard C101OO LAW F68-77 temper 070 [12]. Gold is denser and has greater dynamic ductility than copper. In theory, it should achieve better penetration performance than other materials [26].

In 2001, Bourne et al. [13] used zirconium, silver, titanium and depleted uranium to study their shaped charge jet characteristics when same liner masses were used to compare the

cumulative jet length produced from these metal liners. They designed a hemispherical liner to test the liner material performance. This design produced a jet containing 80% of the full liner mass. The characteristics of these jets for different liner materials including copper are listed in Table 2-3 [13].

Table 2-3 The produced jet characteristics using different liner materials [13].

Metal	Jet length (mm)	V_{tip} (km/s)	V_{tail} (km/s)	Breakup time (μs)	Material ductility factor (Q)
Silver (Ag)	1456.0	6.48	3.01	419.6	181.90
Zirconium (Zr)	2058.9	6.75	2.34	603.8	246.10
Titanium (Ti)	1327.4	6.34	2.99	396.2	175.70
Depletted Uranium (DU)	1700.0	6.40	3.30	548.4	217.67
Copper (Cu)	1130.5	5.90	2.56	338.5	161.53

It was concluded that silver, zirconium and depleted uranium liner materials can produce more ductile jets than copper with larger breakup times and effective jet lengths than those of the copper liner material. However, toxicity of the depleted uranium prevents its usage in liner manufacturing [13].

Bimetallic liners or multi-material alloys have been fabricated and successfully tested by many researchers. In 1996, Wang and Zhu [33] stated that the liner alloys could be manufactured from Copper (Cu), Tungsten (W), Nickel (Ni) and Tellurium (Te). They showed that the penetration capability of a conical shaped charge in Figure 2-12 was increased by 30% of copper by using copper tungsten alloy liners due to the increase in both the breakup time and the jet material density. The alloy was produced by infiltrating technology using W-Cu alloy 80-20% weight ratios with traces of Nickel material (about 0.5%). The produced alloy liner has a density of 15.2g/cm^3 and a hardness HB number of 182. The main difference between a copper-tungsten jet and a copper jet is that the copper tungsten jet produces fragmentation or disintegrating spray particles rather than segmented jets in the case of copper liner. It has been shown that the copper-tungsten jet produced larger penetration depth than copper jet especially at the short stand-off distances of 3CD, where CD is the shaped charge calibre) under the same experimental conditions. However, the copper-tungsten jet exhibited an anomalous behaviour at large stand-off distance (≥3 CD) as shown in Figure 2-13, due to the incoherency of the jet tip and the radial movement of the fragmented elements near the particulated jet tip, as illustrated in Figure 2-14.

In 1998, Davinson and Pratt [17] modified the design of well perforator to increase its penetration depth into concrete target from 105 cm to 126 cm. The improved bell shape liner was manufactured by low cost powder pressing technique using copper and tungsten powders with average density of 11.4 g/ccm.

In 2001, Lee [11] used a bronze (90% of copper and 10% Sn) in the lower portion of the liner near the apex of 1 cm hole diameter; while the other part of the hemispherical liner was made of copper. This configuration demonstrated an efficient design to generate a bulged jet with large crater diameter into the Westerly granite.

In 2001, Glenn et al. [16] used tungsten alloy liner to study the effect of surrounding medium on the jet characteristics and the penetration potential of such perforators. The surrounding media was pressurized by inert gases hydrogen and helium. The compacted powder liner consists of 45.2% tungsten (by weight), 11.05% tin, 43.19% copper, 0.53% graphite and 0.03% lubricating oil. The produced density of the liner was 11.19 g/cm^3. It was found that the increase of the surrounding inert gas pressure increases the coherency of the jet and hence increases the penetration depth.

In 2008, Bogdan and Zenon [15] used electrolytic copper (ECu) and tungsten (W) powders to produce some liners of (ECu/W) by the matrix press moulding method. The final dimensions of the liner were achieved by further processing, such as low temperature sintering and machining of the pressed metal powder liners. It has been found that the liners made from (ECu/W) exhibited a lower jet tip velocity than that of the monolithic Cu. However it exhibited a higher depth of penetration due to its high density (12.5 g/cm^3) [15]. Figure 2-15 illustrates the coherent jet profile produced from ECu/W alloy at different times.

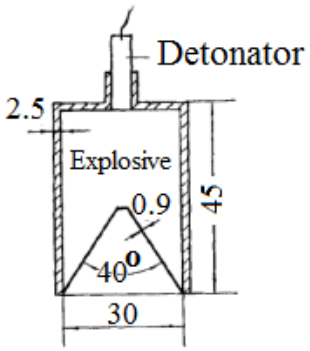

Figure 2-12 The shaped charge in Wang and Zhu [33].

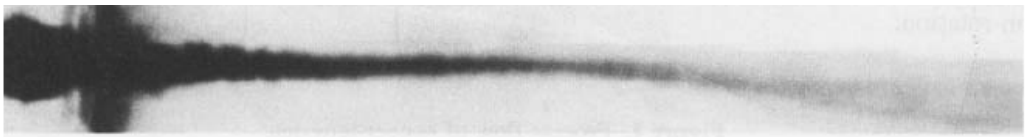

Figure 2-13 Anomalous behavior of Cu-W jet at large stand-off distance [33].

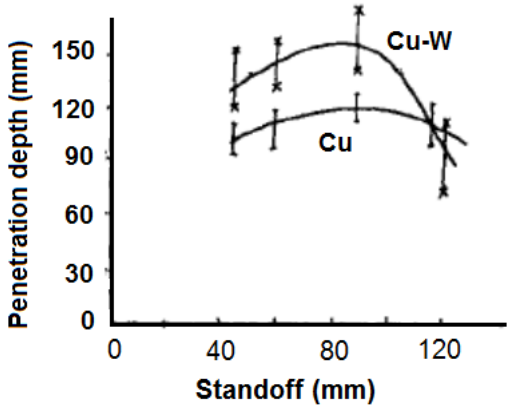

Figure 2-14 Variation of penetration depth with stand-off distance for Cu-W and Cu jets [33].

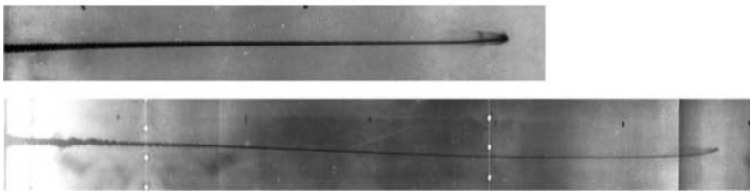

Figure 2-15 The radiographs of the jet formed by ECu/W powder after 50 and 90 μs from initiation. Lengths of jets: 292 and 572 mm corresponding to instantaneous jet velocity of 7.25 and 7.0 km/s, respectively [15].

2.2.6.2 Liner material grain size

The jet cohesion, breakup time and effective jet length are the predominant governing parameters affecting the penetration depth of a shaped charge into target material, which depend on the grain size and crystal shape of the liner material [34]. Many papers have been published to discuss the effect of grain size of liner material on its mechanical properties and the validity of Hall-Petch relation over wide range of copper grain size from nano meter to hundred micrometres. For example, Gertsman et al. [35] measured the yield strength of copper with different grain size particles and compared the measured yield strength with that obtained by the Hall-Petch relation:

$$\sigma_y = \sigma_o + kd^{-a} \qquad 2\text{-}1$$

where σ_y is the yield stress, d is the average grain size, σ_o and k are material constants and a = 0.5 [35].

The apparatus used to determine the yield stress was miniaturized disk bend test (MDBT). The copper sample with micrometer grain size was produced from copper rod of diameter 2mm and 4N purity (99.99). The produced sample was 0.2mm thickness and annealed at 300-600 ^oC for 30 minutes to produce different grain sizes. The nano copper was produced by the evaporation of pure copper from tungsten boat under 1kPa pressure of helium and then compacted under vacuum to produce a pellet of 0.3mm thickness [35].

It was found that the yield stress of the coarse grain size could be approximated by Eq. (2-1), where σ_o =92(±12) MPa, *k*=399(±61) MPa/$\mu m^{-0.5}$ and a=0.5.

However, the classic Hall–Petch relation could not be applied to nano-crystal copper because of the lattice dislocation that can move across the crystallite of a polycrystalline. It was difficult to deduce global equation governing the dependence of yield strength on the entire grain size range of the copper material. But, an empirical relation based on experimental test was suggested by Gertsman et al. [35] :

$$\sigma_y = 104.9+111.8e^{(-d/10.3)}+54.9\ e^{(-d/135.6)}+235.6\ e^{(-d/0.13)} \qquad 2\text{-}2$$

where σ_y is in MPa and d in μm.

Another study of the relationship between average grain size and mechanical properties of copper used as shaped charge liner was investigated by Meyers et al. [36]. They performed an experimental investigation on pure copper OFHC (4N purity) in order to correlate the relation between the average grain size of copper and the resulted mechanical strength under severe plastic deformation [36]. The experimental work was performed by a flyer plate of 4.7mm thickness stainless steel accelerated by PBX 9501 explosive to an impact velocity of 2.2 km/s. The purpose of this experiment is to create exactly the same conditions of the high pressure and strain-rate as those during the shaped charge liner collapse mechanism. The impact pressure of the flyer plate was approximately 50 GPa, while the pulse time duration was only 2μs [36]. It has been shown that the Hall-Petch relation is not applicable in the Nano-scale grain size [36].

In 1995, Fujiwara and Abiko [37] tested the mechanical properties of three copper samples of 3N, 6N and 8N with average grain size of 30 μm, 50 μm and 100 μm, respectively,

under strain-rate of 4.2×10^{-5} s^{-1}. It was found that both yield and maximum stresses in 3N sample were higher than those of both 6N and 8N samples except that the ductility of 3N (82%) is lower than that of the others (91% and 96% for 6N and 8N respectively) due to the effect of grain size on the ductility as shown in Figure 2-16.

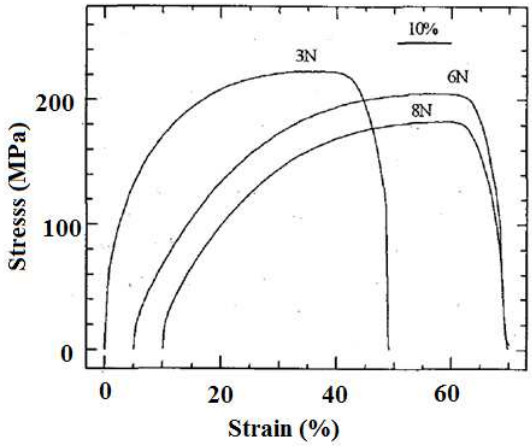

Figure 2-16 Stress-strain curves of 3N, 6N and 8N copper samples at strain-rate of 4.2×10^{-5} s^{-1} [37].

In 1993, Bourne et al. [34] used copper liner manufactured by shear forming in order to investigate the effect of both grain size and texture severity on the jet length and its breakup time. They used both Defence Research Agency (DRA) analytical model JETPEN and flash x-ray to determine the fragmentation of shaped charge jet and particulation time as well as effective jet length. In 1996, Renfre et al. [12] confirmed that the spinning or flow turn machining of the copper material affects not only the liner performance during detonation, but also the grain shape orientation, which has a direct relation to breakup time.

In Table 2-4, nine copper liner samples were used to record both effective jet length and breakup time of the jet. The used shaped charge has a calibre of 102mm and height of 151mm. The cone apex angle is 60^{o} and the liner wall thickness is 2mm. The 3mm thickness casing is made of aluminium material [34].

Table 2-4 Breakup time and effective jet length for nine different copper samples.

Liner code	Average grain diameter (μm)	Breakup time (μs)	Effective jet length (mm)
ME1A	10	195	1450-1500
IE2C	15	172	1300-1250
IE2B	20	172	1270-1280
IE1B	22	174	1248-1330
IE1A	26	182	1400-1330
E175A	42	161	1175
IE1C	43	172	1190-1350
IE2D	43	149	1000-1140
IEE1A	48	126	870-880

In addition to the well-known Hall-Petch relation between average grain size and liner mechanical properties, Zerilli–Armstrong model [38], as discussed by Bourne et al. [13], describes the relation among the deviatoric flow stresses (σ), plastic strain (ε), strain-rate ($\dot{\varepsilon}$), temperature (T) and grain size (d).

The general form of Zerilli–Armstrong model is [38]:

$$\sigma = C_1 \varepsilon^n e^{(-C_2 T + C_3 T \ln \dot{\varepsilon})} + C_4 + C_5 d^{-0.5} + C_6 \varepsilon^m \qquad 2\text{-}3$$

where parameters C_1, C_2, C_3, C_4, C_5, C_6, m and n are constants given in Table 2-5, d is the average grain size in (mm) and $\dot{\varepsilon}$ is the strain-rate in (s^{-1}).

The first term represents the effect of the thermal activation on the motion of dislocations. The second and the third terms represent the additional stress due to the grain size effect (i.e. Hall-Petch effect), while the last term represents the strain hardening. This equation describes the stress-strain behaviour of the bcc (body centred cubic), fcc (face centred cubic) and hcp (hexagonal close packed) materials.

Table 2-5 The constants of the Zerilli–Armstrong model [13].

Metal	C_1 (MPa)	C_2 (K^{-1})	C_3 (K^{-1})	C_4 (MPa)	C_5 ($MPa.mm^{0.5}$)	C_6 (MPa)	n	m
Cu	980	0.0028	0.000115	46.5	5	0	0.5	0
Ta	1125	0.00535	0.000327	0	19	310	0	0.44
W	16500	0.591	0.000279	0	25.6	860	0	0.443
Mo	937	0.0036	0.000107	0	22.65	647	0	0.401
Zr	600	0.0024	0.000132	21	7.9	76	0	0.51
Ti	1100	0.00226	0.00017	54	14.86	300	0	0.5
Fe	1033	0.00698	0.000415	0	22	266	0	0.289

As a direct measure of the jet efficiency and its dependence on stress, strain and strain-rate, the breakup time model developed by DERA [39] is:

$$t_b = \frac{\pi r_o}{\Delta V_{PL}} - \frac{1}{\dot{\varepsilon}_o} \qquad 2\text{-}4$$

where r_o is the radius of the jet and $\dot{\varepsilon}_o$ is the strain-rate of the jet material, ΔV_{PL} is the maximum plastic wave velocity in the metallic liner (i.e. the velocity difference between two neighbouring jet fragments), which is defined as:

$$\Delta V_{PL} = \sqrt{\frac{1}{\rho_o}\frac{d\sigma}{d\varepsilon}} \qquad 2\text{-}5$$

where ρ_o is the original density of the liner.

Both the breakup time of the jet and the cumulative jet length (breakup time multiplied by jet tip velocity) are inverse functions of the plastic wave velocity [13].

In a separate study, Tian et al. [40] found that changes of the liner microstructure and grain size influence the dynamic behaviour of liner material. Hence, it affects the penetration depth into target materials.

2.2.6.3 Liner crystal shape

For the fine crystal structure, it is expected that particulation time is longer and the transverse movement of the particulated jet elements can be avoided [31]. It was found that the sharpness or severity texture of the liner material has less influence than the grain size effect on the jet breakup time and effective jet length [34].

It was also found that the crystal shape and its deformation due to manufacturing process affect the particulation behaviour in the later time when the jet is fully stretched causing transverse movement of the particulated elements or even jet tumbling [31]. Held verified that the shaped charge jet is very sensitive to the small deviations of the liner structure, which can be amplified in the stage of jet collapse and formation [31]. As a result, a tumbling and spinning particulated jet elements around the jet axis can decrease the jet coherency, and therefore, decrease the penetration performance of the shaped charge jet. Moreover, the shaped charge jet undergoes a dynamic recrytallization due to large deformation and dislocation movement of the grain [32].

2.2.6.4 Liner impurities

Recently, researchers have shown increased interest in the effect of copper material impurities on the ductility of the copper used as shaped charge liners. In 2003, Schwartz et al. [7] described the dependence of cooper ductility on the total type and number of impurity atoms. The copper used was 4N (99.99%) purity and this liner was manufactured by cold forging technique to extrude it to a hollow cone shape. After the cold forging process, the produced liners are annealed at 315^{o}C for one hour or 400^{o}C for 10 minutes to stabilize the microstructure of sulphur doping. Table 2-6 illustrates the impurities percentage in the tested sample in ppm, while Table 2-7 indicates the effect of sulphur content on the breakup time of the shaped charge jet at constant grain size of 40μm [7]. It has been shown that the total number of impurities decreases the ductility of the copper due to the segregation of the impurities at the grain boundaries [7].

In 1995, Fujiwara and Abiko [37] performed experiments on the ultra high purity copper in order to investigate the effect of impurity presence and operating temperatures on the copper ductility. In this study, the ultra high purity copper was produced by electronic beam refining and vacuum melting technique. The tensile test was performed on the ultra high purity copper 6N, 8N and compared with commercial purity copper rod 3N (99.9%) under high vacuum of 7×10^{-4} Pa at a strain-rate of 4.2×10^{-5} s^{-1}. The average grain size for the three copper specimens was 30, 50 and 100 μm for 3N, 6N and 8N, respectively [37]. This implies that the copper impurities have a significant effect on its mechanical properties and performance as a shaped charge liner.

Table 2-6 The impurity presence of the tested samples and its concentration in ppm measured by chemical analysis [7].

Impurity	Concentration (ppm)
H	0.9
C	5
N	< 0.1
O	6
Si	0.2
P	0.4
S	4
Fe	2

Impurity	Concentration (ppm)
Ni	1
As	0.4
Se	0.3
Ag	6.4
Sb	0.3
Pb	0.2
Bi	0.2

Table 2-7 The dependence of the jet breakup time on the sulphur content [7].

Sulphur concentration (ppm)	Breakup time (μs)
3	186
4	185
7	147

2.2.6.5 Strain-rate

It has been demonstrated by Lu et al. [41] that the fracture strain of nano-crystalline copper increases with increasing strain-rate from 6×10^{-5} to $1.8\times10^{3}s^{-1}$. This may be attributed to the creep rate and super-plasticity that have been found in the nano scale metals and alloys at much lower temperatures. The governing deformation mechanism of the nano-scale copper at low temperatures is the grain boundary mechanism rather than lattice dislocation mechanism.

In Ref. [41], nano copper was produced by electro-deposition technique using electro-discharge machining, where the produced copper has an average grain size of 20nm, a purity of 99.993% and oxygen content of 24ppm. Two dog bone samples of the nano copper in Figure 2-17 were prepared for the tensile test at both low and high strain-rates. The low strain-rate test at 6×10^{-5} to $6\times10^{-1}s^{-1}$ were conducted using standard uniaxial tensile Shimadzu servo-hydraulic test machine (1 kN). The high strain-rate test at 1.8×10^{3} s^{-1} was conducted using rotating disk-bar tensile impact apparatus [41].

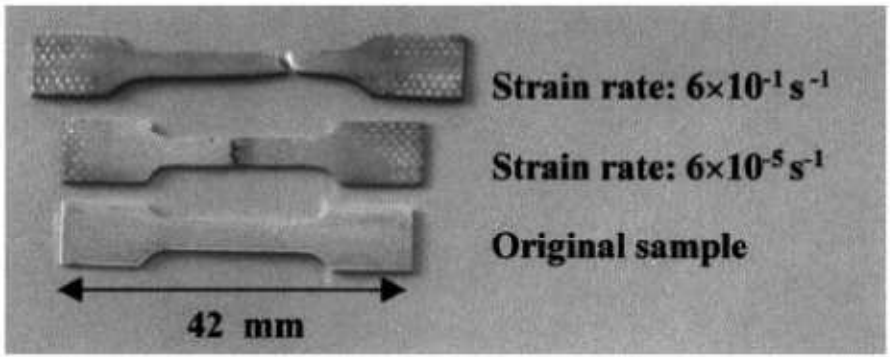

Figure 2-17 Dogbone samples of the nano copper [41].

It was found from the experiments that the fracture strain increases from 15% to 39% when the strain-rate increases from 6×10^{-5} to $6\times10^{-1}s^{-1}$ and increased to 55% at the high strain-rate of $1.8\times10^{3}s^{-1}$. This is different from the behaviour of cg (coarse grain) copper, in which the fracture strain decreases slightly at higher strain-rates [41].

The general relation between material stress and strain-rate:

$$\sigma \propto \dot{\varepsilon}^{m} \qquad 2\text{-}6$$

where m is the strain-rate coefficient. For nano copper, m= 0.036 within the strain-rate range of 6×10^{-5} to $1.8\times10^{3}s^{-1}$. For cg copper, this coefficient was 0.011 in the same strain-rate range [41].

The nano grain copper exhibits much sensitivity of its mechanical properties to the strain-rate because of lattice dislocation activities, grain boundary effects and high resistance to crack nucleation [41].

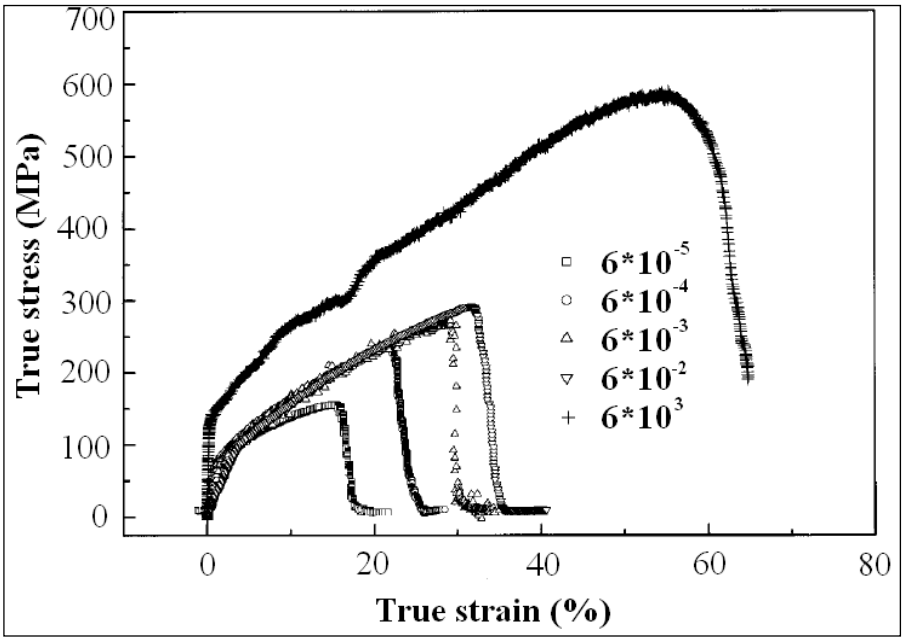

Figure 2-18 The stress-strain curve at different strain-rates [41].

2.2.7 Liner manufacturing

There are many methods that can be used to manufacture the shaped charge liner element. The manufacturing technique is determined according to the applications of the shaped charge. For military warhead applications, high precision and accuracy liners are required, therefore high cost precision forging and flow turn techniques are normally applied. In the oil industry, the low cost manufacturing is the predominant feature of liner production, and thus most liners are made by powder metal technology and low precision forging technique [16]. These methods are briefly introduced in the rest of this section.

2.2.7.1 Flow turning (spinning or shear forming)

The liner plate is deformed by the turning roller against a core as shown in Figure 2-19. The produced liners are fully annealed at 450^{o}C (i.e. for copper) for one hour to reduce strain hardening, hence improving its ductility [34].

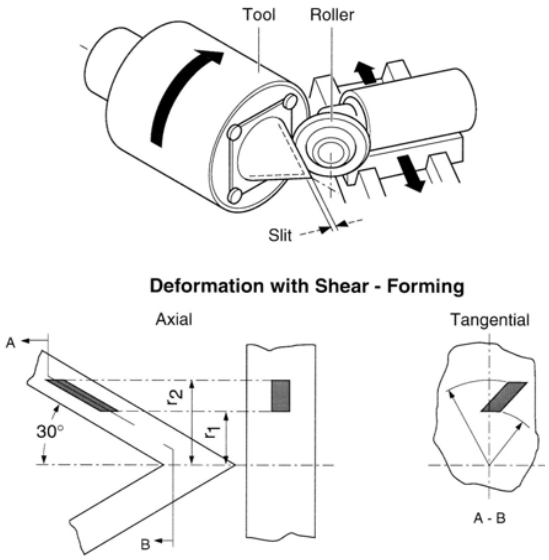

Figure 2-19 Flow turning technique [31].

Advantages:

- The production is completed in one-step,
- Both internal and external surfaces are smooth,
- Small grain size texture is produced,
- There is lower symmetrical deformation around liner axis.

Disadvantages:

A rotational component is observed due to shear process involved in this manufacturing process, which may result in the spinning of the jet during formation.

2.2.7.2 Deep drawing

This is a cheap method for producing small liners in large numbers. The process is shown in Figure 2-20. It has following disadvantages:

- Different crystal structure along the liner height due to the existence of different drawing ring zones,
- Intermediate annealing steps are required for large cones to reduce strain hardening, which is a high cost technique.

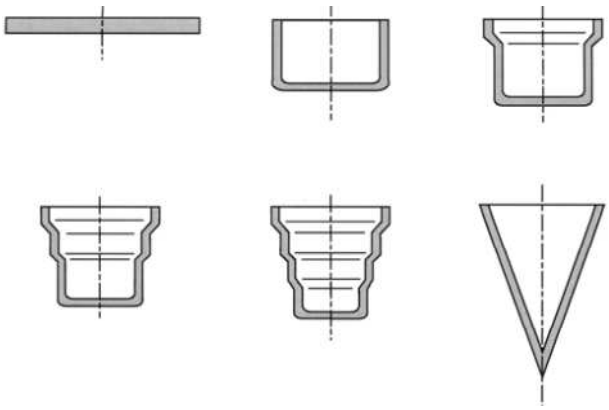

Figure 2-20 Deep drawing technique [31].

2.2.7.3 Cold forging

Cold forging can produce very fine crystal structure. The final liner wall thickness is produced by machining. The process is shown in Figure 2-21.

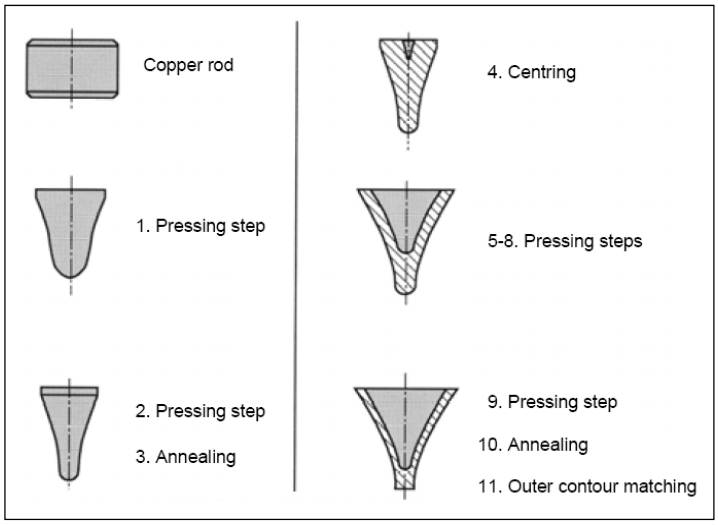

Figure 2-21 Cold forging technique.

2.2.7.4 Warm forging

This technique is characterized by the use of lower step distance than those used in cold forging technique. It can produce very fine crystal structure without spin effect when the temperature is controlled below the re-crystallization temperature of the liner material. This technique, illustrated in Figure 2-22, is still a research topic [31].

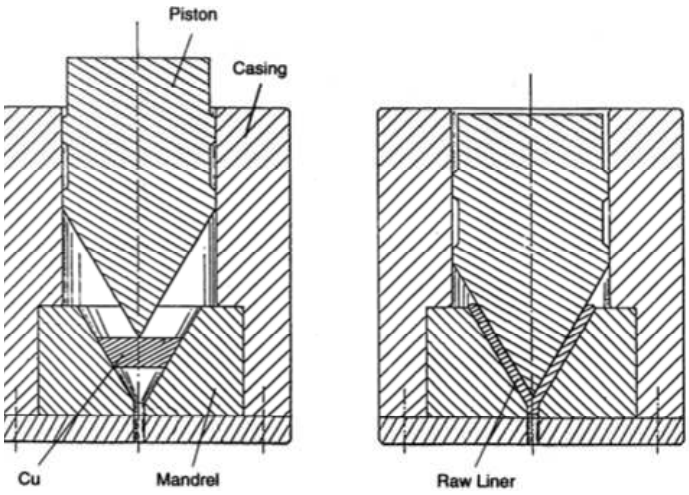

Figure 2-22 Warm forging technique [31].

2.2.7.5 Hot forging

One step liner is produced by the forging of the heated material up to 800^{o}C. The oxidized layer can be removed by machining; hence, it is considered a cheap technique. However, forging above crystallization temperature will produce coarse crystal structure of the product, and therefore, this process could no longer be used for the high precision shaped charge liners.

2.2.7.6 High energy rate fabrication (HERF)

A special impact machine is used, in which the liner rod is pressed at a velocity of around 20m/s, where a very fine crystal structure is produced.

2.2.7.7 Electroforming copper

The very fine grain liner is produced by the anode electron deposition of pure copper on a polished mandrel, i.e. the electroforming technique, in which the electrolytic solution $CuSO_4.7H_2O$ (300g/l) was used. The anode material is 4N pure copper; while the cathode is titanium bar. The substrate, on which the copper ions will be deposited is a stainless steel conical shape molud. The surface of this substrate is mechanically polished in order to allow the separation of the copper liner from it. The produced grains, which are columnar shape parallel to the direction of the growth, could be finer and more equi-axial if the substrate has a high rotational velocity. The average grain size of the copper material produced by this technique is 1-3 μm [40]. Advantages of this technique are the produced small grain size and rotational symmetric structure. This technique could also be applied to produce other liner materials such as Nickel and Cobalt materials. However, this method

has some disadvantages, such as early jet breakup time and brittle jet is produced if smooth surface inhibitors are used. It is a very expensive technique and is time consuming.

2.2.7.8 Infiltrating technology

In 1996, Wang and Zhu [33] manufactured shaped charge conical liner by infiltrating technology using W-Cu alloy of 80:20% mass ratio with traces of Nickel material (about 0.5%). First, the Tungsten powder with average particle size of 6μm and Nickel powder of 5μm average particle size were mixed together with some rubber and copper (3%) in a mixer. The homogeneously mixed powders are pressed under high pressure (200MPa) to form a cylinder of diameter 35mm. The pre-sintered cylinder at 1200^{o}C will be infiltrated by copper powder at 1150^{o}C under protective atmosphere to form the blank, which eventually can be machined to the required liner dimensions. The produced alloy liner has a density of 15.2g/cm^{3} and a hardness of HB number of 182. The whole production steps are illustrated in a schematic drawing of Figure 2-23.

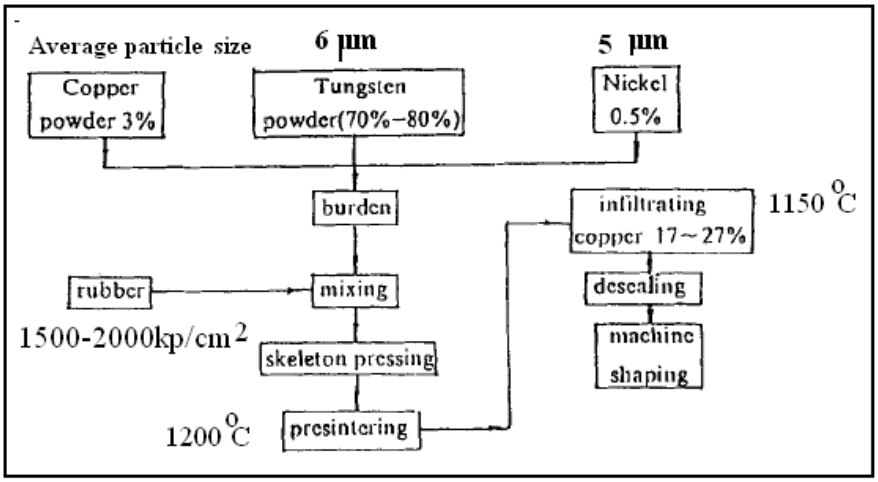

Figure 2-23 Sketch diagram of infiltrating technology [33].

This technique exhibits better coherent jet at short stand-off distances and longer breakup times, hence the penetration capability of the produced shaped charge liner by Wang and Zhu was increased by 30%, especially in the short stand-off distances (3 times calibre) due to the increase in both the breakup time and the jet material density [33]. But, at long stand-off distances, the penetrability dramatically decreases due to the anomalous behaviour of the jet tip incoherency and the radial movement of the fragmented elements near the particulated jet tip.

2.2.7.9 Press moulding or powder metallurgy technique

The metal powder technology is extensively used nowadays to manufacture the liner material of the OWP in order to overcome the problem of the traditional solid liners formed by cold working, whose slug is a carrot-like, which clogs the hole and prevents the hydrocarbon from reaching the well bore [42]. Besides, it is a very low cost manufacture in comparison with the traditional manufacturing techniques [24].

In 2010, Liu and Shen [43] used a Copper-Tungsten powder liner against a steel target. The used shaped charge had a calibre of 36mm and the stand-off distance was 30mm. It exhibited an improved penetration depth at short stand-off distances in comparison with the traditional copper liner.

The powder metallurgy technique was also used by Bogdan and Zenon [15] to produce liners using electrolytic copper (ECu) and tungsten (W) powders. The final dimension of the liner was achieved by further processing, such as low temperature sintering and machining of the pressed metal powder liners. The average grain sizes were 10 μm for the electrolytic copper and 3 μm for the tungsten powders, respectively, and the used liner has base diameter 33.3 mm and a cone angle of 45 degree. It has been found that the liners made from (ECu/W) exhibited a lower jet tip velocity than that of the monolithic Cu. However, it exhibited a higher depth of penetration due to its high density (12.5 g/cm^3) [15].

In 2001, Halliburton energy services located in Alvarado, TX, USA used this technique to produce OMNI perforator charge liner with material composition shown inTable 2-8.

Table 2-8 The mass percentages of the OMNI powder pressed liner composition [44].

Material	Copper	Tungsten	Tin	Graphite
Mass ratio %	43	45	11	1
Function	Binder	Main powder	Binder coating	Lubricant

The maximum penetration was obtained when a 3CD stand-off distance was applied where the total penetration was 203mm (ie: 6 CD into Rolled Homogeneous Armor (RHA)).

Advantages of powder metal liners are [44]

- Optimum performance at short stand-off distance
- Short charge length and short head height
- Low charge cost

Disadvantages of powder metallurgy include

- The material creeping, which is the slight expansion of the powder pressed liner, after assembly and storage [42].

2.2.8 Applied pressure on perforators

The penetration of oil well perforators can be enhanced by at least 25% by applying high pressure light gas atmosphere (hydrogen or helium) during the detonation of shaped charge. This may be attributed to the gas that confines the shaped charge jet before breakup. As a result, the breakup time increases and consequently, the effective jet length increases [16]. Similarly, the well bore fluid pressure also influences the jet penetration. The well bore fluid pressure mainly depends on the well drilling techniques, which can be described as under-balnce and over-balance techniques.

2.2.8.1 Under-balance technique

The detonation of the perforators produces a crushed damage zone of low permeability and porosity due to the production of fine particles and detonation residual debris. For many years, much extensive work has been done in order to minimize the damaged zone area, hence to improve the well productivity. The under-balanced pressure technique is widely used and offers optimizing approach in the oil well. This technique involves the implementation of static wellbore pressure lower than the corresponding rock formation pressure. In the conventional overbalance drilling, the hydrostatic drilling fluid pressure is designed to exceed the pressure of the hydrocarbon fluids in the rock so that fluids and fine particles are lost to the formation [45]. These losses cause damage near wellbore area resulting in severe reduction in the productivity of the well. In under-balncing drilling operations, the hydrostatic drilling fluid pressure is designed to be less than the reservoir hydrocarbon fluids pressure. Thus, there is a continuous flow of hydrocarbon fluid into the well during the drilling process and no near well bore damage occurs, which results in ultimate production. The difference between balanced and unbalanced perforation hole profiles is illustrated in Figure 2-24.

The advantages of under-balance drilling technique include:

a- The prevention of damage by:

- Increasing well productivity
- Decreasing clean-up time [45].

b- The reduction of drilling problems by:

- Eliminating differential sticking

- Increasing the rate of penetration

c- The increase reservoir knowledge by:

- Well testing while drilling
- Identifying prolific zones
- Production steering.

d- The continuation of well production.

Moreover, the under-balance technique known as PURE or (Perforating for Ultimate Reservoir Exploitation) not only cleans the perforation tunnel; but also produces wellbore pressure fluctuations that can causes the effective cleanup due to the surge flow of the liquids. Under-balanced drilling uses a variety of drilling fluids to control the bottom hole pressure, such as water and dizel aerated with light gas nitrogen or natural gas.

Core fluid efficiency (CFE) is defined as the ratio of the steady state flow through a perforated core to theoretical flow through a drilled hole with the same dimensions as that of the perforation [45]. For example, applying under-balance pressure of 16.5MPa for Berea sandstone core is capable of completely cleaning the tunnel resulting in CFE up to 0.92 [45]. The under-balance pressure of 27.6 MPa can produces a clean tunnel with zero perforation skin and permeability from 0.01 to 100 mD (milli Darcy) in the Nugget sandstone rock [45].

The most important factor in the PURE technique is the sharp drop of the wellbore pressure, which results in a few hundreds oscillations a second. These oscillations produces an instantaneous surge flow of the fluids [45].

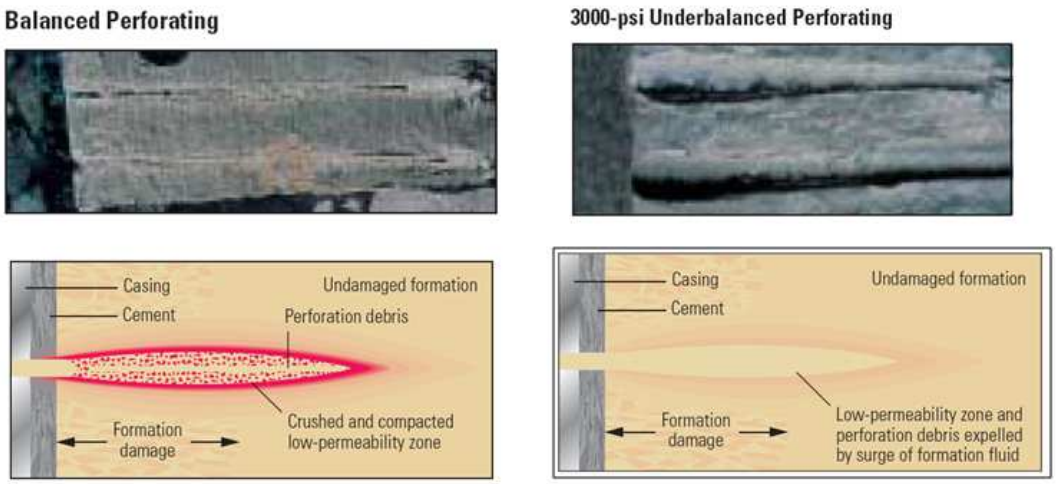

Figure 2-24 The penetration hole; the damaged and the crushed area profiles for both the balanced (left) and the 300-psi under-balanced perforation (right).

Moreover, the difference between the fluid pressure and the rock confining pressure has a significant effect on the penetration depth (i.e. the effective stresses) as discussed by Grove et al. [46].

2.2.8.2 Overbalance (traditional) drilling technique

In 2001, Glenn [16] found that imploding the liner of the perforator into a pressurized (from 1500 to 5000 psi) light inert gas such as hydrogen or helium can improve the penetration potential of the perforator into the reservoir rock by 40% compared with the air medium. It was found that the pressurized light gas does not influence the liner collapse but helps the jet to be confined especially in the latter stages of jet formation; hence the total depth of penetration is increased [16].

The well completion can be accomplished by pressuring fluid into the perforated hole in the rock reservoir to expand the cracks. In this way, the hydrocarbons can be easily pumped to the surface and the well productivity will be increased [16].

The stand-off distance of well gun perforator is limited because of the limited space inside the tube casing. Thus, the decrease in the penetration due to the inadequate stand-off distance can be compensated by the technique provided by Glenn [16] when high pressure light gas (hydrogen or helium) was applied to compensate the reduction of the stand-off distance. The light gas applied to the perforator caused the jet to be confined to its axis, especially in the latter stages of jet instability to improve the total penetration [16].

2.3 Oil well perforator testing according to API-RP43

The recently revised API (American Petroleum Institute) Recommended Procedures for Evaluating Shaped-Charge Perforators (RP43, 5th edition), which includes procedures for testing the penetration of gun perforating system into concrete and measuring well productivity through core fluid efficiency [11]. This edition contains two tests to evaluate the OWP. The first one is the Quality Control (QC) concrete target, while the second is the API target. The test setup according to preliminary QC testing is illustrated in Figure 2-25, while Figure 2-26 illustrates the orientation and dimension of the concrete material to be tested according to API target. A complete description about the mechanical properties of the layers of steel, water and API-concrete is illustrated in Table 2-9.

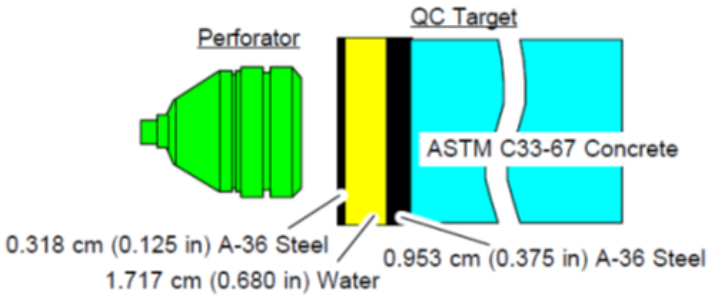

Figure 2-25 Test setup of the perforating gun [17].

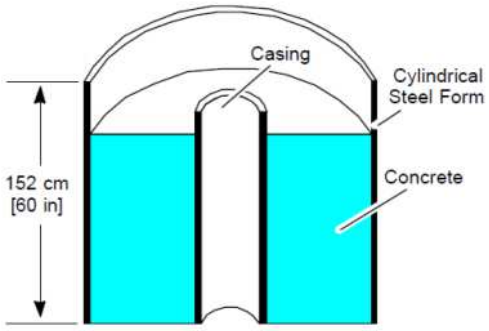

Figure 2-26 A schematic diagram indicating the concrete API testing configuration [17].

Table 2-9 The testing configuration according to API-RP43-API target [17].

Layer	Material	Density (g/cm^3)	Strength (kbar)	Thickness (cm)
Gap	Air	0.0013	-	1.575
Scallop	4140 Steel	7.86	10.3	0.318
Fluid	Water	1	-	1.727
Casing	L80 Steel	7.86	6.2	1.151
Concrete	ASTM C33-67	2.2	0.37	140

2.4 Rock material properties

2.4.1 Introduction

When the OWP is detonated in front of rock target, it forms a metallic jet together with the explosive detonation products create a region of mechanically deformed rock with lower permeability and porosity around the tunnel border [47]. As the jet stretches and penetrates the rock, it loses its kinetic energy in the later stages, and therefore, the rock damage decreases with the distance from the entrance [47]. The reservoir rock has different characteristics that affect its resistance to the penetration by OWP. These characteristics are the material strength related to the confining pressure, the volume fraction of void

filled with pore fluid in the well termed as porosity, and the permeability which is the ability of the pore fluid to flow through the pore cracks network [47].

To study the jet penetration in sandstone saturated by gas and liquid, Karacan et al. [47] used a gun perforator containing 6 g of HMX explosive to face a Berea sandstone core of 10.2cm in diameter and 18.5 cm in length with a porosity around 20% and permeability ranging from 100 to 600 md. They used liquid to saturate the sandstone was a mixture of heavy silicone oil and 1-iododo-decane, which is used as a tracer in the tomography. On the other hand the nitrogen gas was used in the case of gas saturated cores. An under-balance condition of 5.2 MPa was applied during the perforation flow tests, in which the porosity and permeability tests were performed according to API-RP43 standard procedures in order to obtain the core fluid efficiency via the measurement of perforation tunnel dimensions [47].

It was found that both the total penetration depth and average tunnel diameter are higher in case of liquid saturated Berea sandstone compared to that of gas saturated one. Also, the core fluid efficiency for the liquid saturated Berea sandstone showed better flow performance of the core, which is five times better than that of gas saturated one when applying 750 psi under-balance as illustrated in Table 2-10. This good enhancement for the liquid saturated cores may be attributed to the following factors, i.e.:

- The gas saturated cores have a lower cleaning-up capability of fine fragments in the perforated tunnel, thus a lower permeability cores will be obtained,
- The drag force that can cause cleaning-up to the damaged regions is much greater in case of liquid than that of gas because of its high viscosity,
- The liquid has lower compressibility compared to gas. Therefore, the core damage is much lower than the gas case. As a result, the damaged rock and perforation debris are excluded on small area of the core boundary, thus more severe permeability damage in case of gas saturated cores is obtained.

Table 2-10 Tunnel characteristics in both liquid and gas saturated Berea sandstones.

Test layer	Average tunnel diameter (cm)	Total penetration depth (cm)	Core fluid efficiency (CFE)
Berea (liquid saturated)	1.2-1.4	16	0.45
Berea (gas saturated)	0.5-0.7	14	0.11

2.4.2 Rock stresses and penetration of jet into its material

Grove et al. [46] performed some experimental testing on the stressed rocks to investigate the effects of the confining stress and pore fluid pressure on the performance of OWP in terms of the penetration depth into the stressed rock. Both the radial (σ_r) and the axial (σ_a) stresses were considered to study the penetration of OWP into both stressed and unstressed Berea sandstone cores. The applied pressure value was 69 MPa on the Berea sandstone of fine to medium grain with ultimate compression strength of 55MPa, a porosity of 20% and a permeability of 200 md. The standard saturation liquid was a brine solution containing 3% potassium chloride. The purpose of this work was to create exactly the same conditions in down-hole rock at depth of 3km below ground level.

Following assumptions were made in test:

- The pressure in the front of the jet is composed of two components, i.e. dynamic component, which is related to the kinetic energy density of the jet and the static component due to the geologic stresses.
- The penetration of the perforator jet into geologically stressed rock is related to shear strength, which depends on the confining pressure in the rock.
- The principle stresses that characterize the rock are the vertical and the horizontal stresses. Generally the vertical component is much greater than those of the horizontal components. This may be attributed to the greater depth of the rocks near the well pore. At this depth, the confining pressure and the rock overburden make the rocks much stronger than the rocks near the surface [46].

The effect of the well-bore fluid pressure on the effective stress was described by

$$\sigma_{eff} = P_c - aP_p \qquad 2\text{-}7$$

where σ_{eff} is the effective stress or the general measure of net stresses, P_c is the rock confining pressure, P_p is the pore fluid pressure, a = 0.5 is a constant. a is noted as the Biot's poro-elastic constant, pore pressure multiplier or ballistic pore pressure coefficient for high pore pressure. This constant is an intrinsic property of the rock material and varies from 0 to 1 depending on both permeability and porosity of the rock material. For rocks with high porosity and permeability, the parameter "a" tends to be one. Eq.(2-7) reprenents more general situations than Hallec Equation that is a special case of Eq.(2-7) when a=1. The former gives better prediction of penetration depth than the latter [46]. Grove et al.

[46] suggested a model that governs the relation between the penetration depth into Berea sandstone and the effective stress for a wide range of pore pressure, i.e.

$$P = C_1 \sigma^2_{eff} + C_2 \sigma_{eff} + C_3 \qquad 2\text{-}8$$

where P is the normalized penetration depth, C_1, C_2, C_3 are constants calculated from the P- σ_{eff} curve fitting.

In addition to the perforation tunnel caused by the jet, the local damage termed as the cumulative energy effect of the shaped charge liner into rock, is called “Mohaupt effect”. This cumulative damage results from the gaseous products evolved from the shaped charge detonation; these gaseous products, which exhibit a high pressure and temperature together with the resultant metallic jet will cause the cracks to extend behind the initial guide fracture; thus forming wedging action. These cracks into rock can propagate if the tension stresses intensity exceeds the fracture toughness limit [48].

2.5 Summary

This chapter summarized the different applications of the shaped charge devices in both civil and military fields. The application of shaped charge OWP in the oil industry to complete the well was introduced. The different manufacturing techniques for both the solid- and the powder-based liners were reviewed. Moreover, the main parameters governing the performance of the shaped charge devices were discussed.

CHAPTER.3 SHAPED CHARGE JET FORMATION AND PENETRATION MODELS

3.1 Introduction

Upon the detonation of a shaped charge, three different phases are observed. These phases are jet formation, jet breakup and jet interaction with a target. For the first phase, Birkhoff et al. [49] proposed the steady state theory, which was developed into the well known PER (Pugh, Eichelberger and Rostoker) theory, the most commonly used unsteady state model [50]. Also, Godunov et al. in 1975 [51] modified the steady state theory to include the strain-rate effect, which was further developed by Walters [52].

In this chapter, a detailed discussion about the established theories of the jet formation will be performed. The Gurney velocity approximation from the simplest explosive-metal configuration, which may be applied to the conical liner shaped charge, will be discussed. Since the efficiency of the shaped charge is characterized by its breakup time and its penetration capability, a survey about the different empirical formulae of the breakup models and hydrodynamic penetration models will be investigated and discussed in this chapter.

3.1.1 Steady state Birkhoff theory for jet formation

The steady state theory for the shaped charge jet formation was established by Birkhoff et al. [49], which had the following assumptions:

- The liner elements are accelerated instantaneously to the final collapse velocity at the liner axis with the same value V_o,
- A constant jet length equal to the slant cone height is assumed,
- Moreover, the pressure applied to the liner wall is assumed to be equal and the collapse angle 2β is greater than the original cone apex angle 2α,
- Both the velocities and the cross-sectional areas of jet and slug are constants.

Figure 3-1 presents a schematic drawing of the steady state jet collapse process, in which β represents the collapse angle and α is the half cone angle. V_o is the collapse velocity, V_1 is the velocity of the moving coordinates (or stagnation velocity of point A), V_2 is the flow velocity, U_D is the detonation wave speed of the explosive.

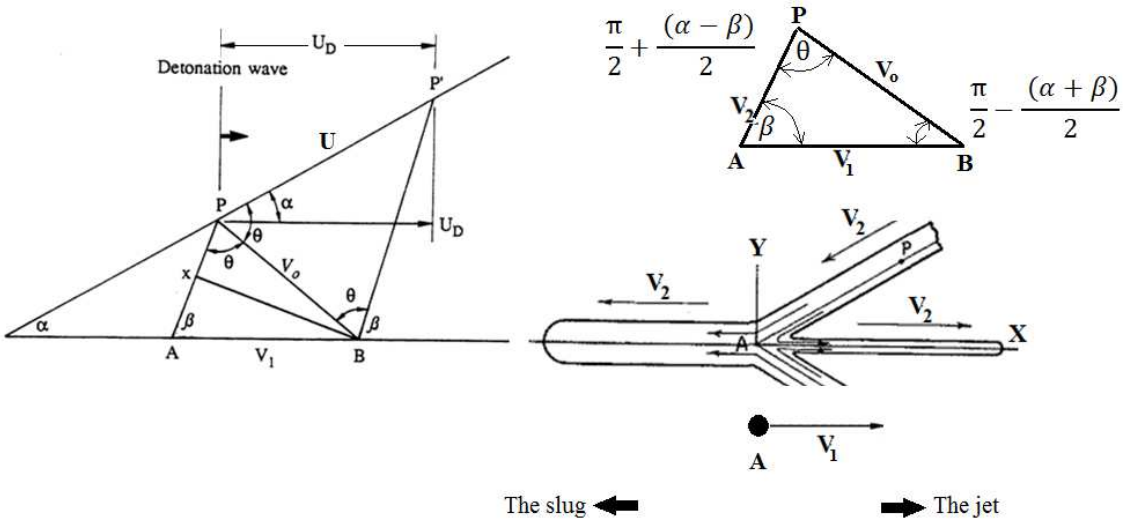

Figure 3-1 The collapse process according to the steady state theory [49].

From the trigonometric relations, the angles in triangle PAB can be calculated as a function of β and α as follow:

$$\angle(\mathrm{PBA}) = \frac{\pi}{2} - \frac{(\alpha+\beta)}{2} \qquad 3\text{-}1$$

$$\angle(\mathrm{BPA}) = \theta = \frac{\pi}{2} + \frac{(\alpha-\beta)}{2} \qquad 3\text{-}2$$

An observer at point A will feel point P approaches him by a velocity V_2, while point A itself moves towards right by a velocity V_1, therefore the velocities of both the jet and the slug can be calculated from

$$V_{jet}=V_1+V_2 \qquad 3\text{-}3$$

$$V_{slug}=V_1-V_2 \qquad 3\text{-}4$$

where V_1 and V_2 are the stagnation and the flow velocities, respectively. They can be estimated according to the sin rule from:

$$\frac{V_o}{sin\,\beta} = \frac{V_1}{\sin\left(\frac{\pi}{2}+\frac{(\alpha-\beta)}{2}\right)} = \frac{V_2}{sin\left(\frac{\pi}{2}-\frac{(\alpha+\beta)}{2}\right)} \qquad 3\text{-}5$$

Thus, V_1 and V_2 can be expressed as

$$V_1 = \frac{V_o cos\,[(\beta-\alpha)/2]}{sin\,\beta} \qquad 3\text{-}6$$

$$V_2 = V_o\left(\frac{cos\,[(\beta-\alpha)/2]}{\tan\beta} + sin\left(\frac{\beta-\alpha}{2}\right)\right) \qquad 3\text{-}7$$

in which the collapse angle β can be calculated from

$$U = \frac{V_o cos\,[(\beta - \alpha)/2]}{\sin(\beta - \alpha)}. \quad 3\text{-}8$$

where U is the deonation wave velocity along the $\overline{PP'}$ and can be calculated by $U = U_D / \cos\alpha$, where U_D is the detonation velocity of the used explosive.

Thus, the jet and slug velocities can be calculated as follow:

$$V_{Jet} = \frac{U_D}{\cos\alpha}\sin(\beta - \alpha)[\csc\beta + ctn\beta + \tan(\frac{\beta - \alpha}{2})] \quad 3\text{-}9$$

$$V_{Slug} = \frac{U_D}{\cos\alpha}\sin(\beta - \alpha)[\csc\beta - ctn\beta - \tan(\frac{\beta - \alpha}{2})] \quad 3\text{-}10$$

The masses of the jet (m_j) and the slug (m_s) can be calculated using the mass and the momentum conservation equations for the jet and the slug. Thus, their masses can be estimated according to the following equations:

$$m_j = \frac{1}{2}m(1 - \cos\beta) \quad 3\text{-}11$$

$$m_s = \frac{1}{2}m(1 + \cos\beta) \quad 3\text{-}12$$

where m is the original mass of the liner.

This model over-predicts the jet tip velocity. The calculated jet length is greater than the slant height of the cone (original length of the liner), which contradicts the initial assumption that the jet length is the same as the slant hight of the cone. Moreover, the steady state model does not consider the velocity gradient, which is the main reason for the jet breakup phenomenon [49].

3.1.2 Unsteady state PER theory

The basic principle of this theory is the same as that of the steady state theory except that the collapse velocity of a liner element is different from other elements depending on its original position on the liner material [50]. The collapse velocity has its maximum value at the apex but decreases gradually toward the base of the cone. It is assumed that the collapse angle increases towards the liner base, therefore, the jet velocity decreases when the new liner elements are added into the jet. PER model is illustrated in Figure 3-2 based on an assumption of constant thickness and cone angle of the liner material [50]. In

addition, the strength of the liner material may be neglected because of the extremely high pressures on liner during the collapse process. Moreover, the formed jet has a velocity gradient, in which the tip travels much faster than the tail leading jet elongation and eventually breakup.

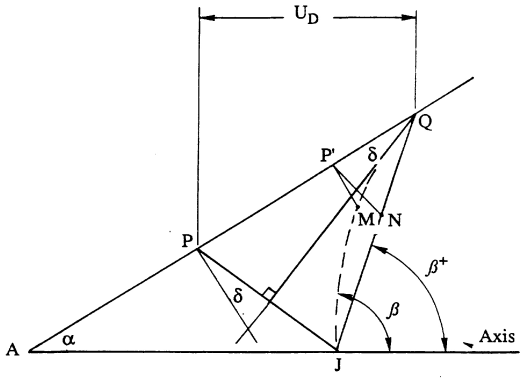

Figure 3-2 A schematic drawing of non steady state jet formation according to PER theory [50].

The element P' would have reached N when element P reached J if their collapse velocities were identical, and therefore, QNJ remains a straight line. However, in PER model, P' has a slower collapse velocity than P, the collapsing liner has a curved contour QMJ as shown in Figure 3-2. As a result, the unsteady state collapse angle β is greater than the steady state collapse angle β^+. This assumption is based on the assumption that each liner element is thin and will not be affected by its neighbours. The liner element is not moving perpendicular to its original surface but has a small (Taylor) deflection angle (δ) with the normal to the liner surface as shown in Figure 3-3. In Ref. [6] Richter proposed a formula to determine the Taylor deflection angle (δ)

$$\frac{1}{2\delta} = \frac{1}{\emptyset_o} + \frac{T_L K \rho_l}{T_e} \qquad 3\text{-}13$$

where ρ_l and T_L are the density and the thickness of the liner wall, respectively. K and $\emptyset_o$ are constants that are determined from the type of the used explosive and the angle of incidence, which the detonation wave makes with the liner. T_e is the thickness of the explosive that drives the liner.

The geometry that shows different angles according to the unsteady state PER theory is illustrated in Figure 3-3.

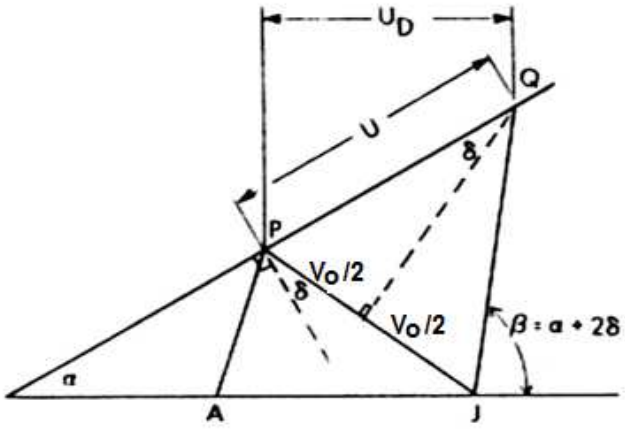

Figure 3-3 Geometry showing parameters in unsteady state theory [50].

$$\delta = \sin^{-1}(V_o/2U) \tag{3-14}$$

where V_o is the collapse velocity of the liner element in a stationary reference system and

$$U = U_D/\cos\alpha\,. \tag{3-15}$$

The relation among the collapse velocity, the stagnation velocity and the flow velocity is illustrated in Figure 3-4, where V_1 and V_2 can be calculated using V_o from the sin rule as follow:

$$\frac{V_o}{\sin\beta} = \frac{V_1}{\sin\left(\frac{\pi}{2} - (\beta - \alpha - \delta)\right)} = \frac{V_2}{\sin\left(\frac{\pi}{2} - (\alpha + \delta)\right)} \tag{3-16}$$

Thus,

$$V_1 = \frac{V_o\cos(\beta - \alpha - \delta)}{\sin\beta} \tag{3-17}$$

$$V_2 = \frac{V_o\cos(\alpha + \delta)}{\sin\beta} \tag{3-18}$$

where V_1 is the velocity of the moving reference (stagnation velocity), V_2 is the element flow velocity in the moving reference and V_o is the collapse velocity of liner elements in the stationary reference.

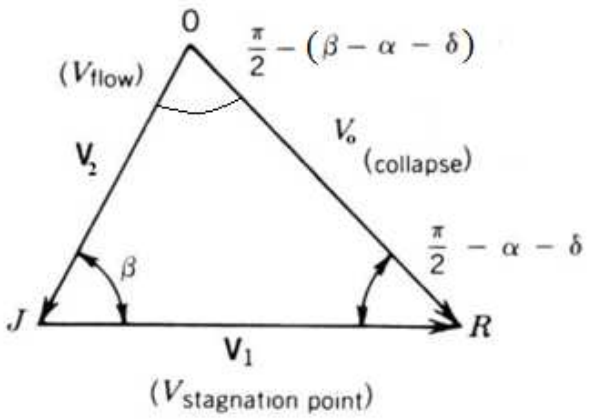

Figure 3-4 Relation among collapse, flow and stagnation velocities.

The collapse angle β for the unsteady state theory, can be calculated according to Hirsh [53] and Liu [54] by

$$\beta = \beta^{+} + \Delta\beta \tag{3-19}$$

where β^{+} is the collapse angle for the steady state theory, where β^{+} is given by

$$\beta^{+} = \alpha + 2\delta\ , \tag{3-20}$$

$$\Delta\beta = \tan^{-1}\left(\frac{-(x\sin\alpha)}{\cos(\alpha+\delta)\cos\delta}\left(\frac{V_o'}{V_o}\right)\right) \tag{3-21}$$

where x is the distance along the liner axis from the apex and prime denotes differentiation with respect to x.

Thus, the jet and the slug velocities can be calculated by:

$$V_{Jet} = V_o \csc\frac{\beta}{2}\cos(\alpha+\delta-\frac{\beta}{2}) \tag{3-22}$$

$$V_{Slug} = V_o \sec\frac{\beta}{2}\sin(\alpha+\delta-\frac{\beta}{2}) \tag{3-23}$$

These equations are valid in both steady state (V_o is constant) and unsteady state (V_o varies) theories.

The masses of the jet and slug satisfy:

$$\frac{dm_j}{dm} = \sin^2\frac{\beta}{2} \tag{3-24}$$

$$\frac{dm_s}{dm} = \cos^2\frac{\beta}{2} \tag{3-25}$$

3.1.3 Modifications to PER theory

Allison and Vitalli [55] obtained good agreement between their experimental results and the PER theory predictions. However, Eichelberger [56] found some discrepancies between the experimental results and predictions from PER model because PER model assumed that the acceleration to the liner axis is instantaneous (i.e. infinite acceleration), as shown in Figure 3-5 (a). Eichelberger [56] suggested that the acceleration of the liner collapse is a constant, which could be calculated by Eq. (3-26) and Figure 3-5 (b). This assumption was used by Carleone et al. [57], where the acceleration is given by

$$a = c\frac{P_{CJ}}{T_L \rho_l} \tag{3-26}$$

where P_{CJ} is the Chapman-Jouguet pressure of the used explosive, T_L and ρ_l are the thickness and density of the liner, respectively, and *c* is an empirical constant.

The more realistic equation describing the liner acceleration was recommended by Randers-Pehrson [58], as illustrated by Eq. (3-27) and Figure 3-5 (c).

$$V(t) = V_O[1 - e^{-\frac{t-t_o}{\tau}}] \tag{3-27}$$

where τ is the time constant and could be calculated from the following equation:

$$\tau = c_1\frac{MV_O}{P_{CJ}} + c_2 \tag{3-28}$$

wher M is the original mass per unit area of the liner and c_1 and c_2 are empirical constants.

Theoretically, the apex portion of the liner should have its maximum velocity because it has the maximum explosive-liner mass ratio. However, this is not the case because the liner material near the apex does not have sufficient time to reach its theoretical collapse velocity, and therefore, the first collapsed elements do not posses the maximum velocity. Instead, the elements that collapse after the apex elements will have the maximum velocity. This piling up of the velocity will cause a phenomenon called the inverse velocity gradient as illustrated in Figure 3-6.

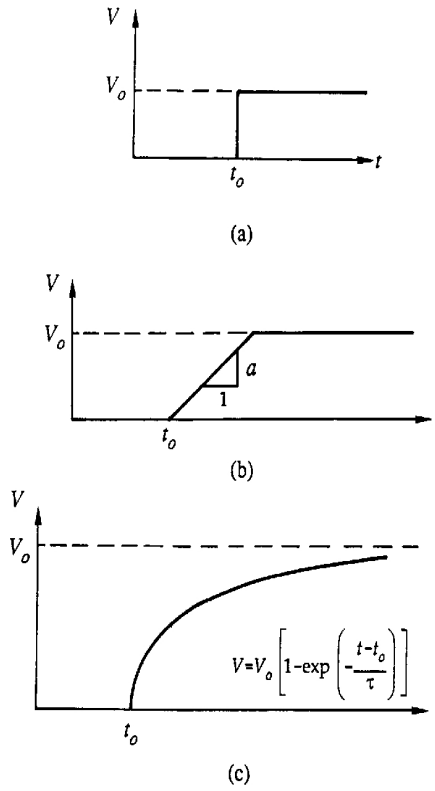

Figure 3-5 The acceleration of the liner element with the time, (a) infinite acceleration, (b) linear, (c) exponential.

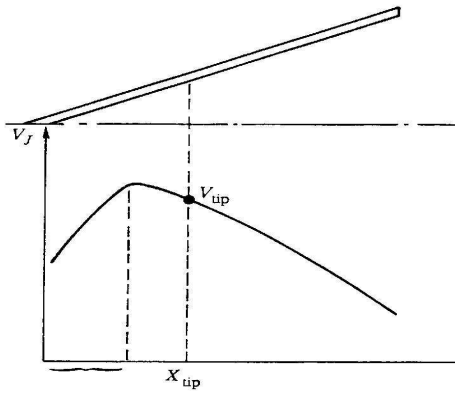

Figure 3-6 The inverse velocity gradient [6].

Many authors have attempted to account for the dependence of jet velocity on the shape of the detonation wave when it meets the metallic liner. Behrmann and Birnbaum [59] and Carleone [60] modified the PER jet formation model to consider the effect of the detonation wave on the jet formation.

The detonation velocity of the detonated explosive along the liner surface (U) is replaced by $U_D/\cos\zeta(x)$ where U_D is the detonation velocity of the used explosive and $\zeta(x)$ is the

angle between the normal to the detonation wave front and the liner surface. Therefore, the Taylor deflection angle, Eq.(3-14) is generalized to be:

$$\sin\delta = \frac{V_o \cos\zeta}{2U_D}. \qquad 3\text{-}29$$

3.1.4 Jet elongation behaviour

Since there is a velocity gradient between the jet tip and its tail, the jet elongates (or stretches) during its flight. To study the jet stretching behaviour, the position of each jet element at any time is expressed in terms of its initial position (x) and time. The element jet position at certain time (t) can be estimated by:

$$z(x,t) = z_o(x) + (t - t_o)V_j(x) \qquad 3\text{-}30$$

where z is the coordinate measured along the central axis of the shaped charge with an origin of user's choice. (i.e. the Lagrangian liner element position). t_o is time when the jet element just reaches the jet axis. When $t=t_o$ then $z=z_o$. Using the above expression and assuming the jet incompressibility, time dependent jet length can be determined [6].

3.2 The Gurney velocity approximation

3.2.1 Introduction to Gurney formulae

The model of an explosively-driven metal is used to predict the fragmentation velocities, the flyer plate motions and the collapse velocities of the shaped charge liners. Many authors have attempted to deduce simple relations governing the driven metal velocity under the effect of detonation gaseous products. Gurney [61], Thomas [62] and Sterne [63] tried to identify the chemical energy liberated from the detonation of high explosive that could be imparted to the metal in contact with the explosive, causing its acceleration and attaining terminal velocity [6]. This energy is called Gurney energy (E) and is considered as an intrinsic property for each explosive. It was defined as the part of the total chemical energy of explosive that are released during detonation and converted to the kinetic energy of the metal. The final kinetic energy from the detonation of explosive was partitioned between the kinetic energy of the driven metal and the gaseous product by an estimated linear velocity profile. To simplify the calculations of the terminal velocity of the metal, following assumptions were normally made:

- The detonation products are assumed to expand uniformly with constant density;

- Rarefaction and shock wave effect within the solid metals due to shock waves are neglected;
- The total Gurney energy is divided into the kinetic energy of the gas expansion and the kinetic energy of the driven elements in contact with the explosive.

The Gurney model was essentially based on the principles of momentum and energy conservations. It could be applied to any one-dimensional explosive-metal interaction system. The Gurney approximation exhibits high accuracy for the prediction of the final metal velocity over the range of mass ratio between metal (M) and explosive (C) from 0.1 to 10 [6].

Many investigators introduced their analytical formulae used to determine the Gurney velocity [64]. Kennedy [65] and Jones et al. [66] discussed the most well-known configurations of metal and explosive. But for the common shaped charges, the liner collapse velocity was determined using the formulae derived by Chou and Flis [67], Duvall et al. [68] and Shushko et al. [69]. Hirsch [70] extended the Gurney model to small shaped charges, whereas he also deduced another formula considering the effect of the confinement of the charge on the collapse velocity [54, 71].

These studies show that the terminal velocity of the metal depends on the configurations of the metal-explosive interactions, the explosive Gurney energy and the mass ratio M/C.

3.2.2 Determination of Gurney energy and Gurney velocity

Kennedy [65] provided an easy approximation to determine the Gurney energy for some explosives. This approximation is:

$$E = 0.7\ Q_v \qquad 3\text{-}31$$

where Q_v is the heat of explosion of the explosive. However, for most commonly used explosives, E varies between 0.61 Q_v and 0.7Q_v.

In 2006, Keshavarz and Abolfazl [22] extended this definition to include the detonation gaseous and solid products and their heat of formation. The proposed new relationship between E and Qv is similar to those calculated by the existing approximations for a range of different exolosives. In 2002, Koch et al. [72] used the law of energy conservation to get a relation between the explosive detonation velocity and its Gurney velocity ($\sqrt{2E}$). They applied the law of energy conservation to different explosive metal configuration, symmetrical plates, cylinder filled with explosive core and hollow metallic sphere filled

with a solid explosive. For common explosives, it was found that the Gurney velocity $\sqrt{2E}$ = U_D/3.08, where U_D is the detonation velocity of the explosive, which generally agrees with existing estimations [72]. Furthermore, Gurney velocity has been experimentally determined for certain explosives, which are listed in Table 3-1. The average value calculated for these explosives is 3.19 with a standard deviation of 0.2, which means that this formula presents a reliable tool to estimate the Gurney velocity for certain explosives based on their detonation velocity.

Table 3-1 Explosive characteristics and Gurney velocity for some common explosives [72].

Explosive	Density (g/cm^3)	U_D (km/s)	$(2E)^{1/2}$ (km/s)	$U_D/(2E)^{1/2}$
Comp B.	1.717	7.89	2.35	3.36
HMX	1.89	9.11	2.97	3.07
LX-14	1.835	8.83	2.80	3.15
PETN	1.76	8.26	2.93	2.82
RDX	1.59	8.25	2.45	3.37
TNT	1.63	6.73	2.04	3.32
Tetryl	1.63	7.50	2.27	3.30

3.2.3 Formulae for different configurations

Many authors investigated the terminal velocity of different configuration models in order to deduce a relation connecting the metal velocity as a function of the Gurney velocity and the mass ratio between explosive and metal. In 1943, Gurney [61] deduced the well-known formulae for the cylindrical and spherical configurations. In 1967 Henry [73] made a complete review of Gurney approximations. In 1970, Kennedy [65] independently got the same formulae. The different formulae for the open faced sandwich, the symmetrical sandwich the cylindrical and spherical shells are listed below with the schematic diagram for each configuration.

3.2.3.1 Open faced sandwich

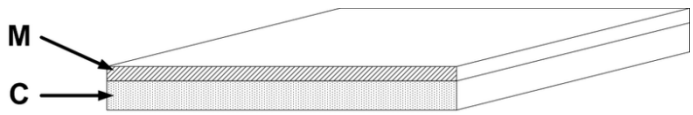

Figure 3-7 The open faced sandwich configuration [6].

$$V = \sqrt{2E}\left[\frac{1+\left(1+2\frac{M}{C}\right)^3}{6\left(1+\frac{M}{C}\right)}+\frac{M}{C}\right]^{-\frac{1}{2}} \qquad 3\text{-}32$$

3.2.3.2 Symmetrical sandwich [74]

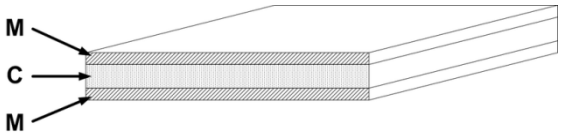

Figure 3-8 The symmetrical configuration.

$$V_M = \sqrt{2E}\left[2\frac{M}{C}+\frac{1}{3}\right]^{-\frac{1}{2}} \qquad 3\text{-}33$$

3.2.3.3 Asymmetrical sandwich [74]

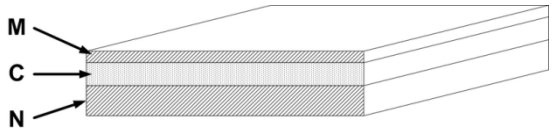

Figure 3-9 The asymmetric configuration.

$$V_M = \sqrt{2E}\left[\frac{M}{N}\frac{M+N}{c}+\frac{1}{3}\right]^{-\frac{1}{2}} \qquad 3\text{-}34$$

$$V_N = \sqrt{2E}\left[\frac{N}{M}\frac{M+N}{c}+\frac{1}{3}\right]^{-\frac{1}{2}} \qquad 3\text{-}35$$

3.2.3.4 Infinitely tamped sandwich

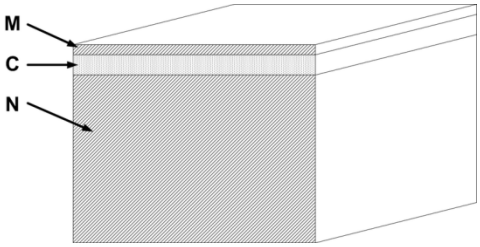

Figure 3-10 The Infinitely tamped sandwich configuration.

$$V_M = \sqrt{2E}\left[\frac{M}{C}+\frac{1}{3}\right]^{-\frac{1}{2}} \qquad 3\text{-}36$$

3.2.3.5 Cylinderical shell

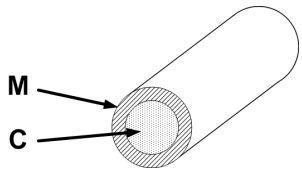

Figure 3-11 The cylindrical configuration [6].

$$V_M = \sqrt{2E}\left[\frac{M}{C}+\frac{1}{2}\right]^{-\frac{1}{2}} \qquad 3\text{-}37$$

3.2.3.6 Spherical shell

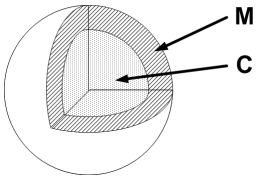

Figure 3-12 The spherical configuration [6].

$$V_M = \sqrt{2E}\left[\frac{M}{C}+\frac{3}{5}\right]^{-\frac{1}{2}} \qquad 3\text{-}38$$

3.2.3.7 Formulae for the Gurney approximation in the shaped charge

As the detonation wave passes the liner, it forces the liner material to collapse towards the axisymmetrical axis of the liner, after which the stretching of the collapsed elements of the liner start to form jet and slug. The collapse velocity is so important that it can be used directly to predict the jet and slug velocities.

The Gurney equations mentioned previously are much simplified and cannot be applied to conical and other liner geometries. Therefore, several Gurney velocity approximations have been derived for shaped charge analysis as discussed in details by Walters and Zukas [6]. One of these approximations was developed by Chou and Flis in 1986 [67], where they summarized the different models used to calculate the terminal collapse velocity starting from the general form of:

$$V_o = \sqrt{2E}\, f(\mu) \qquad 3\text{-}39$$

where μ is the M/C ratio and f(μ) is a function of μ depending on the metal and explosive configuration geometry. They showed that the collapse velocity V_o of the shaped charge liner can be estimated by the approximation used to calculate a single flat plate backed by a slab of explosive:

$$V_o = \sqrt{2E}\left[\frac{3}{4\mu^2 + 5\mu + 1}\right]^{0.5}. \qquad 3\text{-}40$$

For the same flat plate, Duvall et al. [68] used hydrodynamic theory to get a formula provided that the detonation wave propagation is in a direction tangent to the liner. They obtained the following equation by hydrodynamic theory:

$$V_o = U_D\left[1 + \frac{27\mu}{16}\left(1 - \sqrt{1 + ({}^{32}/_{(27\mu)})}\right)\right]. \qquad 3\text{-}41$$

In 1972, Deribas [75] concluded a similar equation:

$$V_o = 1.2U_D\left[\frac{\sqrt{1+32/(27\mu)}-1}{\sqrt{1+32/(27\mu)}+1}\right]. \qquad 3\text{-}42$$

Kleinhanss [76] presented an empirical equation, which, however, does not account for the curvature in geometry such as shaped charge liner, i.e.,

$$V_o = 0.36U_D\, tan^{-1}\left(\frac{2}{3\mu}\right). \qquad 3\text{-}43$$

Kleinhanss [76] also showed experimentally that the liner collapse velocity depends upon the radius of the cylinder explosive charges, i.e.

$$V_o = U_D\left[\frac{r_i - \sqrt{\varepsilon(2r_i - \varepsilon)}}{r_i - \varepsilon}\cdot\frac{1}{[C_o + \varepsilon f(b)]}\right] \qquad 3\text{-}44$$

where ε is the metal liner thickness, $b=r_o-r_i$ is the explosive thickness, r_0 and r_i are the outer and inner explosive radii, repectively. C_o and f(b) are empirical parameters that depend on the used explosive and metal liner.

Chou and Flis [67] reused Gurney model to analyze the liner element velocity under the detonation of explosive cylinder. They included the impulse generated from the explosive into the velocity equation, i.e.

$$V_o = f\left(\mu, \frac{R_o}{R_I}, I\right) \qquad 3\text{-}45$$

where I is the specific impulse, which could be obtained from 2-D hydrocode, R_o and R_I are the outer and inner radius of the explosive, respectively, as illustrated in Figure 3-13.

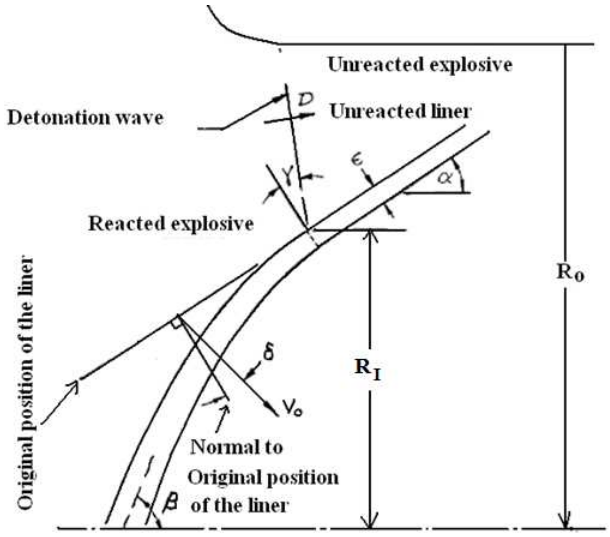

Figure 3-13 A schematic diagram of the collapsing liner under explosive load [67].

3.3 Visco-plastic model and jet coherency

The visco plastic model according to Godunov et al. [51] assumes that the jet flow is an incompressible flow and its stress is dependent upon the strain-rate and viscosity coefficient i.e.

$$\sigma = \sigma_y + \mu\dot{\varepsilon} \qquad 3\text{-}46$$

where σ is the stress, σ_y is the yield stress, $\dot{\varepsilon}$ is the strain-rate and μ is the dynamic viscosity coefficient. Many experiments have been conducted in USSR [77], [78] and USA [52], [79] in order to determine the values of μ, which depends on temperature, pressure and strain-rate. It was found that the dynamic viscosity coefficient ranges from 10^2 to 10^6 poise (i. e. g/cm.s).

Godunov et al. in 1975 [51] calculated the strain-rates for certain shaped charge liners and found that they are in the range of $10^6 s^{-1}$. However, Bauer and Bless [80] showed that the strain-rate in shaped charge jet is in the order of 10^4 s^{-1} based on the measurements of copper cylinder deformed at extreme loading due to explosion. In addition, Chou and

Carleone [81] calculated the strain-rate for a 81mm calibre shaped charge, which was found to be 10^5 s^{-1} for copper liner.

The visco-plasticity is an important model to describe the jet coherency. The coherent jet should have no radial velocity component. Otherwise, after certain travelling distance of jet tip, some particles start to deviate from its travel axis, decreasing the effect of jet on the target. This incoherent jet is called overdriven or diverging jet and could happen when Reynold's number is greater than 2 according to the following equation based on a visco-plastic model proposed in USSR [6]:

$$Re = \frac{T_L V_2 \sin^2 \beta}{\nu(1 - \sin \beta)} \quad 3\text{-}47$$

$$\nu = \frac{\mu}{\rho} \quad 3\text{-}48$$

where T_L is the liner wall thickness, ν is the kinematic viscosity, μ is the jet viscocity, β is the collapse angle and V_2 is the inviscid flow velocity. This equation could be used to determine the critical flow velocity of the jet.

The stagnation velocity V_1 is given by:

$$V_1 = U_D \frac{\sin(\beta - \alpha) - \sin(\beta - \alpha - \emptyset)}{\sin \beta} \quad 3\text{-}49$$

where U_D is detonation wave speed, α is the half of the conical liner apex angle, Ø = 2δ is the plate bending angle. The flow velocity V_2 is given by:

$$V_2 = U_D \frac{\sin(\alpha + \emptyset) - \sin \alpha}{\sin \beta}. \quad 3\text{-}50$$

The jet and slug velocities can be obtained according Eqns.(3-3) and (3-4), respectively.

The visco-plastic model predicts a lower jet velocity than that calculated by PER theory, however, its slug velocity is higher than that of PER theory [6].

To characterize the cohesion of the jet, Walsh et al. [82] concluded that, the jetting occurs only when the fluid is incompressible or if the flow velocity is subsonic [6]. Besides, Chou et al. [83] presented the criteria conditions for jetting formation and jet cohesion i.e.,

a. The flow velocity is subsonic, then a solid coherent jet can always be formed,

b. In the supersonic regimes, the jetting occurs only if collapse angle, β is greater than the critical collapse angle, β_c and incoherent jet is produced.
c. In the supersonic collisions when β is lower than β_c, the jet will not be formed.

As a general rule, for shaped charge with a copper liner, the produced jet will be coherent if the flow velocity of the liner is below critical Mach number 1.2 for the copper material [83].

3.4 Breakup time models

Since shaped charge jet elements have a velocity gradient from its tip to its tail or slug, the shaped charge jet breaksup into small elements at large travelling distances. In the breakup stage, the penetration efficiency of the shaped charge starts to decrease steadily due to the decrease of the effective jet length prior to impact and the presence of the air gaps between the jet segments or particles. Therefore, the understanding of the jet breakup phenomenon and the methods of delaying the onset of jet breakup are the major interests of the shaped charge designer. Recently, many investigators studied this phenomenon, e.g. Cowan [84], Hirsch [4], and Hennequin [85]. They used empirical formulae, hydrocode simulations and one-dimensional analytical models to determine the jet breakup time.

3.4.1 Empirical formulae

A few empirical formulae are presented herein. Hirsch [4] suggested a phenomenological formula for the jet breakup time. This formula calculates the breakup time (t_b) as

$$t_b = \frac{d_{jo}}{V_{PL}}, \tag{3-51}$$

where d_{jo} is the initial diameter of jet element when the elongation starts and V_{PL} is the characteristic plastic velocity or the velocity difference between successive fragments.

Hirsch's formula for breakup time based on Eq. (3-51) and the liner geometry is

$$t_b = \frac{1}{V_{PL}}\sqrt{8RT_L}\sin\left(\frac{\beta}{2}\right) \tag{3-52}$$

where T_L is the original liner thickness, β is the collapse angle and R is the radius of each element from the liner axis.

Hirsch [5] further used SCAN code and a set of experiments with charges of varying liner thicknesses to study the breakup time, in which V_{PL} was found to be a function of liner

thickness and charge diameter. $1/V_{PL}$ was named as specific breakup time of the liner and was given by:

$$\frac{1}{V_{PL}} = 13.886 - 101.49\frac{T_L}{C_D} \qquad 3\text{-}53$$

where C_D is the charge diameter and T_L is the liner element thickness.

Eq. (3-53) predicts reasonable jet breakup times for certain shaped charges. However, its application is limited because it is independent of the stretching rate of the formed jet [86].

Pfeffer [87] deduced an empirical equation to determine the jet breakup time using the results of a two-dimensional hydrocode simulation of jet stability, i.e.

$$t_b = \frac{1.4}{\dot{\varepsilon}} + 48.5\frac{r_o}{C_o} \qquad 3\text{-}54$$

where $\dot{\varepsilon}$ is the initial strain-rate of the jet material, r_o is the initial jet radius, and C_o is the sound speed in the jet material. This model is also limited because it is independent of the jet strength [6].

Haugstad [86] presented an empirical formula based on Eq. (3-46). For the case where μ tends to zero, the breakup time equation can be predicted by

$$t_b = \frac{\alpha d_o}{\sqrt{(\sigma_y/\rho)}} - \frac{1}{\dot{\varepsilon}}, \qquad 3\text{-}55$$

where α is an empirical constant, ρ is the liner material density and d_o is the initial diameter of jet.

For μ >>0, the empirical equation has the following form:

$$t_b = \beta\frac{\mu}{\sigma_y} - \frac{1}{\dot{\varepsilon}} \qquad 3\text{-}56$$

where β is an empirical constant.

Haugstad [86] pointed out that the exact determination of the jet breakup time might not be obtained by this formula since it does not account for material microstructure. Haugstad [86] also concluded that the increase in the breakup time of a shaped charge jet could correlate to the decrease in σ_y and the increase in μ.

Chou and Carleone [88] deduced a formula predicting the breakup time. The formula had good agreements with the experimental measurements and has the following expression:

$$t_b = \frac{r_o}{C_o}\left[3.75 - 0.125\frac{r_o\eta_o}{C_o} + \frac{C_o}{\eta_o r_o}\right] \quad 3\text{-}57$$

where $C_o = \sqrt{\sigma_y/\rho}$, σ_y is the yield strength, η_o is the initial deformation rate of the jet material, which equals to V_{PL}/l_{jo}, where l_{jo} is the initial length of the jet material and V_{PL} is the velocity difference between neighbouring jet fragments and r_o is the initial jet radius when the jet elongation starts. Table 3-2 lists some values of jet yield strength for some common liner materials.

Table 3-2 The yield strength of some liner materials [6].

Liner material	Jet yield strength: σ_y (MPa)
Copper ETP	200
Copper OFHC	270
Aluminum	100

Hennequin [85] developed a new formula providing a better estimation of the jet breakup time and the accumulated length of the jet. To determine the time t_b, only one parameter is needed, which is the fragment shape index I_{FG} that can be calculated by the initial jet length and the final length of the fragment. This parameter characterizes the type of jet material in terms of ductility or brittleness. It was taken to be 1.46 in Hennequin experiments [85]. The equation has the form:

$$t_b = \frac{2r_o}{V_{PL}}\left[I_{FG} + (I_{FG} - 1)\frac{1}{\eta_o}\frac{V_{PL}}{2r_o}\right]. \quad 3\text{-}58$$

The comparison among the above mentioned equations shows that the breakup time of jet predicted by Eq.(3-58) is similar to that predicted by Eq.(3-57), but the former gave a more accurate results than the latter [88].

Held [18] defined the average breakup time of several shaped charges using flash x-ray to calculate the fragments length. He defined the breakup time by

$$\bar{t}_b = \frac{\sum l}{V_{j,o} - V_{j,cut}}, \quad 3\text{-}59$$

where $\sum l$ is the summation of broken-up jet elements, $V_{j,o}$ and $V_{j,cut}$ are the velocities of the jet tip (V_{jo}) and the cut off element (i.e. the velocity of last penetrating element), respectively.

Held also described the quality of the copper liner material by the scaled breakup time, which is defined by

$$\bar{t}_{bs} = \frac{\bar{t}_p}{c_D} \qquad 3\text{-}60$$

where $\bar{t}_{bs}$ is the scaled breakup time and C_D is the charge calibre or liner diameter at the base.

3.4.2 Hydrocode Simulations

Using the Lagrangian code HEMP, Chou and Carleone [89], and Karpp and Simone [90] determined the jet breakup time by following the jet profile changes with time. Karpp and Simone [90] demonstrated that a jet with a uniform initial radius under continuous stretching eventually developed necking, which depends on the wavelength of the initial surface perturbation. They also estimated the strength of copper under dynamic conditions, which was found to be 0.1 GPa. This is needed for the prediction of the jet breakup time. Chou and Carleone [89] used the same code to predict the effects of the yield strength, jet density, the initial disturbance wavelength and its amplitude on jet breakup time. They showed that the perturbation in jet strength or velocity causes plastic instability. The critical wavelength seems independent of the perturbed physical quantity that initiates the instability. Figure 3-14 shows a comparison of their hydrocode simulation with the flash radiograph of a typical jet.

In 1981, Miller [91] used the two-dimensional hydrocode named PISCES in order to predict the breakup time of copper jet. Miller used Steinberg-Guinan constitutive equation in the hydrocode in order to account for the strain hardening and thermal softening by considering the effect of temperature, pressure and large plastic strain. Miller [91] used unconfined BRL-105mm diameter 42^o conical shaped charge to compare the experimental results with the numerical results. It was found that the predicted breakup time for the subsequent elements is longer than that calculated by the hydrocode. Later in 1982, Miller [92] concluded that the difference between the hyrocode simulation and the experimental test was attributed to the random necking of the jet due to imperfect formation of the jet.

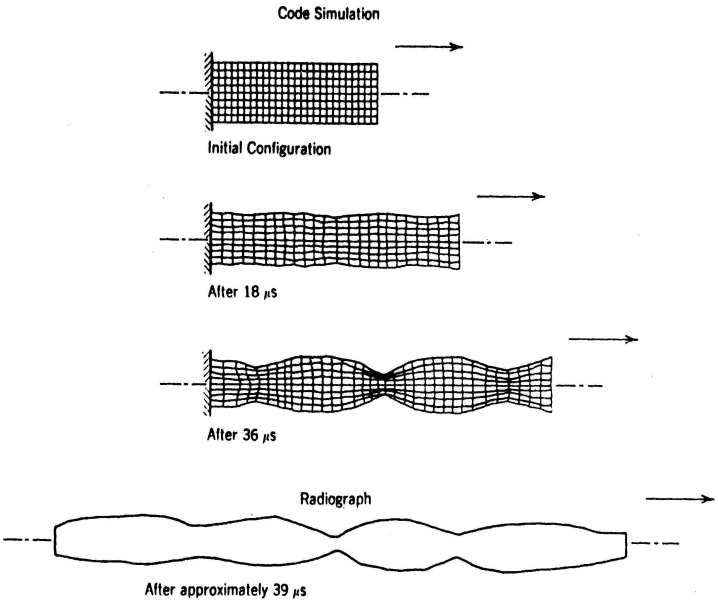

Figure 3-14 Comparison between hydrocode simulation of jet necking due to instability and flash radiograph of a jet at approximately the same time [89].

Osborn used the two-dimensional code named TOODY to study the jet breakup problem while Pfeffer simulated the jet breakup using the STRESS-2 to study the same phenomena [6].

3.4.3 Analytical Models

In 1976, Chou and Carleone [89] studied the jet breakup phenomenon using a one-dimensional model. They focused on the influences of jet material strength and its inertia force and showed that the ratio of jet flow stress to its material density controls the growth of the instability. They predicted that the breakup time increases with the decrease of this ratio.

The one-dimensional model was extended by Carleone and Chou in 1977 [93] in order to include the stress concentration at the jet necks. The solution of their theory showed that the critical wavelength was independent of the jet-stretching rate, where it had a value of 2.22 in terms of the jet diameter at the beginning of the jet instability. However, a two-dimensional hydrocode simulation by Carleone and Chou [93] predicted that the critical wavelength was a function of the jet-stretching rate. The correct number of jet segments was also determined from the two-dimensional solution.

In 1982, Miller [92] also developed a one-dimensional model to study the jet necking problem. The model was based on the separation of variables and Fourier integral

technique. Miller [92] assumed that a long and nearly cylindrical jet with a small neck at the centre of the jet has a linear velocity gradient. A perfectly plastic constitutive equation was used. Although the predicted results were in good agreement with experiments, the initial material conditions such as temperature and flow stress had to be assumed. The results obtained by the one-dimensional model in [92] using perfectly plastic constitutive equation were similar to that obtained using Steinberg-Guinan constitutive equation [6].

Walsh [94] developed an analytical model to perform a detailed analysis of the effects of surface roughness, the non-uniform initial velocity gradients and the non-uniform yield strength on jet breakup. The predicted results were similar to those of Carleone and Chou [93]. The model predicted that the breakup time was only mildly dependent on the amplitude of the initial disturbance. Walsh [94] also concluded that the jet breakup time could be delayed by reducing the shaped charge fabrication tolerances or increasing the homogeneity of the shaped charge elements.

In 1993, Backofen [95] used an analytical model to calculate the different parameters of the produced jet. These parameters include the virtual origin, the breakup time and jet penetration capability into different target materials. It was found that the used analytical model gives reasonable results to the breakup time estimated by using flash x-ray during the detonation of the shaped charge.

3.5 Shaped charge jet penetration models

Shaped charge penetration models were initially proposed based upon Bernoulli equation, which was subsequentially modified to account for jet particulation, compressibility and strength effect. This section will discuss the fixed and variable velocity jets and the effects of stand-off distance, target material strength and breakup time on jet penetration.

3.5.1 Uniform velocity jet

As the first approximation, the Bernoulli equation assumes that the jet is an inviscid and incompressible fluid. The pressure generated during the impact of jet on the target is much higher than the yield strength of many materials. The penetration process is also assumed to be a steady state process and the length of the jet is assumed to be constant [6]. Diagrammatic schemes of the initial length of jet (l) prior to impact and the jet penetration into target are shown in Figure 3-15.

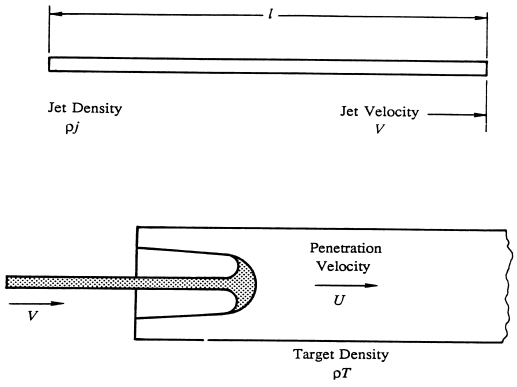

Figure 3-15 Hydrodynamic penetration of jet into target [6].

The hydrodynamic model assumes that pressure on both sides of the interface is in equilibrium, i. e.

$$\frac{1}{2}\rho_j(V-U)^2 = \frac{1}{2}\rho_T U^2. \tag{3-61}$$

The consumption of the jet ($\frac{-dl}{dt}$) can be linked to the penetrator velocity and the penetration velocity U, i.e.

$$V - U = -\frac{dl}{dt}. \tag{3-62}$$

The relation between penetration depth (P) and penetration velocity is

$$U = \frac{dP}{dt}\ . \tag{3-63}$$

Therefore, $\frac{dP}{dt} = -\sqrt{\frac{\rho_j}{\rho_T}}\ .\frac{dl}{dt}$, which can be integrated from the start of impact (i.e. *l*=L at t=0) to the moment when the jet is completely consumed (i.e. *l*=0 at t=t_f),

$$P = -\sqrt{\frac{\rho_j}{\rho_T}}\ .\int_L^0 dl = L\sqrt{\frac{\rho_j}{\rho_T}}. \tag{3-64}$$

Eq.(3-64) gives a first order approximation of the shaped charge jet penetration. However, the hydrodynamic model neglects several important factors, which may influence jet penetration. These factors include [6]:

- Strength of both jet and target materials, which become important when the jet velocity is low.
- Secondary penetration due to the crater inertia after the jet is completely consumed,

- Velocity gradient in the jet, which requires suitable stand-off distance to maximize the jet penetration,
- The jet tip velocity affects the penetration depth and
- Other factors such as jet-target interactions, jet alignment, jet compressibility, aerodynamic drag and variable-area of jets.

3.5.1.1 Jet breakup effect

To account for the jet breakup effect, Evans in 1950 [6] developed the hydrodynamic theory by applying the dynamic pressure produced by jet particles, which is the jet force (rate of the change of jet momentum with time) divided by the total cross sectional area of the jet. This term equals to the pressure generated in the target during the impact. Therefore,

$$\lambda\bar{\rho}_j(V-U)^2 = \rho_T U^2 \qquad 3\text{-}65$$

where $\bar{\rho}_j$ is the average jet density including gaps between the particles and λ is a constant, which equals one for a continuous jet and two for a particulated jet. Thus, the Bernoulli's equation primary penetration is given by:

$$P = L\left[\frac{\lambda\bar{\rho}_j}{\rho_T}\right]^{0.5} \qquad 3\text{-}66$$

This model also neglected those factors ignored in the hydrodynamic model for fixed velocity.

3.5.1.2 Stand–off distance effect

Another model had been suggested by Birkhoff et al. [49] in order to account for the stand-off distance effect on the penetration depth. The suggested semi-empirical formula for the continuous jet is:

$$P = \frac{P_o(1+\alpha S)}{1+\beta S} \qquad 3\text{-}67$$

where S is the stand-off distance, P_o is the penetration at zero stand-off (i.e. S=0), α is a constant depending on the jet velocity gradient and β is a constant representing the jet spreading. Constants α and β can be determined from curve fitting of the penetration-stand-off curve.

For the broken-up jet, the penetration formula is:

$$P = P'_O \frac{\sqrt{2}(1+\psi S)^{0.5}}{1+\beta S} \qquad 3\text{-}68$$

where P'$_o$ is the penetration depth from the previous equation (P) for the continuous jet and ψ is a constant depending on the velocity gradient.

3.5.1.3 Target material effect

Many investigators attempted to improve the accuracy of the simplified theory. Pack and Evan [96] considered the importance of the strength of target material on jet penetration. They modified Eq.(3-64) by multiplying it with a correction term as follows:

$$P = L\sqrt{\frac{\rho_j}{\rho_T}}\left(1 - \frac{\alpha Y}{\rho_j V^2}\right) \qquad 3\text{-}69$$

where α is a constant and Y is the yield strength of the target material. They showed that for steel, the correction term $\alpha Y/\rho_j V^2$ is 0.3, which means that the penetration is reduced by 30% due to the effect of the target strength.

Eichelberger [97] made extensive measurements of jet penetration histories. It was shown that the hydrodynamic formulae Eq. (3-64) could not be used in the later stages of penetration as the jet velocity decreases. The later stage penetration mechanism is somehow different from the earlier stage penetration mechanism, during which both the target and the jet behave hydrodynamically. It was also found that when the jet was brokenup, λ in Eq. (3-66) would be less than unity if ρ_j was taken as the same as the original density of the liner material. Thus, Eichelberger [97] proposed a formula that includes the strengths of jet and target materials, i.e.

$$\frac{1}{2}\lambda\rho_j(V-U)^2 = \frac{1}{2}\rho_T U^2 + \sigma \qquad 3\text{-}70$$

$$\text{with} \qquad \sigma = \sigma_T - \sigma_j \qquad 3\text{-}71$$

where σ_T and σ_j are the resistances to plastic deformation for target and jet materials, respectively. Each resistance term was taken as one to three times the value of its static uniaxial yield stress [97]. The importance of the strength term effect on the penetration was demonstrated by Pugh [98] and Klamer [99] when they found that the penetration into armoured steel is 15% ~ 20% less than that into mild steel.

3.5.2 Variable velocity jet

The jet has non-uniform velocity distribution and its length is increasing with time, therefore, the fixed length jet should be modified. Abrahamson and Goodier [100] extended the hydrodynamic penetration model to include non-uniform jet velocity distribution and stand-off distance. This model strated from an arbitrarily selected initial time and required the initial jet length at this moment to be given, which makes this model difficult in practical use. Allison and Vitali [2] developped a penetration model based on following assumptions:

a. Existence of a virtual origin, from which each jet element is emitted at its own velocity that remains constant during its travelling between the virtual origin and target.
b. Negligible strength of the jet and target materials: To ensure the validity of this assumption, a minimum jet velocity for penetration, V_{min}, must be defined to represent the termination of penetration by slow moving jet elements.
c. Negligible compressibility of the jet and target materials,
d. Simultaneous breakup of the entire jet, and
e. That each broken jet segment penetrates as a continuous jet.

Allison and Vitali [2] derived the following penetration equation for the continuous jet:

$$P(t) = V_o t (\frac{t_o}{t})^{\frac{\gamma}{\gamma+1}} - t_o V_o \qquad 3\text{-}72$$

where t_o is the time at which the jet moving with a tip velocity V_o arrives the target and γ is the square root of the density ratio, i.e .

$$\gamma = \sqrt{\frac{\rho_T}{\rho_j}} . \qquad 3\text{-}73$$

Eq.(3-72) is only valid before the jet breaks up because the penetration depth predicted by Eq.(3-72) is independent of stand-off distance. In reality, penetration decreases with the increase of stand-off distance after the jet is broken.

Allison and Vitali [2] model is still a useful model for the study of jet penetration. Dipersio et al. [101] and Schwartz [102] presented explicit formulae based on Allison and Vitali [6] model, for the following three cases:

a) Penetration before jet breakup ($T \le t_b$)

b) Jet breakup during penetration ($t_o \le t_b \le T$)

c) Jet breakup before reaching the target ($t_b \leq t_o \leq T$),

where T is the total time at the end of penetration, t_b is the jet break-up time and t_o is the time when the tip reaches the target.

For case (a), the total penetration depth P is:

$$P = S\left[\left(\frac{V_o}{V_{\min}}\right)^{\frac{1}{\gamma}} - 1\right] \qquad 3\text{-}74$$

where S is the distance from the virtual origin to the target and V_{min} is the minimum jet velocity for penetration.

For case (b), the depth of penetration is

$$P = \frac{(\gamma+1)(V_o t_b)^{\frac{1}{\gamma+1}} S^{\frac{\gamma}{\gamma+1}} - V_{min} t_b}{\gamma} - S \qquad 3\text{-}75$$

Finally, for case (c), the depth of penetration is

$$P = \frac{(V_o - V_{\min})t_b}{\gamma} \quad . \qquad 3\text{-}76$$

Eqns. (3-74 to 3-76) are called DSM (Dipersio, Simon and Merendino) model, which can also be used to obtain the exit velocity V_P of a continuous jet after perforating a finite thickness (T_t) [103] i.e.

$$V_P = V_o \left\{\frac{S}{S+T_t}\right\}^{\gamma} \quad . \qquad 3\text{-}77$$

It was found that at larger stand-off distance, these formula, give larger penetrations than the measured values due to the occurrence of asymmetric wavering of the jet, which is not considered in the model [103]. This over-prediction may also be caused by the occurrence of the tumbling or the deceleration due to air friction [103].

3.5.3 Particulated jet

For the particulated jet, the gaps between the resulted jet elements decrease the penetration capability of the jet. The penetration depth of a particulated jet, P', can be calculated using a formula developed by Carleone et al. [6]:

$$P' = P\left(1 - \frac{g_i}{g_o}\right) \qquad 3\text{-}78$$

where g_i is the gap distance between two subsequent broken-up jet elements nondimensionalized with respect to the increment of the jet length, g_o is an empirical constant equals 6.5 for precision shaped charges (relatively large calibre) and 4~6 for small charges (non-precised). An average value of the gap distance g_{ave}, may be used to replace g_i in Eq. (3-78);

$$g_{ave} = \frac{\sum_{i=1}^{k} g_i}{K} \qquad 3\text{-}79$$

where K is the number of broken-up elements.

Hence, to calculate the jet penetration at a given stand-off distance, it is necessary to consider the jet traveling time and to check if the the jet is continuous or broken-up. If the jet reaches the target after it has been broken-up, its penetration is first calculated using the same procedures for continuous jet and then it is corrected using the Eq. (3-78).

3.5.4 Target strength

Various penetration models have considered the target strength effect on the penetration depth. The most frequently used model for the shaped charge jet penetration was suggested by Alekseevskii [104] and Sanasaryan [105] based on the modified Bernoulli equation [6]:

$$HD + k_T \rho_T U^2 = \sigma_{SD} + k_j \rho_j (V - U)^2 \qquad 3\text{-}80$$

where HD is the dynamic hardness of the target material (Vickers hardness), k_T and k_j are the body shape factors of the target and jet respectively, Alekseevskii [104] takes both of them as 0.5 and σ_{SD} is the dynamic yield stress of the jet material.

The cutoff velocity was calculated from Eq. (3-80) when U=0, therefore,

$$V_{\min} = \sqrt{\frac{HD - \sigma_{SD}}{k_j \rho_j}}. \qquad 3\text{-}81$$

Christman and Gehring [106] developed a model with the consideration of four different penetration phases according to the generated pressure, i.e. the transient, the primary, the secondary, and the recovery phases. This model was applied to long rod penetrator in the velocity range of 2-6.7km/s, i.e.,

$$\frac{P}{L} = \left(1 - \frac{D}{L}\right)\left(\frac{\rho_p}{\rho_T}\right)^{0.5} + 2.42\left(\frac{D}{L}\right)\left(\frac{\rho_p}{\rho_T}\right)^{2/3}\left(\frac{\rho_T V^2}{B_{max}}\right)^{1/3} \qquad 3\text{-}82$$

where B_{max} is the Brinell hardness of the target material. The first term represents the hydrodynamic penetration in the primary phase, while the secondary penetration phase is

represented by the second empirical term. This model was modified by Doyle and Buchholz [107] to predict the penetration of EFP (Explosively formed projectiles). The modified formula is:

$$\frac{P}{L} = \left(1 - \frac{D}{L}\right)\left(\frac{\rho_P}{\rho_T}\right)^{0.5} + \frac{0.13}{L}\left(\frac{D}{L}\right)\left(\frac{\rho_p}{\rho_T}\right)^{1/3}\left(\frac{E_1}{B_{max}}\right)^{1/3} \quad 3\text{-}83$$

where P is the target penetration depth, L is the projectile length, D is the diameter of projectile. ρ_P and ρ_T are the densities of the penetrator and target materials, respectively. E_1 is the energy in last part of projectile (Joule) and B_{max} is the Brinell hardness of the target (kg/mm^2).

Semi-hydrodynamic model with the consideration of material strength was presented by Alekseevskii in 1966 [104], and Tate in 1967 [108].

The dynamic equation of the projectile is

$$\rho_p L \frac{dV}{dt} = \sigma_p \quad 3\text{-}84$$

and the geometrical relationship is

$$V - U = -\frac{dl}{dt}, \quad 3\text{-}85$$

where L is the current length of the rod. The explicit solution of this model was suggested by Tate [109], where the values for σ_p and σ_T are taken to be the Hugoniot elastic limit of the penetrator and 3.5 times that of the target material, respectively. However, Walters et al. [103] suggested different value for σ_T to be 2.5 times the Hugoniot elastic limit and σ_p to be the uniaxial yield strength of the penetrator, which led to a good agreement with their experimental work.

Tate 1986 [110] has provided methods to estimate R_t and Y_p based on dynamic yield strength [111].

$$\frac{1}{2}\rho_P (V - U)^2 + Y_P = \frac{1}{2}\rho_T U^2 + R_t \quad 3\text{-}86$$

where Y_p and R_t are the projectile and target strength factors and are defined by Tate [112] to be:

$$Y_p = (1 + \lambda)\sigma_{yp} \quad 3\text{-}87$$

$$R_t = \sigma_{yt}\left(\frac{2}{3} + \ln\left(\frac{2E_t}{\sigma_{yt}}\right)\left(4 - e^{-\lambda}\right)\right) \quad 3\text{-}88$$

where λ is a constant independent of the jet velocity (taken to be 0.7 for steel material), σ_{yp} is the dynamic yield strength of the jet material and E_t is the its Young's modulus.

In 1982, Matuska [113] presented the steady state jet penetration using the HULL software to empirically determine the modified Bernoulli equation parameters, i.e.

$$\frac{\Omega}{2}\rho_j(V-U)^2 + \beta\sigma_j = \frac{1}{2}\rho_T U^2 + \alpha\sigma_t. \quad 3\text{-}89$$

It was found that α=1, β=0.3 and

$$\Omega = 0.47 + 0.028\rho_j + 0.00086{\rho_j}^2 + 0.072\ln V \quad 3\text{-}90$$

where ρ_j is in g/cm^3, V in km/s and Ω is the deviation parameter which accounts for the decrease from unity due to the resistance of the target material to the radial flow.

3.6 Crater growth process

Like penetration formulae discussed previously, many models have been proposed to describe the radius of a crater created by shaped charge penetration [114]. One of these models was proposed by Held and Kozhushko [111] where the hydrodynamic equation was used to calculate the maximum crater radius (r_{cm}) in aluminium and glass fibre reinforced plastic targets by shaped charge jet. The experimental crater radius had a good agreement with model prediction according to the following equation:

$$r_{cm} = \frac{r_j V_j \sqrt{\rho_T / 2R_t}}{\left(1 + \sqrt{\rho_T / \rho_j}\right)} \quad 3\text{-}91$$

where r_j is the jet radius, ρ_T is the target density and R_t is the target resistance to radial crater growth, which is different from the target resistance term used in the penetration depth formulas. R_t can be determined by the simultaneous measurement of the projectile and the penetration velocities. It was found that the resistance of target to radial cratering is lower than to the axial penetration.

3.7 Summary

Models of shaped charge jet formation were presented in this chapter. The steady state Birkhoff model assumes constant collapse velocity along the liner surface, while the collapse velocity in the unsteady state PER model varies along the liner. The analytical, numerical and semi-epempirical breakup models of a shaped charge jet were presented. Finally, jet penetration models with the consideration of the breakup time, the stand-off distance, the jet and target material strengths and the jet velocity gradient were described.

CHAPTER.4 HYDROCODE SIMULATION

4.1 Introduction

The numerical simulation is performed using AUTODYN, which can be used to solve non linear problems related to impact, penetration, perforation and explosion and has built-in mathematical models such as shaped charge jetting analysis [115]. Autodyn hydrocode is based on mass, momentum and energy conservation equations, where the materials can be defined by its equation of state and its strength model [116]. This hydrocode is capable of performing the shaped charge jetting analysis, jet formation and penetration into concrete materials, which are briefly described below.

The jetting analysis is based on both the numerical finite difference technique to calculate the collapse velocities and the analytical unsteady PER theory [50] to calculate the jet and the slug velocities and masses as well as the collapse and the deflection angles of the liner elements. In this algorithm, the liner is described as a thin shell composed of a series of nodes having the real thickness of the liner, while its apex point should be fixed by a boundary condition to prevent its motion [115]. An interaction between the Lagrangian shell liner and the Euler explosive and charge casing is defined by Euler-Lagrange polygon surface. The jetting points are defined for all the liner nodes except the first one fixed by the boundary condition. Once the jetting is completed, the jetting summary including the concerned angles, velocities and masses of all liner elements will be obtained.

The jet formation is simulated using Euler method based on continuum mechanics to obtain the jet profiles at different time stages. In this scheme, the explosive, the charge casing and the liner materials are filled into the global Euler multi-material part [116]. This processor is suitable in the early jet formation stages, where large distortions will be caused by extremely high strain-rate in the order of $10^7 s^{-1}$ [7, 31]. These distortions will cause the solver to stop working if a Lagrange solver is selected for the jet formation. The Euler multi-material processor describes the detonation wave propagation inside the charge and shows the jet profile as it elongates with time. The jet is allowed to move on the Euler grids up to the moment when it just impacts the target. At this moment, the formed jet will be remapped as a Lagrangian mass having non-uniform velocity distribution. The output of this scheme will be used as the input of next scheme.

The jet interaction (penetration) with the laminated target layers is simulated using Lagrange method. In this scheme, the jet obtained from the jet formation Euler solver is remapped to Lagrange moving grids and impacts the multilayered target. To overcome the mesh distortion problem in Lagrange solver, a mesh discard option or ‘‘erosion strain’’ is applied to the jet and the target materials. The erosion strain does not represent a physical phenomenon, but a numerical algorithm to prevent the mesh distortions [117].

The input, the solver type and the output data from the jetting analysis and the two different modeling schemes (solvers) are illustrated in the flow chart in Figure 4-1.

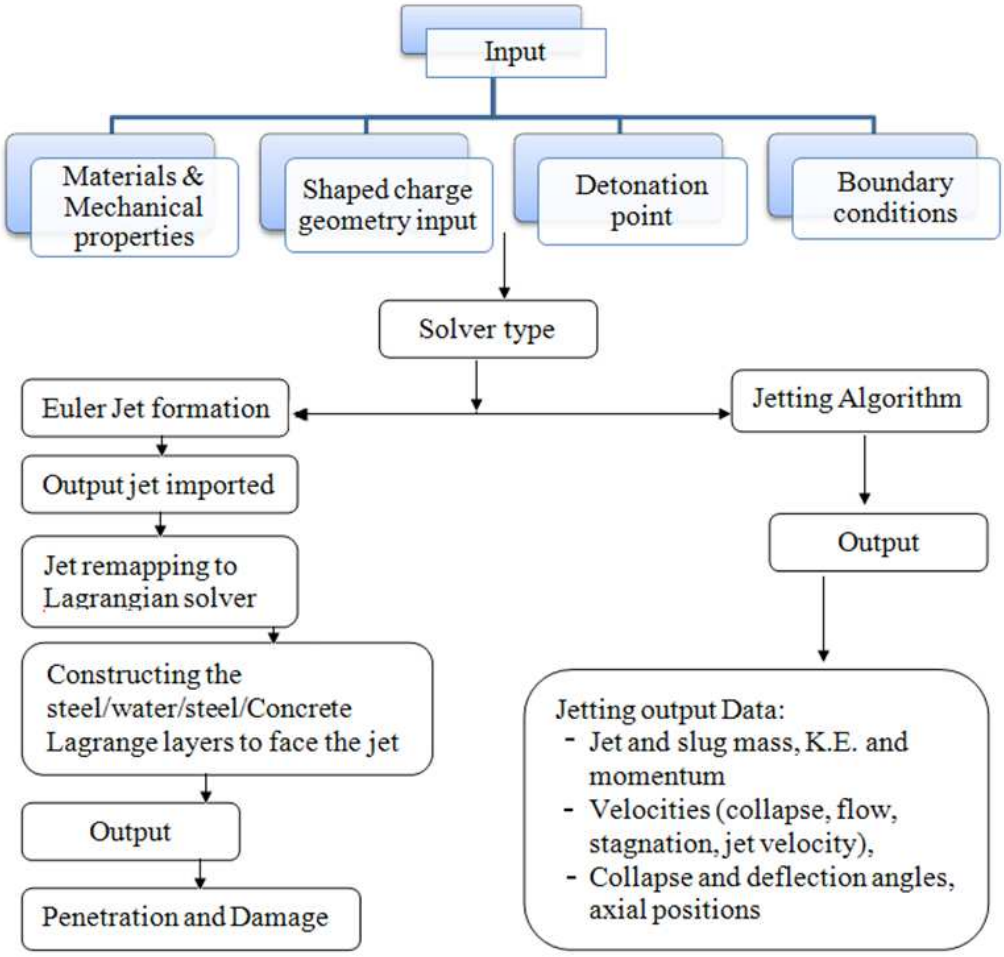

Figure 4-1 The flow chart of the different stages and input and output results from the jetting analysis and the two solvers (Euler and Lagrange) of the Autodyn hydrocode.

4.2 Studied parameters

- High explosive type: six different explosives were used to study the effect of detonation characteristics of explosive on the formed jet characteristics and its

effects on the penetration capability. These explosives were TNT, RDX, Cyclotol, HMX, LX-14 and PETN.

- Cone apex angle: the used design cone apex angles were 22^o, 32^o, 40^o, 46^o, 56^o, 60^o and 70^o with the same explosive charge RDX. The liner thickness was also changed with different cone apex angles in order to maintain the same explosive to metal mass ratios. Hence, the jet characteristics are presented as a dependence of the cone apex angle. Furthermore, numerical simulations were conducted for constant liner thickness of 1.77mm with four different cone apex angles.
- Liner thickness: the liner thickness is varied for the same explosive, RDX. The varied liner thickness was 0.8, 1, 1.2, 1.4, 1.6, 1.8, 2mm and 3mm with constant cone apex angle of 40^o.
- Liner material: the selected materials for the liner were OFHC solid copper, solid pure zirconium and copper-tungsten powder.
- Degree of confinement: 1, 2, 4, 6 and 8mm steel casing thickness were used for RDX OWP of 1.4mm liner wall thickness with cone apex angle of 46^o.
- Detonation point: the behavior of the detonation wave inside the explosive charge was studied by selecting two different initiation methods, i.e. a central point on the charge axis and a point on the side of charge.
- Target material effect: four different target materials were selected to investigate the effect of target material strength on the penetration depth of perforators. These were concrete targets with compression strengths of 26, 40, 47 and 55 MPa.
- Water stand-off distance: the performance of an OWP is tested for penetration after its jet penetrated through 0.5, 1.7, 2, 4 and 6cm of water layers.

4.3 Autodyn jetting analysis description

Autodyn-2D and 3D finite difference codes have a built-in jetting routine, which is included in the code, where PER theory calculations (explained in chapter 3) is performed to estimate the jetting parameters for every liner element [115]. In the jetting analysis, the explosive and the casing parts can be modeled as a Lagrangian or Eulerian grid, but the liner must be modeled as a shell, in which specified mass points are defined as “jetting” points. The boundary condition applied to the liner is ‘Fix’ because The first node is on the axis of symmetry and is therefore not able to jet. Instead, the boundary condition fixes this node in its starting position and prevents its motion [115]. After the shaped charge is detonated and the jet is formed, the following jet data will be obtained:

- Initial X coordinate
- Initial Y coordinate
- Initial liner mass
- Time of jet formation
- X coordinate of jet formation
- X component of collapse velocity at jet formation
- Y component of collapse velocity at jet formation
- Liner collapse angle (β) at jet formation
- Deflection angle (δ) in the jetting equations
- Collapse speed at jet formation (V_o)
- Jet velocity (V_j)
- Velocity of the stagnation point (V_1)
- Velocity of jet relative to stagnation point (V_2)
- Jet and slug masses
- Cumulative jet mass and its kinetic energy.

Figure 4-2 illustrates the OWP assembly including the Lagrangan casing, the Eulerian explosive and the Shell liner with fixed apex node as a complete representation of jetting model.

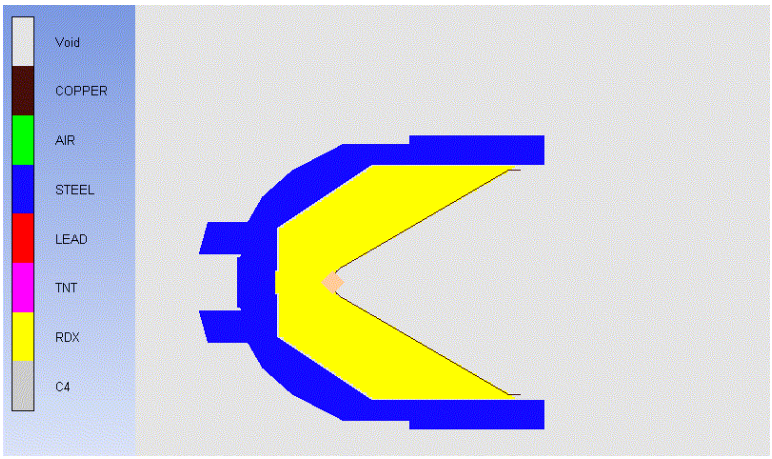

Figure 4-2 The jetting model of OWP with cone apex angle 60^o and liner thickness 1.74mm under fixed apex node boundary condition.

4.4 Autodyn jet formation model description

The jet formation model was established in order to obtain the jet profile, the contours of different jet parameters and the jet breakup phenomena, which were needed to test the performance of the perforator. The model uses Euler solver with outflow boundary

condition, which allows the detonation gaseous products and the casing material to expand smoothly towards the Euler part boundary and prevents them from returning back to avoid their effect on the jet and the slug formation as shown in Figure 4-3. The large deformation occurs inside the liner, and a continuous jet is formed while the fixed meshes allow the jet to moving over it without being stopped because of mesh distortion. The code output from the Euler solver will create jet and slug profiles according to the Conical Shaped Charge (CSC) perforator design. This jet (Figure 4-4) will be remapped to a new Lagrange model, which is suitable for simulating the jet penetration into laminated configuration of the target layers, as shown in Figure 4-5. The physical parameters of the jet, such as its kinetic energy will be almost unchanged during the remapping and exporting process.

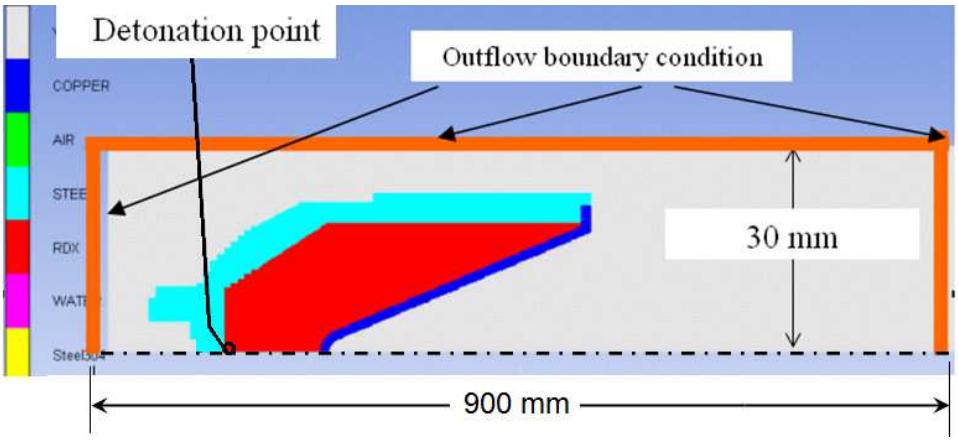

Figure 4-3 The Euler part in 2-D Visualizer showing the geometry and the boundaries of the jet formation model.

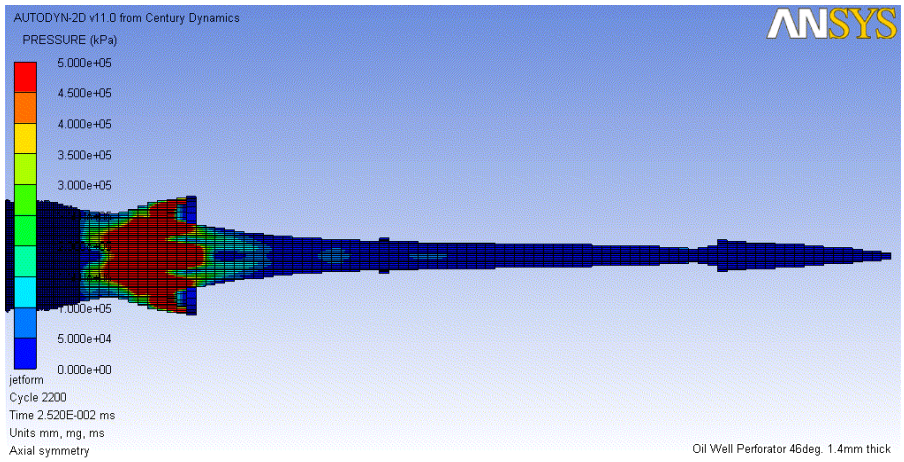

Figure 4-4 The produced jet obtained from Euler solver and remapped to Lagrange processor for penetration analysis.

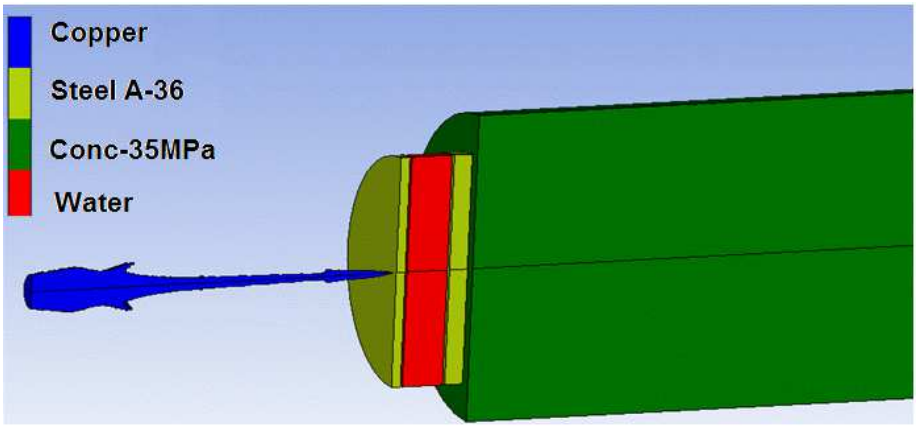

Figure 4-5 The produced jet impacting on steel gun casing, water wellbore fluid, steel casing and concrete material.

4.5 Material modeling description

4.5.1 Description of the used explosives

The explosive required for shaped charges must have high velocity of detonation and high density to provide a high detonation pressure, which results in fast jet tip velocity and larger depth of penetration [6]. The explosive materials used for filling CSC perforators were TNT, HMX, PETN, Cyclotol, RDX and LX-14. The equation of state for the used explosives is "Jones-Wilkins-Lee" (JWL) equation, which is a simple pressure, volume, energy (PVE) relation that has been developed to describe the adiabatic expansion of the detonation products of explosives [118].

$$p = \mathrm{A}\left(1 - \frac{\omega}{\mathrm{r_1 v}}\right)e^{-\mathrm{r_1 v}} + B\left(1 - \frac{\omega}{\mathrm{r_2 v}}\right)e^{-\mathrm{r_2 v}} + \frac{\omega E}{\mathrm{v}} \qquad 4\text{-}1$$

where p is the pressure, v is the relative volume (1/ρ), A, B, r_1, r_2, C and ω are constants [119]. The values of the experimental constants for some explosives have been determined from sideways plate push dynamic test experiments [120]. These values were determined experimentally by the cylinder expansion test. For the listed explosives, the values of the above mentioned constants are available in the material library of Autodyn. The input data to Autodyn hydrocode for the explosive materials are listed in Table 4-1.

4.5.2 Explosive initiation and wave propagation

The detonation wave is assumed to travel at the prescribed detonation velocity U_D and its path from the predefined initiation point can be determined. The detonation wave propagates in the spherical direction to engulf the whole un-burnt explosive meshes. The

use of JWL constitutive model assumes that the detonation wave is strong enough to completely detonate the explosive and an instantaneous transition to the CJ state is achieved. At this state, the full reaction of the explosive is completed and the full energy of the explosive is liberated, after which the detonation gaseous products will start to expand. The different stages of a CSC detonation are illustrated in Figure 4-6, where the propagation direction of the contours shape spreading from the initiation point source can be observed.

Table 4-1 Input data to the code for the used explosive materials.

Parameter	Explosive Type					
	TNT	HMX	Cyclotol	LX-17	PETN	RDX
Density (g/cm^3)	1.630	1.891	1.754	1.900	1.500	1.600
Parameter A (kPa)	3.740×10^8	7.782×10^8	6.034×10^8	4.46×10^8	6.253×10^8	6.539×10^8
Parameter B (kPa)	3.747×10^6	7.071×10^6	9.923×10^6	1.339×10^6	2.329×10^7	7.293×10^7
Parameter r_1	4.15	4.2	4.3	3.85	5.25	4.83
Parameter r_2	0.9	1	1.1	1.03	1.6	2.24
C-J detonation velocity (m/s)	6930	9100	8250	7600	7450	8100
C-J energy per unit volume (kJ/m^3)	6.00×10^6	1.05×10^7	9.2×10^6	6.9×10^6	8.56×10^6	5.62×10^6
C-J pressure (kPa)	2.1×10^7	4.2×10^7	3.2×10^7	3.0×10^7	2.2×10^7	2.6×10^7
Parameter ω	0.3	0.3	0.35	0.46	0.28	0.3

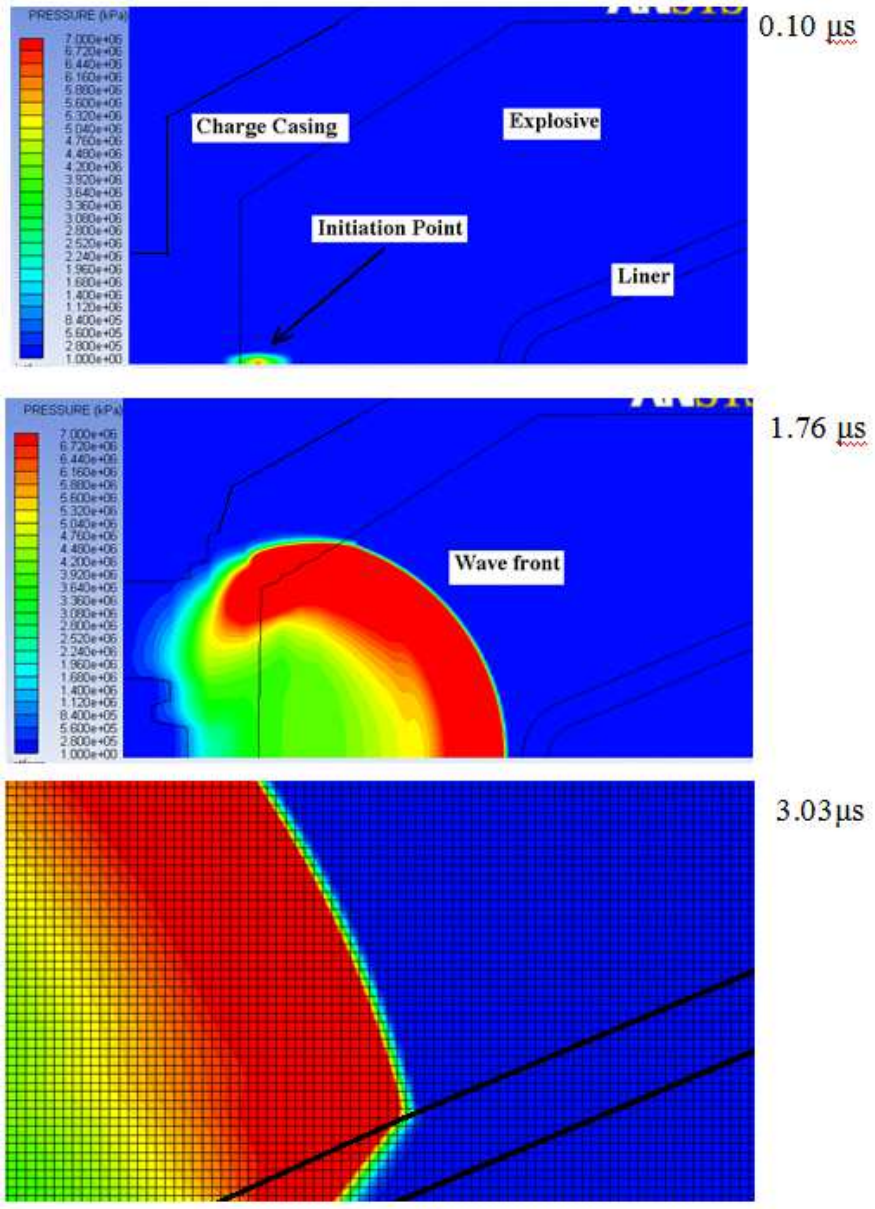

Figure 4-6 The different stages of detonation wave spherical propagation through the explosive charge inside CSC.

4.5.3 Description of the liner materials

The materials that have been used for liner element were solid copper-OFHC, solid zirconium, and copper-tungsten powder mixture. The equations of state (EOS) of these materials were shock, while their strength models were neglected because shock pressure is much higher than material strength [116]. This EOS is suitable for both monolithic liner material manufactured by spinning or drawing and powder mixture liner manufactured by powder metallurgy technique. In 2010, Liu and Shen [43] used Autodyn hydrocode to model the Copper-Tungsten liner manufactured by powder pressing. Liu and Shen used shock equation of state to model the solid liner. The mixture theory was used to determine

the parameters of the shock EOS, in which each parameter was calculated according to the mass fraction of its material in the mixture. Good agreement between the numerical and the experimental results were obtained.

It has been shown experimentally that, for most solids and liquids that do not undergo a phase change, the shock Hugoniot values of shock velocity (U) and material velocity behind the shock (u_p) can be adequately fitted to a straight line (Figure 4-7).

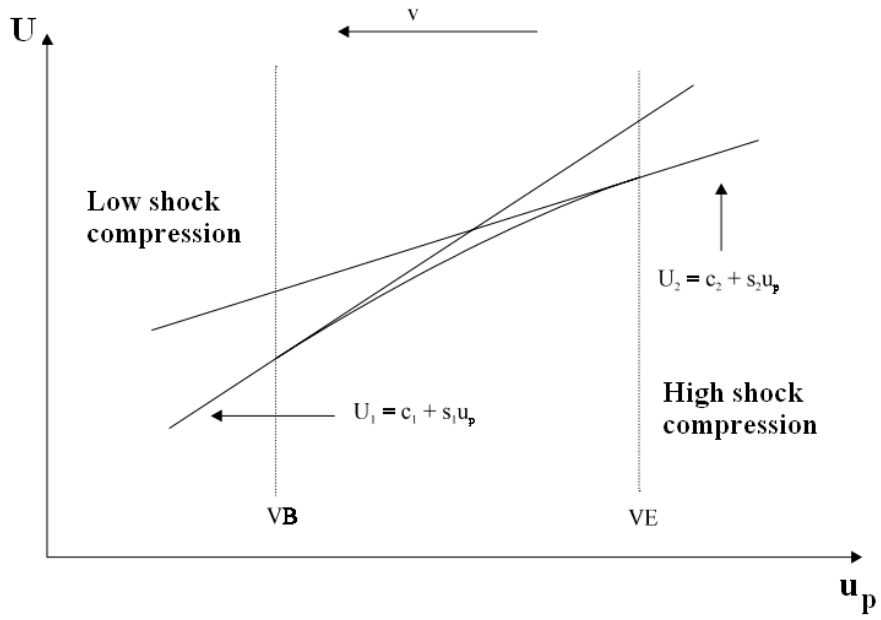

Figure 4-7 The shock velocity against particle velocity for the EOS of the liner material [116].

$$U = C_o + su_p \ . \qquad 4\text{-}2$$

This is valid up to shock velocities around twice the initial sound speed C_0 and shock pressures in the order of 100 GPa. For materials where a linear fit is not adequate, a quadratic relation between U and u_p has been used. Generally, piecewise linear or piecewise quadratic relations (U, u_p) can be applied [116].

The Mie-Gruneisen EOS based on the shock Hugoniot is expressed as:

$$p = p_H + \Gamma\rho(e - e_H) \qquad 4\text{-}3$$

where Γ is the Gruneisen Gamma coefficient and equal to $B_o/(1+\mu)$ where B_o is a constant, $\Gamma\rho = \Gamma_o\rho_o$ =constant is assumed; ρ is the density. p_H and e_H are the Hugoniot pressure and energy, respectively, given by

$$p_H = \frac{\rho_o c_o^2 \mu(1+\mu)}{[1-(s-1)\mu]^2} \quad 4\text{-}4$$

and

$$e_H = \frac{1}{2}\frac{p_H}{\rho_o}\left(\frac{\mu}{1+\mu}\right) \quad 4\text{-}5$$

where $\mu=(\rho/\rho_o)-1$ is the compressibility, C_o is the sound speed in the material and s is a constant giving the slope of shock velocity-particle velocity relationship. The mechanical properties of these materials are illustrated in Table 4-2, where the constants in the previous equations were taken from the material library.

Table 4-2 The mechanical properties of liner materials [116].

Parameter	OFHC Copper	Tungsten Alloy	Zirconium
Equation of state	Shock	Shock	Shock
Reference density (g/cm^3)	8.90	17.00	6.51
Gruneisen Coefficient	2.02	1.54	1.09
Parameter C (m/s)	3940	4029	3757
Parameter s (non)	1.489	1.237	1.018
Ref. temperature (K)	300	300	300
Strength	None	None	None

4.5.4 Description of the charge case

Unlike shaped charge, oil well perforator has a thick confinement in order to afford the high pressure in the well bore of about 68 MPa at depth of 3km below ground level and also the elevated temperature of 300^{o}C at this depth, which is close to the ignition temperature of some high explosives [11]. The confinement degree does not affect the jet velocity of the liner elements near the charge axis. However, collapse velocities associated with the liner elements near the charge edges (i.e. base of the conical liner) are strongly affected by the degree of confinement. The material used for the charge case was steel 4340. The equation of state for the steel is shock EOS which has been described previously for the liner material, while its strength model was Johnson-Cook. This constitutive model aims to model the strength behavior of materials subjected to large strains, high strain-rates and high temperatures [116]. The model defines the dynamic yield stress Y [121] as:

$$\sigma = (A + B\varepsilon^n)(1 + C ln\dot{\varepsilon}^*)(1 - T_H^m) \quad 4\text{-}6$$

where σ is the dynamic flow stress, ε is the effective plastic strain, A is the yield strength, B is the hardening constant, n is the hardening exponent, C is the strain-rate constant and m is the thermal exponent constant. $\dot{\varepsilon}^*$ is the normalized effective plastic strain-rate (i.e. the applied true strain-rate divided by the reference strain-rate). T_H is the homologous temperature that can be calculated by:

$$T_H = \frac{T - T_{room}}{T_{melt} - T_{room}}. \qquad 4\text{-}7$$

The five material constants are A, B, C, n and m. The expression in the first set of brackets gives the stress as a function of strain when ε^* equal to1.0 sec $^{-1}$ and $T_H = 0$ for laboratory experiments at room temperature. The expressions in the second and third sets of brackets represent the effects of strain-rate and temperature, respectively. In particular, the third term represents the thermal softening so that the yield stress drops to zero at the melting temperature T_{melt}. The constants in these expressions determined by means of material tests over a range of temperatures and strain-rates. The input data to Autodyn for the case material are listed in Table 4-3.

Table 4-3 Input data to the code for the charge casing material [116].

Reference density (g/cm^3)	7.83
Tensile strength (MPa)	744
A (MPa)	792
B (MPa)	510
n (non)	0.26
C (non)	0.014
m (non)	1.03
Gruneisen coefficient	1.93
Parameter C1 (m/s)	4569
Parameter S1 (non)	1.4
Ref. temperature (K)	300

4.5.5 Description of the concrete material

4.5.5.1 General

The concrete material is modeled by P-α EOS, which was presented by Herrmann [122]. This model provides a good description of matreial behavior at high stresses and a reasonable description of the compaction process at low stress levels. This model was validated by Heider and Hiermaier [123]. The strength model used with P-α was the RHT (Riedel-Hiermaier-Thoma) brittle material constitutive model [124]. This model describes

the dynamic resistance of concrete and other brittle material such as rock and ceramics by the combined plasticity and shear damage, in which the deviatoric stress in the material is limited by the generalised failure surface. Further details of RHT model can be found from reference [125]. The P-α porous model and the RHT brittle material model were validated by Berg and Preece [117] and Leppänen [126], who implemented a bi-linear softening law that modifies the strain-rate dependency in tension, hence improves the spalling, cracking and scabbing of concrete impacted by a K.E. projectile or fragments. Hayhurst et al. [127] validated these models using SPH, Lagrange and Euler solvers for hard penetrator impacting on ceramic armour. The difference between the measured and calculated Lagrange penetration depths was small (6.7%).

4.5.5.2 Equation of state of the concrete material

According to API-RP43, the concrete material used for testing oil well perforator is ASTM C33-67 concrete. This concrete contains agglomeration sand conditioned to simulate the down-hole hardness, porosity and compressive strength of the rock formation [128].

The EOS used to simulate the concrete material is P-α for the porous material, while the fully compacted one will be modeled by polynomial EOS [122], which will be described below. The complete parameters of both the two used EOS are illustrated in Table 4-4, while the general behavior of the concrete material is illustrated in Figure 4-8.

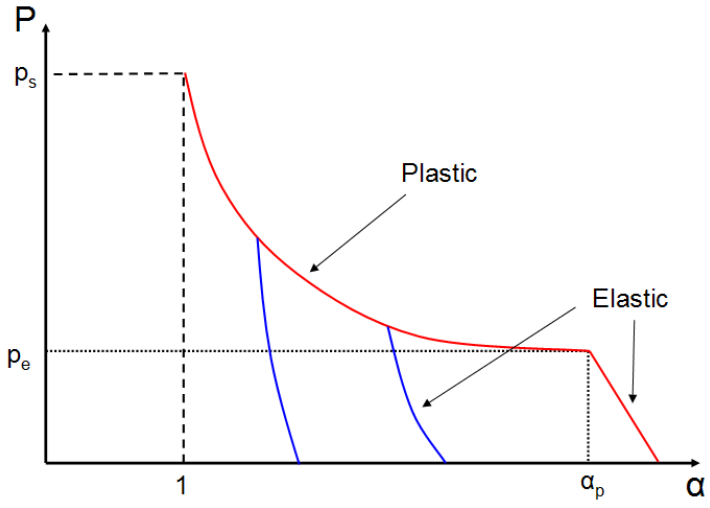

Figure 4-8 The pressure-porosity curve for the concrete material [116].

The porosity α is given by:

$$\alpha = \frac{V}{V_s} = \frac{\rho_s}{\rho} \qquad 4\text{-}8$$

where, $V=1/\rho$ and $V_s=1/\rho_s$ are the specific densities of the porous and solid materials, respectively.

The P-α relation for the porous materials was suggested by Herrmann [122].

$$\alpha = 1 + (\alpha_P - 1)\left[\frac{P_s - P}{P_s - P_e}\right]^n \qquad 4\text{-}9$$

where n is the pressure exponent (n=3 is normally used). P_e and P_s are the elastic pressure and the fully compaction pressure, respectively. α_P is the material porosity at the beginning of the plastic deformation.

The pressure exponent in this model was modified by many authors in order to fit the experimental date to this model.

The general formula of the polynomial EOS for the compacted material is:

$$P = A_1\mu + A_2\mu^2 + A_3\mu^3 + (B_0 + B_1\mu)\rho_o e \qquad 4\text{-}10$$

where A_1, A_2, A_3, B_0 and B_1 are constants; μ is the compressibility; e is the specific internal energy per unit mass. The parameters of this equation are listed in Table 4-4 for the concrete materials.

Table 4-4 The input parameters for P-α and the polynomial EOS for the concrete targets [116].

	26MPa	35MPa	40MPa	47MPa	55MPa
Porous EOS	P-α				
Reference density (g/cm^3)	2.75	2.75	2.75	2.75	2.75
Porous sound speed (m/s)	2892	2920	2935	2957	2981
Initial compaction pressure (MPa) P_e	17.3	23.3	26.6	31.3	36.6
Solid compaction pressure (GPa) P_s	6	6	6	6	6
Compaction exponent n	3	3	3	3	3
Solid EOS	Polynomial				
Bulk modulus A_1 (GPa)	35.27	35.27	35.27	35.27	35.27
Parameter A_2 (GPa)	39.58	39.58	39.58	39.58	39.58
Parameter A_3 (GPa)	9.04	9.04	9.04	9.04	9.04
Parameter B_0 (none)	1.22	1.22	1.22	1.22	1.22
Parameter B_1 (none)	1.22	1.22	1.22	1.22	1.22

4.5.5.3 Strength model for concrete

Over the past decades, extensive number of papers have been published on experimental, analytical and computational methods to study penetration mechanics of hypervelocity projectiles into concrete and rock materials [129]. Adel [130] used AUTODYN 3-D in order to select the optimum strength model and failure criteria related to limestone and concrete targets penetrated by kinetic energy penetrator moving with a velocity up to 1500m/s. The strength models that have been tested were RHT- brittle material model [131], Von Mises model and Druker-Prager model. It was found that the RHT brittle material constitutive model can be used efficiently in characterizing the non-linear behaviour of the rock during penetration especially when RHT failure damage model is taken into consideration. It demonstrated a correct physical mechanism for the penetration process proved by crater profile and a good agreement between the experimental and the calculated penetration depths.

The RHT brittle material constitutive model is an advanced plastic model proposed by Riedel, Hiermaier and Thoma at the Ernst Mach Institute (EMI). This model describes the dynamic resistance of concrete and other brittle material such as rock and ceramic by the combined plasticity and shear damage in which the deviatoric stress in the material is limited by the generalised failure surface. Generally, the RHT model could be divided into five parts, which are [125]:

4.5.5.3.1 The failure surface:

The failure surface, Y_{fail}, is defined as a function of hydrostatic pressure (P), lode angle (θ) and strain-rate ($\dot{\varepsilon}$).

$$Y_{fail}(P^*, \theta, \dot{\varepsilon}) = Y_{TXC}(P) \times R_3(\theta) \times F_{RATE}(\dot{\varepsilon}) \qquad 4\text{-}11$$

where Y_{TXC} is the compressive meridian and is given by:

$$Y_{TXC} = f_c\left[A(P^* - P^*_{spall}F_{RATE})^N\right] \qquad 4\text{-}12$$

where f_c is the unconfined uniaxial compressive strength, A is the failure surface constant, N is the failure surface exponent, P^* is the pressure normalized by f_c, $P^*_{spall} = f_t/f_c$, f_t is the uniaxial tensile strength and F_{RATE} is the dynamic increase factor and is defined by*:*

$$F_{RATE} = \left[\frac{\dot{\varepsilon}}{\dot{\varepsilon}_o}\right]^D \text{ for P> } f_c/3 \qquad \text{(compression)} \qquad 4\text{-}13$$

$$F_{RATE} = \left[\frac{\dot{\varepsilon}}{\dot{\varepsilon}_o}\right]^a \text{ for P< } f_c/3 \qquad \text{(tension)} \qquad 4\text{-}14$$

where D and a are the compressive and tensile strain-rate factor exponents, respectively.

$R_3(\theta)$ defines the third invariant dependency of the model through the tension/compression meridian ratio.

4.5.5.3.2 Elastic limit surface:

The elastic limit surface is scaled from the failure surface using:

$$Y_{elastic} = Y_{fail} \times F_{elastic} \times F_{CAP(P)} \qquad 4\text{-}15$$

where $F_{elastic}$ is the ratio of elastic strength to failure surface strength based on the tensile elastic strength (f_t) and compressive elastic strength (f_c) shown in Figure 4-9. $F_{CAP(P)}$ is a function that limits the deviatoric elastic stresses under hydrostatic compression. The model provides an option to close the elastic limit surface towards high pressures to ensure the consistency between the deviatoric and inelastic volumetric stresses.

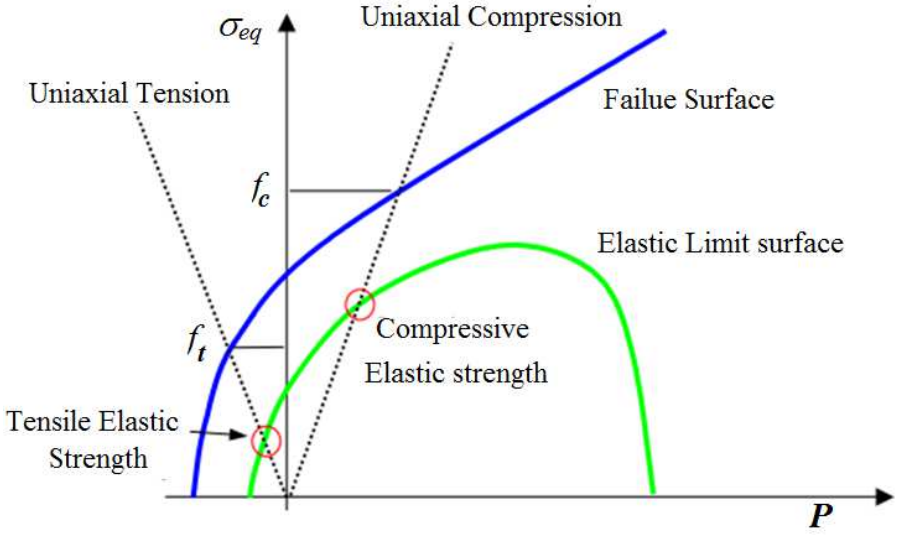

Figure 4-9 Stress loading curve for the RHT strength material model [116].

4.5.5.3.3 Strain hardening

Linear hardening is used in RHT model prior to the peak load. During hardening, the current yield surface, Y^*, is scaled between the elastic limit surface and the failure surface.

$$Y^* = Y_{elastic} + \frac{\varepsilon_{pl}}{\varepsilon_{pl(pre-softening)}}(Y_{fail} - Y_{elastic}) \quad 4\text{-}16$$

The values of ε_{pl} and $\varepsilon_{pl(pre\text{-}softening)}$ are shown in Figure 4-10.

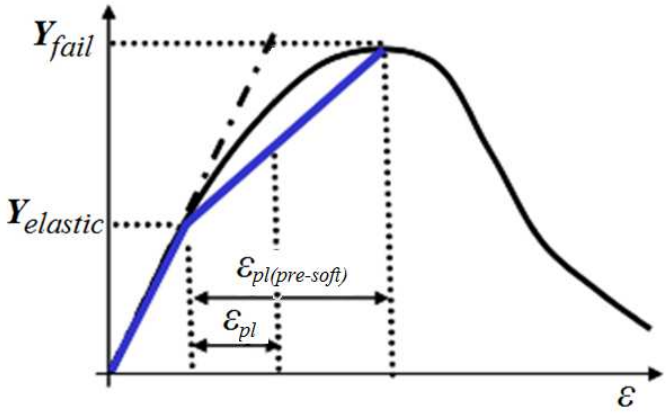

Figure 4-10 The concrete strain hardening curve according to RHT model.

4.5.5.3.4 Residual failure surface

The residual frictional failure surface is defined by:

$$Y^*_{resid} = BP^{*M} \quad 4\text{-}17$$

where B is the residual failure surface constant and M is the residual failure surface exponent.

4.5.5.3.5 Damage

The plastic straining of the material leads to accumulated damage and strength reduction i.e.,

$$D = \sum \frac{\Delta\varepsilon_{pl}}{\varepsilon_p^{failure}} \quad 4\text{-}18$$

$$\varepsilon_p^{failure} = D_1(P^* - P^*_{spall})^{D_2} \geq \varepsilon_f^{\min}, \quad 4\text{-}19$$

where D_1 and D_2 are the damage constants and ε_f^{min} is the minimum strain to failure (input parameter). The post-damaged failure surface is interpolated by:

$$Y^*_{fractured} = (1-D)Y^*_{failure} + DY^*_{residual}\,. \quad 4\text{-}20$$

The post-damaged shear modulus is interpolated by:

$$G_{fractured} = (1 - D)G + DG_{residual} \ , \qquad 4\text{-}21$$

where $G_{residual}$ is the residual shear modulus fraction (input parameter). The strength model parameters are listed in Table 4-5 for concrete materials.

Table 4-5 The input parameters for the RHT strength and failure model for concrete materials [116].

Concrete strength (MPa)	units	26	35	40	47	55
Equation of State	P-α					
Porous density	g/cm^3	2.30	2.31	2.32	2.34	2.35
Porous sound speed	m/s	2892	2920	2935	2957	2981
Initial compaction pressure	MPa	17.3	23.3	26.6	31.3	36.6
Solid compaction pressure	GPa	6	6	6	6	6
Compaction exponent	-	3	3	3	3	3
Strength	RHT Concrete					
Shear Modulus	GPa	16.2	16.7	17.0	17.3	17.7
Compressive Strength (fc)	MPa	26	35	40	47	55
Tensile Strength (ft/fc)	-	0.1	0.1	0.1	0.1	0.1
Shear Strength (fs/fc)	-	0.18	0.18	0.18	0.18	0.18
Intact Failure Surface Constant A	-	1.6	1.6	1.6	1.6	1.6
Intact Failure Surface Exponent N	-	0.61	0.61	0.61	0.61	0.61
Tens./Comp. Meridian Ratio (Q)	-	0.68	0.68	0.68	0.68	0.68
Brittle to Ductile Transition	-	0.01	0.01	0.01	0.01	0.01
Elastic Strength / ft	-	0.70	0.70	0.70	0.70	0.70
Elastic Strength / fc	-	0.53	0.53	0.53	0.53	0.53
Fractured Strength Constant B	-	1.60	1.60	1.60	1.60	1.60
Fractured Strength Exponent M	-	0.61	0.61	0.61	0.61	0.61
Compressive Strain-rate Exp. δ	-	0.034	0.032	0.031	0.029	0.028
Tensile Strain-rate Exp. α	-	0.038	0.036	0.035	0.033	0.032

4.5.6 Description of the layer of the steel gun carrier and the wellbore casing

The selected material for both gun carrier and wellbore casing is Steel A-36 according to the previously mentioned API standard. The equation of state for the steel is shock model while the selected strength model is Johnson-Cook model. The input parameters for the A-36 steel material are listed in Table 4-6.

4.5.7 Description of the water layer

Water is the standard wellbore fluid used to test the oil well perforator performance. The selected equation of state of the water layer is linear with no strength model. The reference density of water is 1 g/cm^3 and its bulk modulus is 2.23 GPa [116] with reference temperature of 300 K.

Table 4-6 The input parameters for the A-36 steel material [116].

Parameter	Steel A-36
Reference density (g/cm^3)	7.85
A (MPa)	250
B (MPa)	477
n (non)	0.18
C (non)	0.012
m (non)	1
Gruneisen coefficient	2.17
Parameter C (m/s)	4569
Parameter S (non)	1.49
Ref. temperature (K)	300

4.6 Solution stability

Since the numerical algorithm used in Autodyn is an explicit scheme, there is an optimum time step of integration, which must be determined to obtain a reasonable representation of solution. The local time step ensuring stability is calculated for each mesh point. The minimum value of all these local values multiplied by a safety factor (a default value of 2/3 is built into the code) is chosen as the time step for the next update. In Lagrangian mesh, the time step must satisfy the Courant condition [116], i.e.,

$$\Delta t \leq d / c \qquad 4\text{-}22$$

where d is the typical length of a mesh (defined as the area of the mesh divided by its longer diagonal) and c is the local sound speed. This ensures that a disturbance does not propagate across a mesh in a single time step.

The minimum value of "Δt" must be found for all zones and this value will be used for all meshes for the next time step of integration.

4.7 Output of numerical modeling

In the following, the predicted parameters associated with the different simulation studies herein are listed. The histories of these parameters during their simulation processes will also be presented in the next chapter. The histories of the following parameters are predicted from the jetting analysis solver in Autodyn:

- Jetting points parameters (collapse velocity, collapse angles, elemental velocity history, jet tip velocity, jet momentum and kinetic energy, jet and liner masses)
- Cumulative jet mass and length.
- The time at which each liner node point will be jetted on the jet axis

Output of jet formation model (Euler)

The histories of the following parameters from the jet formation model are predicted:

- Jet profile at different times
- Jet breakup phenomena
- Different jet contours (pressure, temperature, sound speed, velocity, etc.)
- Energy history plots (momentum, kinetic and internal energies).

In addition to the selected gauge point histories at the specified spatial locations and the Lagrangian jet that could be obtained from the remapping model, outputs of jet penetration into laminated layers configuration (all Lagrange layers) include:

- Jet penetration into concrete at different times,
- Crater profile along the penetration path,
- The damage contours accompanied with the penetration process, and
- The history plot of gauge points at different times.

CHAPTER.5 PARAMETRIC ANALYSIS RESULTS

5.1 Introduction

This chapter presents parametric analyses for the numerical algorithms and models used in this project. The Autodyn hydro-code package is used to perform the shaped charge jetting analysis, the jet formation modelling and the modeling of the formed jet interaction with A-36 steel, water and A-36 steel layers backed by concrete targets, according to the standard API-RP 43 (quality control target). Generally, this chapter presents the obtained parametric analysis results on the following main issues

- General features of the shaped charge jetting analysis, the jet formation and jet penetration models,
- The mesh sensitivity study for the jetting analysis and the jet penetration,
- The verification and validation of the hydro-code software,
- The effect of the surrounding medium (air or void) on the jet velocity,
- The parametric analysis of the OWP including the liner, the explosive and the charge design as well as the detonation point effect,
- The liner portioning into jet and slug portions, and
- The Gurney velocity approximation.

5.2 The main features of the jetting analysis and the jet formation and penetration solvers

5.2.1 Standard shaped charge jetting analysis model

A series of the standard jetting analysis at different times is shown in Figure 5-1 for the OWP of 1.74mm liner wall thickness and 60^{o} cone apex angle. The model stopped at 19.6μs from the moment of detonation. The time represents the total time, at which the entire liner elements arrive at its axis and take part in the jet and slug portions.

Figure 5-1 The different stages of the jetting analysis of the OWP 60^{o} cone apex angle and liner wall thickness of 1.74mm.

The standard jetting analysis output is a HTML file and contains the jetting data of all the liner elements. The data may be used for further calculations such as in virtual origin model and in the determination of the breakup time. They also can be used directly to predict the jet characteristics such as its kinetic energy and its momentum. The jetting solution summary is listed in Table 5-1. The data file gives a range of jetting parameters of

jet elements with respect to their original distances from the liner apex, as shown in Figure 5-2, as an example.

Table 5-1 The jetting summary of OWP 60^o with liner wall thickness of 1.74mm

liner mass (g)	28.3	Jet mass (g)	5.35
Liner momentum (kg.m/s)	24.3	Jet momentum (kg.m/s)	16.7
Liner kinetic energy (kJ)	31.9	Jet kinetic energy (kJ)	30.2

J	X_o (mm)	Y_o (mm)	Lin. mass (g)	X-jet (mm)	T-jet (μs)	V_o (m/s)	Angle β	V_1 (m/s)	V_2 (m/s)	V_{jet} (m/s)	Jet mass (g)
2	2.72	3.66	0.355	34.9	2.30	576.0	32.2	1080.2	941.9	2022.1	0.0273
3	3.58	4.17	0.403	35.9	2.96	761.9	34.7	1337.6	1146.0	2483.6	0.0358
4	4.44	4.67	0.452	37.0	3.50	883.1	35.6	1515.1	1284.9	2800.0	0.0422
5	5.30	5.17	0.501	38.0	4.01	985.1	36.2	1664.5	1404.4	3068.9	0.0483
6	6.16	5.67	0.549	39.1	4.49	1077.0	36.7	1799.3	1512.4	3311.6	0.0544
7	7.02	6.17	0.598	40.2	4.94	1172.5	37.0	1945.4	1631.6	3577.0	0.0601
8	7.88	6.67	0.646	41.3	5.38	1256.0	37.5	2057.3	1718.1	3775.4	0.0668
9	8.74	7.17	0.695	42.4	5.82	1331.9	38.3	2142.8	1781.6	3924.5	0.0748
10	9.60	7.67	0.743	43.5	6.21	1429.1	38.1	2310.3	1917.5	4227.8	0.0792
11	10.46	8.18	0.792	44.6	6.59	1515.9	38.0	2459.8	2035.8	4495.5	0.0837
12	11.32	8.68	0.840	45.7	6.97	1572.8	38.3	2530.9	2087.1	4618.1	0.0906
13	12.18	9.18	0.889	46.8	7.31	1611.6	38.0	2615.4	2156.5	4771.9	0.0940
14	13.04	9.68	0.937	47.9	7.66	1643.5	37.8	2677.5	2207.1	4884.6	0.0983
15	13.90	10.18	0.986	49.0	8.02	1664.5	37.7	2714.8	2236.9	4951.8	0.1032
16	14.76	10.68	1.035	50.1	8.37	1680.1	38.1	2717	2237.0	4954.1	0.1103
17	15.62	11.18	1.083	51.2	8.73	1681.9	38.6	2692.1	2213.9	4906.1	0.1181
18	16.48	11.68	1.132	52.3	9.09	1681.1	38.5	2696.3	2219.5	4915.8	0.1229
19	17.34	12.19	1.180	53.5	9.48	1679.6	39.6	2626.1	2160.2	4786.3	0.1354
20	18.20	12.69	1.229	54.6	9.87	1664.9	40.7	2539.9	2090.0	4629.9	0.1487
21	19.06	13.19	1.277	55.8	10.27	1648.1	41.5	2471.8	2038.3	4510.1	0.1602
22	19.92	13.69	1.326	56.9	10.73	1627.7	43.1	2358.4	1950.5	4308.9	0.1789
23	20.78	14.19	1.374	58.1	11.24	1601.9	45.7	2201.9	1831.5	4033.3	0.2069
24	21.64	14.69	1.423	59.3	11.82	1571.3	49.0	2024.1	1701.5	3725.5	0.2443
25	22.50	15.19	1.472	60.6	12.51	1535.2	52.8	1838.8	1572.0	3410.8	0.2909
26	23.36	15.69	1.520	62.0	13.41	1493.1	58.4	1617.8	1424.2	3042.0	0.3615
27	24.22	16.20	1.569	63.7	14.72	1451.2	64.5	1420.6	1292.9	2713.5	0.4462
28	25.08	16.70	1.617	66.6	17.33	1413.1	87.7	949.1	1085.1	2034.2	0.7767
29	25.94	17.20	1.666	68.8	20.56	1240.3	108.1	526.06	971.6	1497.6	1.0917

In Table 5-1, X_o, Y_o are the initial position of the liner element; X-jet is the element jet position, T-jet is the time to jet formation, V_1, V_2 are the stagnation and flow velocities, respectively; V_o is the collapse velocity and β is the collapse angle.

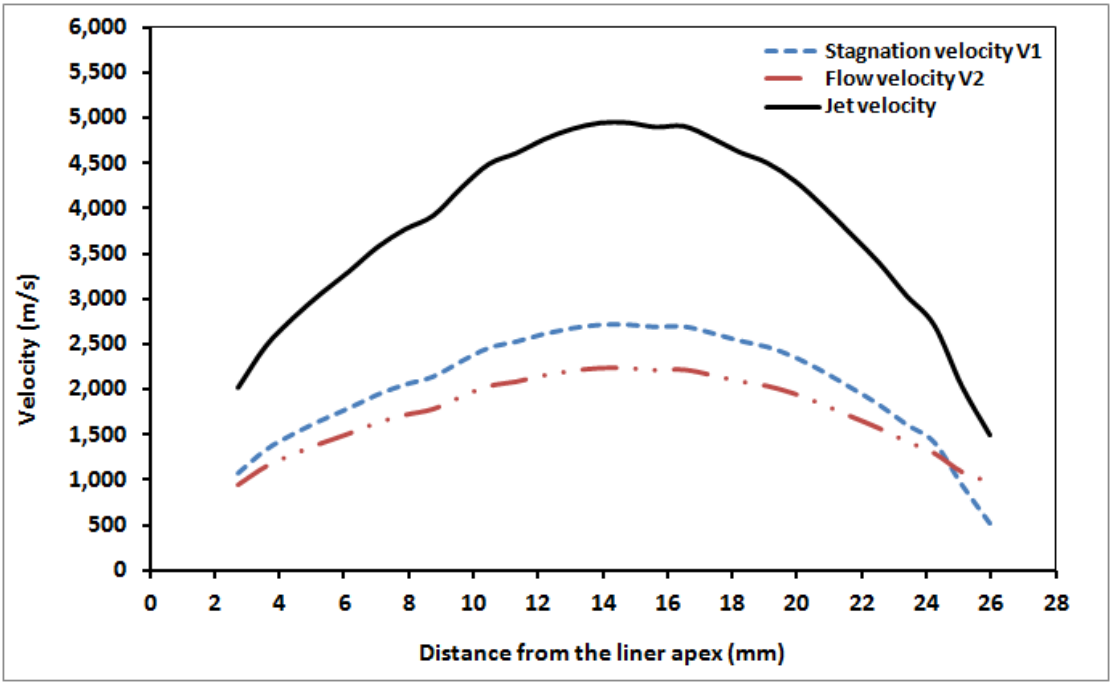

Figure 5-2 The stagnation, the flow and the jet velocities of the OWP calculated using jetting analysis.

5.2.2 Shaped charge jet formation and penetration

In the following part, the jet profile for each conical shaped charge (CSC) OWP after detonation is obtained as illustrated in Figure 5-3 and Figure 5-4. Figure 5-3 shows the sequence of events from detonation to the breakup of the formed jet. The jet tip velocity, cut-off velocity (velocity of the last penetrating element), jet breakup time (the time after which the jet elements starts to particulate and hence its penetration capability decreases dramatically) and the penetration depth into concrete target were obtained and analyzed. Figure 5-4 illustrates the jet, slug and cut-off elements; while Figure 5-5 illustrates the grid plot of the same jet remapped from the jet formation using Euler solver and imported to the Lagrange solver. This jet will hit a laminated target (steel/water/steel) layers backed by the tested concrete as illustrated in Figure 5-6.

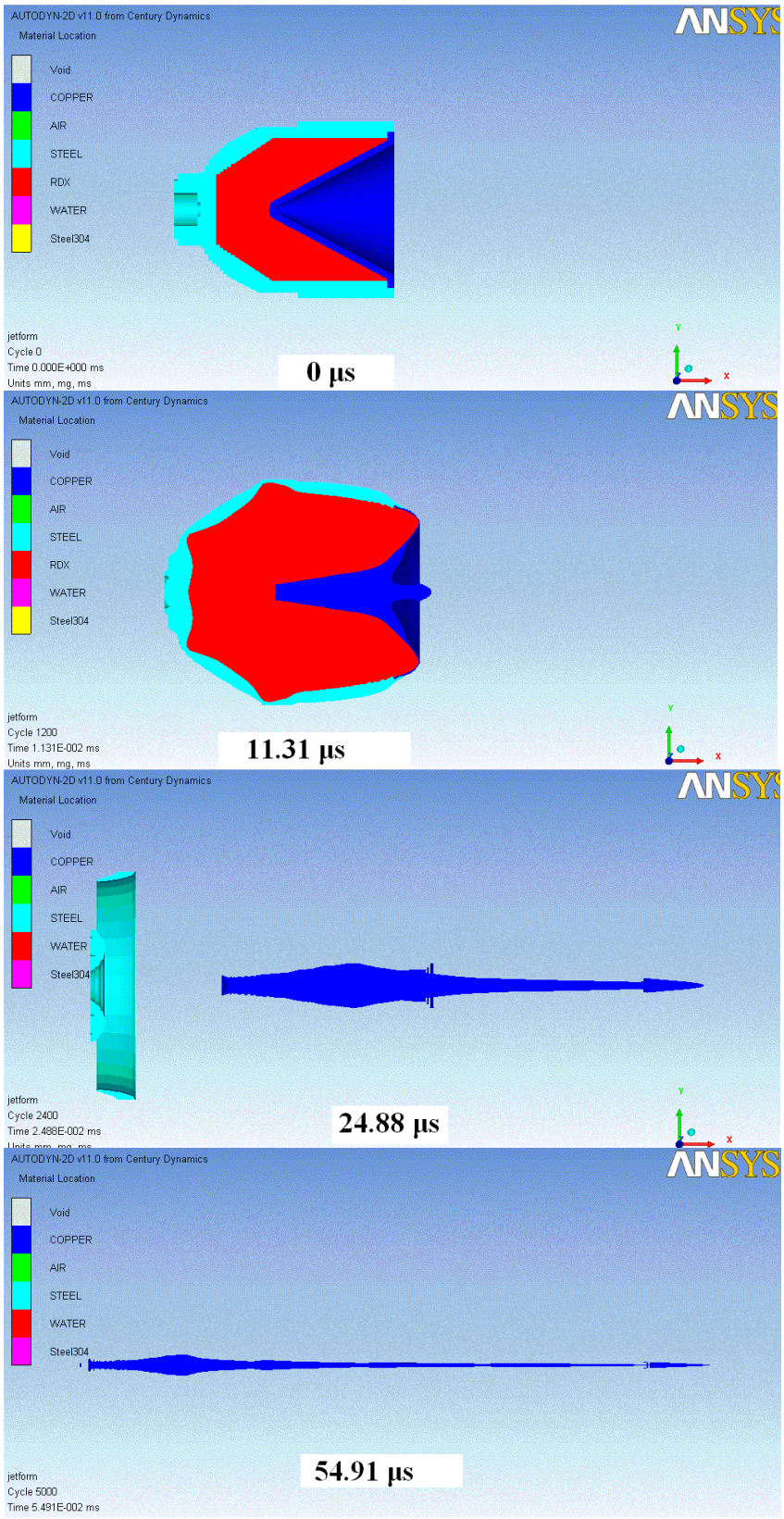

Figure 5-3 The different stages of the detonation of CSC at different times indicating the start of the jet breakup at 54.91 µs.

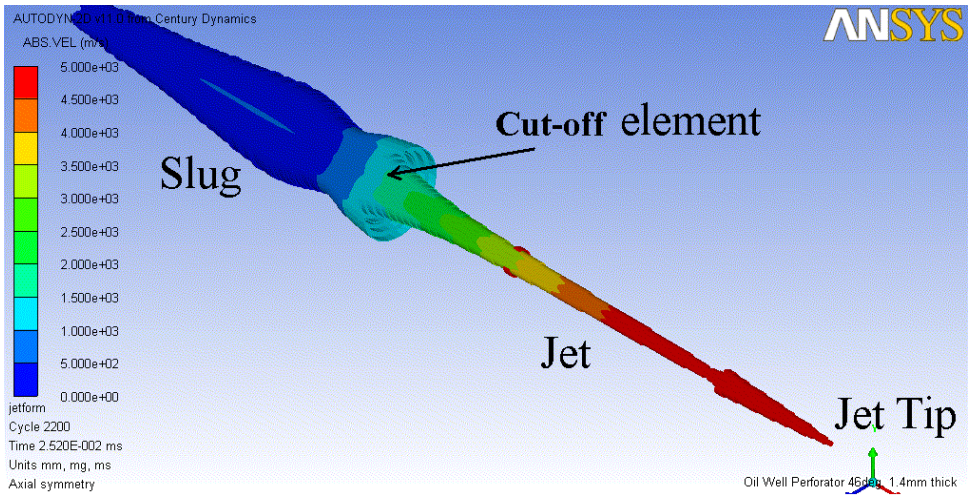

Figure 5-4 Velocity vectors of the shaped charge jet indicating the velocity gradient.

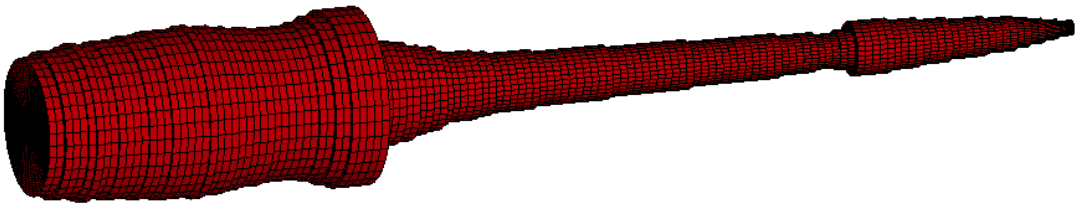

Figure 5-5 Grid plot of the shaped charge jet remapped into Lagrange processor.

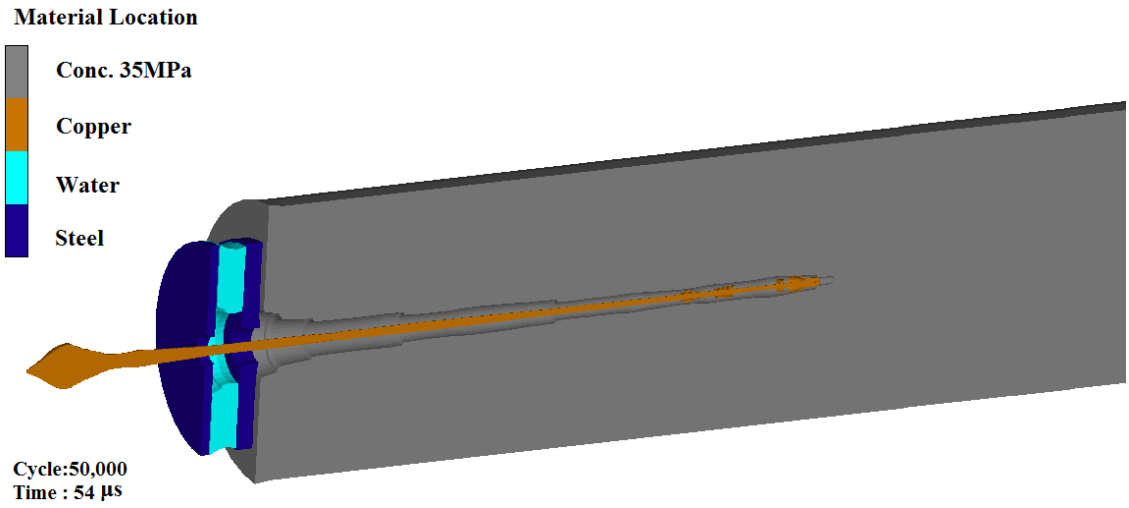

Figure 5-6 OWP remapped jet penetrating the gun wall, water wellbore fluid, steel tube casing and concrete (35MPa).

5.3 Mesh sensitivity study

5.3.1 Mesh sensitivity for the jetting analysis

It is well known that the shape and the density of the mesh affect the simulation results. Generally, simulation with fine meshes produces an accurate solution; but it consumes longer time than that needed for coarse meshing simulations. The mesh sensitivity study for the jetting analysis is performed on a conical OWP of apex angle of 46 degree and copper liner with tapered profile. The Euler grids containing the explosive charge had four uniform square cells with different sizes of 0.3, 0.6, 1.4 and 2mm. The four jetting models with different mesh sizes were allowed to run until the jetting analysis is completed for the entire liner elements. Table 5-2 lists some of the jetting summary output data obtained from the four models. Little change can be observed in the jet mass for the four models, but significant difference was shown for the jet kinetic energy. The difference in the jet masses is explained by variation of the jet collapse angle β for the four models as shown in Figure 5-7. The collapse angle has a direct effect on the mass ratio of the liner that flows to form the jet and the slug [50]. The variation among the four models in their kinetic energy is mainly caused by the different velocities of jet elements for the four meshes as indicated in Figure 5-8. The jet elemental velocities at the liner apex and its base are almost independant of the mesh size, but the velocity difference for different mesh sizes become obvious at certain middle part of the liner, at which most of the jet will be formed. Thus, the velocity drift in this area is the main reason for different kinetic energies. The jet velocity curves seem to be convergent to the curve of 0.3mm mesh model curve, which means that this mesh size is expected to be close to the asymptote limit. On the other hand, the computational time for the model using the finest mesh size of 0.3mm is only 25% longer than that needed for the coarse mesh of 2mm due to the semi-analytical nature of the jetting analysis. Therefore, the mesh size of 0.3×0.3mm was used for the rest of parametric studies of jetting models.

Table 5-2 The jet mass and its kinetic energy for different mesh sizes.

Mesh size(mm)	0.3×0.3	0.6×0.6	1.4×1.4	2×2
Jet mass (g)	6.02	6.14	6.29	6.69
Jet K.E. (kJ)	49.30	47.40	43.20	41.20

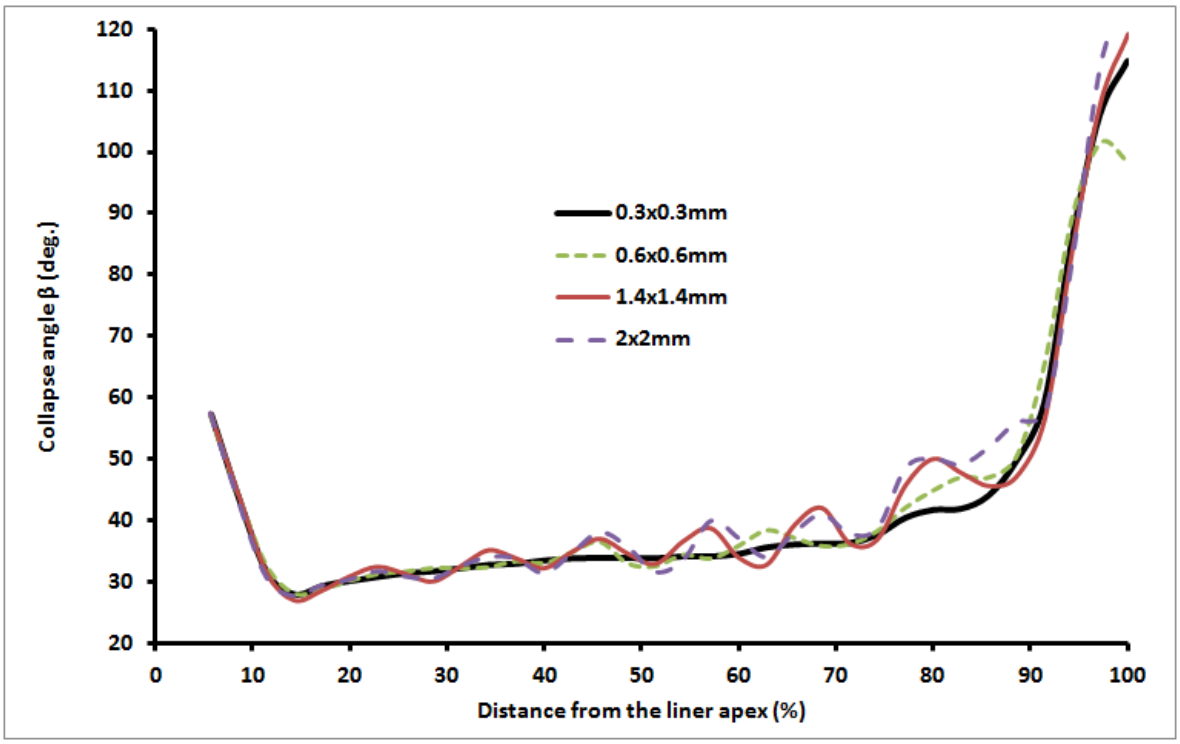

Figure 5-7 The collapse angle at different distances from the liner apex using different meshes.

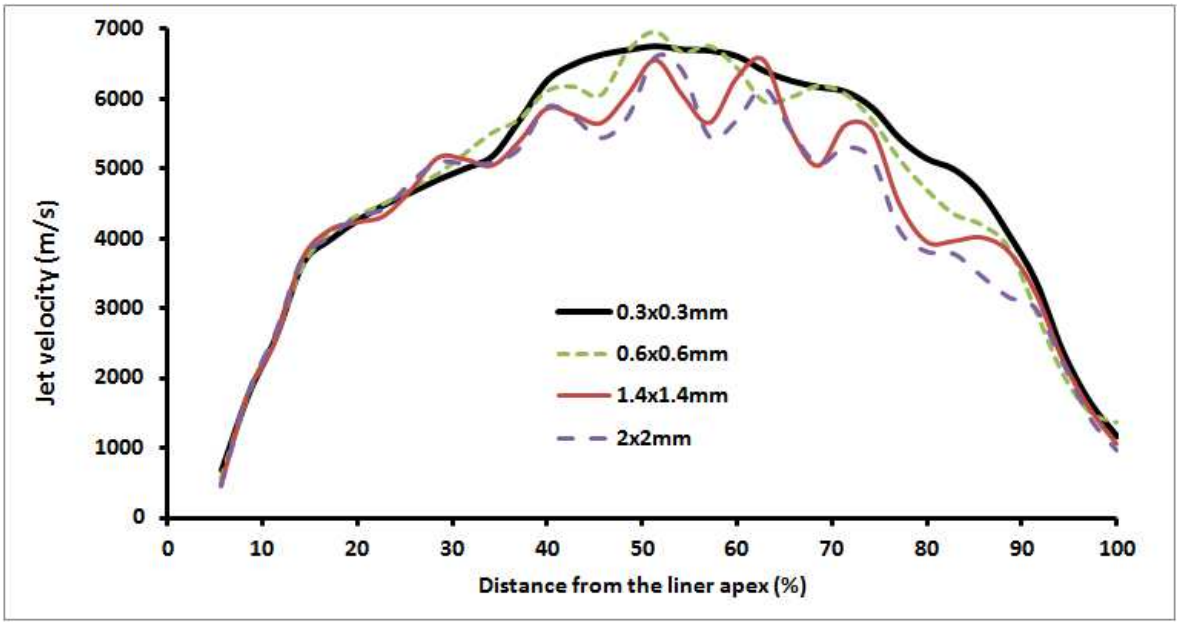

Figure 5-8 The elemental jet velocities at different distances using different mesh sizes.

5.3.2 Mesh sensitivity for the jet penetration

Mesh sensitivity is also an important issue in jet penetration. In order to find how the penetration depth into the concrete material is related to the mesh size, five different uniform square mesh sizes of 0.5, 1, 2, 3 and 4mm were used for the laminated target i.e. the steel, the water and the concrete targets, while the copper jet mesh density of 0.5×0.5mm remains unchanged for the five models. The penetration depth into the concrete using different mesh sizes is depicted in Figure 5-9. This figure shows a convergent penetration depth to the value of 65.3 cm corresponding to the mesh size of 0.5mm; however, the time consumption for this mesh size is eight times more than that needed with the mesh size of 4mm. On the other hand the penetration depth using mesh size of 1mm has only 0.3% (i.e. 0.2cm) difference in comparison with the result obtained for finest mesh size of 0.5mm, but its time consumption is less than half the time needed for the 0.5mm mesh size. Thus the mesh size of 1mm×1mm is used for the rest of simulations.

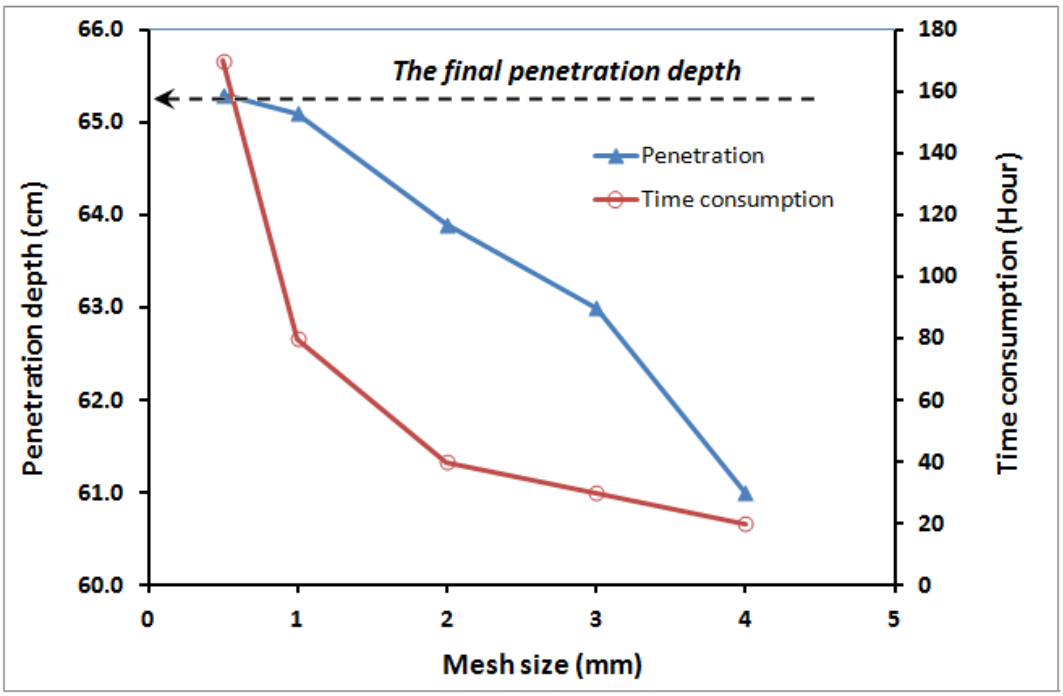

Figure 5-9 The penetration depths into the concrete using different mesh sizes and the relevant time consumption.

5.4 The verification and Validation (V&V) of the hydro-code results

Autodyn hydro-code has been verified by the code developer during their development process and by numerous applications of the code. Thus, only validation issue will be addressed in this section.

5.4.1 The jetting analysis and the jet formation Validation

The numerical Autodyn jetting analysis algorithm was validated by Century Dynamics for a shaped charge of 90mm liner diameter and a cone angle of 18^{o}. The results of the Autodyn numerical jetting analysis agreed with the experimental results for this shaped charge and other analytical models (i.e. HEMP and PISCES) [115]. In the present research, the flash x-ray is used to measure the jet tip velocity and to depict the jet profile at different times to compare with the numerical results in this study. The flash x-ray trial was performed in COTEC (Cranfield Ordnance Test and Evaluation Center) field. Two heads were used to capture photos of the jet profile at different times. The aluminium foil layers were used to trigger the time when the jet tip penetrates through them. Figure 5-10 shows the setup of the x-ray trial field test, while Figure 5-11 shows the jet shapes from x-ray photos and the numerical jet formations at 34μs and 122μs, respectively. A curved shape is observed for the real x-ray jet, which may be caused either by some asymmetries in the liner positioning during the manual filling of the charge or due to the non-uniform explosive mass distribution inside the charge cavity. The main reason for these possible defects is due to the COTEC safety regulation requirements, which demand the charge filling at the test location. Nevertheless, the general aspects of the jet shapes are similar. Besides, the jet tip velocities were found to be 6100m/s and 6182m/s from the x-ray measurements and the numerical simulation, respectively, as shown in Figure 5-12. This means that the error percent is only 1.34% in terms of jet tip velocity, which implies that the numerical hydro-code can be used effectively to model and calculate the shaped charge jet characteristics.

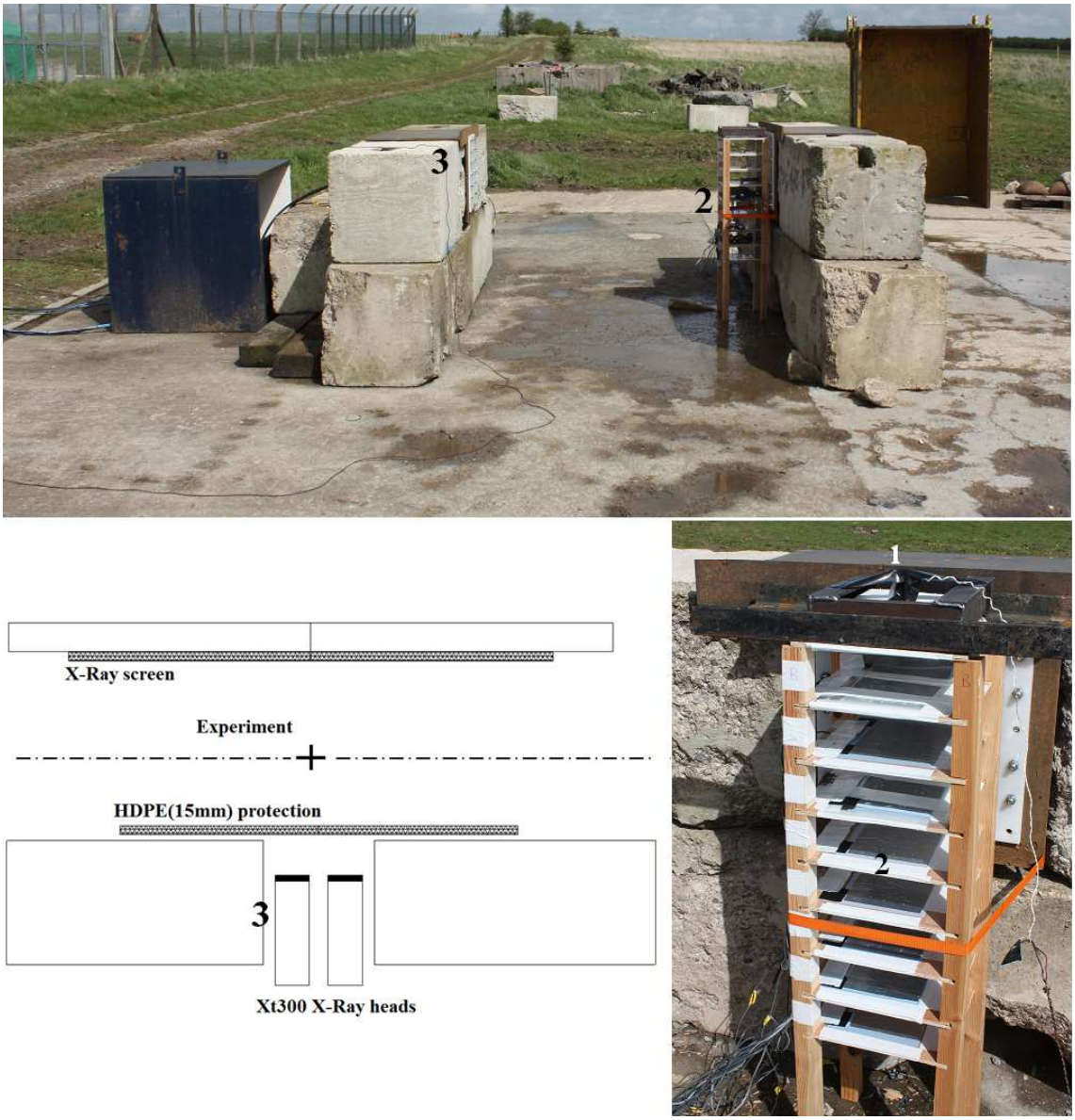

Figure 5-10 The flash x-ray trial setup, 1: the tested OWP, 2: the aluminium foil layers, 3: the x-ray heads.

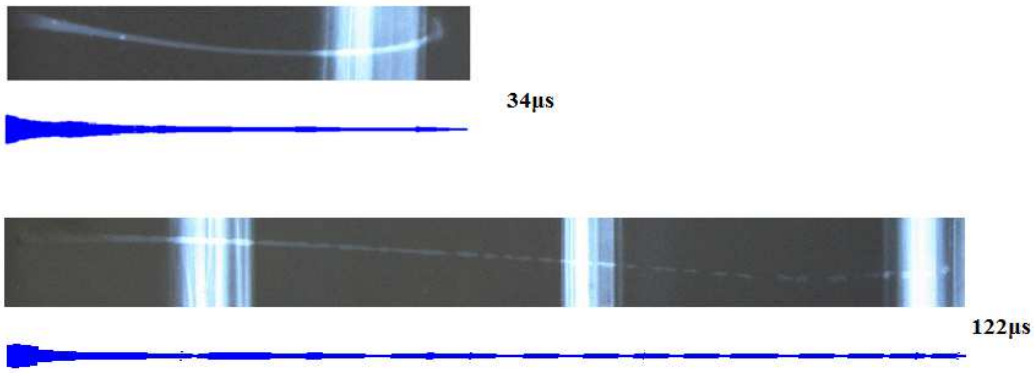

Figure 5-11 The real x-ray jet and the numerical Euler jet at 34µs and 122µs from the moment of detonation.

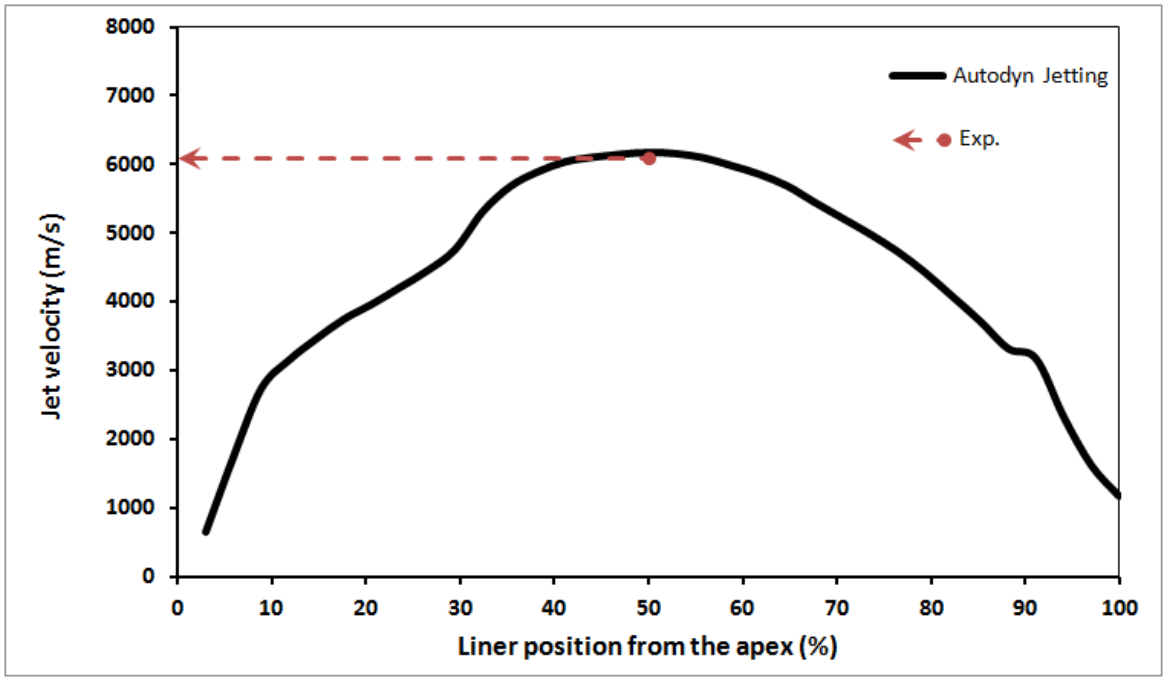

Figure 5-12 The numerical jet velocity at different distances from the liner apex and the real tip velocity estimated experimentally.

5.4.2 The validation of the hydro-code penetration modeling

The Autodyn simulations for penetration into concrete materials using Lagrange solver have been validated experimentally by many authors [117, 124, 130, 132-133]. In this research, the validity of the numerical hydro-code penetration model will be demonstrated by several penetration tests of OWP into API-RP43 configurations. A sample of these tests for a copper liner OWP is shown in Figure 5-13 with the crater profile obtained by the Autodyn penetration modeling. The experimental and the numerical penetration depths were 64cm and 65cm, respectively. The penetration craters are almost identical in experiment and simulation. Thus, the Lagrange numerical model can be used effectively to predict the penetration depth into concrete target with sufficient accuracy (i.e. a small difference of 1.6% was observed between experimental and numerical results).

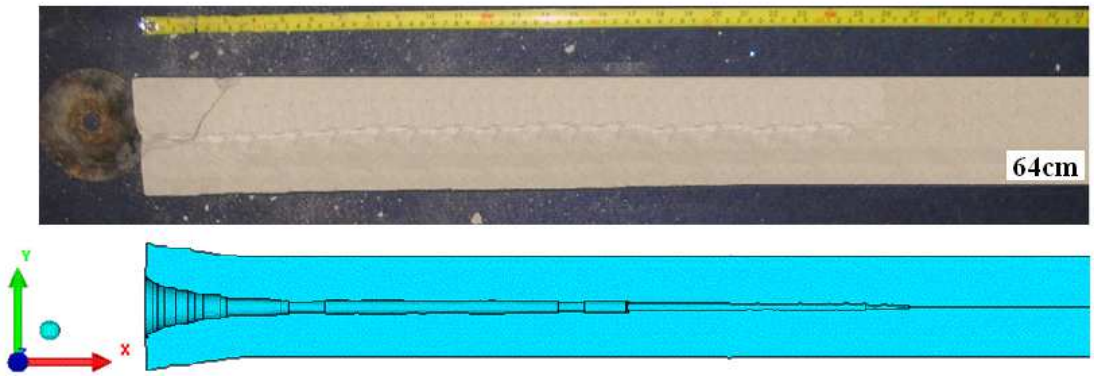

Figure 5-13 The experimental (upper) and the numerical (lower) penetration depths into 40MPa concrete.

5.5 Effect of the surrounding medium on the jet characteristics

The medium surrounding the jet during its flight has a direct effect on the jet velocity as it travels through this medium [134]. To study this effect numerically, two identical shaped charge OWP were fired in air and void mediums, while the jet tip velocities in both media were tracked using the fixed gauge point facility. The gauge points were located at a distance of 1 CD (i.e. charge calibre of 36mm) from each other. A sketch of the gauge points and their locations is shown in Figure 5-14. Figure 5-15 shows the measured maximum jet tip velocities for the three gauges in both media. This figure indicates that the jet tip velocity slightly decreases as it travels short distances (i.e. 3CD). The rates of velocity decrease are 50m/s and 53m/s per 1CD for the jet tip travelling through air and void materials, respectively. Generally, the difference in the jet tip velocity in both cases at short stand-off distance is negligible, which means that the void medium can be used instead of air because it has some advantages to largely reduce the calculation time. Besides, most of the modelled OWPs have to be tested against the laminated target at short stand-off distance (i.e. 1CD), which means that this medium can be used effectively without major changes in the velocity of the jet elements. On the other hand, the jet tip velocity measured in air medium is higher than that in a void medium. This can be explained by the jet velocity-time histories in both mediums as shown in Figure 5-16 for the three gauges. Both the histories are similar except for their peak values that have very small difference between them. Such difference may be attributed to the air motion in front of the jet that can cause little increase in the recorded peak velocity values, but the overall velocity shapes and their arrival times are almost identical in both media.

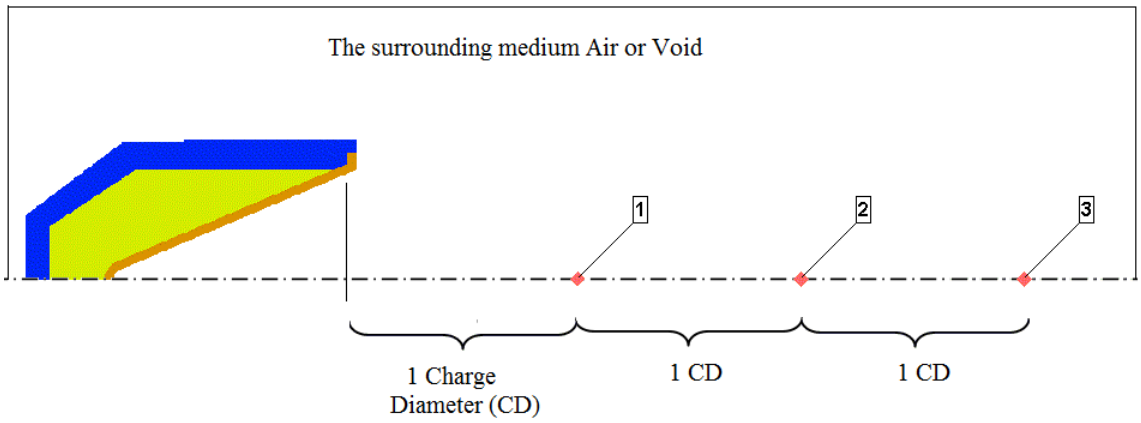

Figure 5-14 The located fixed gauge points used to predict the surrounding medium effect on the tip velocity.

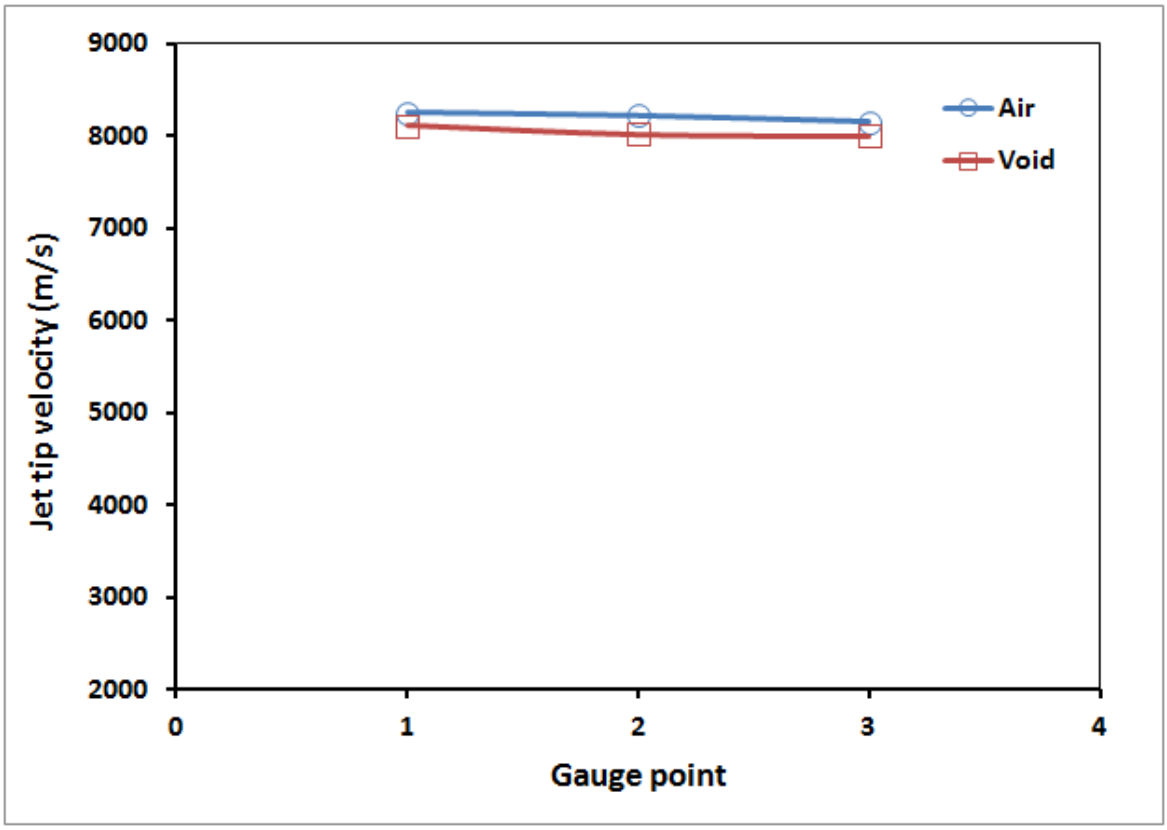

Figure 5-15 The jet tip velocities at different gauges for the air and void media.

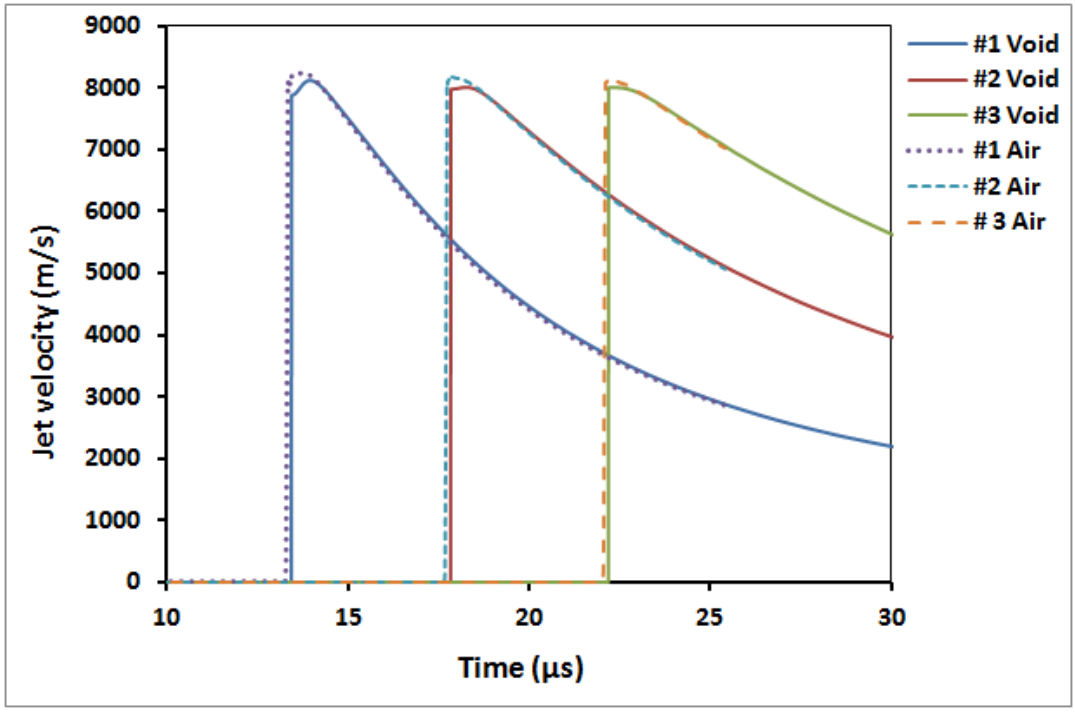

Figure 5-16 The velocity-time histories for the three jets stretching through air and void mediums.

5.6 Shaped charge parametric study results

5.6.1 High explosive effect on jet performance

Gurney energy or Gurney velocity is a measure of explosive power or its efficiency. The higher the Gurney energy, the higher the velocity of the produced jet, and hence the higher the penetration capability of the shaped charge. Figure 5-17 shows the dependence of the jet tip velocity and the Gurney velocity on the explosion heat (Qv) of the used explosive charge. The details of the used explosives and the produced jet characteristics obtained from standard jetting analysis are listed in Table 5-3. The relation between the jet tip velocity and the detonation velocity of the explosive is illustrated in Figure 5-18**.** It shows that the most powerful explosive is HMX, which has a Gurney velocity of 2960m/s and detonation velocity of 9100 m/s. This explosive produces a jet tip velocity of 7103m/s and a jet mass ratio of 17.76%. This result was confirmed by the jet formation model and penetration model tests where the OWP filled by HMX produced the largest penetration depth of 74.88cm. Table 5-4 lists the penetration depths, jet tip and tail velocities and exit hole diameter of the different OWP obtained from jet formation and penetration models using different explosive charges.

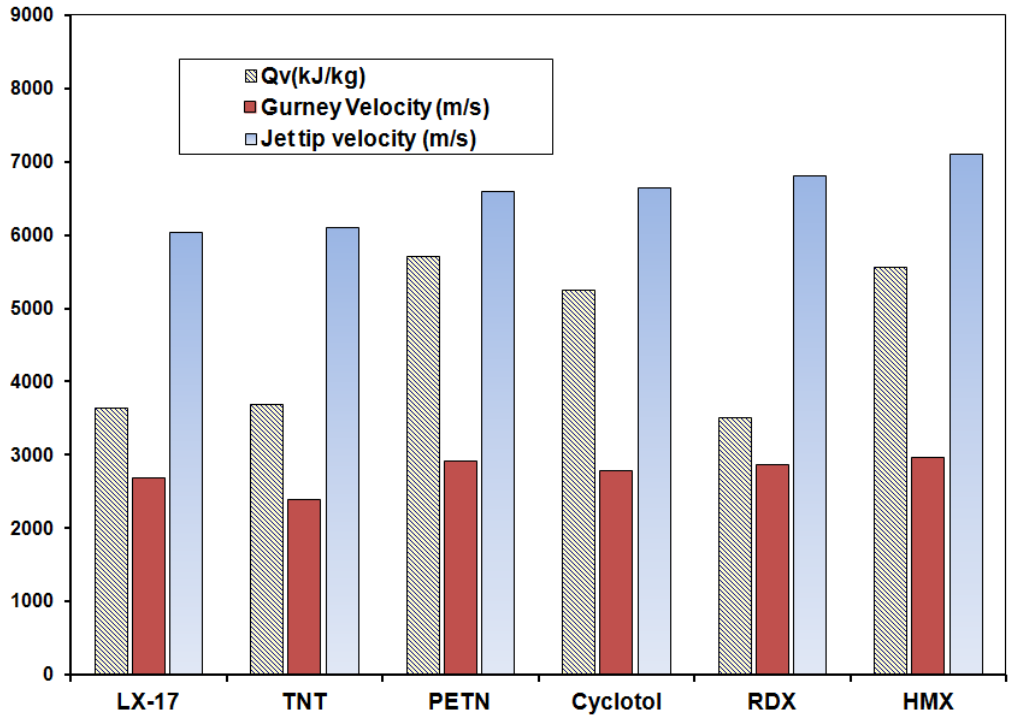

Figure 5-17 The dependence of jet tip velocity and Gurney velocity on the explosion heat of explosives.

Table 5-3 Effect of the explosive type on the jet characteristics of 46° conical copper liner of wall thickness of 1.4mm and 29.32g liner mass with 4.5 mm steel casing thickness.

Explosive properties					Output			
Explosive	ρ_o (g/cm^3)	D (m/s)	Qv (kJ/kg)	$\sqrt{2E}$ (m/s)	Jet mass (g)	Jet %	Jet tip vel. (m/s)	Jet K.E. (kJ)
TNT	1.63	6930	3681	2390	5.45	16.47	6108	38.19
PETN	1.50	7450	5707	2920	5.33	16.10	6605	49.70
LX-17	1.90	7600	6900	2680	5.73	17.30	6046	36.06
RDX	1.73	8100	4118	2870	5.68	17.16	6813	44.59
Cyclotol	1.75	8250	5245	2790	5.82	17.59	6652	43.35
HMX	1.89	9100	5553	2960	5.89	17.76	7103	44.00

Qv is the explosion heat of the explosive material.

Table 5-4 The jet output data and penetration results of CSC with 46° cone apex angle, 1.4mm liner of thickness using different filling explosive charges and 4mm steel casing into 35 MPa concrete target.

Parameter	Explosive Type					
	TNT	Cyclotol	RDX	HMX	TNPE	LX-17
Jet tip velocity (m/s)	6108	6652	6813	7103	6605	6046
Jet momentum (kg.m/s)	15.46	16.64	16.78	15.03	17.72	15.05
Jet tail velocity (m/s)	722	744	656	709	815	674
Penetration depth (cm)	60.96	64.38	71.20	74.88	72.90	66.80
Exit hole diameter (mm)	12.04	16.24	18.80	14.00	19.80	15.52

Note: LX-17 is a mixture of 92.5% TATB and 7.5% Kel F binder.

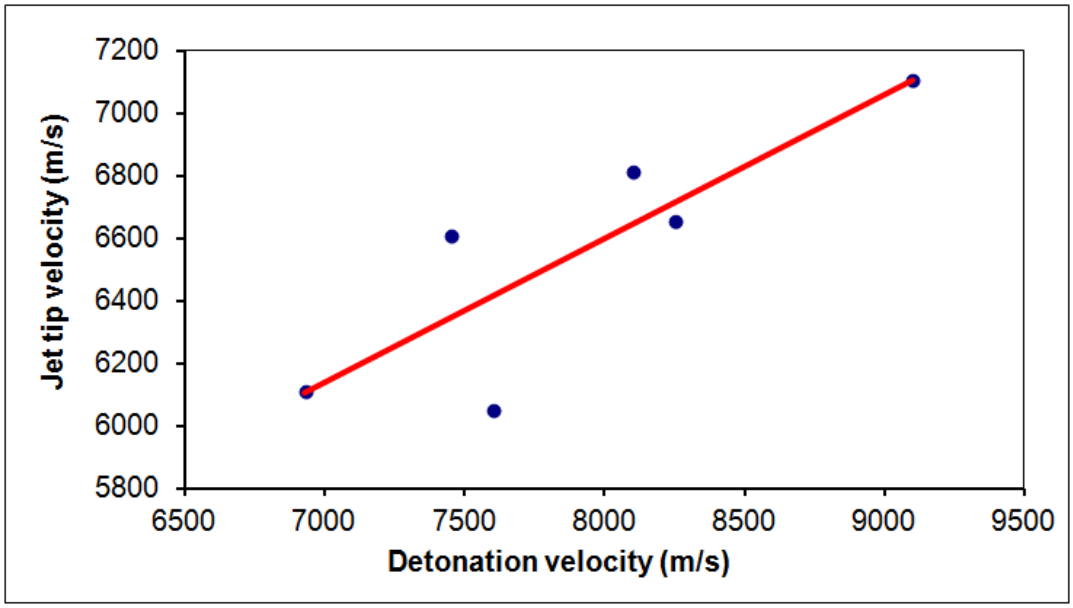

Figure 5-18 The relation between the jet tip velocity and the detonation velocity of the used explosive.

The scaled jet tip velocity to the detonation velocity and the Gurney velocity of the explosive are shown in Figure 5-19 as a function of detonation velocity of the used explosive. It can be concluded that these ratios are nearly constant for the used six explosives. The scaled jet tip to explosive detonation velocity ratio is 0.82, while the scaled jet tip to the Gurney velocity ratio is 2.38. This indicates a nearly constant ratio of jet velocity to the explosive detonation characteristics over a wide range of explosive materials.

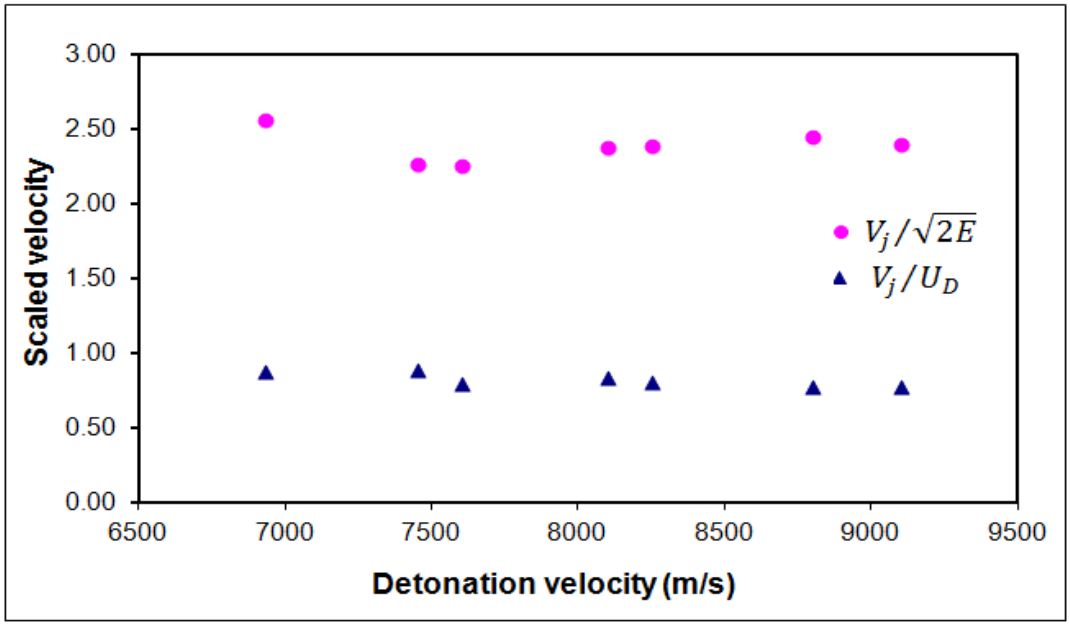

Figure 5-19 The ratio of the jet tip velocity to the detonation velocity and the Gurney velocity of the used explosives.

5.6.2 Liner wall thickness effect

5.6.2.1 Uniform liner wall thickness

According to Zukas [6], the optimum liner wall thickness is 1-4% of the charge calibre. The liner thickness values in this study range between 0.8mm and 3mm for the same OWP of calibre 36mm, which are 2.2% and 8.3% of the charge calibre, respectively. The details of copper liners and the jet output data together with their penetration results are listed in Table 5-5 and illustrated in Figure 5-20. This table illustrates the dependence of jet characteristics on the liner wall thickness. It can be observed that the decrease of the liner wall thickness will reduce the liner mass. Hence, the corresponding jet velocity will increase depending on the mass ratio between the liner and the explosive. The variations of the jet velocity with its cumulative jet mass for the different liner wall thicknesses are illustrated in Figure 5-22. It can be observed that the smallest liner thickness 0.8mm exhibited the highest tip velocity, but has the lowest mass despite its highest jet to liner mass ratio. This thickness does not give the maximum penetration depth, which can be directly related to the jet momentum. On the other hand, the liner thickness of 1.4mm (i.e. about 4% of the charge calibre) has achieved the largest penetration depth, which supports Zukas [6]'s recommendation of optimum liner wall thickness. The jet momentum is correlated with the jet penetration depth as shown in Table 5-5.

Table 5-5 The produced jet characteristics and its penetration for 46° conical OWP for different liner thickness with HMX explosive charge.

HMX Mass (gm)	M/C	Liner Geometry		Output					
		Thick. (mm)	Mass (g)	Jet mass (g)	% jet	Jet tip vel. (m/s)	Jet momentum (kg.m/s)	Pen. (cm)	Hole diam. (mm)
50.74	0.37	0.8	18.9	3.9	20.6	8135	17.22	42.7	14.4
50.74	0.46	1.0	23.7	4.6	19.4	7619	18.27	56.1	15.0
50.74	0.55	1.2	28.3	5.3	18.5	7251	19.00	62.9	16.4
50.74	0.65	1.4	33.1	5.9	17.7	7103	19.56	74.8	14.0
50.74	0.81	1.8	41.5	6.9	16.6	5852	20.32	73.9	16.6
50.74	0.91	2.0	46.1	7.4	15.9	5533	20.52	71.0	10.2
50.74	1.29	3.0	65.5	9.1	13.8	4331	20.30	72.4	18.0

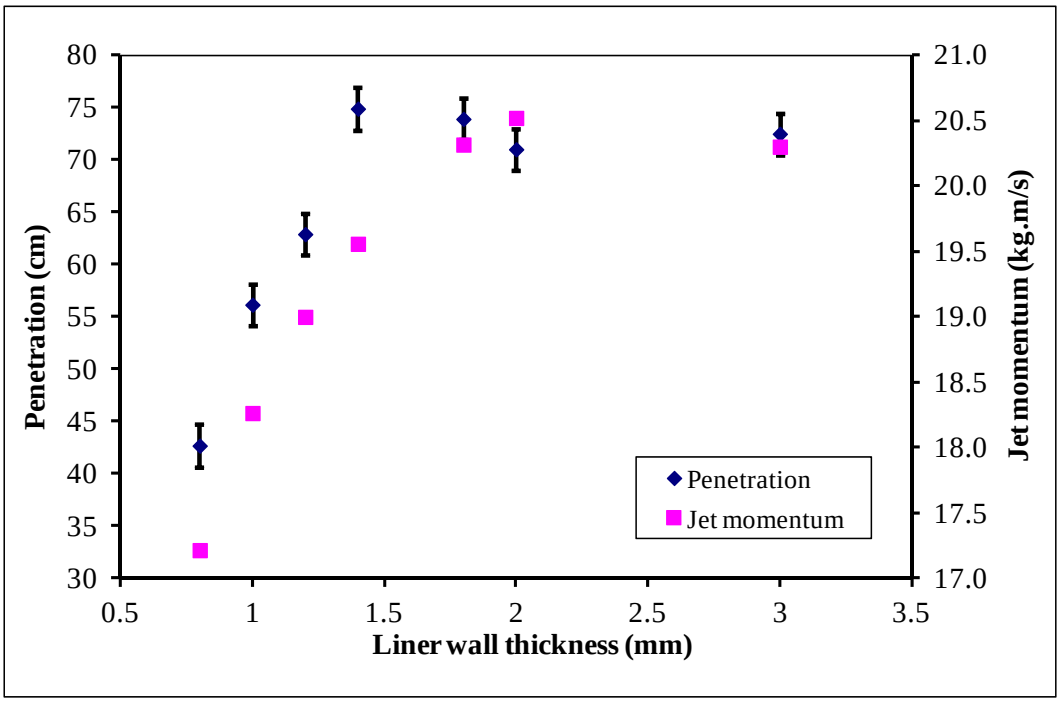

Figure 5-20 The penetration depth of 46° conical OWP for different liner thicknesses with HMX explosive charge and steel casing thickness.

The penetration of a shaped charge OWP with different liner thicknesses as a function of jet momentum is shown in Figure 5-21. The penetration relation seems to be directly propotional to the jet momentum upto a certain value, after which the penetration decreases due to the massive jet and the large diameter of jet produced from large thickness liners.

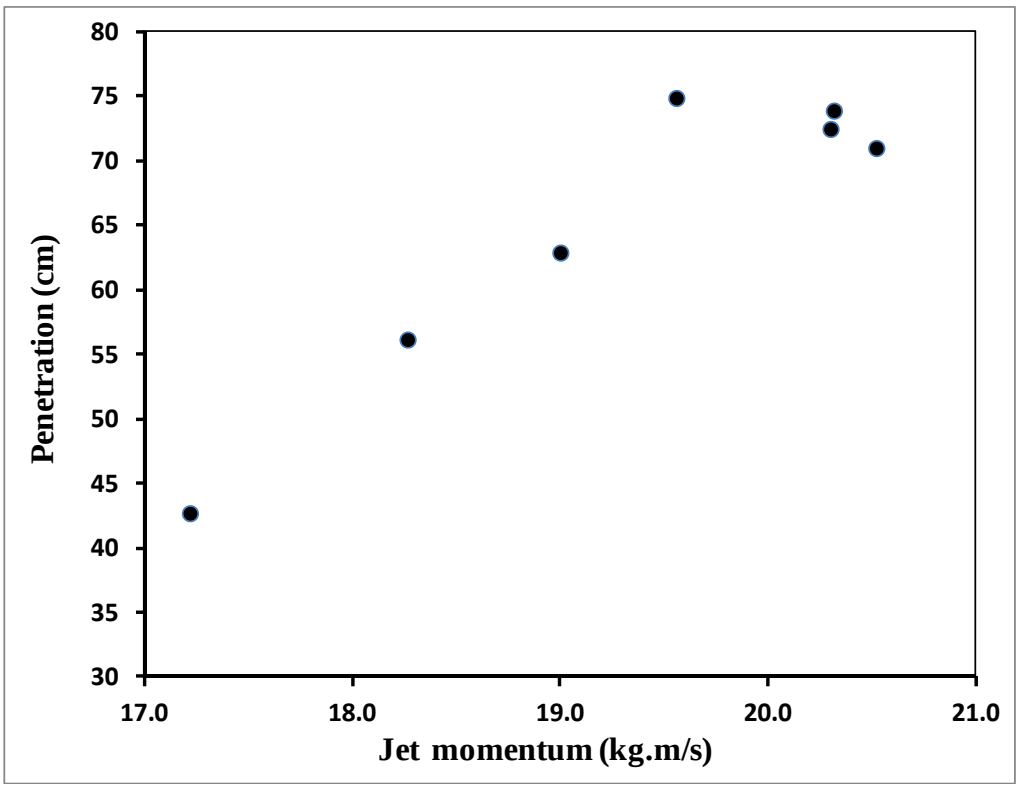

Figure 5-21 The penetration as a function of the jet momentum

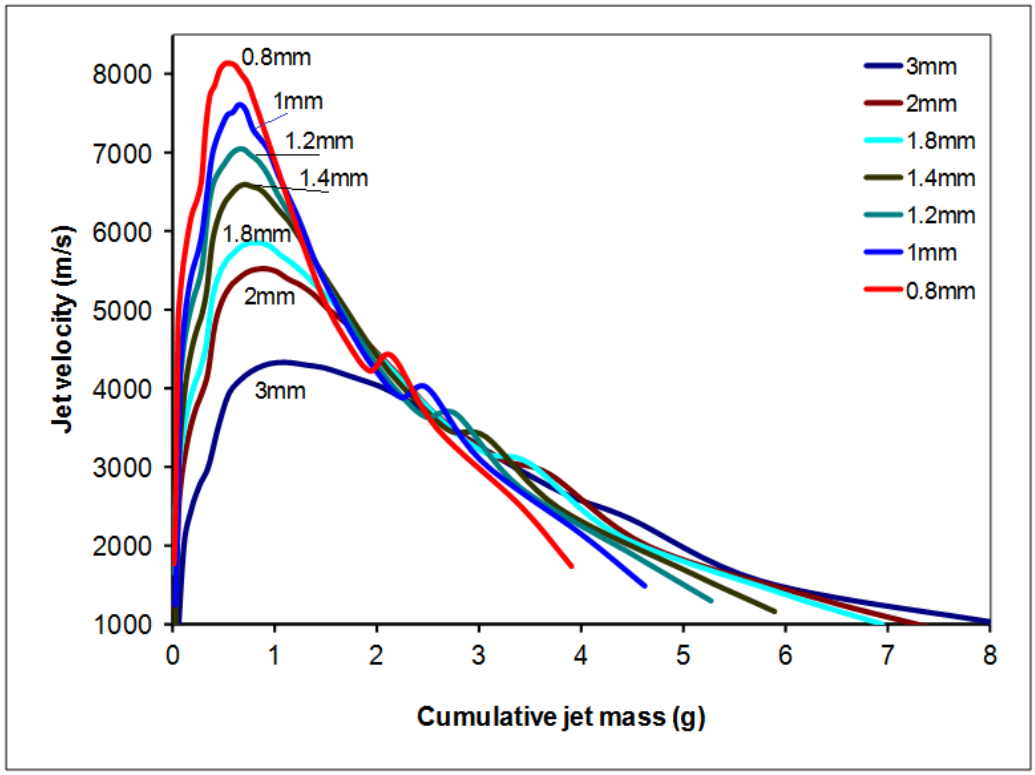

Figure 5-22 The jet tip velocities as a function of cumulative jet mass for different liner wall thicknesses according to standard jetting analysis algorithm.

5.6.2.2 Varied liner wall thickness

Effects of the tapered liner wall thickness on jet performance were also studied, in which the wall thickness at the cone apex is different from that at the liner base. The two studied shapes are illustrated in Figure 5-23 .

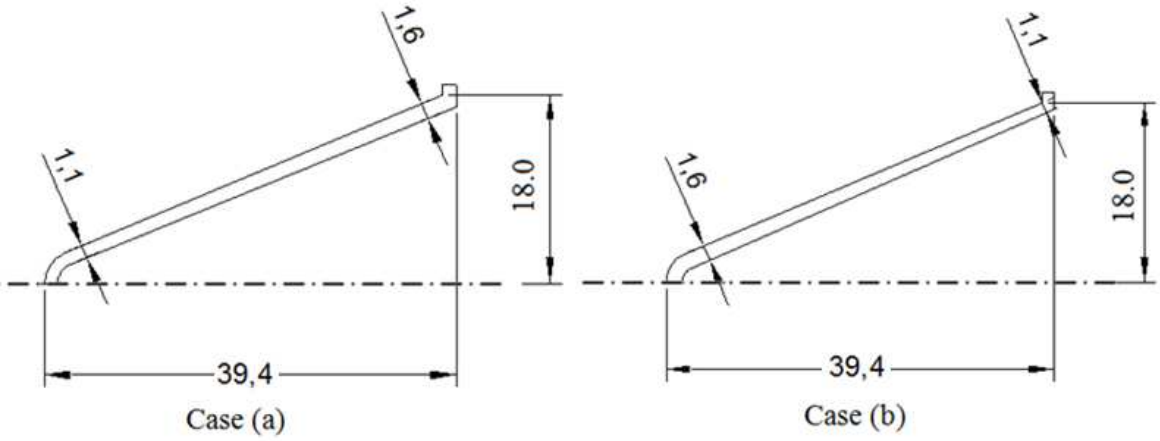

Figure 5-23 Liner walls with varied (tapered) thicknesses.

The jet output data and the penetration results for the two liner shapes are illustrated in Table 5-6. Case (b) exhibited higher jet tip velocity but lower jet mass than that of case (a). However, its total momentum is 15% lower than that of case (a), which explains the difference between them in the achieved penetration depth.

Table 5-6 The jet output data and the penetration results for OWP with two different liner wall thicknesses of nearly the same weight.

	Varied thickness 1.1-1.6 Case (a)	Varied thickness 1.6-1.1 Case (b)
Mass of jet (g)	6.25	4.17
Jet %	18.80	14.63
Jet tip velocity (m/s)	6213	7050
Momentum (kg.m/s)	19.30	16.38
Penetration depth (cm)	61.40	57.00
Hole diameter (mm)	13.80	14.76

5.6.3 Cone apex angle

The characteristics of the shaped charges jet mainly depend on the explosive to metal mass ratio and the liner geometry (i.e wall thickness and its cone apex angle). The mass ratio will normally be changed as the cone angle changes, which should be considered in the

study of the cone angle effect on the jet characteristics. To consider this effect, seven shaped charge models with different cone apex angles, but a constant explosive to metallic liner mass ratios (C/M) and a constant liner wall thickness were studied in order to differentiate the effect of cone apex angle on the jet characteristics from other effects. The seven different cone angles are 22, 32, 40, 46, 56, 60 and 70^o, which were used to estimate the produced jet characteristics and its efficiency using the standard jetting analysis, the jet formation and penetration codes in Autodyn. The constant C/M ratio and the liner thickness are 1.069 and 1.77mm, respectively.

5.6.3.1 Standard jetting analysis

The jet characteristic data according to the jetting analysis for different cone angles at constant mass ratios are listed in Table 5-7. The jetting analysis shows that the jet tip velocities for the 22^o and 70^o cone apex angles were 8243 and 5538 m/s, respectively. However, the jet mass percentage in the case of 22^o is less than that for 70^o, which explains the big difference on the jet kinetic energy between these two designs. Such difference is attributed only to the cone apex angle effect because their mass ratios are kept constant. On the other hand, the calculated maximum collapse velocities of both models were 2136 and 1755 m/s, respectively, which have direct influence on the jet formation. This comparative study supports the theory, which states that narrow cone angles produce fast jet but with lower jet mass.

Table 5-7 Effect of the cone apex angle on the jet characteristics at the same explosive to metal mass ratios (C/M = 1.069, RDX to Copper liner mass ratio).

Liner Geometry			Output			
Apex angle	Liner thick. (mm)	Liner mass (g)	Jet mass (g)	% jet	Jet tip velocity (m/s)	Jet K.E. (kJ)
22	2.72	24.53	1.54	6.27	8243	18.25
32	2.34	45.43	1.87	4.12	6674	38.38
40	1.87	43.53	4.04	9.27	6500	52.62
46	1.79	36.94	3.82	10.34	6088	41.36
56	1.77	29.62	3.37	11.36	5855	39.66
60	1.74	26.62	3.40	12.77	5603	36.30
70	1.47	27.63	4.30	15.56	5538	44.58

For the constant liner wall thickness of 1.77, a liner with cone apex angle of 22^o is expected theoretically to achieve a deep penetration depth due to its high velocity; but the mass ratio of the produced jet is only 6.15% of the total liner mass as shown in Table 5-8. The model with cone apex angle of 40^o produces a jet with a tip velocity of 6995 m/s and a

jet mass ratio of 9.89%. As a result, the total kinetic energy of this jet is more than twice that of the former one. The dependence of the tip velocity of the jet resultant from the same liner wall thickness of 1.77 for the entire apex angles is illustrated in Figure 5-24.

Table 5-8 Effect of the cone apex angle on the jet characteristics for the same 1.77mm liner wall thickness and 6mm steel casing.

RDX mass (gm)	C/M	Liner Geometry			Output			
		Apex angle	Liner thick. (mm)	Liner mass (g)	Jet mass (g)	% jet	Jet tip velocity (m/s)	Jet K.E. (kJ)
26.25	1.33	22	1.77	19.67	1.21	6.15	9531	25.37
66.04	1.72	32	1.77	38.30	2.54	6.63	7629	48.29
56.47	1.33	40	1.77	42.34	4.19	9.89	6995	54.77
48.47	1.29	46	1.77	37.66	4.05	10.75	6097	42.59
31.66	1.38	56	1.77	29.62	3.37	11.36	5855	39.66
37.99	1.49	60	1.77	25.43	3.05	11.99	5554	33.03
29.53	0.89	70	1.77	32.97	5.02	15.22	4862	43.10

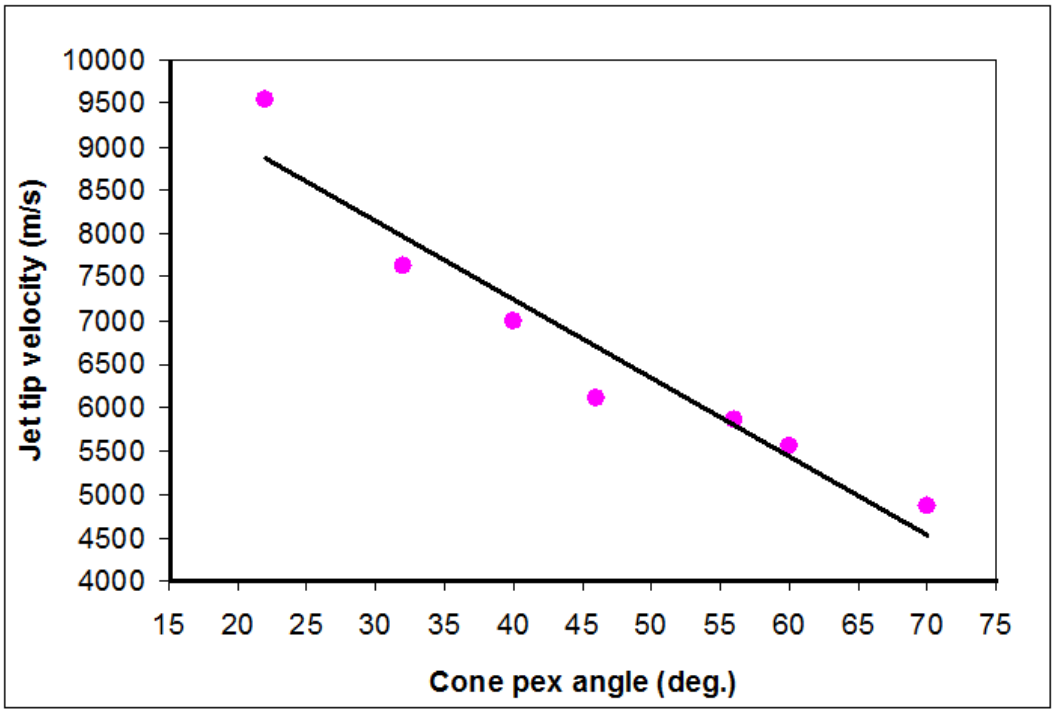

Figure 5-24 The jet tip velocity as a function of cone apex angle with uniform liner wall thickness of 1.77mm.

5.6.3.2 Jet formation and penetration calculations

For uniform liners, as the cone angle widens, the jet becomes shorter, thicker, and less penetrative [26], which can be illustrated by Table 5-9 and Figure 5-25 obtained from the jet formation and penetration results. The smallest apex angle gives the fastest jet tip

velocity as illustrated in Figure 5-26; but with the smallest jet mass. However, for the wider angles, the charge performance is better than the small apex angles when they have the same mass ratio between explosive and liner as illustrated in Table 5-10. This result illustrates the effect of the liner thickness on the penetration and jet characteristics. However, this parametric study is not sufficient to judge the best design, therefore, an optimization study for the cone apex angle and the liner thickness will be performed to achieve the largest penetration depth with the lowest mass of explosive.

Table 5-9 The jet characteristics and penetration results of OWP of 1.77 mm liner thickness for different cone apex angles.

Cone Apex angle. (deg.)	Liner thickness (mm)	Code output			
		Jet tip velocity (m/s)	Jet tail velocity (m/s)	Penetration depth (cm)	Hole diam. (mm)
22	1.77	9531	4254	50.48	12.8
32	1.77	7629	2614	69.72	12.4
40	1.77	6995	2560	64.72	14.4
46	1.77	6097	1023	62.88	17.8
56	1.77	5855	1172	60.96	18.3
60	1.77	5554	1921	58.00	15.0
70	1.77	4862	1753	54.64	13.6

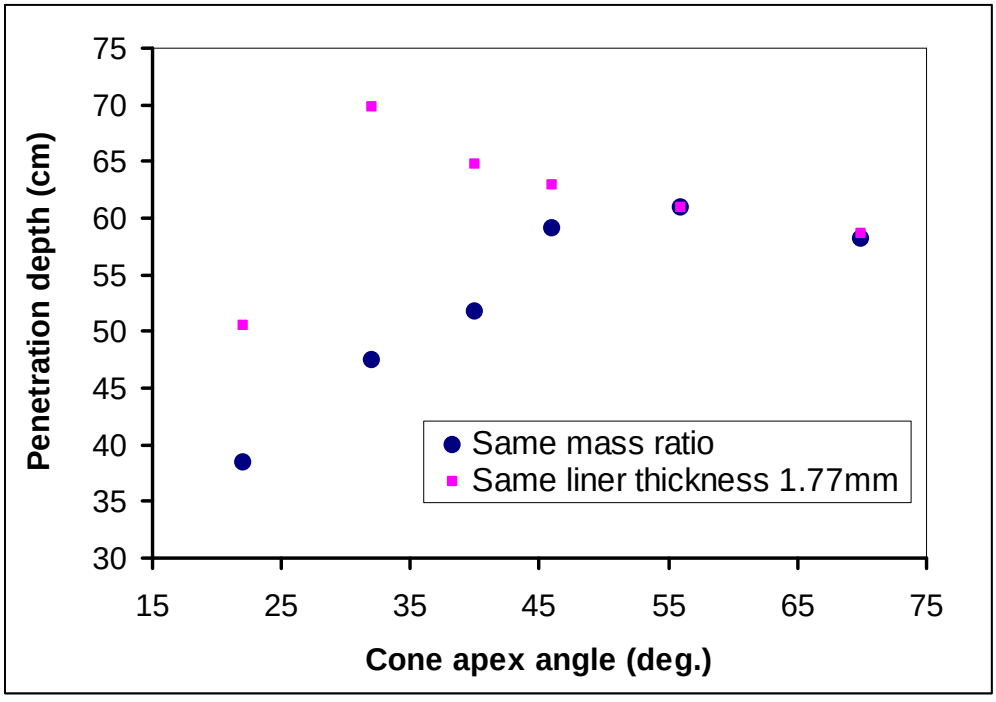

Figure 5-25 The calculated penetration depth for OWP at different cone apex angles.

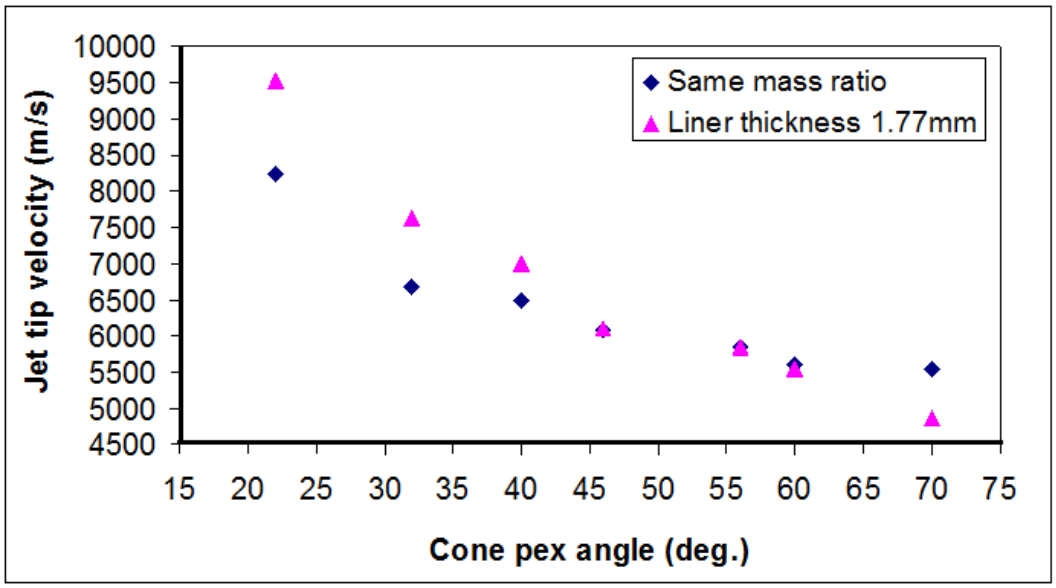

Figure 5-26 A comparison between the jet tip velocity for different apex angles at both the same mass ratio and the same thickness.

Table 5-10 The jet output data and penetration results for OWPs with different liner cone apex angles and the same explosive to metal mass ratio (C/M = 1.069).

Cone apex angle. (deg.)	Liner thickness (mm)	Code output			
		Jet tip velocity (m/s)	Jet tail velocity (m/s)	Penetration depth (cm)	Hole diam. (mm)
22	2.72	8243	2774	38.36	8.2
32	2.34	6674	2896	47.40	21.4
40	1.87	6500	1724	51.80	17.8
46	1.79	6088	1400	59.04	16.4
56	1.77	5855	1172	60.96	18.3
60	1.74	5603	2033	59.00	18.5
70	1.47	5538	2030	58.16	19.4

5.6.3.3 The optimization of the cone apex angle and liner thickness parameters

The objective of this optimization is to obtain the maximum penetration depth into concrete with the convenient explosive mass and apex angle of the cone. Table 5-11 lists the input parameters for the design expert software used to do the optimization calculations. The selected effective design parameters in the optimization are the cone apex angle, its liner wall thickness and the masses of both the liner and the explosive material. The response parameters that will be considered are the penetration depth (to be maximized) and the explosive mass (to be minimized).

Table 5-11 The input factors and their response values for the optimization study.

Factors		Responses	
Apex angle (deg.)	Liner thick. (mm)	RDX mass (gm)	Penet. depth (cm)
22	2.72	26.25	38.36
32	2.34	66.04	47.40
40	1.87	56.47	51.80
46	1.79	48.47	59.04
56	1.77	41.06	60.96
60	1.74	37.99	59.00
70	1.47	29.53	58.16
22	1.77	26.25	50.48
32	1.77	66.04	69.72
40	1.77	56.47	64.72
46	1.77	48.47	62.88
56	1.77	41.06	60.96
60	1.77	37.99	58.00
70	1.77	29.53	58.64

The goals, the importance and the boundary constrains of the studied factors are listed in Table 5-12, in which the penetration depth is set to be the most important objective design response, while the next one to be considered is the explosive charge mass.

Table 5-12 The input constrains, the governing limits and the response importances.

Name	Goal	Lower limit	Upper limit	Importance
Cos (α)*	is in range	0.819	0.982	++
Liner thickness (mm)	is in range	1.47	2.72	++
Explosive mass (g)	Minimize	26.25	66.04	+++
Penetration depth (cm)	Maximize	-	-	+++++

Note: α is half of the apex angle of the conical liner

Table 5-13 summarizes the results that were obtained from the optimization run. The thirty solutions in this table are arranged according to their desirability, which is observed to be almost unity for the whole range. This represents a high degree of accuracy between the expected response calculated by the statistical objective function based on the fitting data of the input factors and that presented as a real experiment. In general, desirability value of zero respresents a completely undesirable response, while the desirability value of unity represents an ideally desirable response. However, the manufacturing capability of the suggested optimum designs should be considered from the manufacturing point of view.

For instance, the suggested designs that have a liner wall thickness greater than 2mm should be ignored if the spinning is the method that will be used to manufacture the liner with the small perforator dimensions. This is because of the difficulty of machining the thick liners with small details and high precesion. Generally, the first two designs are considered as the optimum designs that can be easily manufactured due to the facts that their angle and their liner thickness can be done easily without further manufacturing limitations. The combinations between the two columns, which are the liner thickness and the Cos (α) will be changed if the used exolsive amount is greater than 26.25g. This means that different varieties for liner thickness and Cos (α) will be obtained depending on the used explosive mass. Similarly, different desirability values corresponding to different explosive charges will be obtained.

Table 5-13 The optimum solutions and their corresponding desirability calculated by the steepest slope optimization.

Number	Angle (2α)	Cos (α)	Liner thick. (mm)	Explosive mass (g)	Penetration depth (cm)	Desirability
1	56.96	0.879	1.49	26.25	100.23	1.00
2	43.13	0.93	1.58	26.25	102.50	1.00
3	58.15	0.874	2.05	26.25	76.05	1.00
4	54.25	0.89	2.41	26.25	132.49	1.00
5	26.69	0.973	1.54	26.25	128.67	1.00
6	63.36	0.851	2.49	26.25	219.49	1.00
7	32.11	0.961	2.67	26.25	71.41	1.00
8	39.90	0.94	1.63	26.25	90.19	1.00
9	55.99	0.883	2.1	26.25	75.94	1.00
10	69.63	0.821	2.66	26.25	351.02	1.00
11	61.37	0.86	1.53	26.25	83.51	1.00
12	52.21	0.898	2.21	26.25	78.43	1.00
13	43.44	0.929	1.59	26.25	98.63	1.00
14	36.75	0.949	2.6	26.25	80.28	1.00
15	55.50	0.885	2.1	26.25	73.64	1.00
16	34.12	0.956	1.55	26.25	118.76	1.00
17	67.60	0.831	2.14	26.25	123.05	1.00
18	36.75	0.949	1.56	26.25	115.06	1.00
19	52.98	0.895	2.28	26.25	92.61	1.00
20	37.48	0.947	2.56	26.25	74.35	1.00
21	63.36	0.851	1.5	26.25	81.22	1.00
22	68.21	0.828	2.25	26.25	156.10	1.00
23	59.55	0.868	2.01	26.25	75.00	1.00
24	67.18	0.833	2.63	26.25	314.34	1.00
25	66.14	0.838	2.45	26.25	219.98	1.00
26	52.47	0.897	2.42	26.25	125.44	1.00
27	64.01	0.848	2.69	26.25	321.42	1.00
28	59.31	0.869	2.54	26.25	208.74	1.00
29	43.75	0.928	1.5	26.25	125.65	1.00
30	60.92	0.862	2.21	26.25	114.21	1.00

To illustrate the desirability of the solution with the selected parameters, a graph of the tested factors was selected with the relevant desirability. The graphs illustrated in Figure 5-27 and Figure 5-28 show the two areas, in which the desirability could be very high (i.e. close to the unity). The preferred two areas of the highest desirability are represented by areas A and B, while any combinations of the liner thickness and the apex angle that lead to regions C and D should be avoided.

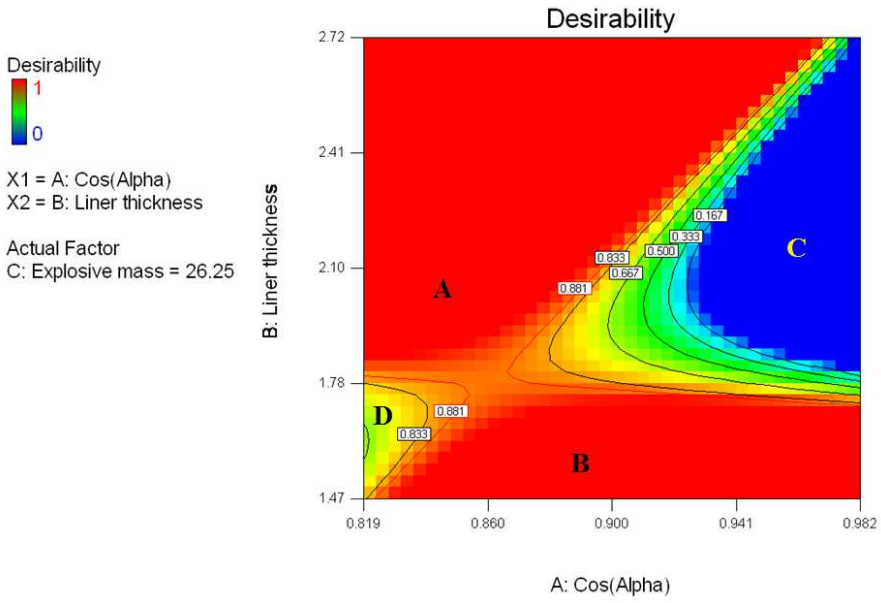

Figure 5-27 2-D contours of the desirability with the liner angle and its thickness.

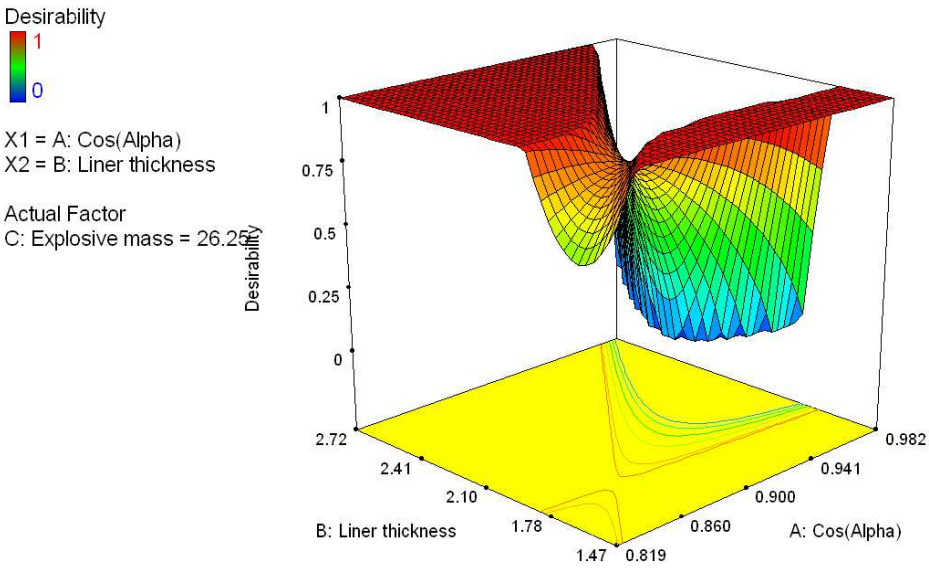

Figure 5-28 3-D surface of the calculated desirability for the optimization problem.

The two optimum areas of this design are shown in Figure 5-29 and Figure 5-30 considering the penetration response, where the penetration contours in the upper area

indicate that the increase in the penetration capability of the perforator demands the increase in both the liner thickness and the cone angle. On the other hand, in the lower area, the the penetration depth increases with the decreases in the liner thickness and its angle, provided that the same amount of explosive remains unchanged (i.e. 26.25 gm). On the other hand, the liner design including angle and thickness that can produce a penetration in both the blue (right) and green (left) regions in Figure 5-29, should be avoided.

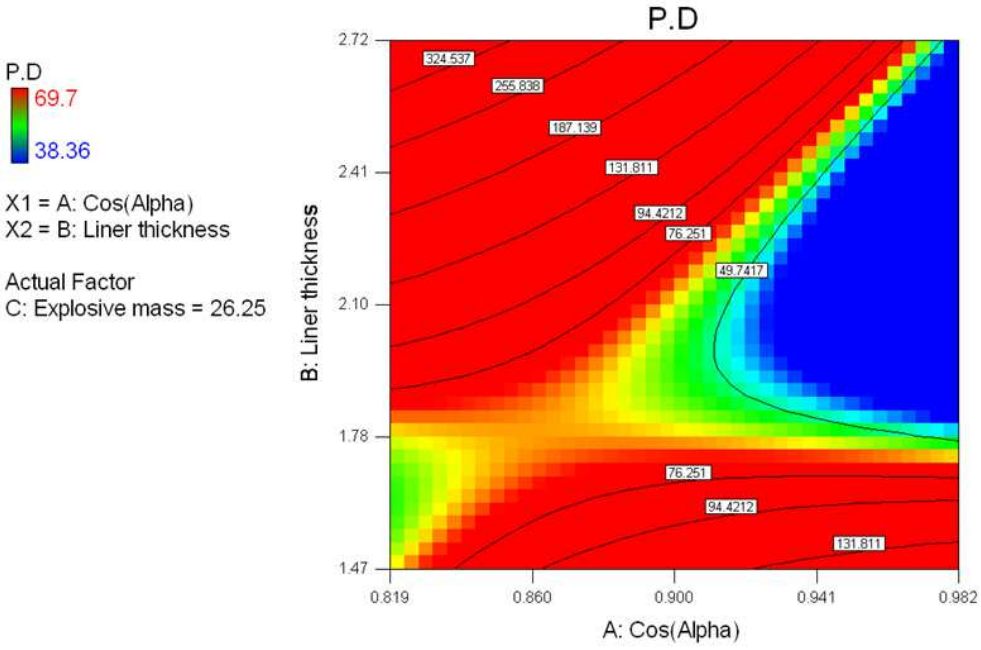

Figure 5-29 The penetration depth 2-D contours with the optimization parameters (angle and liner thickness) using the optimum (minimum) explosive mass 26.25gm.

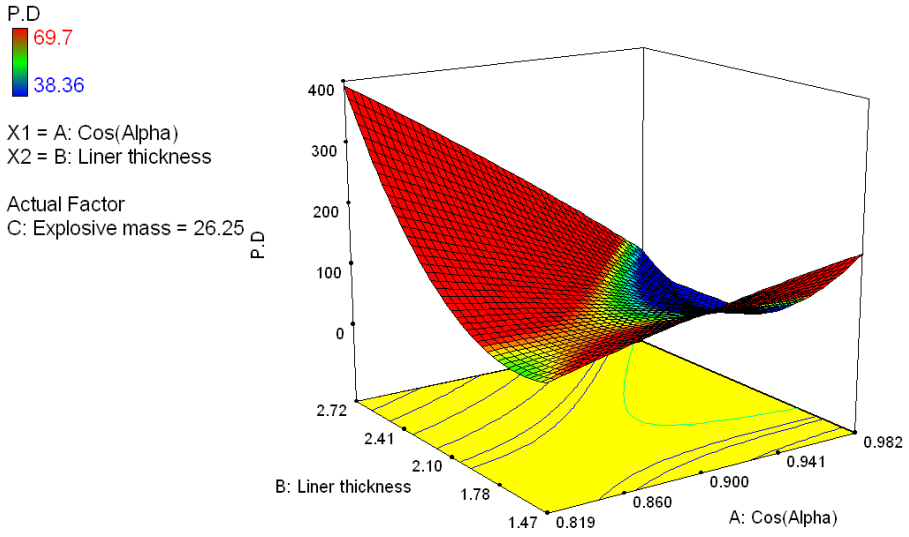

Figure 5-30 3-D surface of the calculated penetration depth for the optimization.

5.6.4 Liner shape and its geometry

In order to investigate the effect of liner geometry, three different geometries of shaped charge liners with nearly the same explosive and liner masses were used. One of these geometries is the conical liner with apex angle of 46^{o} with a liner wall thickness of 1.4mm. The second shape is the trumpet liner with the same liner thickness of 1.4mm. The third one is a bi-conical shape with a uniform liner wall thickness of 1.1mm. Figure 5-31 shows the shapes of the three different liners and Table 5-14 lists the calculated jet characteristics and their penetration depths into concrete targets.

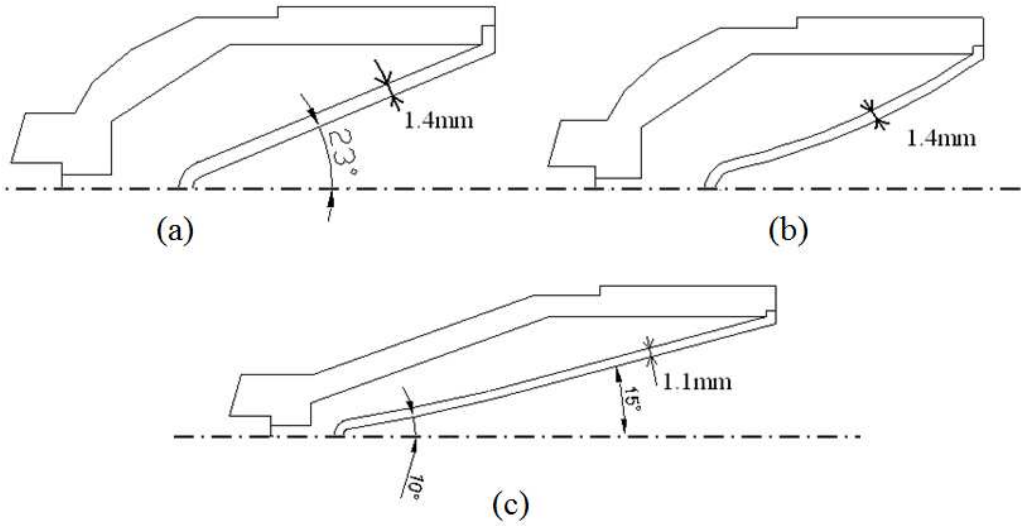

Figure 5-31 The three liner shapes; (a) the conical liner, (b) the trumpet liner, and (c) the bi-conical liner, all with uniform liner wall thickness.

Table 5-14 The jet and penetration characteristics of the three different shaped charge liners.

Liner shape	Conical	Trumpet	Bi-conical
Explosive mass (g)	50.74	50.74	50.74
Liner mass (g)	29.32	28.93	28.78
Jet mass (g)	3.30	4.96	5.40
Jet to liner mass (%)	11.26	17.14	18.76
Jet tip velocity (m/s)	7103	7853	8244
Jet K. E. (kJ)	44.00	51.40	54.11
Penetration depth (cm)	74.88	81.00	87.00
Exit hole diameter (mm)	14.0	11.0	6.6

The changes in the jet velocity and kinetic energy indicate why the bi-conical liner has achieved the maximum penetration depth. Nevertheless, other factors may need to be considered in the practical design such as the charge length and the manufacturing cost.

5.6.5 Explosive amount and head height

The jet velocity and the damage caused in the rock formation depend mainly on the amount of the explosive used in the shaped charge. Minimizing this damage is a key objective when completing the well using OWP. This effect is studied using four similar perforator designs, but with different explosive masses. The liner materials were copper with the same design. A sketch of the four charges is illustrated in Figure 5-32. The jet characteristics and its penetration capability into the standard concrete for the four targets are listed in Table 5-15.

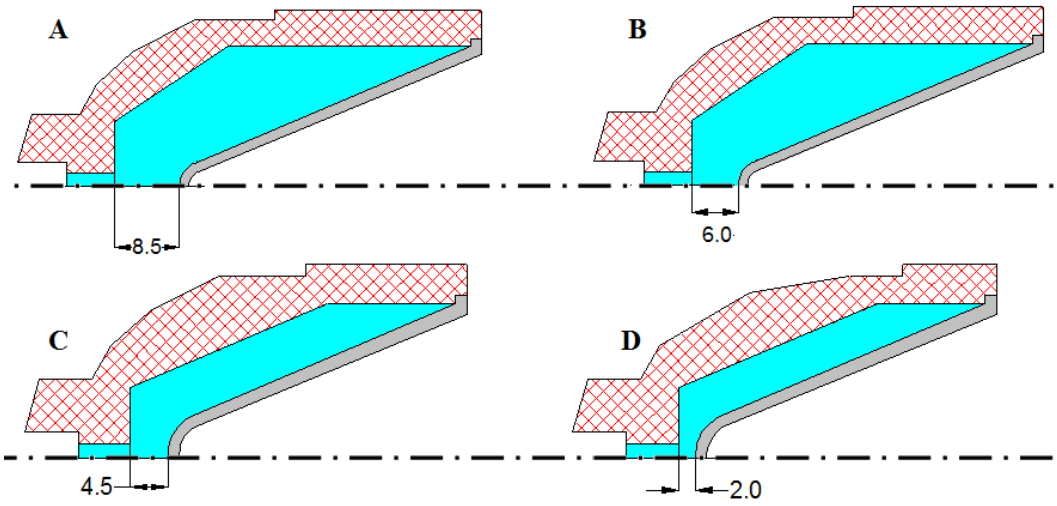

Figure 5-32 The four OWP with different explosive masses.

Table 5-15 The amount of the explosive and its impact on the jet and the penetration depth.

	Case A	Case B	Case C	Case D
Explosive mass (g)	50.74	46.30	40.00	24.57
Liner mass (g)	29.32	30.15	32.04	33.00
Jet mass (g)	3.30	4.06	6.05	5.5
Jet to liner mass (%)	11.26	13.47	18.89	16.66
Jet tip velocity (m/s)	7103	6628	4851	4539
Jet K. E. (kJ)	44.00	38.88	19.8	17.20
Penetration depth (cm)	74.88	69.00	61.00	41.00

The damaged areas around the perforated tunnels in concrete targets are shown in Figure 5-33 for different perforators. The damaged areas along the crater profiles near the impact

areas are similar, but the overall crushed zone thicknesses exhibit different values for the four cases, which implies that the flow productivity will be affected by the amount of the used explosive. However, these qualitative simulations are not sufficient to calculate the well productivity because it demands further permeability calculations, which are not available in the Autodyn hydro-code.

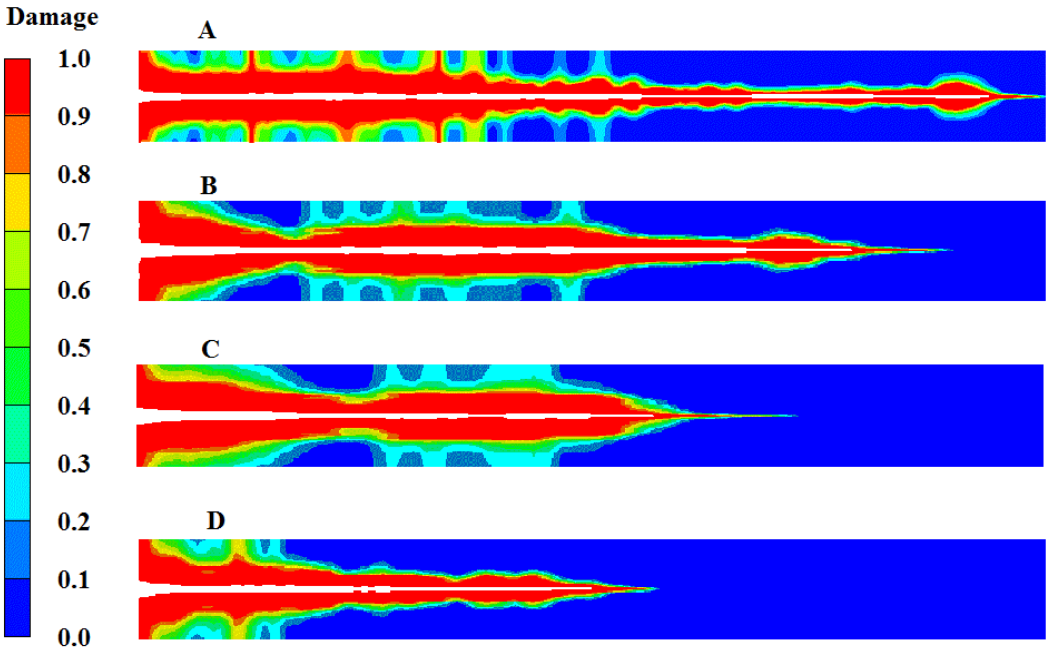

Figure 5-33 The damaged areas around the penetration path using different explosive masses.

5.6.6 Water stand-off distance

In order to properly fit the gun carrying the shaped charge perforators inside the casing, as shown in Figure 5-34, and since the jet travelling distance has a great effect on its penetration capability, the water stand-off distance effect was studied to find its influence on the jet performance and the depth of penetration.

To study this effect, the jet produced from OWP 46^{o} cone angle, HMX main explosive and liner thickness of 1.4mm is studied. This jet penetrates concrete after passing through water layers of different thicknesses of 0.5, 1.7, 2, 4 and 6cm. The penetration depths and the hole diameters relevant to the different water stand-off distances are illustrated in Figure 5-35.

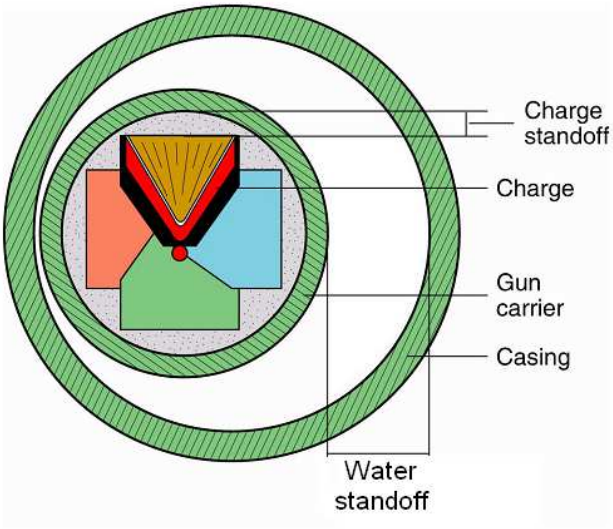

Figure 5-34 The OWP charge fitted inside the gun carrier and water stand-off distance measured from gun casing wall.

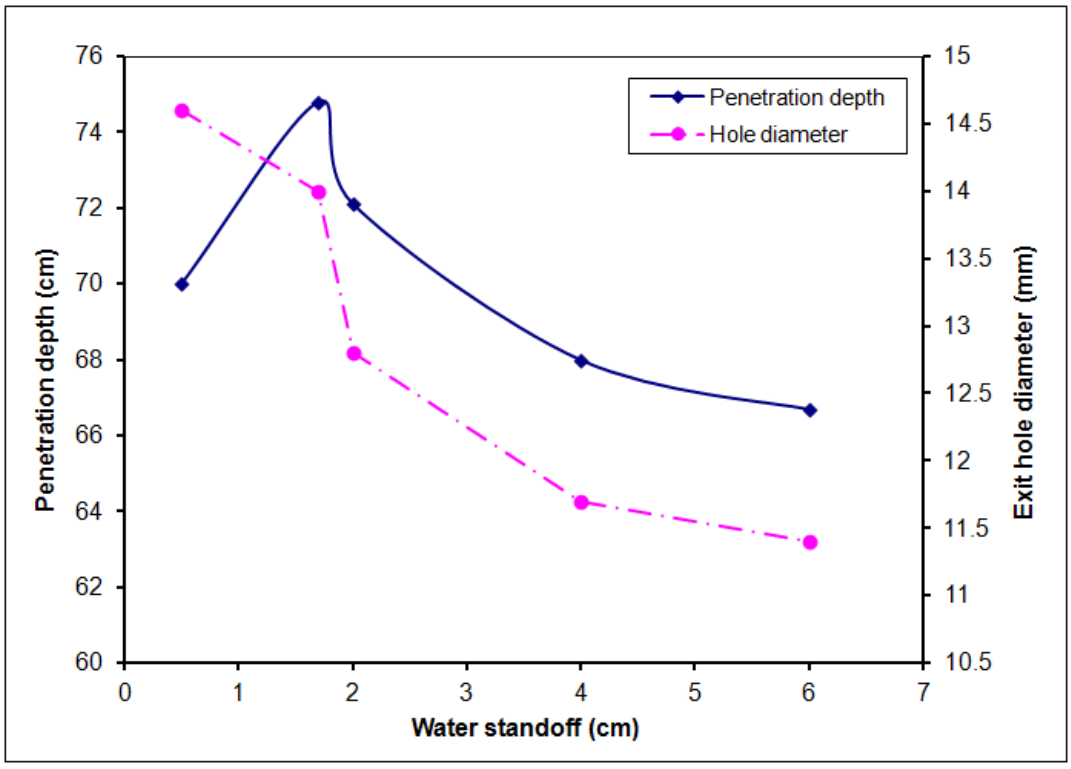

Figure 5-35 The penetration depth and hole diameter for OWP detonated at different water stand-off distance.

From this figure, it can be found that at 1.7cm stand-off distance, the perforator achieves the maximum penetration depth. This may be attributed to the fact that at this short stand-off distance, the jet is not fully stretched, which affects its penetration capability. After 3cm stand-off, the jet has to travel long distance in water, which causes the jet to be

particulated into small fragments or to be eroded and thus, its penetration capability decreases beyond this distance.

5.6.7 Degree of confinement effect on the jet parameters

Unlike shaped charges, OWP casing imposes a thick confinement, which affects the jet parameters, such as the jet tip velocity, especially in the region close to the liner base. This effect may be attributed to the reflection of the detonation waves on the casing surface back into the explosive, which may meet the liner with different incident angles between the detonation front and the liner wall. The subsequently reflected waves can produce regions of high pressure on the liner surface resulting in a jet with higher velocity. This was verified by adding 7 gauge points to the explosive-liner interface as shown in Figure 5-36 and using OWP with cone apex angle of 40^{o}, liner thickness of 1.4mm and casing thicknesses of 1, 2, 4, 6 and 8 mm.

It can be observed that both the obtained pressure-time histories of the two cases (i.e. 1 and 8mm casing thicknesses) have nearly the same pattern. However, the impulse-time histories in Figure 5-37 explained the reason why the obtained collapse velocities of all the relevant jet elements in the entire five models are different from each other, which in turn gave different jet velocities of their elements. Therefore, the jet tip velocity for 8mm case is higher than that for 1mm case. All the jetting analysis data for the casing thicknesses study are listed in Table 5-16.

All the resulting jets are coherent because their maximum flow velocities are lower than the bulk speed of sound of the copper material which is 3940 m/s [135]; where the maximum calculated flow velocity is 3748 m/s for 8mm casing. This means that all the selected casing thicknesses are suitable to produce a coherent jet. But, an optimization should be done based on the lowest casing thickness that is capable of confining the OWP explosive charge and protecting it against premature explosion.

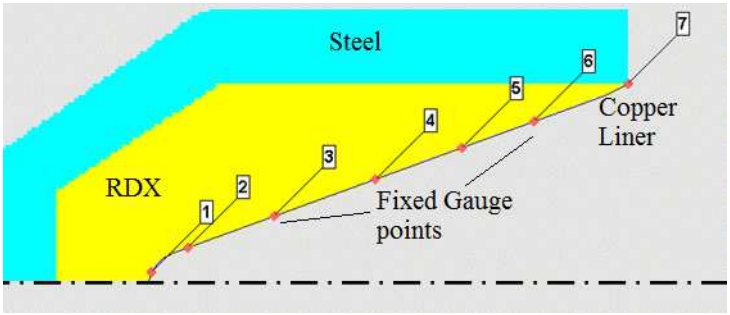

Figure 5-36 Different fixed target points along the liner axis to predict the P-t history on the explosive-charge interface using 8mm casing wall thickness.

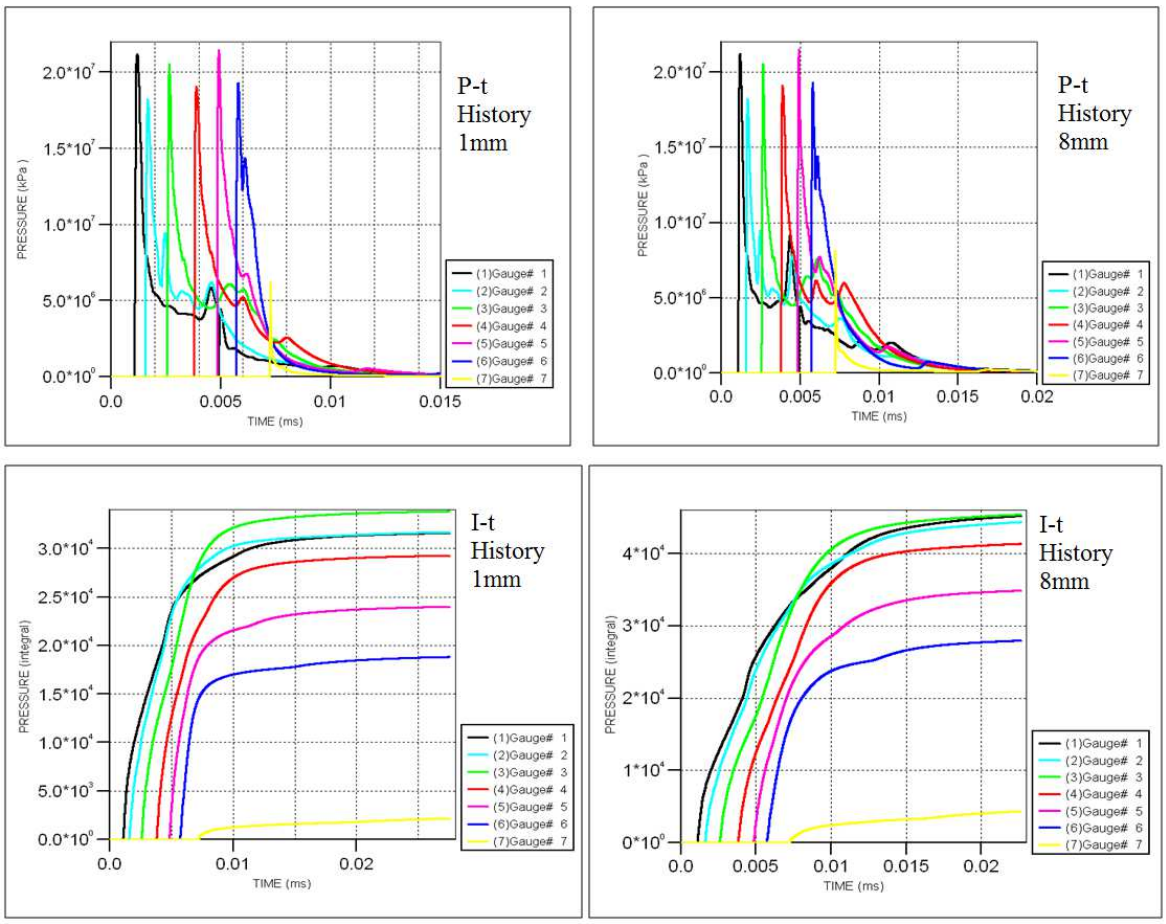

Figure 5-37 The predicted pressure and impulse-time histories for both 1mm casing thickness (left) and 8mm casing thickness (right).

Table 5-16 The jetting analysis data obtained from the jetting analysis of OWP using RDX main charge with different casing thicknesses.

Casing thick. (mm)	Liner Geometry			Output					
	Apex angle (deg.)	Thick. (mm)	Mass (g)	Jet mass (g)	% jet	Max flow vel. (m/s)	Max. coherent flow vel. (m/s)	Jet velocity (m/s)	Jet K.E. (kJ)
1	40	1.4	36.64	5.65	15.41	3115	3940	6489.4	35.6
2	40	1.4	36.64	5.66	15.45	3214	3940	6540.3	39.1
4	40	1.4	36.64	5.69	15.54	3549	3940	6790.5	43.3
6	40	1.4	36.64	5.72	15.61	3671	3940	7035.5	49.2
8	40	1.4	36.64	5.76	15.71	3748	3940	7232.8	54.1

5.6.8 Effect of the initiation point on jet characteristics

The shape of the detonation wave when it meets the liner is so important that it can determine the amount of the produced jet velocity and its degree of coherency after it travels a certain distance. Therefore, an alternative side point of initiation was selected to an OWP as shown in Figure 5-38. The corresponding detonation wave pattern at 1.2 μs from the moment of detonation is illustrated in Figure 5-39.

From the standard jetting analysis of 40^{o} OWP with liner thickness 1.4mm and side initiation point, the produced jet has a mass of 3.01 g and a velocity of 8018.5 m/s. The same perforator with a normal central initiation point gives a jet mass of 2.325 g and a velocity of 7812 m/s. Thus, the whole kinetic energy of the jet for the side initiation is 50.472 kJ, which is 13.3% greater than that of the OWP with normal initiation point, which is 44.542 kJ. Thus, the predicted penetration depth when the detonation wave shape is modified is expected to be better than that without wave shape modification. However, this technique is difficult to be applied industrially, as the whole perforators cannot be instantaneously detonated along their circumferential line.

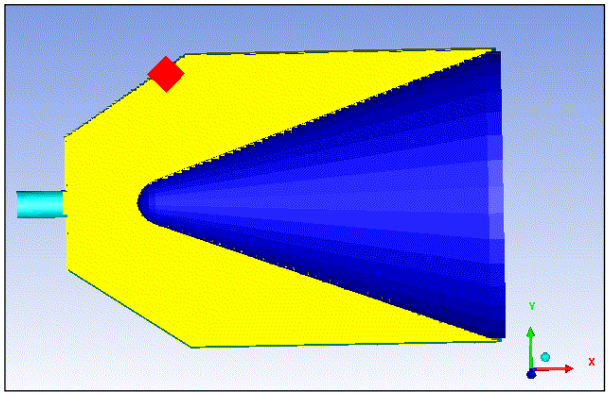

Figure 5-38 Shaped charge with side point of initiation at time 0μs.

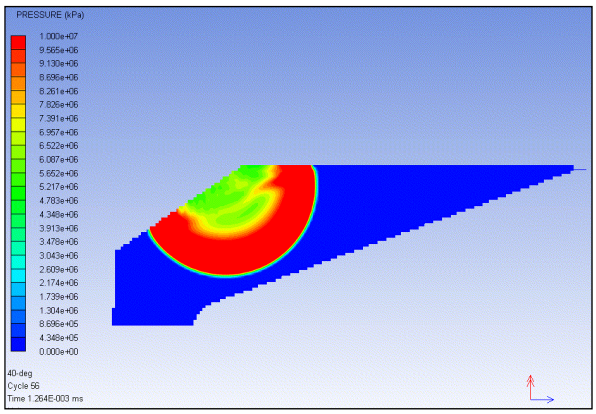

Figure 5-39 The detonation pattern of the side initiation at 1.26μs.

5.7 Liner portioning into jet and slug

In order to properly investigate the liner material portioning into jet and slug, two different techniques were implemented. First one is done by dividing the copper liner material into different colour tracers. The OWP used for this study has 46^{o} liner cone apex angle and 1.4mm wall thickness filled with HMX explosive. The twelve tracer regions are illustrated in Figure 5-40. Figure 5-41 illustrates the coloured tracers for the same liner material using Autodyn jet formation simulation, while Figure 5-42 shows the different coloured contours of the liner flowing into jet and slug portions at different times. The liner collapse figures show that most of the first three tracer portions at the liner apex flow into the slug part, while the twelfth portion and the liner base do not collapse down on the jet axis, and therefore, they will not actually take part in the jetting. The jet is formed from other tracer portions (i.e. from portion four up to eleven), but with different percentage from each individual portion. The percentage of material flow into jet increases from the apex toward the liner base, while their velocities decrease with their position in the same direction. The jet tip is mostly composed of the four tracer regions (i.e. four up to seven), while the pile-up or inverse velocity gradient part is observed near the jet tip. This part is formed because the collapsed points from these regions do not have enough space to be accelerated to their theoretical maximum values.

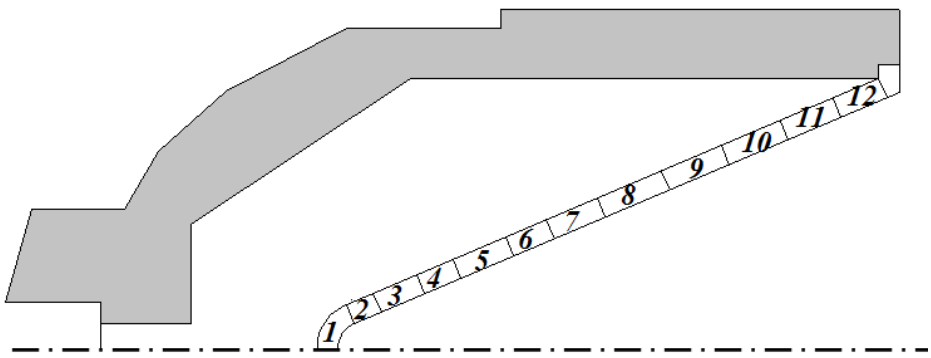

Figure 5-40 The twelve colours of the liner material used to track the liner portioning into jet and slug.

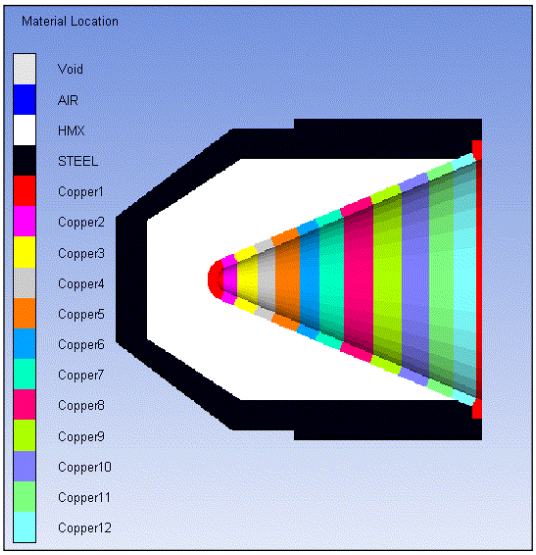

Figure 5-41 Multi-coloured copper liner of OWP of 46 deg. cone apex angle and 1.4mm liner wall thickness at time 0μs.

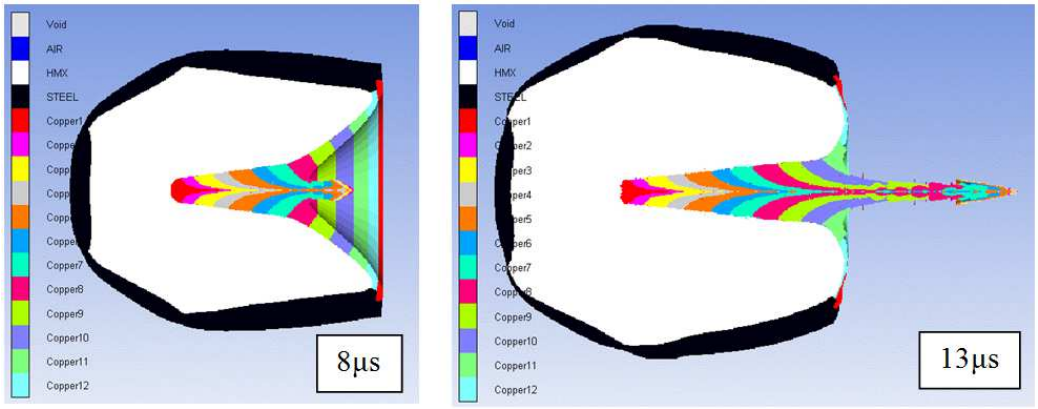

Figure 5-42 The multiple-colours contours of the collapsed liner indicating the jet formation from certain liner regions at different times.

The second method used to investigate the portioning of the liner material to the jet and the slug is done using massive moving Lagrangian target points, which are located on the liner material to facilitate its tracking. The first gauge is placed at the bottom (liner air interface) and the next gauges are placed at selected spacing from each other, (e.g. 0.1 mm distance) as illustrated in Figure 5-43. The output absolute velocity-time histories exactly specify the profiles of collapsing velocities of the gauges forming both the jet and the slug. Figure 5-44 illustrates the absolute velocity-time histories of the selected nine gauges that depict the material flow to form the jet, the slug and the infliction or collision point. This figure is so important that it can be used with the multilayered or laminated liner material research, where a coaxial or outer liner material can be added to delay the breakup of this jet, and therefore, to increase its efficiency [136]. A sketch for the liner material portioning based on the absolute velocity history is shown in Figure 5-45. This figure shows that by moving

from the liner apex to its base, the mass of the liner flows to form a jet increases, while its velocity decreases. This conclusion can be implemented to study the effect of non-uniform liner densitiy distribution produced by powder pressing technique on the jet characteristics (i.e. velocity and mass distribution).

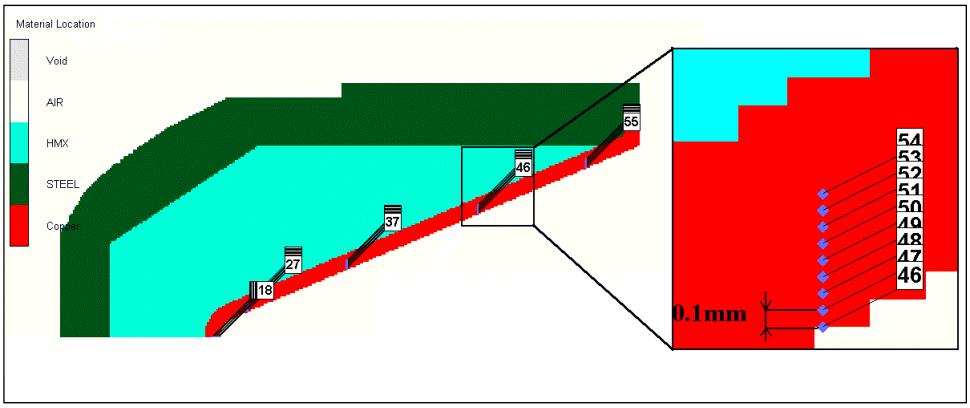

Figure 5-43 The selected moving target points on the liner axis to illustrated the liner portioning into jet and slug.

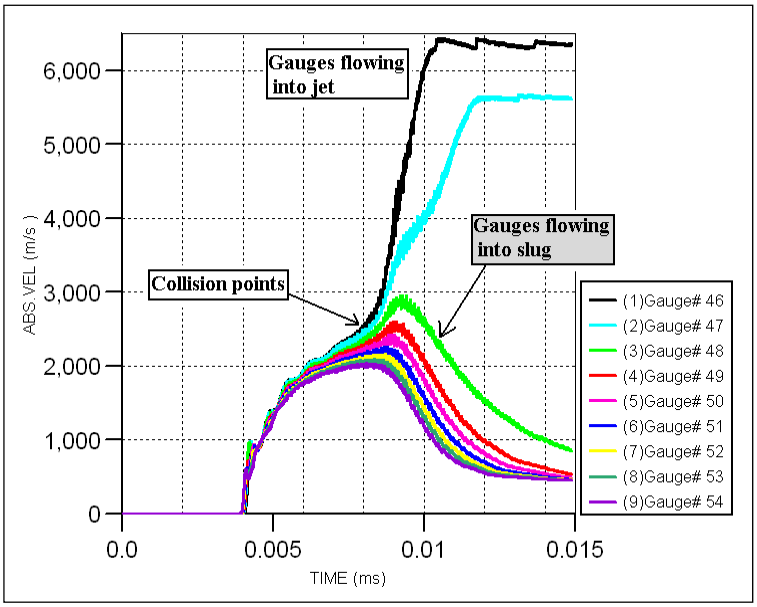

Figure 5-44 Absolute velocity-time history plot for the nine moving gauge points used to illustrate the liner partition into jet and slug.

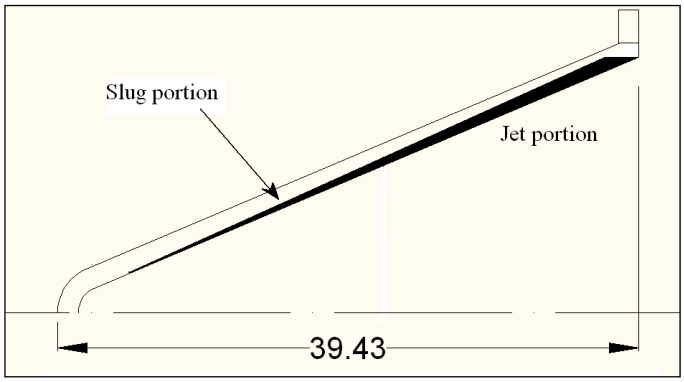

Figure 5-45 A schematic diagram illustrating the jet and slug potions based on the simulation results.

5.8 The Gurney velocity approximation

The Gurney velocity of an explosive is so important that it contributes directly to the analytical calculations of the shaped charge jetting parameters. However, this value is not known for all the well-known explosives, thus, it is linked directly to the Chapman Jouguet-pressure-explosive impulse ratio as depicted in Figure 5-46 for several explosives. The following relation was obtained from the fitting of the previously calculated Gurney velocity against the $P_{CJ}/I_{SP}.\rho_o$ ratio.

$$\sqrt{2E} = 0.2509\left(\frac{P_{CJ}}{I_{SP}\rho_o}\right) + 904.07 \qquad 5\text{-}1$$

where P_{CJ} is the Chapman Jouguet pressure (Pa), I_{sp} is the specific impulse of the explosive used as a monopropellant (Ns/kg) and ρ_o is the explosive density (kg/m^3).

If the impulse of the explosive is not known, it can be calculated using the detonation velocity-impulse relation [137]:

$$I_{sp}\rho_o = 1000\frac{U_D - 1980}{1.453} \qquad 5\text{-}2$$

where U_D is the detonation velocity of the explosive in m/s, ρ_o is in kg/m^3 and I_{sp} in Ns/kg .

The various explosives with their pressure, impulse and densities as well as the calculated and the measured Gurney velocities and the deviation between them are listed in Table 5-17. The greatest deviation between the measured and the calculated Gurney velocities based on Eq. (5-1) is -5.48%, which means that this approximation can be used accurately over a wide range of explosives.

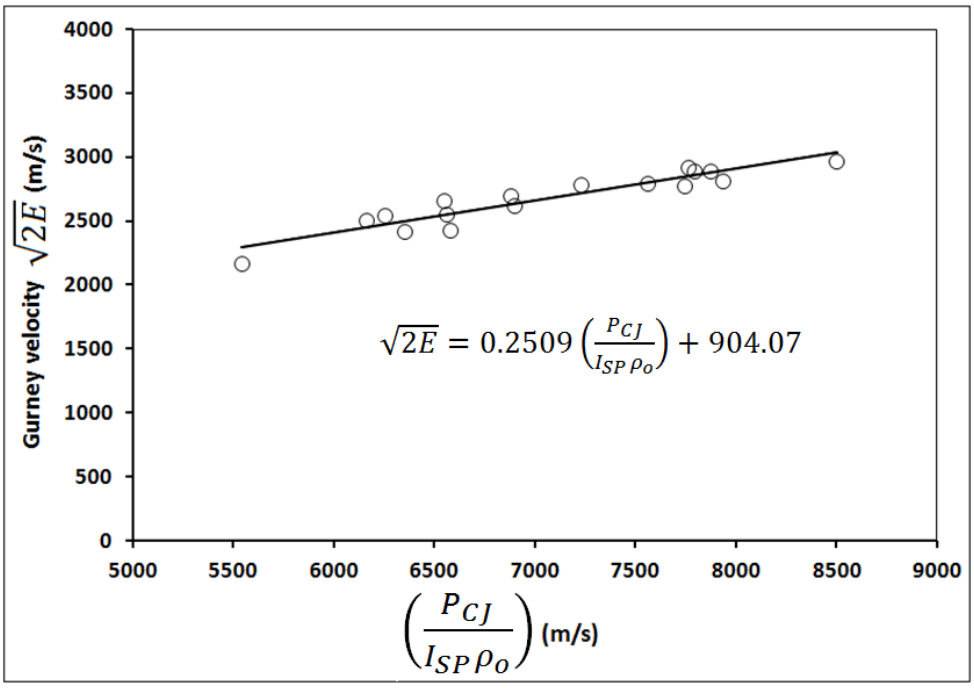

Figure 5-46 The Gurney velocity as a function of and the ($P_{CJ}/I_{SP}\rho_o$) relation.

Table 5-17 The Chapman-Jouguet pressure, the specific impulse, the calculated and the measured Gurney velocities and the deviation between them for various explosives.

Explosive	P_{CJ} (GPa)	I_{SP} (N.s/g)	ρ_o (kg/m^3)	$\sqrt{2E}$ Eq. (5-1) (m/s)	$\sqrt{2E}$ (m/s)	Dev. (%)
FEFO	25.00	2.389	1590	2555.4	2435.0 [72]	-4.94
H6	24.00	2.147	1760	2497.6	2425.0 [72]	-2.99
A3	30.00	2.636	1650	2634.7	2630.0 [72]	-0.18
DIPAM	18.00	2.096	1550	2294.2	2175.0 [72]	-5.48
C4	28.00	2.671	1600	2547.9	2660.0 [6]	4.21
HMX	42.00	2.614	1890	3037.0	2970.0 [22]	-2.26
DATB	25.10	2.139	1788	2550.7	2560.0 [138]	0.36
NG	25.30	2.543	1590	2474.0	2548.7 [72]	2.93
OCTOL	34.20	2.500	1809	2801.4	2800.0 [22]	-0.05
Cyclotol	31.60	2.508	1743	2717.8	2790.0 [22]	2.59
Comp B	28.70	2.434	1713	2631.1	2700.0 [22]	2.55
PBX-9011	34.00	2.425	1767	2894.9	2820.0 [6]	-2.66
PBX-9501	37.00	2.579	1841	2859.3	2900.0 [139]	1.40
PBX-119	24.40	2.422	1635	2450.0	2509.7 [72]	2.38
PBX-9404	37.50	2.583	1844	2879.4	2900.0 [140]	0.71
LX-04	35.00	2.423	1865	2847.4	2776.0 [72]	-2.57
LX-10	37.50	2.596	1860	2852.6	2922.1 [72]	2.38

5.9 Summary

Parametric analysis of OWPs is performed in this chapter, in which the used numerical hydro-code is validated against standard jetting analysis, while the shaped charge jet formation and penetration models are validated using the flash x-ray facility and the static firing of OWPs against laminated target, respectively. The shaped charge design parameters that include the explosive fill, liner thickness, charge casing and the mode of initiation are studied using the jetting analysis and the jet formation algorithms. Besides, the effect of the water layer stand-off distance that simulates the wellbore fluid on the depth of penetration into concrete was also considered. Moreover, a simple relation among the explosive inpulse, its Chapman-Jouguet pressure with the Gurney velocity is presented to give a good approximation for the characteristic Gurney velocity of the explosive materials.

CHAPTER.6 INFLUENCES OF TARGET STRENGTH AND CONFINEMENT ON THE PENETRATION DEPTH OF AN OIL WELL PERFORATOR

6.1 Introduction

Oil well perforator (OWP) uses a shaped charge to open deep hole into the rock formation in a productive oil field. Upon the detonation of an OWP, the high velocity metallic jet perforates the carrier gun wall, wellbore fluid, pipe casing, and finally reaches the rock formation that contains crude oil [11]. The productivity of the oil well increases with the penetration depth. The penetration depth of an OWP depends on the design of a perforator and the strength of rock material. Researches have been done to understand the effect of the target strength on the penetration depth of a shaped charge jet into target material. Pack and Evan [96] introduced a correction term related to the target strength in the hydrodynamic formula of penetration depth, i.e.

$$P = L\sqrt{\frac{\rho_j}{\rho_T}}\left(1-\frac{\alpha Y}{\rho_j V^2}\right) \qquad 6\text{-}1$$

where α is a constant; ρ_j and ρ_T are the densities of jet (rod) and target materials, respectively; L is the length of the rod penetrator; Y is the dynamic yield strength of the target; V is the penetrator velocity. The correction term can be linked to an important non-dimensional number in impact dynamics, i.e., $\frac{\alpha Y}{\rho_j V^2} = \frac{\alpha}{J_D}$ where $J_D = \frac{\rho_j V^2}{Y}$ is Johnson's damage number [141-142]. It shows that the influence of the target strength on penetration depth decreases with the increase of Johnson's number. For a steel target, this correction term is around 0.3, which means that the penetration depth can be reduced by 30% due to the effect of the target strength. This approximation has some limitations for jet penetration as it was developed for a continuous rod projectile. Other parameters, such as the stand-off distance and jet tip velocity, may also influence the penetration depth.

Extensive experimental results on shaped charge jet penetration were reported by Eichelberger [97]. It was shown that the simple hydrodynamic equation is not valid in the

later stages of penetration when the jet velocity decreases. During the later stages of penetration, strengths of both jet and target materials become relatively important. Eichelberger [97] added two strength terms to the hydrodynamic equations to account for their influences. The importance of the strength term effect on penetration was further verified by Pugh [98] and Klamer [99] when they found that the penetration depths into armoured steel are respectively 15% and 20% less than those in a mild steel target. Allison and Vitalli [2] deduced three different models of shaped charge jet penetration based on the assumption of the existence of virtual origin (VO) for a shaped charge, in which the penetration depth for a continuous jet can be described by:

$$P = Z[(\frac{V_j}{V_c})^{\frac{1}{\gamma}} - 1] \qquad 6\text{-}2$$

where Z is the effective jet length measured from VO to the target surface; V_j and V_C are the jet tip and rear velocities, respectively; γ is the square root of the target-jet density ratio (i.e. $\gamma = \sqrt{\rho_T / \rho_j}$).

Predicted penetration depths based on Eq.(6-2) agree well with the experimental results of a 105mm shaped charge against monolithic metallic targets [2]. However, Eq.(6-2) neglected the influence of the target strength on the penetration depth, and therefore, may not be suitable for shaped charges used as OWP because the initial jet tip velocity of an OWP may decrease after the perforation of multiple material layers before the jet reaches the main target. The feature of the multi-layer target in the application of OWP is reflected in the testing standard of American Petroleum Institute (API) [143]. Consequently, Eq.(6-2) may over-predict the penetration depth due to the neglecting of target strength. Therefore, it is necessary to understand the influence of target strength on the penetration depth of a shaped charge jet in an OWP test. On the other hand, the main target in an OWP application is subjected to large underground confinement pressure and the compressive strength of the concerned quasi-brittle materials (i.e. rock, concrete) can be largely enhanced by the confinement pressure, which will also be studied in this chapter.

Section 6.2 describes the experimental set-up and configurations of the shaped charge as well as the standard OWP specimen. Section 6.3 introduces the numerical models, material models and material parameters used to simulate the shaped charge jet and penetration. Results will be presented in Section 6.4 with further analysis, which is followed by conclusions in Section 6.5.

6.2 Experiments

The liners of the OWP used in this study were electrolytic Copper of grade C10100 OFEC (Oxygen Free Electrolytic Copper). This material has a high purity (99.99%) and very low oxygen and phosphorus contents for relatively high ductility, which is needed for the jet material to sustain longer breakup time and have a better coherent performance [7]. The copper liners were manufactured using the deep drawing technique, which is suitable for OWP because this manufacturing method is economical and efficient for producing large quantities of small calibre liners with a reasonable accuracy [31]. It starts with cutting a circular copper disc and applying five steps of drawing by hydraulic press with an intermediate annealing of 1000^{o}C (two minutes) to decrease the strain hardening and maintain the material ductility [31]. The liner has a small base diameter of 33mm, a cone apex angle of 46 degree and a wall thickness of 1.4mm as illustrated in Figure 6-1. The charge casing is steel with an average wall thickness of 4.5mm, while the main explosive charge is PE4 with a total average mass of 40.0g and a standard deviation of 1.3g.

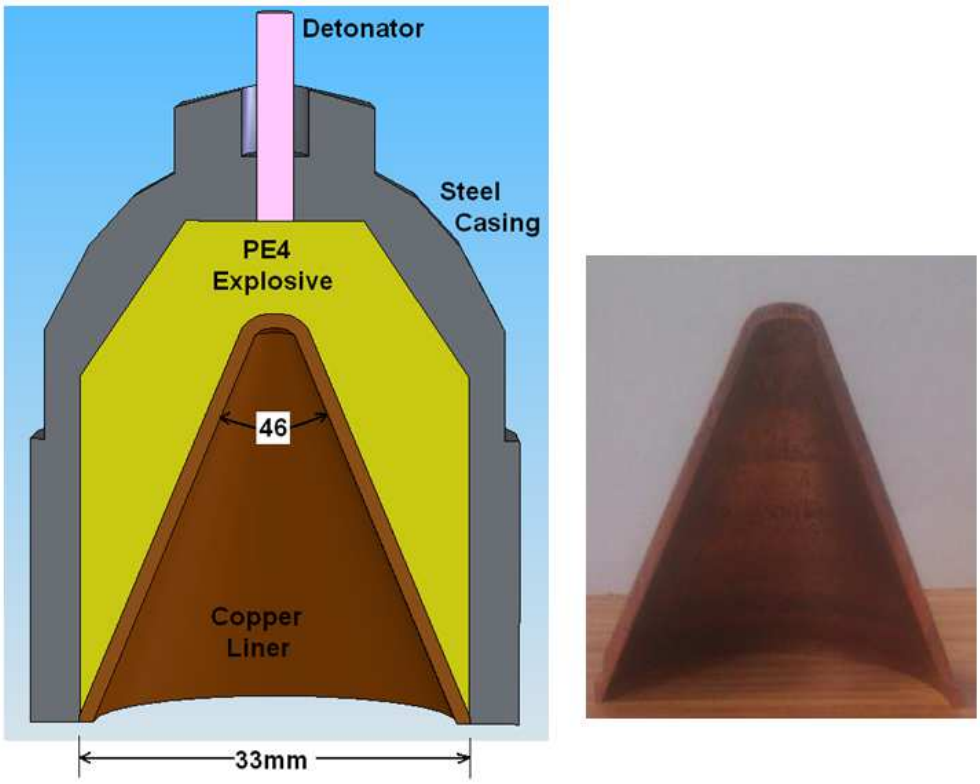

Figure 6-1 The shaped charge used in the concrete strength study (left) and a cross-section of the liner (right).

Concrete targets with four different strengths were poured and cured according to the test evaluation of the well perforator [144]. These concrete targets were tested according to the

standard OWP testing configuration and requirements in the Section-II of API-RP43 [143]. The configuration of the target layers and their dimensions and a picture of the experimental setup are illustrated in Figure 6-2. The strengths of the standard concrete cubes corresponding to concrete targets are 26.0, 40.0, 47.0 and 55.0 MPa with standard deviations of 0.9, 0.9, 1.7 and 0.9 MPa, respectively, measured at 28 days after their casting [145].

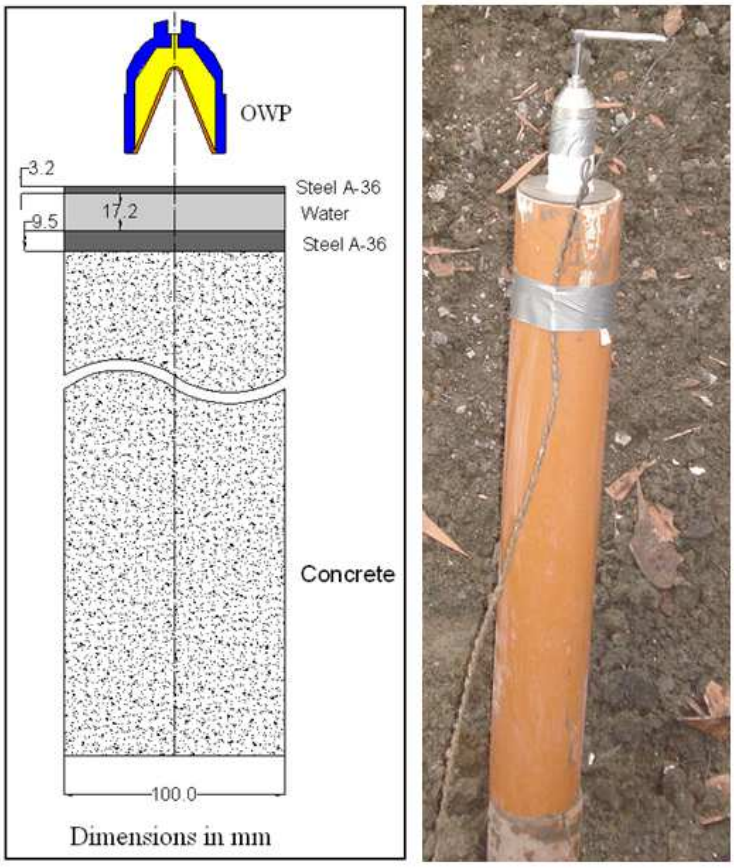

Figure 6-2 The layout and the experimental test setup according to API-RP43.

6.3 Numerical models

6.3.1 Hydro-Code Algorithms

The hydrocode algorithms were presented in details in Chapter 4.

6.3.2 Mesh sensitivity

It is well-known that the shape and the density of the mesh may affect the simulation results. Generally, simulation with fine meshes produces more accurate solution with the cost of longer time consumption in comparison with coarse meshing simulations. When the erosion criterion is applied, effect of the mesh density on simulation results may increase.

In order to study the mesh sensitivity on the jet penetration, nine different mesh densities were proposed for the concrete target material, while the Lagrangian jet meshes remain unchanged (i.e. 0.5mm×0.5mm). Uniform square meshes of 0.2, 0.3, 0.5, 0.8, 1, 1.5, 2, 2.5 and 3mm are selected for concrete target. The mesh sensitivity study was also performed in the jetting analysis where five different Euler mesh sizes of 0.3, 0.6, 1.4, 2 and 4mm were applied to PE4 explosive to examine the variation of the jet characteristics with the mesh density.

Mesh sensitivity for Euler jetting analysis is shown in Figure 6-3, where the relationship between the cumulative jet mass and its axial X-position is shown. It can be observed that the predicted curves for five different mesh sizes have nearly the same shape at the beginning of the jet formation. Then, noticeable variations among five curves occur for different mesh sizes. However, with the decrease of mesh size from 4 mm to 0.3 mm, the convergence of the solution is observed. Thus, 0.3×0.3mm cell is used in all jetting analyses.

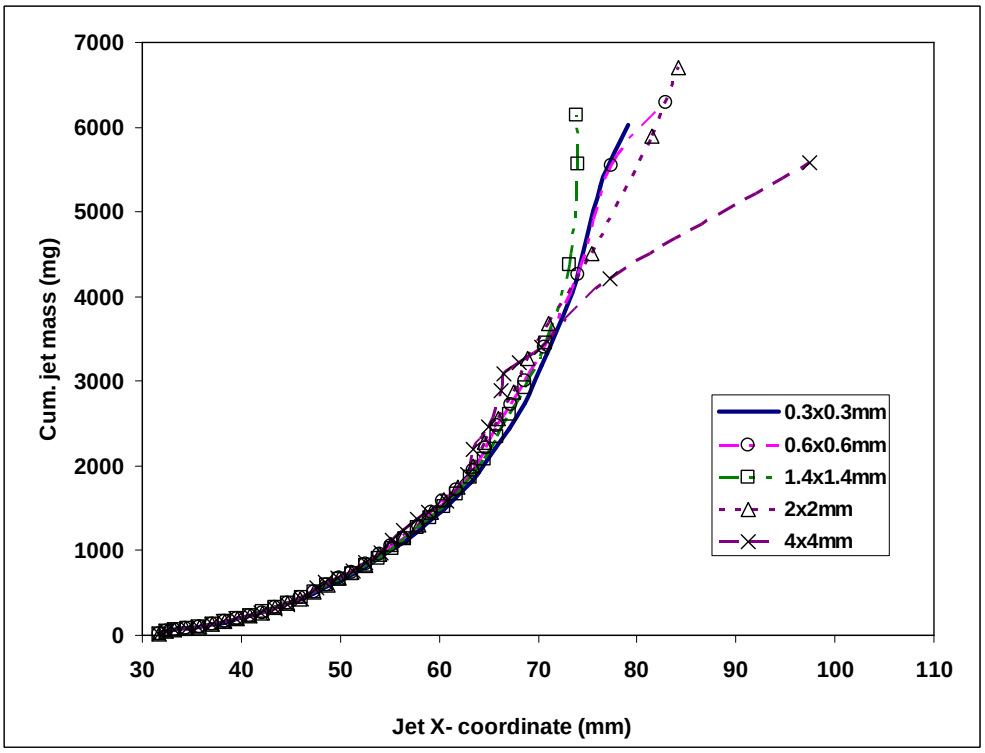

Figure 6-3 The cumulative jet mass versus the jet axial coordinate obtained from the jetting analysis using different mesh sizes.

Figure 6-4 shows the mesh sensitivity for Lagrange penetration analysis where the variation of the predicted penetration depth with mesh size is shown for a 40 MPa concrete target with nine mesh sizes of unity aspect ratio. Penetration depth converges to a value of

68cm using square shape element of size 0.2mm, however, the element size 0.5mm gave a penetration depth of 67.5, which is only 0.7% different from that of the finest mesh, but it save more than half the time needed to do the simulation with the element size of 0.2mm. Thus, the Lagrange mesh size of 0.5mm×0.5mm was applied to all penetration simulation calculations considering its reasonable accuracy and time consumption.

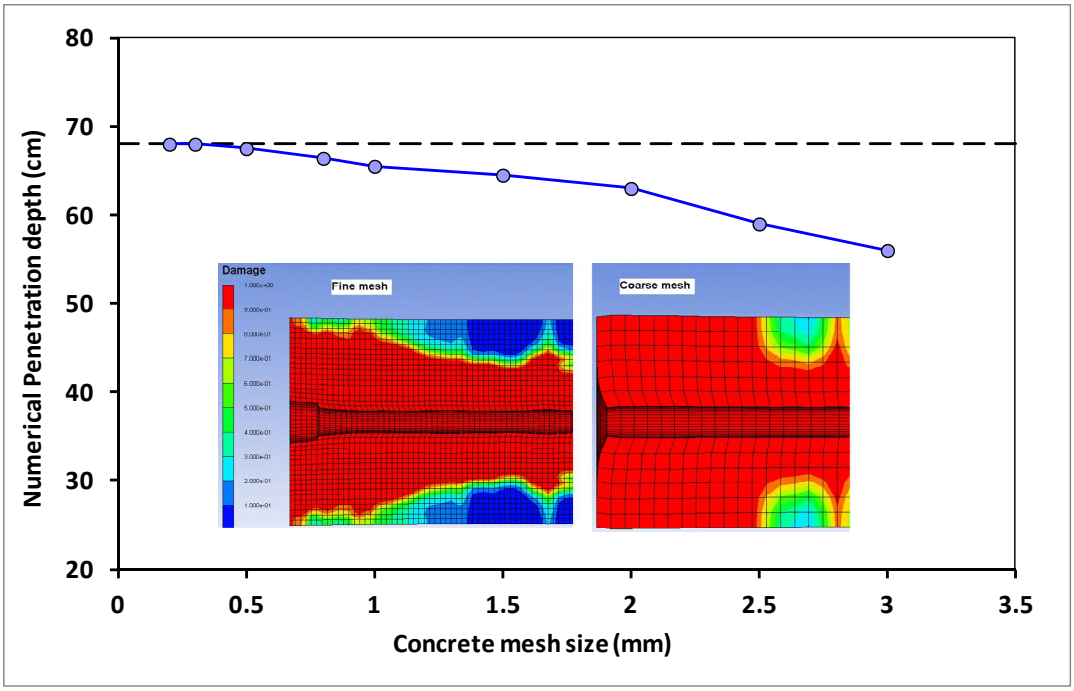

Figure 6-4 The numerical penetration into concrete using different mesh sizes.

6.3.3 Material models

The material models were presented in detail in Chapter 4.

6.4 Results and discussion

The standard jetting analysis of the studied OWP indicated that the produced jet from this perforator is coherent because the flow velocity satisfies the stability condition [83]:

$$v_{flow,\max} \leq 1.23 \times C_o \qquad 6\text{-}3$$

where $v_{flow,max}$ is the maximum flow velocity of all liner material points and C_o=3940m/s is the sound speed in the copper material. The maximum flow velocity was found to be 3161m/s, which means that the produced jet will be coherent during its stretching. A summary of the jetting analysis output is listed in Table 6-1.

Table 6-1 Jet characteristics based on the standard jetting analysis

Liner mass (g)	33.20
Jet mass (g)	6.02
Jet tip velocity (m/s)	6698
Jet tail velocity (m/s)	2054
Jet kinetic energy (kJ)	49.29

The jet elongation at different times is illustrated in Figure 6-5, which shows the jet formation up to 18μs (measured from the moment of detonation), at which the jet starts to interact with the first steel layer of the laminated multi-layer target. The penetration stages of the jet into 55MPa concrete target are illustrated in Figure 6-6, while Figure 6-7 illustrates the contours of concrete damage at different times due to the jet penetration. It can be observed that the jet caused a radial damage along its penetration path into the concrete, thus the penetration depth is measured experimentally based on the remaining witness part of the concrete as shown in Figure 6-8.

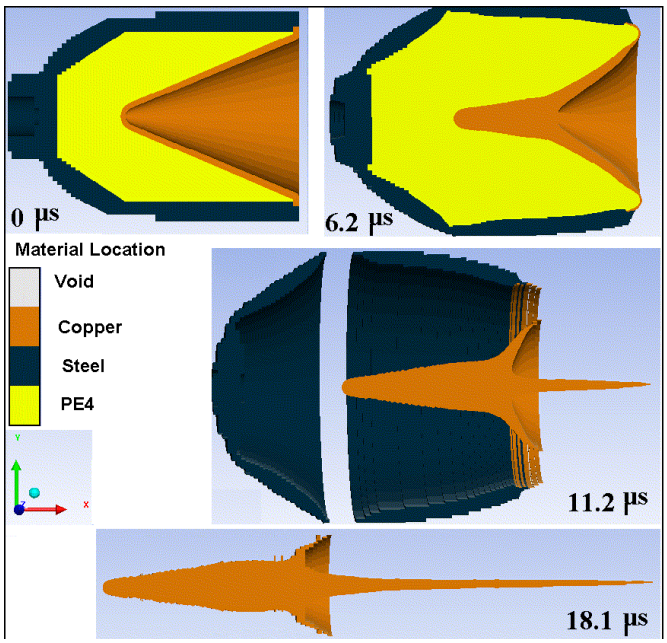

Figure 6-5 The jet generation and stretching at different times.

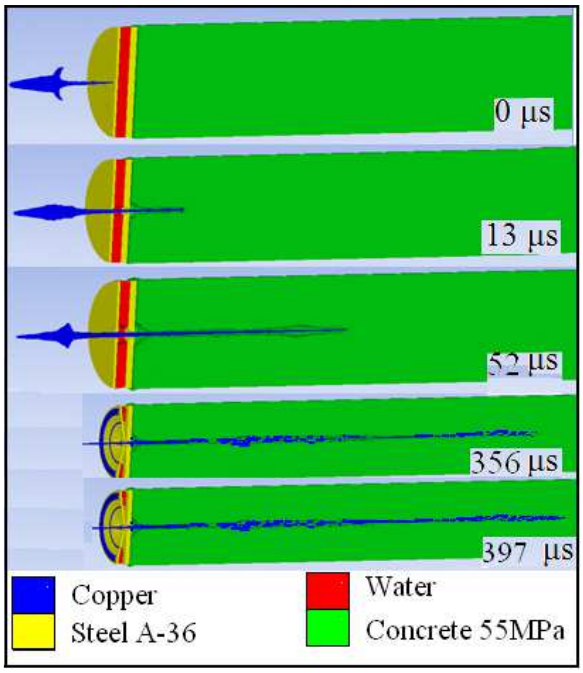

Figure 6-6 The concrete penetration stages.

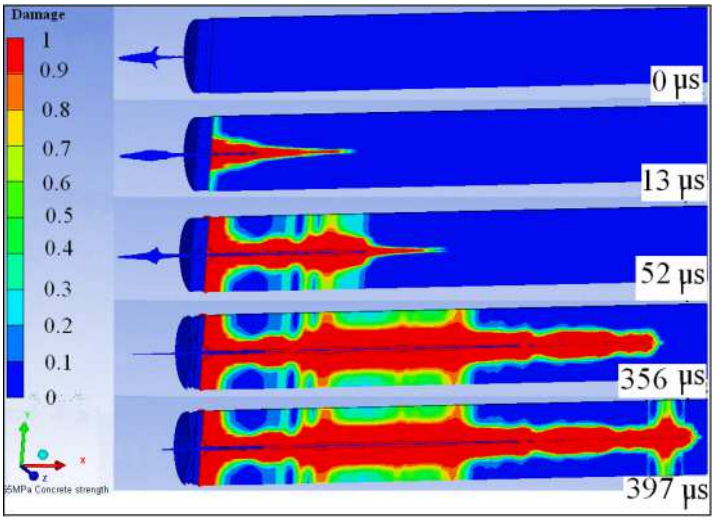

Figure 6-7 The concrete damage contours history.

Figure 6-8 The penetrated tested witness concrete targets and the steel discs.

The jetting data were used to calculate the effective jet length (Z), which is defined as the distance from the source point or the virtual origin to the target surface. It can be calculated by plotting the reciprocal of the jet velocity of each liner element against time, and applying the back projection on the horizontal distance axis at the real interaction time as illustrated Figure 6-9. The projected effective jet length was 127mm at 18μs, at which the jet impacts the first steel layer. However, this value can not be used directly with Eq.(6-2), because the effective jet length and the jet tip velocity have to be modified considering the thicknesses of the laminated steel and water layers. The jet tip velocity was corrected based on the following equation for the exit jet tip velocity perforating a finite thickness target [103]. This correction was derived from Eq.(6-2), in which the penetration P=T (i.e. perforation of a finite thickness T), where V_C is replaced by V_{jex}.

$$V_{jex} = V_{jin}\left\{\frac{Z_i}{Z_i + T_i}\right\}^{\gamma_i} \qquad 6\text{-}4$$

where V_{jex} and V_{jin} are the exit and the input jet tip velocities respectively, Z_i is the effective jet length at the front of the target surface, T_i is the target thickness and i refers to the index of the target layer to be perforated. The values of the exit jet tip velocity and the relevant effective jet length for the testing layers are illustrated in Table 6-2.

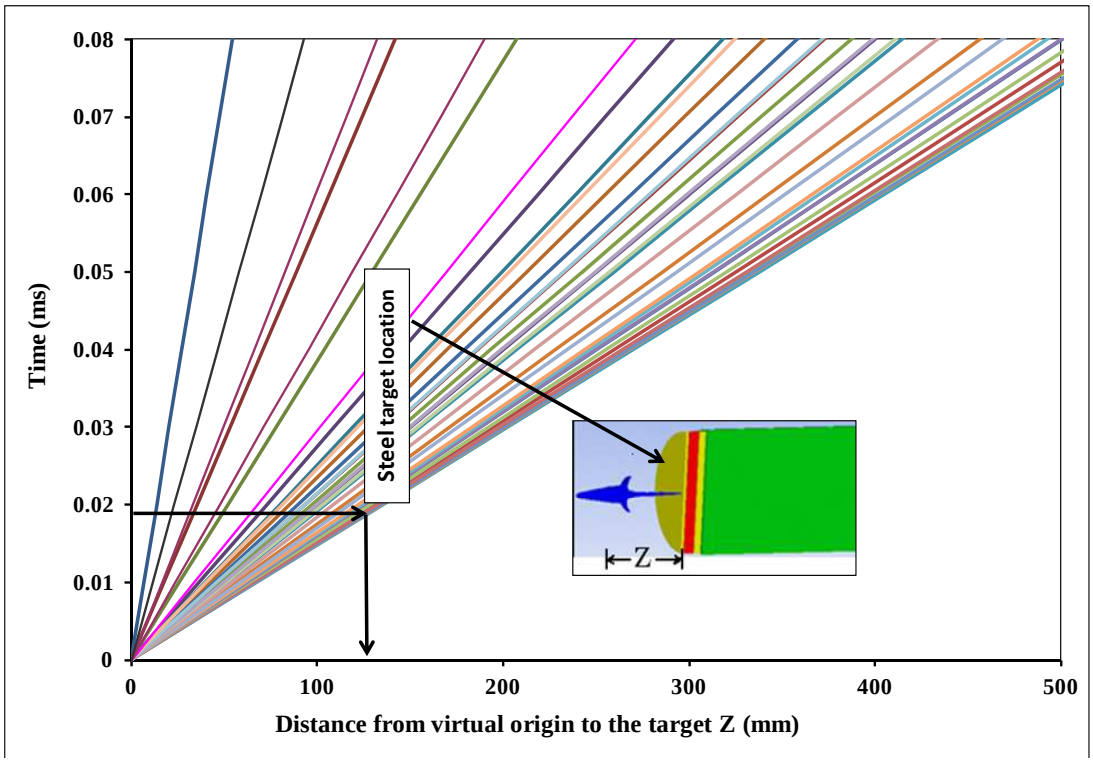

Figure 6-9 The effective jet length and the time relation for virtual origin model.

Table 6-2 The jet tip exit velocity and the relevant effective jet length for the test layers.

	Air	Steel	Water	Steel
T_i (cm)	-	0.3	1.7	0.9
Effective jet length Z (cm)	12.7	13	14.7	15.6
γ	-	0.936	0.335	0.936
Exit jet velocity V_j (m/s)	6698	6556	6320	5997

It is found that the real jet tip velocity just before impacting the concrete layer, V_j, is 5997m/s while the corresponding effective jet length from the VO point to the concrete target is 15.6cm, based on which the penetration depth can be calculated according to Eq.(6-2) (89.78cm in this case). However, Eq.(6-2) is unable to consider the influence of target strength on the penetration depth. In Eq.(6-1), Pack and Evan [96] introduced a target strength correction term in hydrodynamic penetration model. According to Taylor expansion, when $\frac{V_j}{V_c} \to 1$, $\left(\frac{V_j}{V_c}\right)^{\frac{1}{\gamma}} \approx 1 + \frac{1}{\gamma}\frac{V_j}{V_c} - \frac{1}{\gamma} = 1 + \sqrt{\frac{\rho_j}{\rho_T}}\left(\frac{V_j}{V_c} - 1\right)$ when the quadratic and higher order terms are neglected, which reduces Eq.(6-2) to

$$P = Z\left[(\frac{V_j}{V_c})^{\frac{1}{\gamma}} - 1\right] \approx Z\left[1 + \sqrt{\frac{\rho_j}{\rho_T}}\left(\frac{V_j}{V_c} - 1\right) - 1\right] = \frac{Z}{V_c t}\left(V_j t - V_c t\right)\sqrt{\frac{\rho_j}{\rho_T}}$$ where

$Z = V_j t$ is the distance of the jet tip to the virtual origin and $V_j t - V_c t = L$ is the current length of jet. When $\frac{V_j}{V_c} \to 1$, the jet length L is a constant and $Z \to \infty$. Therefore, $\frac{Z}{V_c t} = \frac{Z}{Z - L} \to 1$ and Eq.(6-2) can be reduced to the hydrodynamic equation, which is Eq.(6-1) when the target strength is ignored. This simple analysis for the link between Eqs.(6-1) and (6-2) implies that a same strength correction term can be introduced into the Allison-Vitalli equation [Eq.(6-2)], i.e.

$$P = Z_0\left[\left(\frac{V_j}{V_c}\right)^{\frac{1}{\gamma}} - 1\right](1 - \frac{\lambda f_c'}{\rho_j V_c}) \qquad 6\text{-}5$$

where $f_c^{'}$ is the compression strength of concrete, which is a function of the applied hydrostatic pressure if a confinement is present; V_j is the jet tip velocity corrected after perforating steel-water-steel layers of the testing specimen (5997 m/s in the present case); λ is a constant determined from the real experiments, which was found to be 200.31 as the average of the four experimental tests.

When underground confinement is considered [46], the Drucker-Prager equation can be used to calculate the equivalent compressive strength. When uniform lateral confinement is considered (i.e. $\sigma_2 = \sigma_3 = \sigma_r$, positive in compression), the compressive strength of σ_1 stress can be derived as:

$$f_c^{'} = \left(\frac{2}{3} - \frac{2}{9}\tan\theta\right) f_c + \left(1 + \frac{2\tan\theta}{3}\right) P_H \quad \text{6-6}$$

according to Drucker-Prager equation [146] where f_c is the unconfined uniaxial compression strength; P_H is the applied hydrostatic pressure; θ is the frictional angle, which was found to be 50 degree for concrete [146].

The second bracket in the modified Allison-Vitalli equation [Eq.(6-5)] represents the penetration reduction due to the target strength effect. This equation was used to calculate the penetration depth theoretically for the four concrete materials using the jet velocities and the effective jet lengths predicted from jetting analysis. The predicted results from Eq.(6-5), the measured penetration depth and the numerical simulation results based on Autodyn are listed in Table 6-3 and illustrated in Figure 6-10. It shows that the maximum difference between the analytical and the experimental results was 7.5%, which demonstrates the validity of the analytical model. Also, the maximum difference between the numerical and the experimental penetration is 8.8%. Therefore, the numerical prediction of the penetration depth when underground confinement exists could be used to assess the validity of Eqs.(6-5) and (6-6).

Both numerical results and Eqs.(6-5) and (6-6) indicate that the target material strength has a significant effect on the penetration depth of the OWP jet. When lateral confinement is absent, Eq.(6-5) gives reasonably good predictions when compared with experimental results where the maximum difference between the measured and the calculated penetration depths was 7.52%. With the correction term in Eq.(6-5), the effect of the underground confinement can be taken into account through Eq.(6-6), which agrees with numerical predictions. In addition, the experimental penetration depth was found to decrease about 0.73cm per 1 MPa increase of the compressive strength of the target, which can be extended to situations when the underground confinement of oil field is considered. Besides, the rate of penetration decrease according to the curve fitting of the data obtained from Eq.(6-5) is 0.48cm per 1 MPa increase of the compressive strength of the target.

Table 6-3 The penetration results into concrete materials with different strength values.

Concrete unconfined strength (MPa)	*Hydrostatic pressure (MPa)	Equiv. Strength Eq. (6-6) (MPa)	Penetration depth (cm)			The correction term $(\frac{\lambda f_c^{'}}{\rho_j V_C^2})$
			Simulation	Exp.	Cal. Eq. (6-5)	
26	-	26.0	81.0	78	77.32	0.139
40	-	40.0	68.0	73	70.62	0.213
47	-	47.0	62.0	68	67.27	0.251
55	-	55.0	57.0	59	63.44	0.293
26	40	82.2	50.8	-	50.40	0.439
40	40	87.9	50.0	-	47.71	0.469
47	40	90.7	45.0	-	46.36	0.484
55	40	93.9	40.0	-	44.82	0.501
26	68	132.5	34.3	-	26.33	0.707
40	68	138.1	31.2	-	23.64	0.737
47	68	140.9	29.5	-	22.29	0.752
55	68	144.1	24.0	-	20.75	0.769

*The hydrostatic pressure (i.e. 68MPa) was taken from Ref [46] at a depth of 3km.

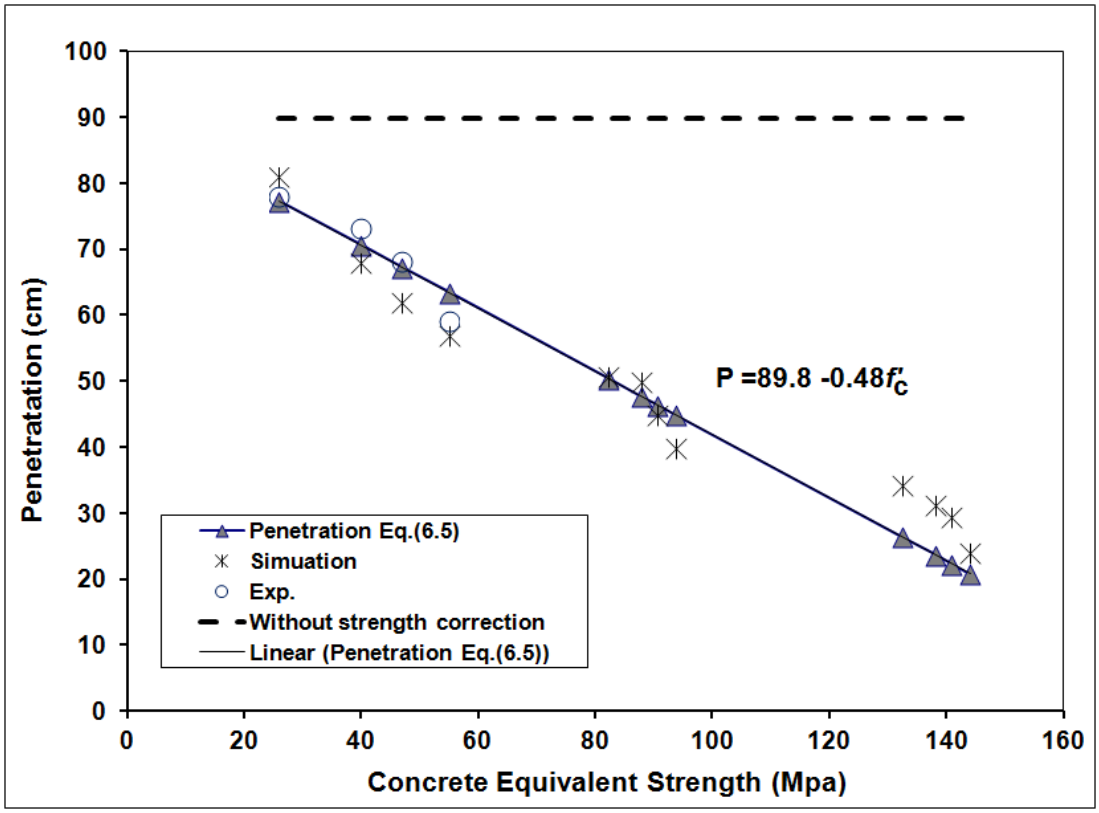

Figure 6-10 The penetration depth dependence on the concrete equivalent strength based on Eq.(6-5).

6.5 Summary

The strength and confinement effects on the OWP jet penetration into standard laminated specimen are studied experimentally and numerically. It is found that the strength of the target can largely reduce the penetration depth of OWP jet. Allison-Vitalli formula of jet penetration depth is modified to include the target strength effect using Johnson's damage number. Furthermore, the effect of the underground confinement pressure on the target compressive strength is considered using Drucker-Prager model and is introduced into the modified Allison-Vitalli equation, which can be easily applied to estimate the OWP jet penetration depth in an underground oil formation.

CHAPTER.7 PERFORMANCE OF ZIRCONIUM JET WITH DIFFERENT LINER SHAPES

7.1 Introduction

Oil well perforator (OWP) has been used in oil and gas wells to connect them to the reservoir [11]. When the OWP is detonated, the hypervelocity jet can achieve a very deep penetration depth into the geological formation material. The velocity and the diameter of the jet depend mainly on the design of the perforator, specifically the liner shape, which has a direct influence on the elemental velocities and their collapse angles. The collapse velocity is an explicit function of the mass ratio between explosive and liner element [6, 68, 147], but its real value may be limited by the short distance available between the liner element and its axis near the apex potion, as shown in Figure 7-1. Figure 7-2 depicts the flow velocity (V_2) in a moving coordinate system with a stagnation velocity (V_1) and their relationship with the collapse velocity (V_o).

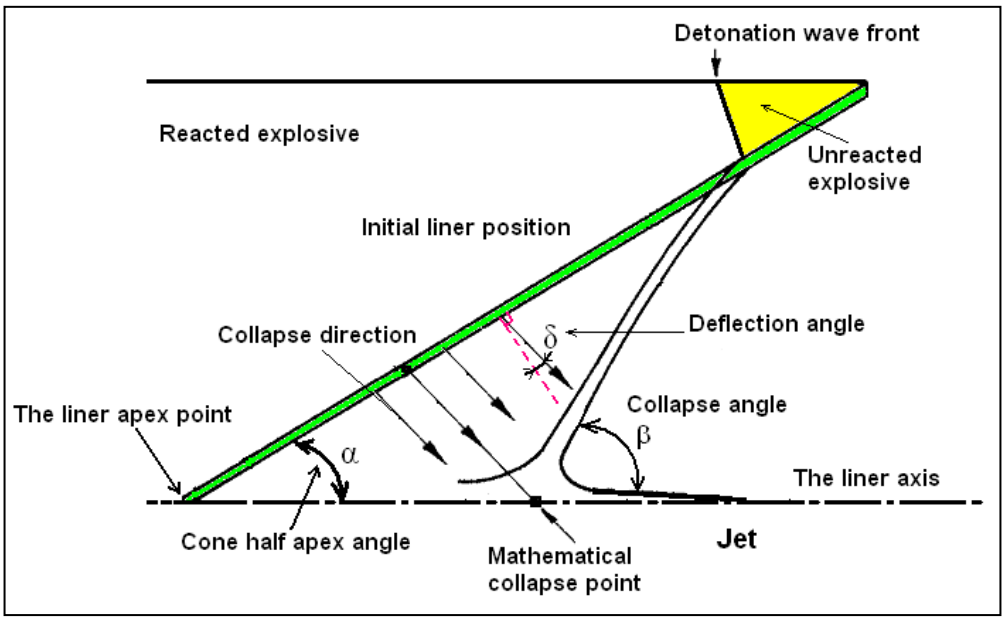

Figure 7-1 A schematic drawing illustrates the collapse process path from the initial liner position to its axis.

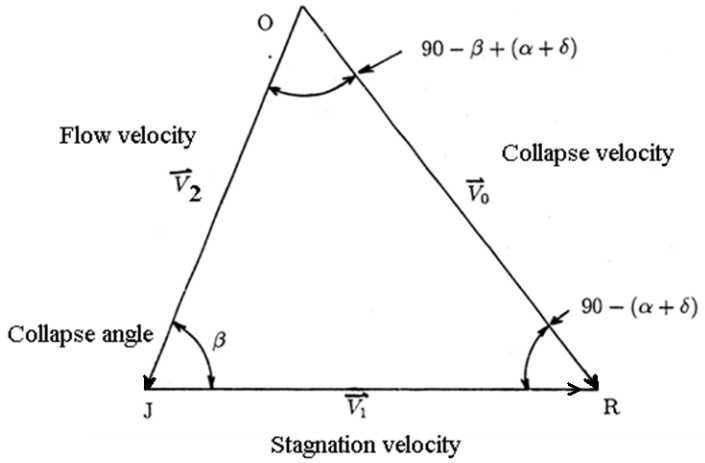

Figure 7-2 Velocity vectors in a moving coordinate system [50].

According to the unsteady state Pugh-Eichelberger-Rostoker (PER theory) analysis, stagnation (V_1) and flow (V_2) velocities can be determined by [50]:

$$V_1 = \frac{V_o \cos(\beta-(\alpha+\delta))}{\sin\beta} \tag{7-1}$$

and

$$V_2 = \frac{V_o \cos\ (\alpha+\delta)}{\sin\beta}, \tag{7-2}$$

respectively. The jet velocity V_j is determined by:

$$V_j = V_1 + V_2 = \frac{V_o}{\sin\beta}(\cos(\beta-\alpha-\delta)+\cos(\alpha+\delta)) \tag{7-3}$$

where 2α is the cone angle, δ is the deflection angle and β is the collapse angle, as shown in Figure 7-1 and Figure 7-2. Based on PER model [50], the deflection angle is given by

$$\delta = \sin^{-1}(\frac{V_o}{2U}) \tag{7-4}$$

where $U=U_D/\cos\alpha$, U_D=8200m/s is the detonation velocity for PE4 explosive charge.

The mass of the jet element m_j has also a direct relation with the collapse angle [50], i.e.

$$m_j = \frac{1}{2}m(1-\cos\beta) \tag{7-5}$$

According to Eq.(7-3), the jet velocity increases with the increase of V_o and with the decreases of the collapse and cone angle β and 2α. On the other hand, according to Eq.(7-5), the jet mass increases with the increase of β. Thus the collapse angle β has opposite influences on the jet velocity and jet mass. Furthermore, when β is very small and the flow velocity V_2 is relatively high, the jet may not form according to [83]. Therefore, a combination of V_2 and β determines whether a jet can be formed for each liner element. Meanwhile, the flow velocity V_2 also determines the coherency of the formed jet. The jetting conditions had been studied by many reaerchers over the past decades. Walsh et al. [82] concluded that the jetting always happens if the jet material is incompressible or if the collision (flow) velocity in the moving coordinates system (V_2) is subsonic. Cowan and Holtzman [3] presented another overview for the jetting condition criteria in the explosive welding applications. Chou et al. [83] summarized the jetting conditions and the cohesion characteristic of the produced jet as shown in Table 7-1, where β_c is the critical collapse angle for an attached oblique jet at a given flow velocity.

Table 7-1 The condition for the jet formation and the state of its cohesion at different collision velocities and collapse angles [83].

Flow regime	Impinging Angle β	Jet formation	Jet coherence
Supersonic ($V_2 > C_L$)	$\beta \leq \beta_c$	No	No
	$\beta > \beta_c$	Yes	No
Subsonic ($V_2 \leq C_L$)	All values	Yes	Yes

In Table 7-1 C_L is the longitudinal sound speed in the solid liner material,

$$C_L = \sqrt{3\frac{1-v}{1+v}}\, C_o \qquad 7\text{-}6$$

in which, $Co = \sqrt{K/\rho_o}$ where ρ_o is the jet density, $K = E/3(1-2v)$ is the bulk modulus, E is Young's modulus and ν is the Poisson's ratio. The conditions in Table 7-1 have been confirmed by Harrison [148], and Walker [149] experimentally where flash x-ray was used to show that a coherent jet is formed when $V_2 < C_L$. Therefore, different regions on β-V_2 domain can be determined for the jet formation/coherency for a given shaped charge, which is useful for the design of shaped charge.

Liner shape has significant influence on the shaped charge jet performance. It has been shown that the conical liners with small apex angles produce relatively deep crater with

small diameter. On the other hand, the hemispherical liners produce shallow crater with large diameter [11]. Various improvements of the liner design have been done in the past fifteen years. For example, Davinson and Prat [17] and Lee [11] proved that modifying the liner shape design can increase the jet kinetic energy and hence the penetration depth. Held [150] used a special flat liner to obtain a superfast jet of tip velocity of 25km/s. Therefore, it is necessary to understand the jet characteristics for different liner shapes and their corresponding penetration performance.

This chapter will study the jet formation, coherence and penetration of four commonly-used liner shapes, i.e. conical, hemispherical, trumpet (or bell shape) and bi-conical shapes, in which explosive mass and outer diameter are kept constant. Conical liner will be treated as a baseline. The enhanced flow velocities and collapse angles for these zirconium linear shapes are discussed based on the conditions of jet formation and coherency in Table 7-1. The performance of the formed jets is characterized by their penetration capability into the standard target in comparison with the penetration capability of the conical liner jet. These liners are tested experimentally against the laminated steel-water-steel-concrete standard target according to API-RP43 (Section II) [143]. Calculations of jetting, jet formation and penetration of four liner designs are performed using the hydro-code Autodyn.

Section 7.2 gives the conditions of jet formation and coherency for the zirconium liners. Section 7.3 describes the liner manufacture and the experimental set-up. Section 7.4 introduces the numerical models, material models and material parameters used to simulate jet formation and penetration of the shaped charges. Results with further analyses are presented in Section 7.5 followed by conclusions in Section 7.6.

7.2 Critical angle calculations conditions for the zirconium jets

It is well known in gas dynamics that for a flow of free stream velocity V_2 impinging on a solid wall, there is a maximum angle β_c, above which an attached shock wave cannot exist as depicted in Figure 7-3 [83]. This mechanism is also applicable to the shaped charge jet formation [82-83].

Relationships between the critical collapse angle and the flow velocity for some liner materials apart from zirconium have been determined analytically in [3]. The β_c-V_2 relationship is important because it defines the boundary between jetting and no jetting

regions on β-V_2 domain, as shown in Figure 7-4. Together with the C_L limit, three regions can be defined on β-V_2 domain, which is explained in Figure 7-4 for the copper (Cu-Cu) liner (C_L=4.84 km/s), i.e. (a) Region-I: the region on the left of C_L limit where coherent jet is formed; (b) Region-II: the region on the right of C_L limit and above the β_c-V_2 curve where non-coherent jet is formed; (c) Region-III: the region on the right of C_L limit and below the β_c-V_2 curve where jet cannot be formed.

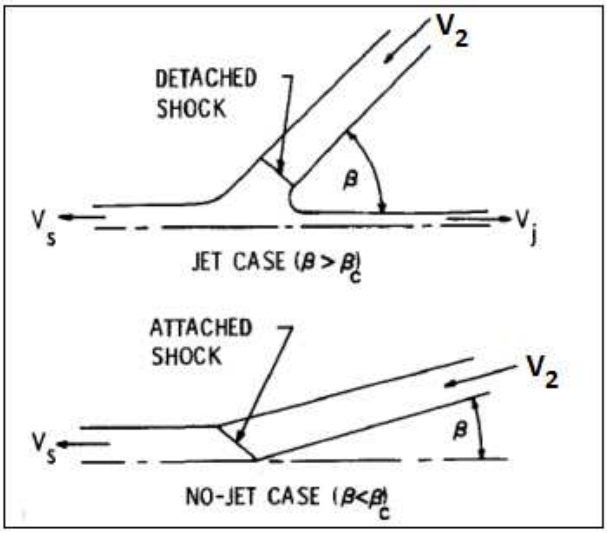

Figure 7-3 The flow configurations in the supersonic regimes detached and attached shocks [83].

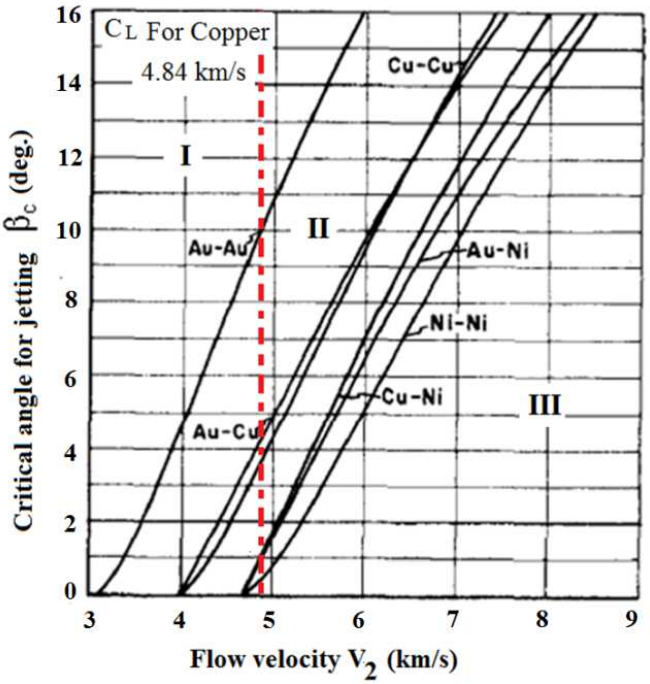

Figure 7-4 The calculated critical angles for different liner materials at different flow velocities [3].

Two methods will be used in this chapter to calculate the critical collapse angles at a given flow velocity.

(i) Method 1:

The analytical model presented in [3, 82], employed the momentum balance to obtain the critical collapse angle. According to [82], the critical collapse angle is given by

$$\tan^2\beta = \frac{P\left[\rho_o V_2^2\left(\frac{\mu}{\mu+1}\right) - P\right]}{(\rho_o V_2^2 - P)^2}, \qquad 7\text{-}7$$

where P is the pressure, ρ_o is the initial liner density, μ is the compressibility (i.e. $\mu=\rho/\rho_o-1$).

The maximum angle can be determined for a given impinging velocity V_2 from the condition $d\beta/d\mu = 0$ at $\beta=\beta_c$ according to [82]. Thus, for $\beta=\beta_c$,

$$\frac{\mathrm{dP}}{\mathrm{d}\mu} = \frac{P[P-\rho_o V_2^2]}{(\mu+1)[\mu\rho_o V_2^2 - P(\mu+2)]}. \qquad 7\text{-}8$$

Eq. (7-8) together with the equation of state (EOS) of the liner material can be used to calculate the critical angles β_c at different values of V_2. Shock EOS takes the form of [116]:

$$P = \frac{\rho C_0^2 \mu(\mu+1)}{(1-(S-1)\mu)^2} \qquad 7\text{-}9$$

where C_o is the sound speed of the liner material and S is the slope of the shock speed-particle velocity line. For the zirconium material, C_o= 3757m/s and S=1.018 [116].

Differentiating Eq.(7-9) with respect to μ gives

$$\frac{dP}{d\mu} = \frac{(1-(S-1)\mu)\rho C_0^2\left((1-(S-1))(2\mu+1)+2(\mu^2+\mu)(S-1)\right)}{(1-(S-1)\mu)^4}. \qquad 7\text{-}10$$

For simplicity, assume S≈1, therefore Eq.(7-10) reduces to:

$$\frac{dP}{d\mu} = \rho C_o^2(2\mu+1). \qquad 7\text{-}11$$

The critical compressibility (i.e. μ_c) and the corresponding critical pressure P_c can be obtained from Eqs. (7-8), (7-9) and (7-11). Therefore, β_c can be derermined from Eq.(7-7). The detailed steps for the calculation procedures are illustrated in Appendix A.

(ii) Method 2:

The second method that was used to calculate the β_c-V_2 curve is the numerical method using Autodyn hydro-code with the Euler solver, which was used to simulate the impinging of the liner with its axis of symmetry, as shown in Figure 7-5. The jet formation was validated by Refs. [133] and [135], where the obtained features of the jet using the Autodyn Euler solver were supported by using the flash x-ray photograph. The problem was approximated by solving a transient oblique impact model with proper initial conditions assuming a steady-state flow configuration. The initial model is a zirconium liner of wall thickness 2mm moving towards its axis at a uniform constant free stream velocity V_2 impacting a rigid boundary at constant angle β, as depicted in Figure 7-5. The rigid boundary is the axis of symmetry for the axisymmetric 2D model [83] and the initial pressure throughout the material is zero. Various combinations of flow velocities and collapse angles were used to sufficiently cover all three regimes, i.e., subsonic, supersonic jetting, and supersonic non-jetting. These calculations were performed for the axisymmetric Euler configurations, in which the jetting and non-jetting criteria will be identified. The flow velocities that were tested are 3, 4, 5, 6, 7 and 8km/s, while the tested collapse angles are 2.5, 5, 7.5, 10, 12, 15, 17 and 20 degrees. The obtained β_c-V_2 curve for the zirconium metal liner can be used to design the liner shape to form a coherent jet.

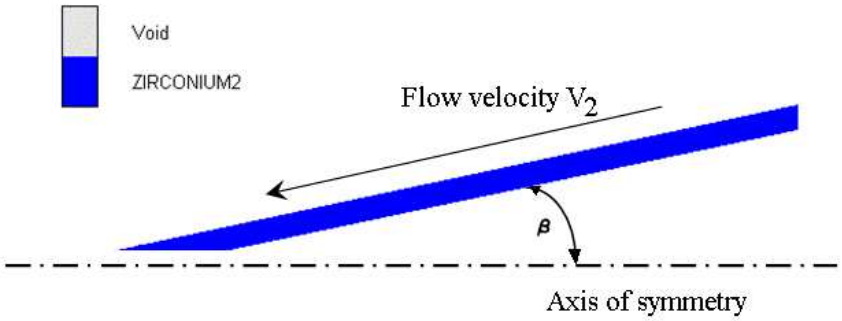

Figure 7-5 The flow configuration Autodyn 2-D model used to estimate the critical angle of jetting.

According to Eqs.(7-2) and (7-4) and the jet formation condition $V_2 \leq C_L$, we have

$$\beta_{c1} \leq \sin^{-1}\left(\frac{V_o}{C_L}\cos\left(\alpha + \sin^{-1}\left(\frac{V_o}{2U}\right)\right)\right) \qquad 7\text{-}12$$

where β_{c1} is the theoretical critical collapse angle (i.e. the minimum collapse angle) for the formation of a coherent jet.

For zirconium liner and PE4 explosive, C_L=4566m/s, $U=U_D/\cos\alpha$ with U_D=8200m/s and α =23°, Eq. (7-12) becomes:

$$\beta_{c1} \leq \sin^{-1}\left(\frac{V_o}{4566}\cos\left(23+\sin^{-1}(\frac{V_o}{17816})\right)\right). \quad 7\text{-}13$$

On the other hand the β_c-V_2 curve can be calculated based on analytical or numerical methods introduced before, which together with Eq.(7-2) can define another critical collapse angle as a function of collapse velocity V_o. As an example, we used the numerical method (i.e. Method-2) to determine the β_c-V_2 curve empirically (i.e. from the fitting of the β_c-V_2 curve), for the zirconium liner as shown in Figure 7-6.

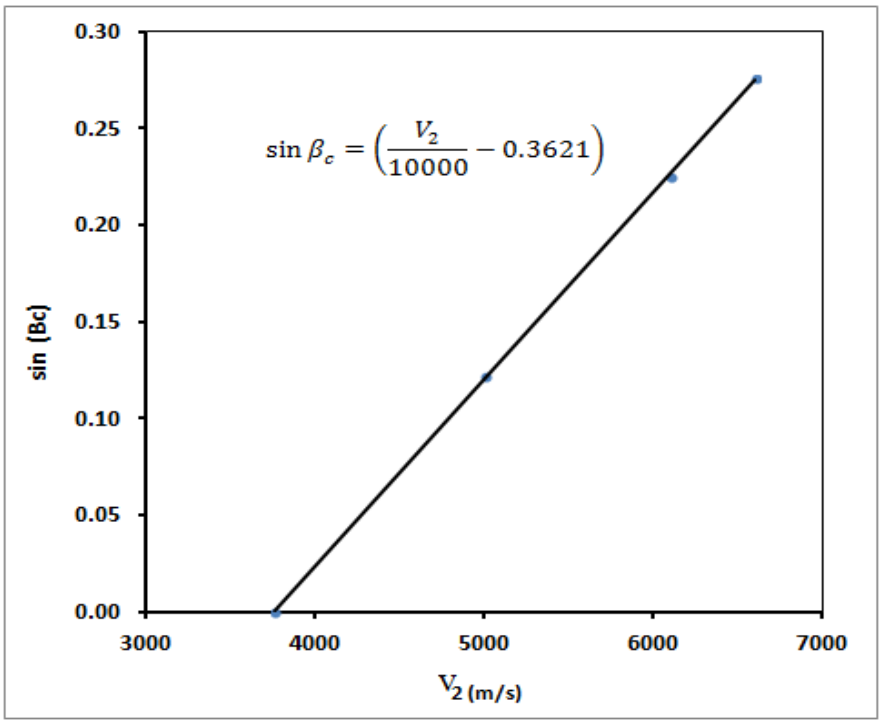

Figure 7-6 The relation between the critical angle and the flow velocity calculated numerically (i.e. method 2).

The relation between V_2 and β_c is

$$\sin\beta_c = \left(\frac{V_2}{10000} - 0.3621\right). \quad 7\text{-}14$$

Substituation the value of the V_2 from Eq. (7-2) into Eq. (7-14) gives

$$\sin\beta_c = \left(\frac{V_o\cos(\alpha+\delta)}{10000\sin\beta_c} - 0.3621\right). \qquad 7\text{-}15$$

Solving Eq. (7-15) for the value of β_c in $0<\beta_c<\pi$ gives

$$\beta_c = \sin^{-1}\left(\sqrt{0.03277 + \frac{V_o}{10^4}\cos(23+\sin^{-1}(\frac{V_o}{17816}))} - 0.18105\right). \qquad 7\text{-}16$$

Plotting Eqns.(7-13) and (7-16) for different values of collapse velocity V_o, three regions were defined in Figure 7-7, which can be compared with those corresponding regions in Figure 7-4. The advantage of Figure 7-7 is that it can be used to check the jet formation and coherence directly from the jet collapse velocity V_o, which is determined by the liner-explosive mass ratio and the used explosive, without further need of calculating flow velocities.

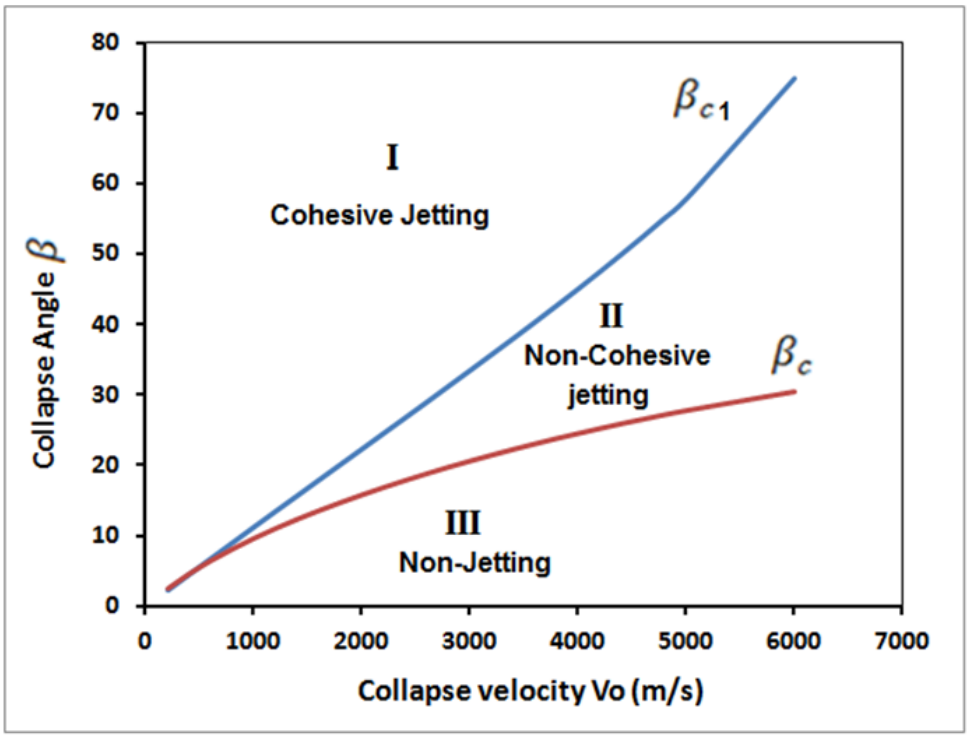

Figure 7-7 Variations of β_{c1} and β_c with collapse velocity.

7.3 Experiments

Amongst different tested liner materials, zirconium exhibited the longest cumulative jet length and the highest ductility factor, which are necessary to sustain longer breakup time and to achieve larger penetration depth [13]. In this study, the zirconium liners were manufactured by high precision CNC machine (i.e. the precision of 5μm). The row material was a solid cylinder of pure zirconium 4N (99.9951) having a diameter of 46.17mm and a length of 99.89mm with a density of 6623kg/m^3. The impurity percentages of the zirconium material are listed in Table 7-2. The zirconium rod was annealed to 900^{o}C for one hour before machining in order to obtain a relative small average grain size, hence to increase its ductility, which in turn increases its breakup time and improve the liner performance [151]. The row material of the zirconium rod and the manufactured liners are illustrated in Figure 7-8.

Table 7-2 The elemental percentage of impurities in the zirconium material.

Element	Impurities amount (%)
Fe	0.005
Cr	0.0009
C	0.001
N	0.008

The zirconium material has two problems with its machining. The first one is related to its high tendency to work hardening during machining, while the second one is the possible ignition of the fine chips that accumulate near the machining equipment [152]. To avoid these problems, slow speed and heavy feed were applied with a continuous coolant supply of water soluble oil lubricant to reduce temperature and prevent flammability of the fine chips.

The PE4 explosive was used with the four shaped charges. PE4 is a RDX-based powerful explosive (i.e. mass composition of 88% RDX and 12% plasticizer and other additives) having a detonation velocity of 8027m/s at 1590kg/m^3 density [153] and 8200m/s at 1600kg/m^3 density [154]. It was chosen for its high performance and low sensitivity to different kinds of stimuli (i.e. friction and impact). The assembly and set-up procedures include: (i) fill PE4 into the steel casing; (ii) press the liner slowly against the steel casings containing high explosives to expel air gaps inside the perforator charge; (iii) attach the shaped charge to the upper steel layer of the test configuration in Figure 7-9.

Figure 7-8 The zirconium solid cylinder (left) and the manufactured liners; 1: conical; 2: hemispherical; 3: bell and 4: bi-conical shape.

The concrete cylinders with the designated strength were cast in 1mm wall thickness PVC tubes and allowed to cure according to the test evaluation of the well perforator [155]. These concrete targets were tested according to the standard OWP testing configuration and requirements in the Section-II of API-RP43 [143]. The measured average strength of the standard concrete cubes was 40.02 MPa with a standard deviation of 0.92 MPa, measured at 28 days from their pouring day [145].

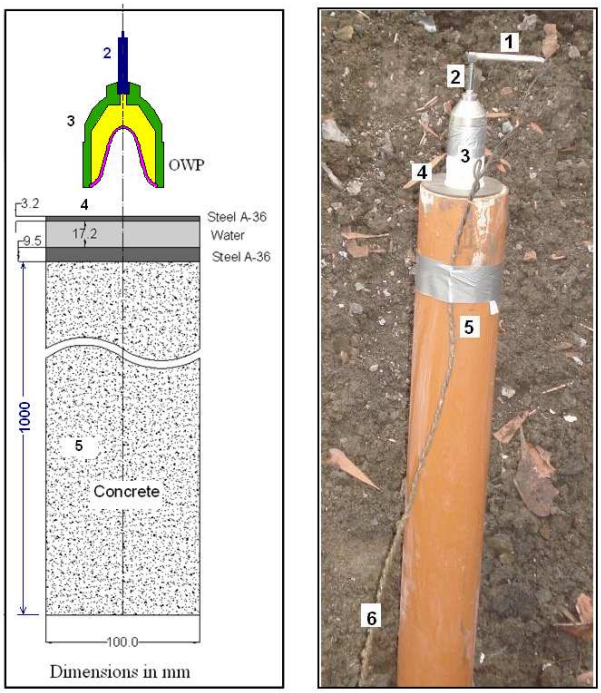

Figure 7-9 Dimensions of the test setup and the experimental test configuration (1: Detonator; 2: Boaster; 3: OWP; 4: Front steel disc; 5: Concrete; 6: Power supply).

7.4 Numerical models

7.4.1 Methodology

General description of the used Autodyn algorithms was presented in Chapter 4.

7.4.2 Mesh sensitivity

In order to study the mesh sensitivity on the jet penetration, five different mesh densities were proposed for the concrete target material, while the Lagrangian bi-conical jet meshes remain unchanged (i.e. 0.5mm×0.5mm) due to its sufficiently small dimensions. Uniform square meshes of 0.25, 0.5, 1, 2 and 3mm are selected for the concrete targets. Figure 7-10 shows a sample of three different mesh sizes at the impact area, while Figure 7-11 shows the concrete damage contours relevant to these meshes at 40μs from the moment of impact. It can be observed that the damage areas of the three mesh sizes are similar, but the crater profiles indicate the main difference in the crater shape due to the different mesh densities.

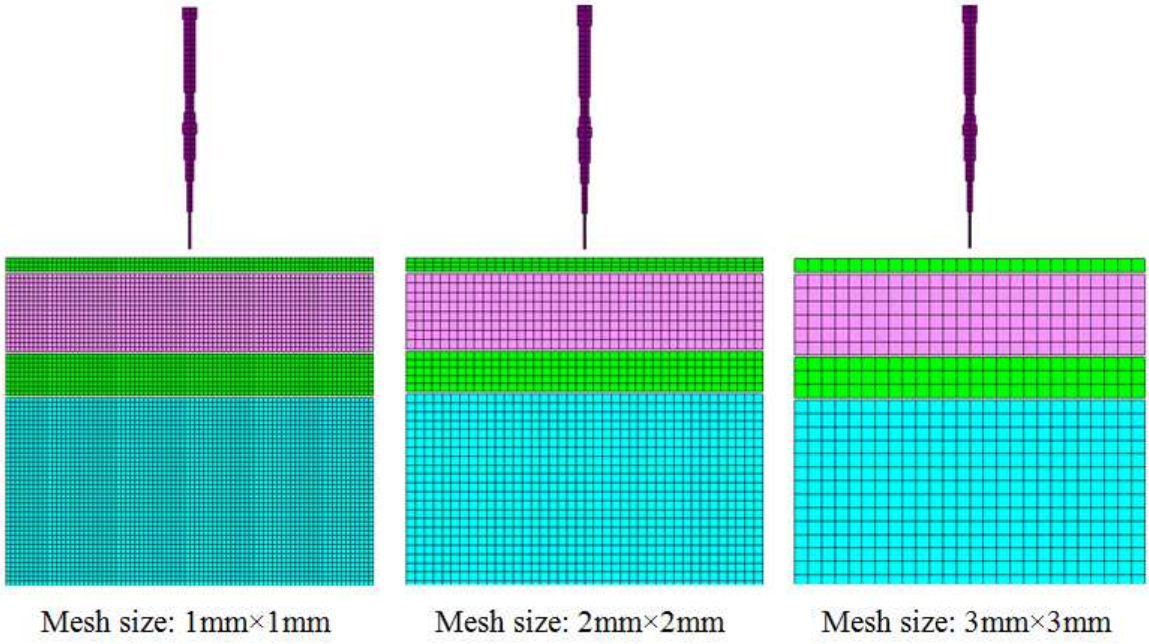

Figure 7-10 The impact area of the jet-test layers modelled by jet solvers using three different mesh sizes.

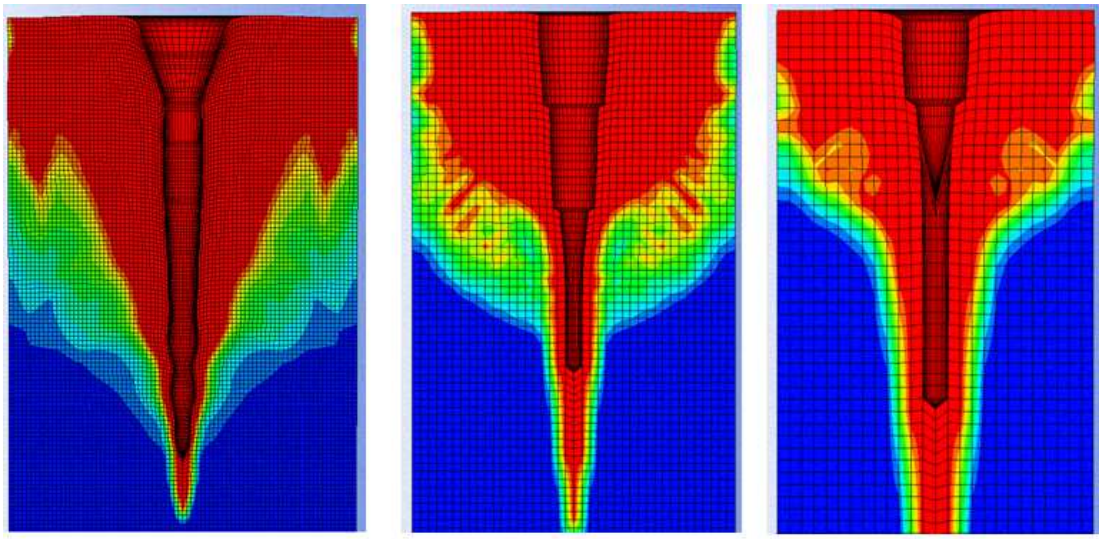

Figure 7-11 The damage contours near the impact surface for the three mesh sizes at 40μs.

All the five simulation models were allowed to proceed until the final penetration is achieved. This happens either when the jet is completely consumed or eroded on the crater walls, or when the jet velocity decays below a certain value, at which no change in the penetration is remarked with time. The total penetration depth for the five mesh sizes is depicted in Figure 7-12.

There is a large difference of the penetration depths for coarse and fine meshes between 1mm and 3mm indicating the sensitivity of the penetration depth to the mesh size. However, when mesh size is smaller than 1mm, this sensitivity is largely reduced, and the penetration depth approaches to an asymptote. According to Figure 7-12, the penetration modelling using 1mm mesh size is 2.75% different from that of 0.25mm mesh size while the latter model costs five times computational time of the 1mm size model. Thus, it was decided to use 1mm concrete mesh size for the rest of modelling to maintain reasonable computation accuracy and time.

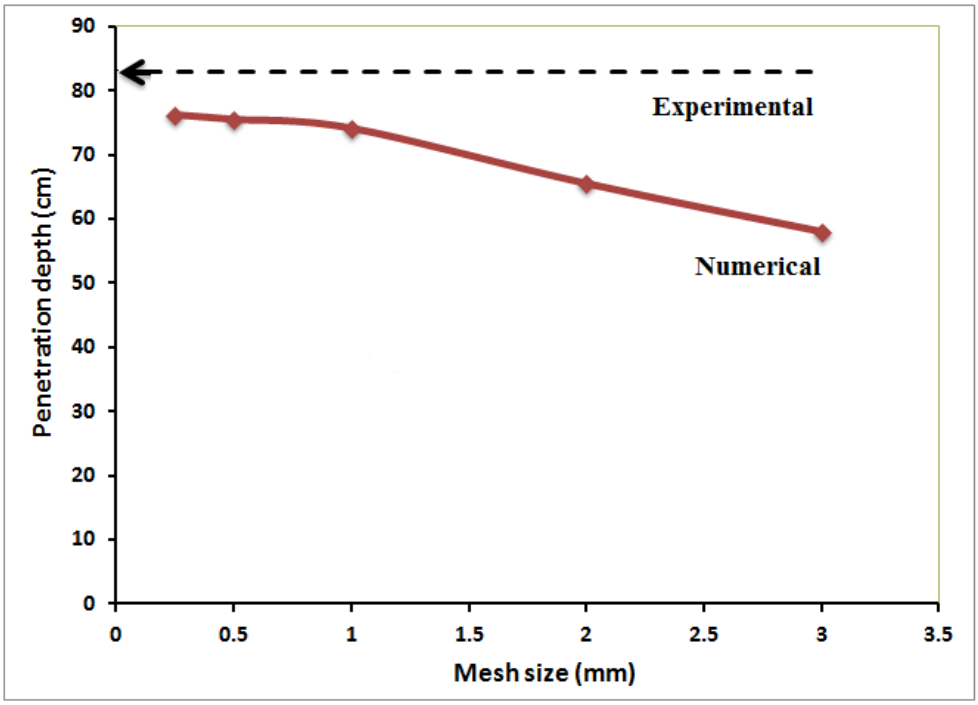

Figure 7-12 The Numerical penetration using different mesh sizes and experimental penetration.

7.4.3 Material models

A general description of the material models used in this chapter is shown in Chapter 4.

7.5 Results

7.5.1 The β_c-V_2calculations

For zirconium material, C_o =3757m/s and ν=0.34. Therefore, the longitudinal sound speed of the zirconium material is C_L=4567m/s according to Eq.(7-6).

Three cases with fixed collapse angle of 12 degree and different flow velocities, i.e. Case (I): V_2=3.0 km/s, Case (II): V_2=5.0 km/s and Case (III): V_2=6.0 km/s, were simulated using Autodyn hydro-code model in Figure 7-5. According to Table 7-1, Cases (I)-(III) belong to coherent jetting, non-coherent jetting and non-jetting situations, respectively. Figure 7-13 (a) shows the cross-sections of the collapsed jet impacting on the symmetrical axis for these three cases, in which, jetting [Cases (I) and (II)] and non-jetting [Case (III)] cases can be easily identified as depicted in Figure 7-13 (b). The jet in Case (II) has a large number of radially dispersed particles representing a non-coherent jet.

The analytical and numerical β_c-V_2 curves for zirconium liner are shown in Figure 7-14, where the numerical β_c-V_2 curve for copper liner was shown as a reference. This figure illustrates the boundary between jetting and non-jetting and the boundary between coherent jetting and non-coherent jetting cases. When V_2 and β are calculated, this figure could be used to determine the jetting formation and behavior in the design of zirconium liner.

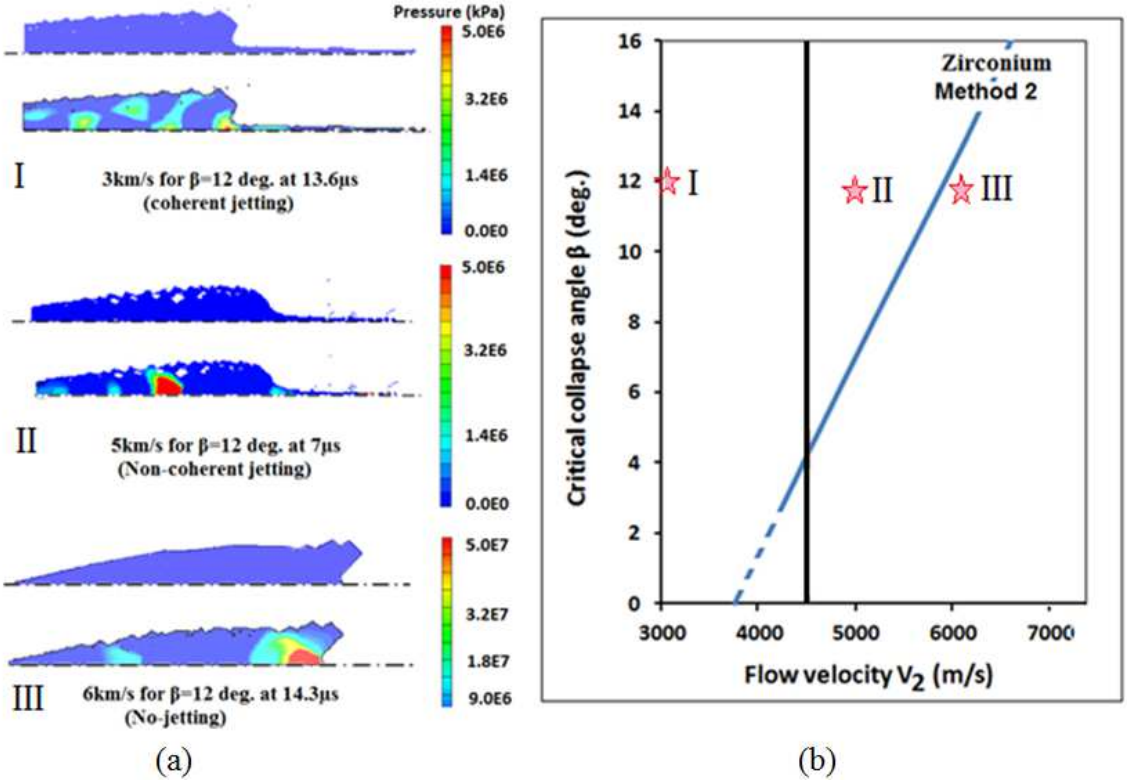

Figure 7-13 (a) the cross-sections of the collapsed zirconium jet impacting on the symmetrical axis at collapse angle of 12 degree and flow velocities of 3, 5 and 6km/s for cases I, II and III respectively; (b) the corresponding regions on the β_c-V_2 curve.

The β and V_2 values were obtained for four zirconium liner shapes from jetting analysis, which are shown in Figure 7-15. This figure confirms that the four liner designs can produce coherent jets and indicates the abnormal high collapse angles for the hemispherical liner, which help forming massive explosively formed projectile (EFP) rather than the traditional thin jet. This can be explained by Eq.(7-5), where large collapse angles were found to be common for all the hemispherical liner elements according to the standard jetting analysis. Therefore, the jet mass, which is directly proportional to the collapse angle, showed that the produced EFP mass is 68% of its liner total mass. The EFP is characterized by its uniform low velocity massive slug, which produces a shallow penetration depth but a large hole diameter.

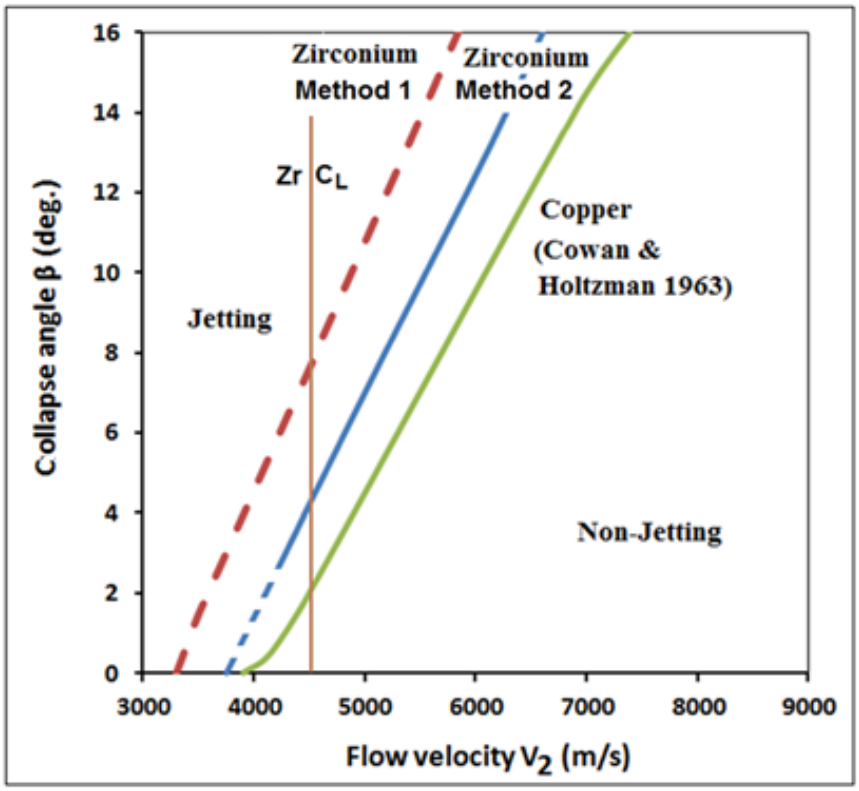

Figure 7-14 The analytical and numerical β_c-V_2 curves for zirconium liner with the numerical β_c-V_2 curve for copper liner as reference.

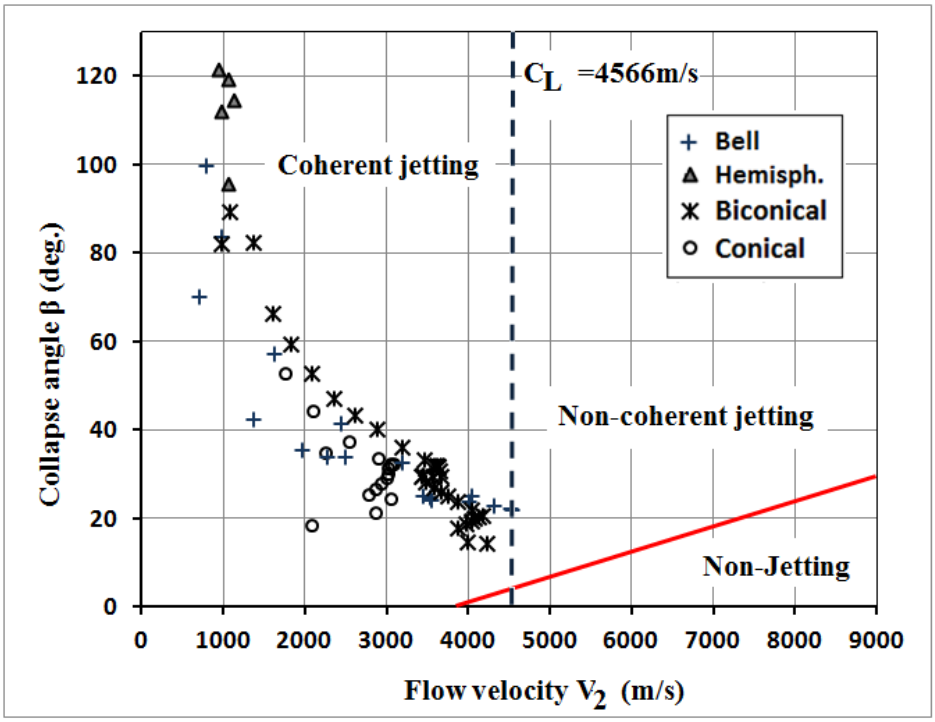

Figure 7-15 β and V_2 values for four zirconium liner shapes from jetting analysis, in which different regions of zirconium jet formation and coherency are shown.

7.5.2 Jet analysis and penetration of different liner shapes

The jetting analysis calculates the jet characteristics until the liner elements reach their axis to form a jet element. Thus, it does not consider the jet elongation and the breakup time resulting from this elongation [115]. In addition, the jet tip velocity correction is not included. This means that the points near the apex region do not have sufficient space to accelerate to its theoretical maximum collapse velocity, which results in a reduced jet tip velocity and the pilling up of the jet mass [6]. Thus, the inverse velocity gradient needs to be removed by adding the piled-up mass to the jetting element with the highest velocity. Then, the jet tip velocity is corrected based on the momentum conversation. The corrected jet tip velocity was calculated according to [156]:

$$V_{tip} = \frac{\int_0^{X_{tip}} V_j (dm_j/dX) dX}{\int_0^{X_{tip}} (dm_j/dX) dX}. \qquad 7\text{-}17$$

where m_j is the jet mass and X is the axial distance of the jet element.

Figure 7-16 shows the jet velocity as a function of the distance from the apex with and without correction. It was predicted by the jetting analysis that the liner with the bell shape has the highest tip velocity exceeding 9km/s. However, after the tip correction, the tip velocity is reduced to 6.63 km/s. The pilled-up tip mass of the bell-shape liner is illustrated in Figure 7-17, which can be compared with the characteristics of the jet mass generated from other three liner shapes. On the other hand, the bi-conical liner shows less difference between the theoretical and the corrected tip velocities, which are 8.6 and 8.4km/s, respectively. The hemispherical liner produces an explosively formed projectile (EFP) rather than the thin jet. As shown in Figure 7-17, most of the hemispherical liner mass flows to form the EFP with the largest diameter and mass, but the slowest velocity (3.8km/s). Therefore, the crater diameter resulted from the interaction of EFP with the concrete targets is expected to be the largest one amongst the caretrs created by four liner shapes.

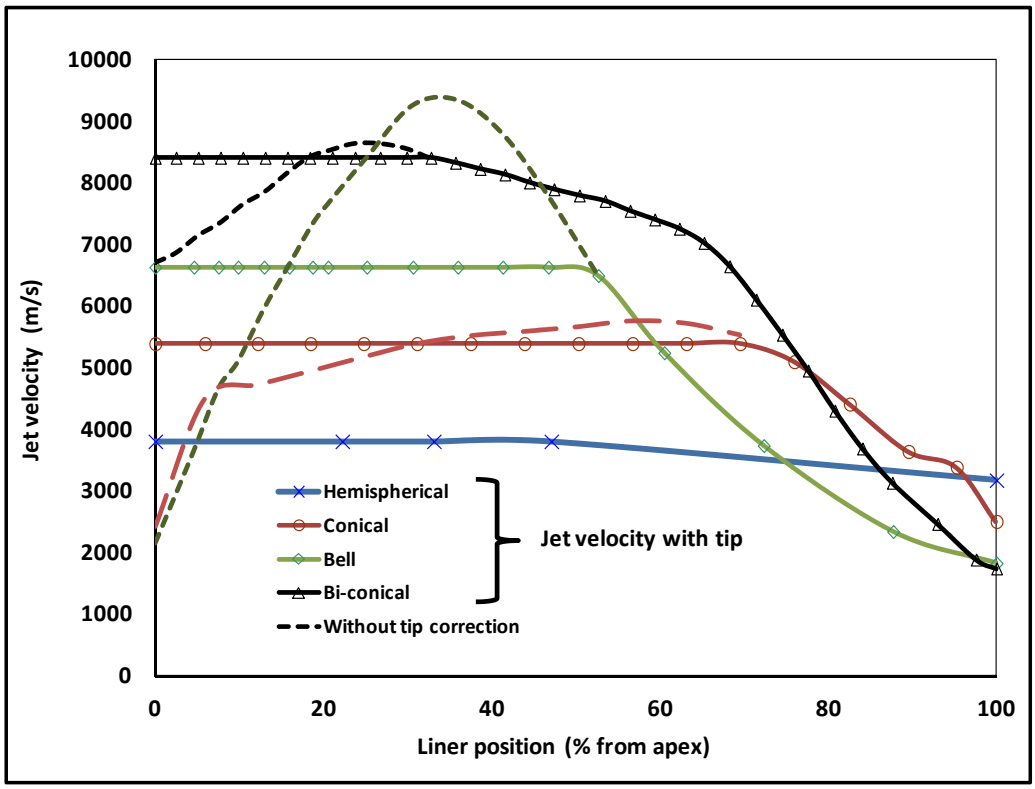

Figure 7-16 Jet velocity profile along the liner axis with and without tip correction.

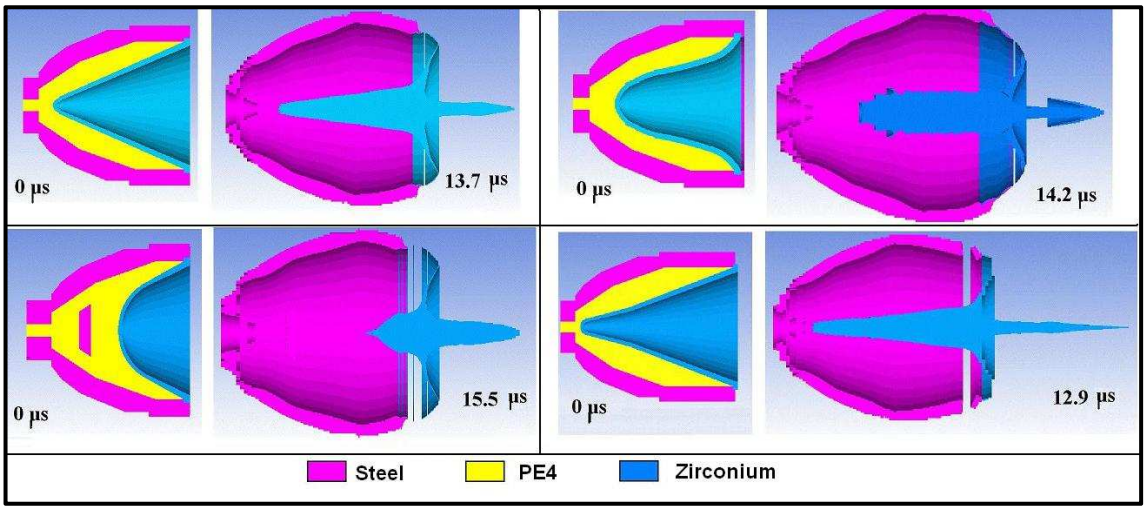

Figure 7-17 The jets shapes for the different liner geometries right before the impact on the test layers.

The collapse velocity can be fully developed either by allowing sufficient acceleration distance between the liner elements and the axisymmetrical axis of the shaped charge (e.g. the bell shape liner) or by using a reduced cone apex angles (e.g. the bi-conical liner). Actually, both methods work in the jet formation of bell shaped liner because in addition to the increased liner distance from its axis, the bell shaped liner close to the base has a small angle, which increases the jet velocity according to the unsteady PER theory [50]. The

collapse velocity-time histories for the studied four liner shapes are shown in Figure 7-18. The hemispherical liner apex angle decreases gradually from the apex to the liner base, and the minimum angle (α) of the hemispherical liner is 29^{o}, which is responsible for the reduced achievable jet velocity. However, the collapse velocity of the hemispherical liner is considered to be the highest among the four liner shapes in the apex region up to 40% of liner position from the apex. This is due to the existence of sufficient space available for its liner elements in the apex region to accelerate. The jetting analysis indicated that the collapse angles of the hemispherical liner ranging from 95 to 120 degree are greater than those of the other liner shapes, which lead to the greatest percentage (i.e. 67.57 %) of the jet mass from the total liner mass according to Eq.(7-5).

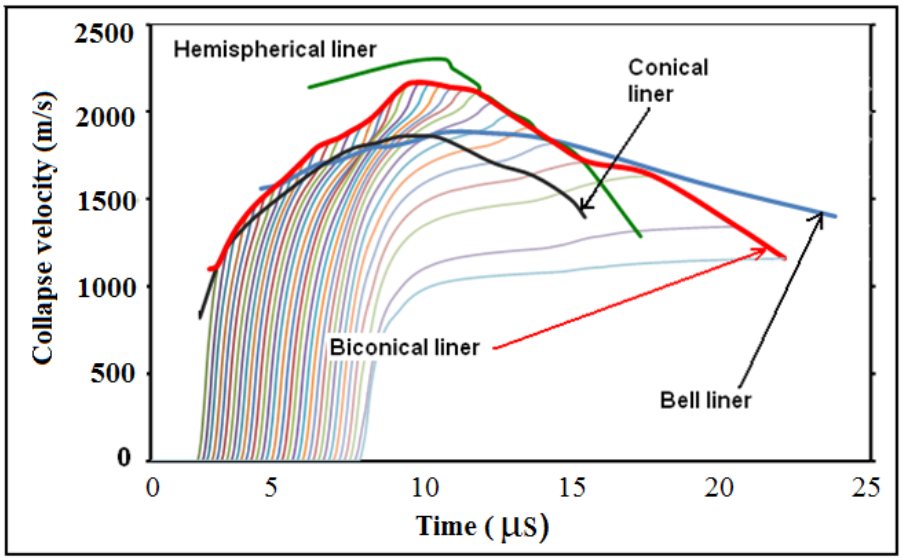

Figure 7-18 The collapse velocity histories for the different liners.

The collapse velocities for both the conical and the bi-conical liners are similar in the region near the liner apex because they nearly have the same inclination angle at that region and only have small difference between their explosive-metal mass ratios. Beyond this region, their collapse velocity difference begins to increase because the bi-conical liner has smaller liner angle, which enhance the explosive-metal mass ratio due to the charge of geometry. The bell shape liner, which has a long distance between its inner surface and the axisymmetrical axis of the shaped charge, gains more collapse velocity than the conical liner near the apex and the bi-conical liner at the liner base. Since the tip velocity of the jet is produced from the liner elements near the apex, the bi-conical liner has the largest jet tip velocity. In addition to the above-discussed factors of the liner shape, another important factor for the remarkable difference of the collapse velocities is the liner surface area that determines the transmission of explosive energy to the liner. According to Table 7-3, the

surface area of the bell and the bi-conical liners are 7% and 25% greater than that of the conical one respectively, which means that both these shapes are capable of absorbing more energy from the explosive although they have nearly the same total mass ratio between the explosive charge and the metallic liner. The transmitted momentum can be indicated by Figure 7-19, where the x-momentum-time histories of the four liner shapes exhibit a similar exponential relation, but the difference between them accounts for the difference in their jet velocities and explain why the liners with a greater surface area have a better performance than those with lower surface area.

Table 7-3 The liner shapes and their jets characteristics.

Liner shape	Hemispherical	Conical	Bell	Biconical
Liner mass (g)	25.90	26.40	23.97	29.30
Explosive mass (g)	20.80	24.20	24.45	31.80
M/C mass ratio	1.25	1.03	0.98	0.95
Jet mass (g)	17.50	3.47	3.77	5.06
% jet to liner	67.57	13.14	15.73	17.27
Jet K.E. (kJ)	31.05	34.70	36.90	49.70
Liner surface area (mm^2)	1785	2400	2568	3005
Jet velocity without corr. (m/s)	3815	5761	8780	8611
Jet velocity with corr. (m/s)	3815	5386	6630	8402
Tip distance from apex (%)	0	63.12	52.65	32.77

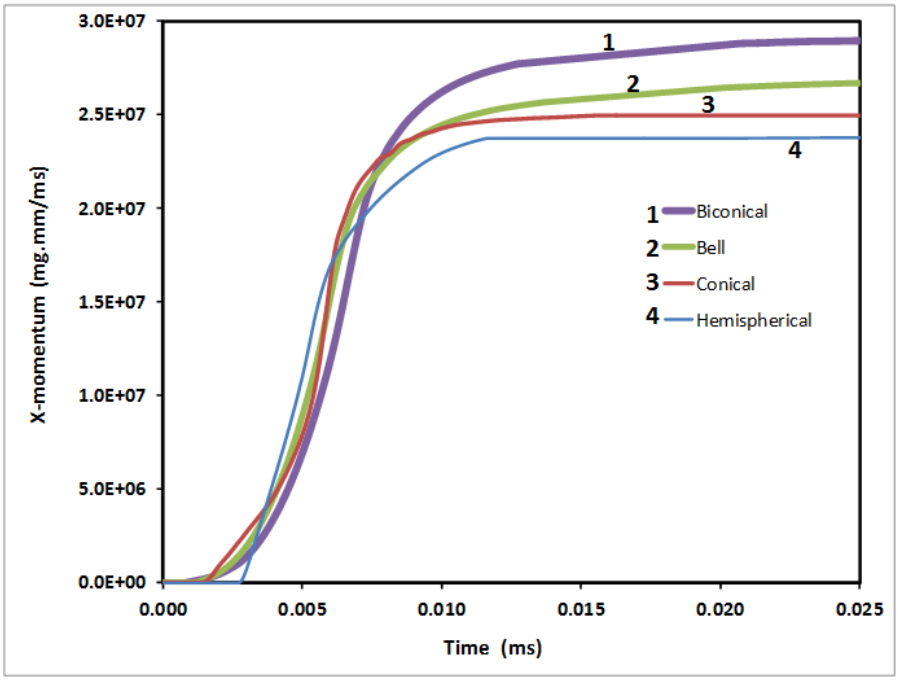

Figure 7-19 The x-momentum histories for the four perforators with different liner shapes.

7.5.3 Penetration

The numerical penetration depths into 40 MPa concrete targets for the four perforators with different liner shapes and their corresponding experimental penetration depths are illustrated in Table 7-4 and Figure 7-20. Samples of the numerical penetration stages of the biconical jet and hemispherical EFP, as two examples representing very different shaped charges, into concrete are illustrated in Figure 7-21 and Figure 7-22, respectively. The difference between their crater profiles is significant. The shortest penetration path with the biggest crater diameter for the hemispherical liner is a typical characteristic of EFP, which has a short length, a large diameter, large mass and a very low tip velocity in comparison with the other jets. On the other hand, the produced jet from the bi-conical liner has a small jet diameter and a high tip velocity, therefore its kinetic energy per unit area of the jet cross-section is considered the greatest one, and hence its penetration depth is the largest one in comparison with the other three liner designs.

Table 7-4 The numerical and experimental penetration depths using different liner shapes.

	Hemisph.	Conical	Bell	Biconical
Penetration (Numerical) (cm)	42.3	55.9	64.7	74.1
Penetration (Exp.) (cm)	48.4	68	75	83
Difference bet. Num. and Exp. (%)	12.6	17.8	13.7	10.72
Num. exit hole diameter (mm)	29.6	16.0	14.5	12.0

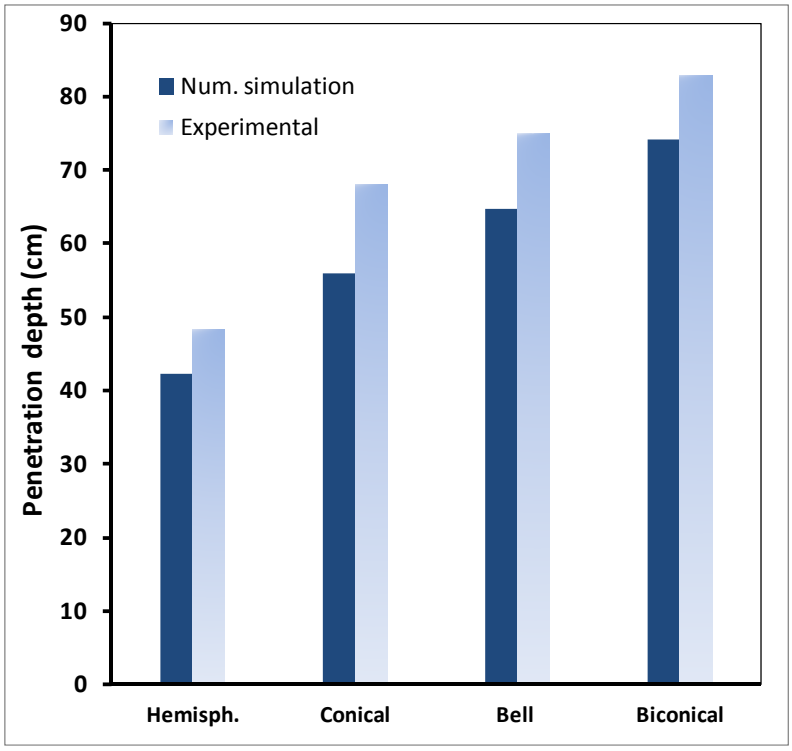

Figure 7-20 The penetration depth dependence on the concrete strength.

The penetration depth of the OWP into the concrete material indicates the importance of the liner shape design on the performance of these perforators. Thus, the longer the penetration depth into the concrete, the greater the flow productivity of the well and the better the performance of the perforator charge.

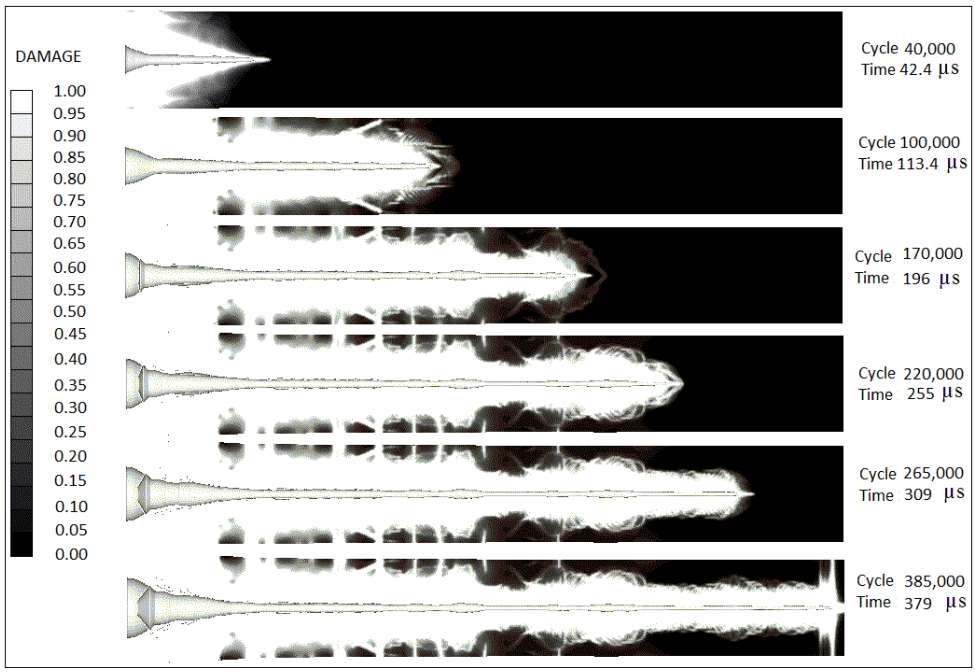

Figure 7-21 The damage contours of the concrete penetrated by the bi-conical jet at different times.

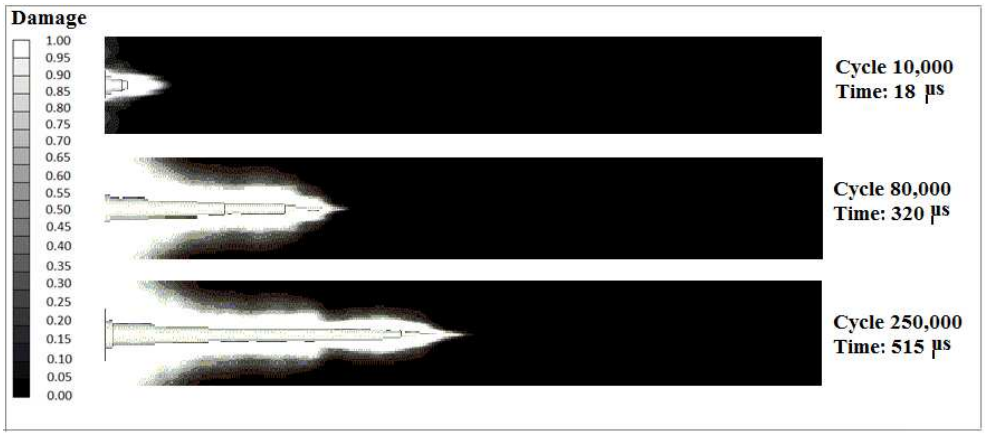

Figure 7-22 The damage contours of the concrete penetrated by the hemispherical EFP at different times.

7.6 Summary

The critical collapse angle as a function of flow velocity was calculated numerically and analytically for the zirconium liner material in this chapter, which, together with the longitudinal sound velocity of the liner material, defines the boundaries among jetting, coherent jetting and non-jetting situations. The regions divided by these boundaries were used to exam the jet characteristics of four zirconium OWP liners with different shapes. It was shown that the jets of four different liners are coherent, but have different collapse, flow and jet velocities because of their different geometries and surface areas. The enhanced performance of the liner shape effect was confirmed by the static firing of four zirconium OWPs against the laminated API-RP43 targets. The bi-conical liner exhibited the largest penetration depth into target, which is 22% greater than that of the baseline conical zirconium liner. The large collapse angles in the hemispherical shape increased its jet mass, but decreased its velocity, and therefore, it is classified as an explosively-formed-projectile (EFP). An EFP achieves the shortest penetration depth, but largest crater diameter among the four OWPs with different liner shapes.

CHAPTER.8 A MODIFIED VIRTUAL ORIGIN MODEL FOR SHAPED CHARGE JET PENETRATION WITH NON-UNIFORM DENSITY DISTRIBUTION

8.1 Introduction

Hypervelocity jet of a shaped charge has excellent penetration capability into various targets. Due to its penetration capability, shaped charge has been successfully used both in the battle field to defeat armours and in the oil and gas wells to perforate tunnels to connect the wellbore to the reservoir. In these applications, it is necessary to predict the depth of penetration, which is an important parameter for the assessment of shaped charge effects on a target.

Since the shaped charge jet travels at hypervelocity, the impact of the jet on target produces much higher pressure than the strength of the target, and thus, the hydrodynamic model [49, 103] can be applied to study the jet penetration. These original hydrodynamic models assumed uniform distributions of jet density and jet velocity along the jet length and applied Bernoulli equation at the interface between jet and target for the pressure equilibrium

$$\frac{1}{2}\rho_j(V_j - U)^2 = \frac{1}{2}\rho_T U^2, \qquad 8\text{-}1$$

where V_j is the velocity of a continuous jet; U is the velocity of the jet-target interface or penetration velocity; ρ_j and ρ_T are jet density and target density around the jet-target interface, respectively. When the distributions of jet density and velocity are uniform, the consumption of the jet is controlled by

$$V - U = -\frac{dl}{dt} \qquad 8\text{-}2$$

where l is the current length of jet.

The depth of penetration of the jet into target is determined by

$$U = \frac{dP}{dt} \quad or \quad P = \int_0^t U dt, \tag{8-3}$$

where t=0 is the time when the jet starts to hit the target. The maximum depth of penetration is achieved when the jet is completely consumed at $t = t_f$, or $l(t_f) = 0$. For a jet with original length of l_0, the maximum depth of penetration is determined by Eqs.(8-1) and (8-3), i.e.

$$P_{max} = l_0 \sqrt{\frac{\rho_j}{\rho_T}}. \tag{8-4}$$

Eq. (8-4) is also applicable to solid rod penetrator.

For a particulated jet, Bernoulli equation cannot be used directly because the internal pressure cannot be supported after the jet is particulated [49]. This study will only consider continuous jet. Interested readers may refer to [103] for the penetration models of particulated jet.

Since the early time of the jet penetration study, it has been realised that the spatial distribution of jet velocity is not uniform [49]. Birkhoff et al. [49] extended the hydrodynamic penetration model [Eq.(8-4)] to the jet with non-uniform velocity distribution. However, this model introduced several parameters that cannot be easily determined, and therefore, it has not been widely used. Abrahamson and Goodier [100] also extended the hydrodynamic penetration model to include non-uniform jet velocity distribution and stand-off distance. This model started from an arbitrarily selected initial time and required the initial jet length at this moment to be given, which makes the model difficult in practical use.

The concept of virtual origin was first proposed by Allison and Bryan [157] and then developed by Allison and Vitali [2] for the penetration of continuous and particulated jets with the consideration of velocity gradient and the stand-off distance between the virtual origin and target surface. This model has been widely accepted, which can be used to predict the depth of penetration before and after jet breakup [101, 103].

The virtual origin model keeps the basic equations in hydrodynamic model, i.e. Eqs.(8-1) and (8-3) where the strengths and the compressibility of the jet and target materials were

neglected. Eq.(8-2) was abandoned because the concept of jet length cannot be applied when it is lengthened as it travels forward from the shaped charge. In addition to these assumptions, following conditions for the existence of a virtual origin need to be satisfied.

Existence of a virtual origin: All jet elements are formed simultaneously at a virtual origin located at a distance Z_0 from the target surface. Each jet element is emitted from the virtual origin at its own velocity that remains constant during its travelling between virtual origin and target. The existence of a unique virtual origin location of the entire jet requires that the spatial distribution of jet velocity is linear.

In the virtual original model and its applications, the density of the jet element is treated as a constant, i.e. the density of each element remains constant during its travelling and the spatial distribution of the jet density is uniform. However, it has been observed that there is a density deficit based on flash x-ray measurements and the soft recovery of jet fragments [1, 158]. Variable density distribution was also observed in the jets formed from powdered metal liners [159-161]. Therefore, it is necessary to extend the virtual origin model to the jet with non-uniform density distribution.

This chapter keeps the assumption that the density of each jet element remains constant during its travelling, but considers the non-uniform jet density distribution to study its effect on the penetration depth. The non-uniform jet density distributions along its axial distance are estimated numerically using the Autodyn jet formation algorithm for the three liners made from electrolytic OFHC copper, zirconium and copper-tungsten un-sintered powder. An analytical approach is introduced to account for the penetration decrease due to the non-uniform density distribution along its axis. The proposed model is validated by experiments and numerical simulations using Autodyn hydro-code.

A modified virtual origin model with non-uniform distribution of jet density is proposed in Section 8.2. Section 8.3 describes the liner manufactures and the experimental set-up configurations. Section 8.4 introduces the numerical models used to simulate the shaped charge jets and penetrations. Results are presented in Section 8.5 with further analysis, which is followed by conclusions in Section 8.6.

8.2 Penetration analytical model

In this chapter, we will focus on the jet penetration before or without jet breakup. Figure 8-1 is a schematic drawing that defines the penetration parameters of a shaped charge jet

penetrating into an incompressible target. Z_o is the stand-off distance from the virtual origin point to the target surface, t is the penetration time, P(t) is the penetration depth at time (t) and V_j is the impinging velocity of the jet onto the target (observed at the jet/target interface), which equals to the velocity of the jet element that impacts the target at the same moment of time t.

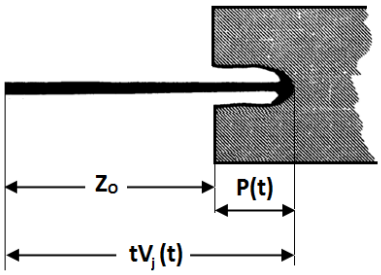

Figure 8-1 The hydrodynamic jet penetration; [2].

Therefore, the depth of penetration P(t) at a given time t is determined by

$$P(t) = tV_j(t) - Z_o. \tag{8-5}$$

The depth of penetration increase monotonically with time, which requires the satisfaction of following condition:

$$\frac{dP}{dt} \geq 0 \text{ for } tV_j(t) \geq Z_o\ . \tag{8-6}$$

This condition was not checked in previous publications. A proof of this necessary condition will be given in Appendix B.

When hydrodynamic Bernoulli equation [Eq.(8-1)] is applied,

$$U = \frac{V_j}{\gamma+1} \tag{8-7}$$

where $\gamma = \sqrt{\rho_T/\rho_j}$.

Following equation can be obtained from Eqs.(8-3 , 8-5, 8-7),

$$V_j(t) + t\frac{dV_j(t)}{dt} = \frac{V_j(t)}{\gamma+1}\,. \tag{8-8}$$

When the jet density is a constant, the solution of Eq.(8-8) predicts the jet velocity $V_j(t)$ as

$$V_j(t) = V_0 \left(\frac{t_o}{t}\right)^{\frac{\gamma}{\gamma+1}} \quad 8\text{-}9$$

where V_0 is the jet tip velocity and t_o is the time when the jet tip reaches the target surface (i.e. $t_0 V_0 = Z_0$).

From Eq.(8-9), time can be expressed as

$$t = t_o \left(\frac{V_0}{V_j(t)}\right)^{\frac{\gamma+1}{\gamma}} , \quad 8\text{-}10$$

and therefore, the depth of penetration at time t can be obtained from Eq.(8-5) when $V_j(t)$ and t in Eq.(8-5) are substituted by those Eqs.(8-9, 8-10)

$$P(t) = Z_0 \left[\left(\frac{V_0}{V_j}\right)^{\frac{1}{\gamma}} - 1\right] = Z_0 \left[\left(\frac{t}{t_0}\right)^{\frac{1}{\gamma+1}} - 1\right] . \quad 8\text{-}11$$

The maximum penetration is achieved at time t_c when the cut-off jet element (i.e. the last jet element that has hydrodynamic penetration capability) hits the target at the cut-off velocity (V_c). Therefore, the maximum depth of penetration is

$$P = Z_0 \left[\left(\frac{V_0}{V_c}\right)^{\frac{1}{\gamma}} - 1\right] . \quad 8\text{-}12$$

In the proposed model, it is assumed that the density of each jet element will be a constant during its travel between virtual origin and target. However, since different jet elements experienced different jet formation processes, their densities are different. Therefore, the spatial distribution of the jet density is non-uniform. At the jet-target interface, the observed jet density should be a function of time, i.e. $\rho_j = \rho_j(t)$. Let ρ_{j0} represent the original density of the liner material and the density of target ρ_T is a constant, then parameters $\gamma_0 = \sqrt{\rho_T/\rho_{j0}}$ and $\gamma(t) = \sqrt{\rho_T/\rho_j(t)}$ are introduced. Thus, $\frac{\gamma(t)}{\gamma_0} = \sqrt{\frac{\rho_{j0}}{\rho_j(t)}}$.

Based on jet formation analysis presented later, it is found that the normalised jet density is directly related to the normalised jet velocity in a linear relationship, as shown in Figure 8-2. According to Figure 8-2, the density reduction at the jet tip is larger than that at the rear jet. The maximum density reductions in the simulated examples are around 15.8% for copper and zirconium liners and 21.7% for copper-tungsten liner, respectively. These

values are in line with the experimental observations by Zernow for the copper liner [1]. Details of the numerical simulation will be presented in Sections 8.4 and 8.5.

The linear relationship between $\frac{\gamma(t)}{\gamma_o}$ and $\frac{V_j(t)}{V_0}$ can be described by

$$\frac{\gamma(t)}{\gamma_o} = a\frac{V_j(t)}{V_0} + b \qquad 8\text{-}13$$

where a and b are constants to be determined from data fitting of numerical results and analytical consideration, which will be given at the end of this section.

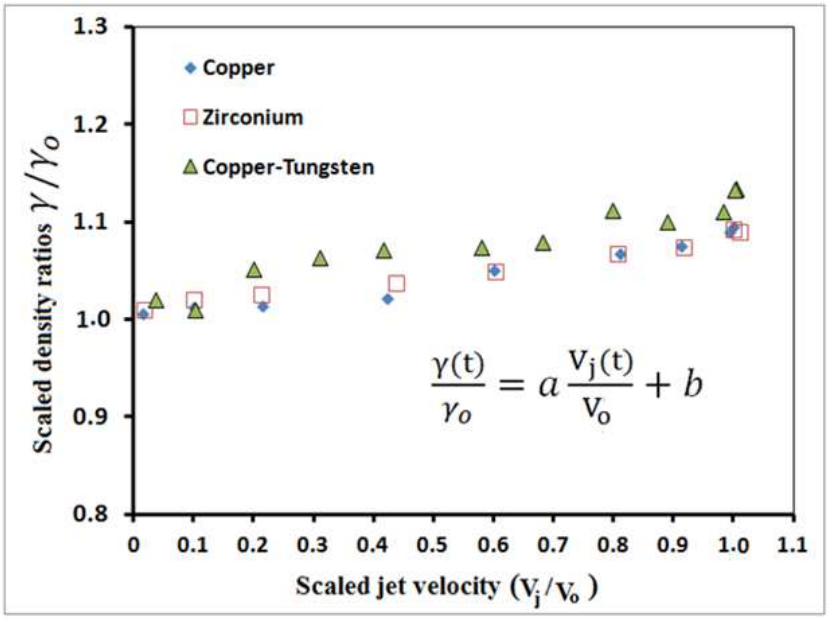

Figure 8-2 The relationship between the scaled density ratio and the scaled jet velocity.

Equation (8-8) can be rearranged as $\frac{-dV_j}{V_j(\tau)} - \frac{dV_j}{\gamma(\tau)V_j(\tau)} = \frac{d\tau}{\tau}$, which can be integrated when Eq.(8-13) is used, i.e. $\int_{V_0}^{V_j(t)} \frac{-dV_j}{V_j(\tau)} - \frac{1}{\gamma_o}\int_{V_0}^{V_j(t)} \frac{dV_j}{V_j(\tau)\left(\frac{a}{V_0}V_j(\tau)+b\right)} = \int_{t_o}^{t} \frac{d\tau}{\tau}$, or

$$t = t_o\left(\frac{V_0}{V_j(t)}\right)^{1+\frac{1}{b\gamma_o}}\left[\frac{\left(\frac{a}{V_0}V_j(t)+b\right)}{\left(\frac{a}{V_0}V_0+b\right)}\right]^{\frac{1}{b\gamma_o}} . \qquad 8\text{-}14$$

This equation is reduced to Eq.(8-10) when $\frac{\gamma(t)}{\gamma_o} = 1$ or a=0 and b=1 in Eq.(8-13).

When $t=t_c$, $V_j(t)=V_c$, the maximum penetration is achieved by the last penetrating element at a cut-off velocity V_c. t_c can be determined by Eq.(8-14), i.e.

$$t_c = t_o \left(\frac{V_0}{V_c}\right)^{1+\frac{1}{b\gamma_o}} \left[\frac{\gamma_C}{\gamma_t}\right]^{\frac{1}{b\gamma_o}} \qquad 8\text{-}15$$

where $\gamma_c = \sqrt{\rho_T/\rho_{jc}} = \gamma_0\left(a\frac{V_c}{V_0}+b\right)$ and $\gamma_t = \sqrt{\rho_T/\rho_{jt}} = \gamma_0(a+b)$ according to Eq.(8-13), in which ρ_{jc} and ρ_{jt} are the densities of last penetrating element and tip element of the jet, respectively.

From Eq.(8-14), the impact velocity of the jet is determined by an algebraic equation of

$$b\left(\frac{V_0}{V_j}\right)^{b\gamma_0+1} + a\left(\frac{V_0}{V_j}\right)^{b\gamma_0} = (a+b)\left(\frac{t}{t_0}\right)^{b\gamma_0}. \qquad 8\text{-}16$$

Eq.(8-16) reduces to Eq.(8-9) for constant jet density when a=0 and b=1.

The penetration depth at time t is determined by Eq.(8-5) when t is substituted from Eq.(8-14) i.e.,

$$P(t) = Z_0\left[\left(\frac{V_0}{V_j}\right)^{\frac{1}{b\gamma_o}}\left(\frac{a\frac{V_j}{V_o}+b}{a+b}\right)^{\frac{1}{b\gamma_0}} - 1\right], \qquad 8\text{-}17$$

which can be reduced to Eq.(8-11) for constant jet density when a=0 and b=1. The solution of Eq.(8-16) is needed to give an explicit expression of P(t) in Eq.(8-17).

The maximum depth of penetration is given by:

$$P = Z_0\left[\left(\frac{V_0}{V_c}\right)^{\frac{1}{b\gamma_o}}\left(\frac{a\frac{V_c}{V_o}+b}{a+b}\right)^{\frac{1}{b\gamma_0}} - 1\right] = Z_o\left[\left(\frac{V_0}{V_c}\right)^{\frac{1}{b\gamma_o}}\left(\frac{\gamma_c}{\gamma_t}\right)^{\frac{1}{b\gamma_o}} - 1\right], \qquad 8\text{-}18$$

when $V_j=V_c$ and $t=t_c$. Eq.(8-18) is reduced to Eq.(8-12) for constant jet density when a=0 and b=1 or when $\gamma_c=\gamma_t=\gamma_o$ and b=1.

The derivation equations for the penetration depth calculation will be given in Appendix C.

The values of 'a' and 'b' in Eq.(8-13) were determined from the curve fitting of γ-V_j relationship along the jet length in Figure 8-2, which are shown in Table 8-1.

Table 8-1 The values of parameters a and b in Eq.(8-13).

Curve fitting using least-square excel fit from Figure 8-2.		a [Eq.(8-19)]
a	b	
0.077	1.0082	0.080
0.089	0.9983	0.086
0.107	1.0179	0.096

It was further found that parameter 'a' is correlated with the density of the liner material (ρ_{j0}), the stand-off distance (Z_o), the total mass of the jet (m_{jet}) from the standard jetting analysis and the radius of the jet (r) from jet formation simulation or flash x-ray experiment. A non-dimensional formula is recommended for the calculation of parameter 'a', i.e.

$$a = \frac{m_{jet}}{\rho_{j_o}\ \pi r^2 Z_o}\ . \qquad 8\text{-}19$$

The values of 'a' using Eq.(8-19) are also listed in Table 1 for three liner materials. It can be seen that values of a predicted by Eq.(8-19) are very close to the corresponding values determined by curve-fitting method. According to Table 8-1, the values of 'b' can be approximated to unity for the three liner materials.

8.3 Liner materials and penetration experiments

The three liners that have been used in this study were the copper, the zirconium and the un-sintered copper-tungsten powder. The liner has a small base diameter of 33mm, a cone apex angle of 46^o and a varied liner wall thickness as illustrated in Figure 8-3.

The copper liner was OFEC (Oxygen Free Electrolytic Copper) of grade C10100 with purity of 4N (99.99%). It was manufactured using the deep drawing technique with an intermediate annealing of 1000^oC (two minutes) to decrease the strain hardening and maintain the material ductility [31].

The zirconium liner was manufactured from a solid pure zirconium cylinder 4N (99.9951) having a density of $6623kg/m^3$ using high accuracy CNC machine in order to guarantee a high precision manufacturing (i.e. the precision of 5μm). The zirconium rod was annealed to 900^oC for one hour before machining in order to obtain a relative small average grain size, hence to increase its ductility, which in turn will increase its breakup time and

improve the liner performance [151]. The type and the percentage of the impurities present in the zirconium material are listed in Table 8-2.

Table 8-2 The elemental percentage of impurities presented in the zirconium material.

Element	Impurities amount (%)
Fe	0.005
Cr	0.0009
C	0.001
N	0.008

Powder metallurgy (PM) technique has been used to manufacture OWP liners. It has good penetration capability especially at short stand-off distances [15, 24, 43-44]. The composition of the powder mixture ingredients is listed in Table 8-3. Small average grain size with irregular particles shapes are chosen for the liner powders. The powders are mixed together with the designated mass ratio until the homogeneous mixture blend is obtained, after which they are pressed using the punch, the die and the ejector, shown in Figure 8-4. The applied pressure was 100MPa using hydraulic press at a low rate (i.e. 1MPa per second) to avoid trapping air voids inside the liner material. The product is a brittle material in the pre-sintering state and is called 'the green', which is tested in this state without sintering. All three tested liners are show in Figure 8-5.

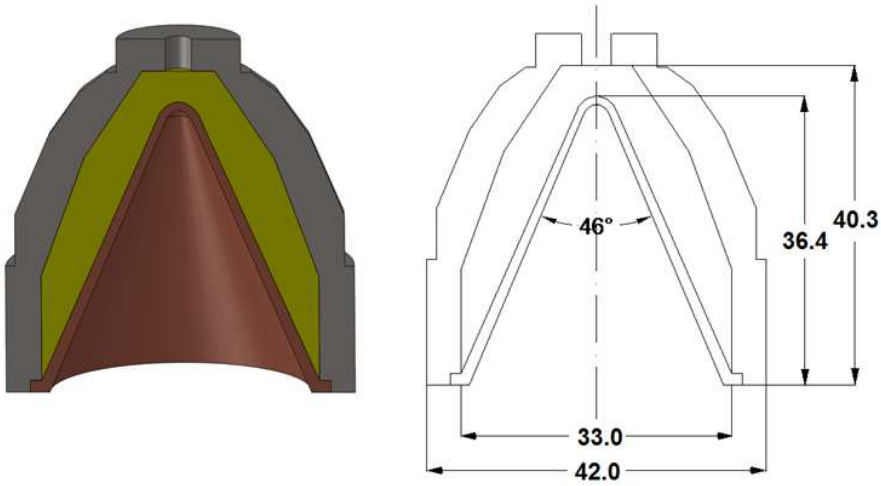

Figure 8-3 A sketch of the designed shaped charge well perforator.

Table 8-3 The mass percentage of the powder liner composition.

Material	Copper	Tungsten	Tin	Graphite
Mass ratio %	43	45	11	1
Average grain size (μm)	3	0.6:1	< 45	< 20
Function	Binder	Main powder	Binder coating	Lubricant

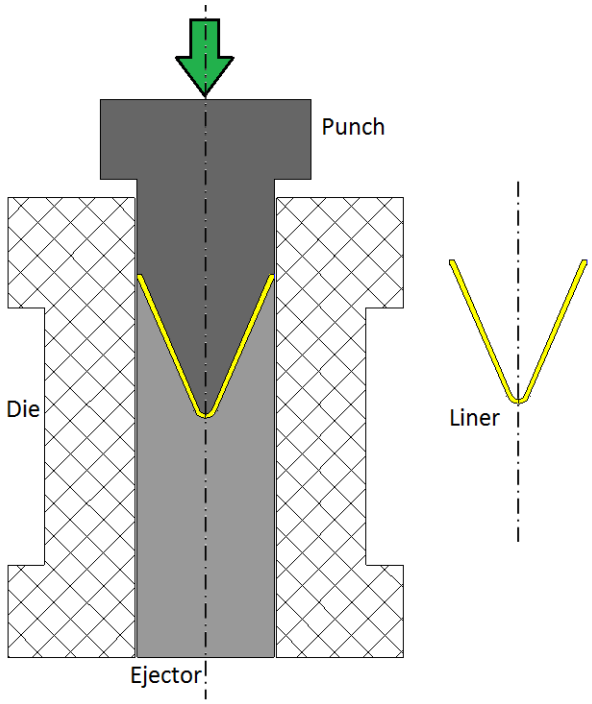

Figure 8-4 A sketch of the punch, the die, the ejector and the produced powder liner.

Figure 8-5 The three liners studied in the work.

The powder liner density is not uniform over the entire liner height because the force distribution is not homogeneous due to the conical liner profile. Therefore, small parts of the same powder liner specimen were cut off and used to measure their densities using the gas pycnometer [162]. The measured densities for the testing specimens as a function of the scaled distance from the cone apex to the liner height are shown in Figure 8-6, which is taken into account in the description of liner physical properties in Autodyn hydro-code simulations.

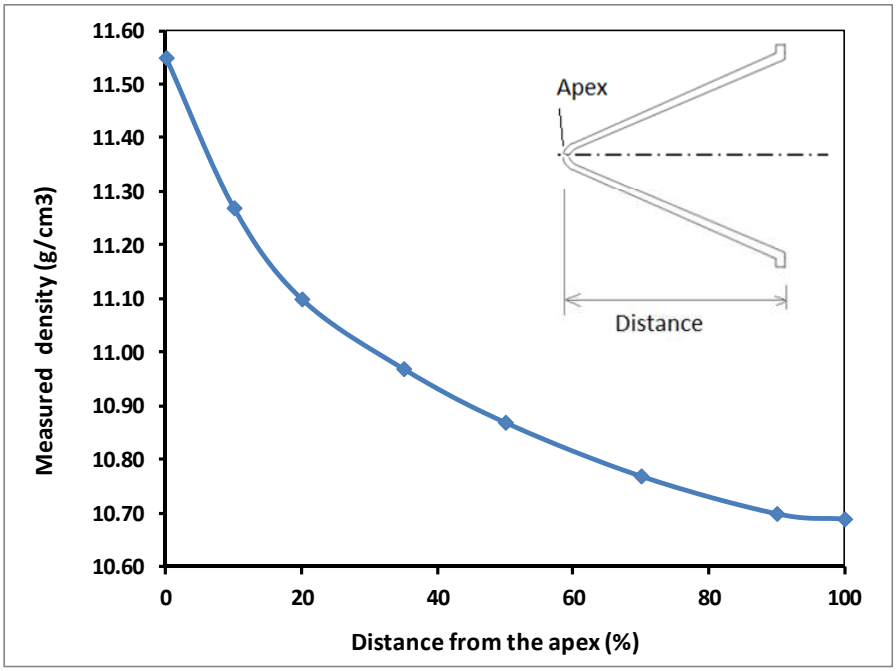

Figure 8-6 The measured densities of the liner elements at different distances from the cone apex point.

The charge casings are steel with an average wall thickness of 4.5mm. The main explosive charges for the three charges are PE4 with a total average mass of 24.5g and a standard deviation of 0.8g. The PE4 explosive is a powerful RDX-based explosive (i.e. 88% RDX in mass, 12% plasticizer and other additives) having a detonation velocity of 8027m/s at 1.59g/cm^3 density [153] and 8200m/s at 1.6g/cm^3 density [154]. The explosive charge was filled into the steel casing first. Then, the liner was pressed slowly against the steel casings containing explosives to avoid holding air gaps inside the explosive. The charges were then attached to the upper steel layer of the test configuration as shown in Figure 8-7.

The concrete cylinders with the designated strength value were cast from the same mixture and allowed to cure according to the test evaluation of the OWP [155]. These targets were tested according to the standard OWP testing configuration and requirements in the Section-II of API-RP43 [143]. The measured average strength of the standard concrete cubes was 40.02 MPa with a standard deviation of 0.92 MPa, measured at 28 days after their casting [145].

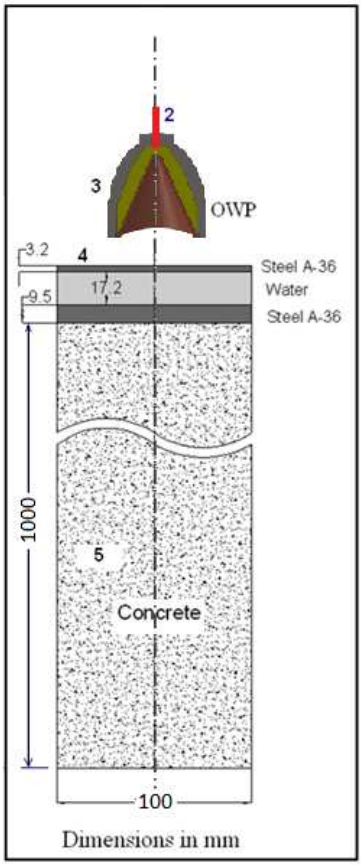

Figure 8-7 Dimensions of the test setup and the experimental test configuration (2: Boaster; 3: OWP; 4: Front steel disc; 5: Concrete; 6: power supply cable).

In a separated test without target, the particulated copper jet fragments were recovered using sand. The densities of two jet fragments were measured using a helium gas pycnometer, which has an accuracy of 10^{-4} g/cm^3. The measured densities of the two jet fragments were 7.4120 and 8.2300 g/cm^3 at the tip and the rear, respectively with a standard deviation of 0.05 g/cm^3. In comparison with the original density of copper liner material (8.930 g/cm^3), they represent 17.0% and 7.8% density reductions, respectively. The density reduction at the tip of jet (17.0%) is very close to the maximum density reduction predicted in Figure 8-2 (15.8%). This again gives evidence to support the existence of density reduction in the formed jet of a shaped charge, which was first observed based on x-ray measurements [1, 158].

8.4 Numerical models

8.4.1 Hydrocode algorithms of the jetting analysis, the jet formation model and the jet penetration model

Hydrocode algorithms and material models were presented in Chapter 4.

8.4.2 Mesh sensitivity for the jet formation model

In order to study the mesh sensitivity on the jet characteristics, five different mesh densities were proposed for the jet formation modelling. The jet formation was used to identify the density and velocity of the jet elements as they pass the gauge point shown in Figure 8-8. The fixed gauge point is located 100mm from the liner base (i.e. 3 time calibre). The uniform square meshes of 0.17, 0.20, 0.25, 0.33 and 0.50mm of the Euler grids were used for mesh sensitivity analysis in the jet formation model.

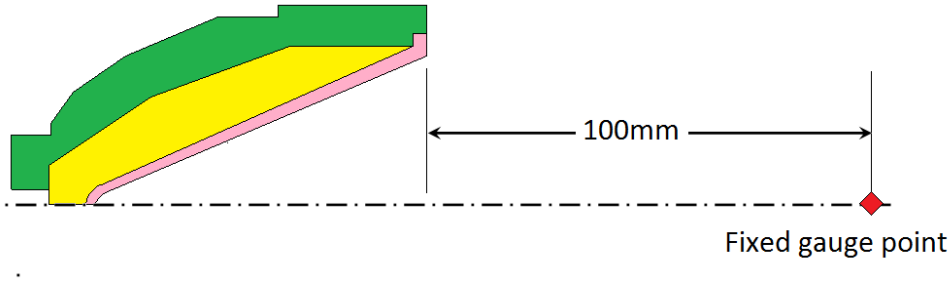

Figure 8-8 Location of the fixed gauge point used to predict the density and the velocity histories for the mesh sensitivity study.

Figure 8-9 shows the recorded density history at the fixed gauge point using five mesh sizes. The density histories for the five mesh sizes are detected between 14 and 16 μs. It shows that finer mesh sizes give higher densities at the beginning. But the density corresponding to each mesh size convergences to the copper solid material density as the jet tail passes through the gauge point. This means that the density of the jet material increases gradually from the tip to its tail due to the existence of velocity gradient. The maximum relative difference of density for the finest and coarsest meshes is about 7%.

The velocities of jet elements passing the gauge point are obtained by the same way used for the calculation of density. The velocity histories for different mesh sizes are depicted in Figure 8-10. It can be observed that the five meshes predict nearly the same shape of the velocity history. The relative difference of the peak velocity between coarsest and finest meshes is 14.8% while the relative difference of the peak velocity between the finest and second finest meshes is reduced to 2.9%, which indicates the convergence with the decrease of mesh size. These evidences ensure that a mesh size of 0.17mm is sufficient while practically affordable, which will be used globally for the calculations of jet velocity and density.

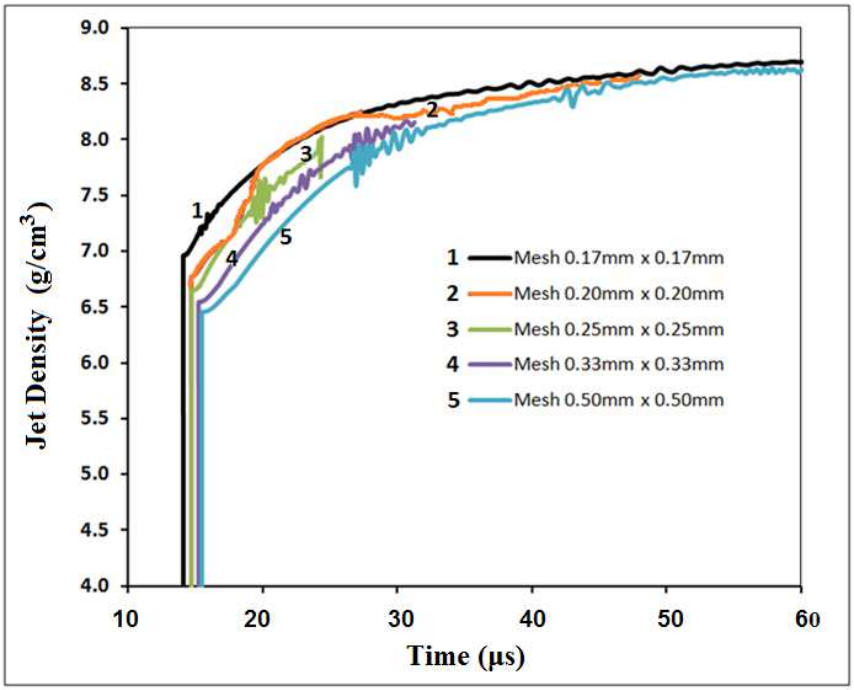

Figure 8-9 The recorded density-time histories for the fixed gauge point using five different mesh sizes.

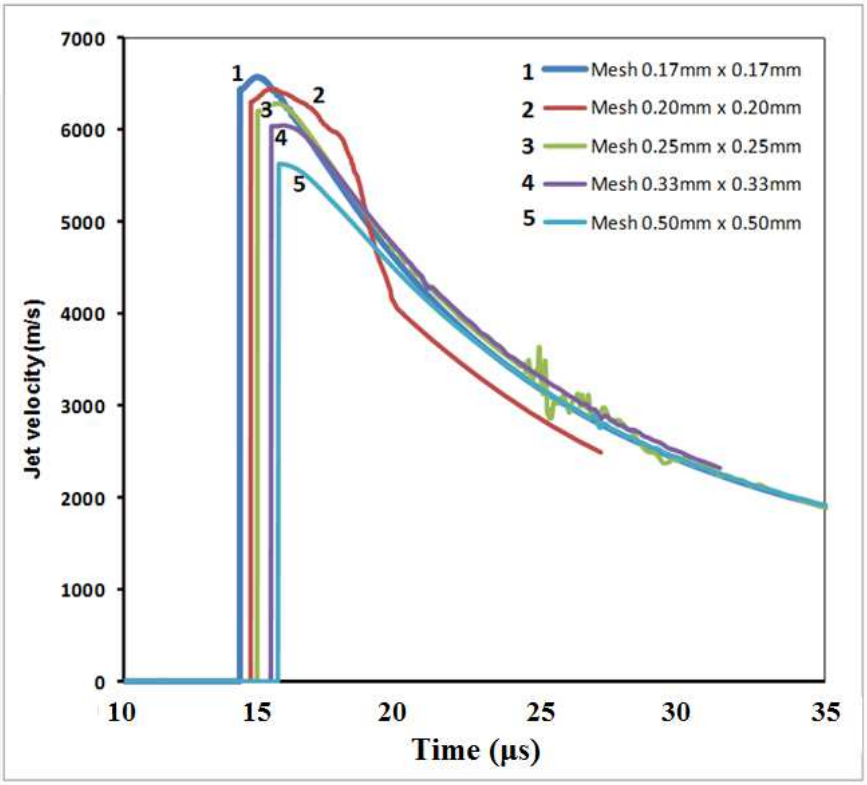

Figure 8-10 The recorded velocity-time histories for the jet material particles moving through the gauge point.

8.4.3 Mesh sensitivity for the jet penetration into target

In order to find the influence of mesh size on the penetration depth into target, five different mesh sizes were used for the laminated target consisting of steel, water and concrete (their dimensions have been shown in Figure 8-7) while the copper jet mesh density remains unchanged for all five models. The different uniform square mesh sizes of 0.5, 1, 2, 3 and 4mm were used for the laminated target. The penetration depths into the target using different mesh sizes are shown in Figure 8-11. It is evident that the penetration depth is convergent with the reduction of mesh size. The relative difference of the penetration depth for 0.5 and 1.0mm meshes is only 0.3%. However, the simulation time for 0.5mm mesh is doubled (about170 hours). Therefore, the mesh size of 1mm×1mm is used globally for the penetration analyses of three liners.

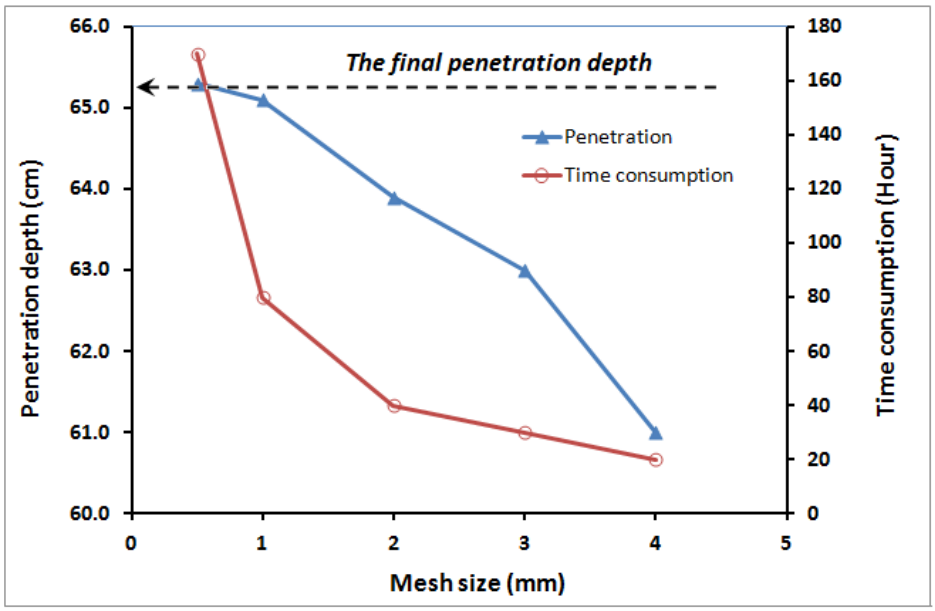

Figure 8-11 The penetration depths into laminated target using different mesh sizes and the relevant time consumption.

8.5 Results

8.5.1 The Jetting analysis results

The outputs of the jetting analysis for the shaped charge perforators with three different liners are summarized in Table 8-4. The kinetic energies of the three produced jets nearly have the same value of 36 kJ because they have the same liner shape and the same amount of explosive. However, the zirconium liner with the lowest density and mass has the highest jet tip velocity of 6075m/s but with the lowest jet mass of 3.1g.

Table 8-4 The different liners and their jet characteristics.

Liner material	Copper	Zirconium	Powder
C_o (m/s)	3757	3940	3849
Liner mass (g)	32.6	25.1	40.2
Jet mass (g)	4.0	3.1	4.5
Jet % from the liner mass	12.31	12.53	11.18
Jet K.E. (kJ)	36.0	37.2	35.7
Jet tip velocity (m/s)	5476	6075	5320
Cut-off velocity (m/s)	1610	1720	1747
Time (t_o at Z_o) (μs)	18.50	16.52	19.30
Initial Z_o (cm)	10.7	11.5	12.2

8.5.2 Jet density distribution

The density of the jet along its length was calculated from the jet formation model for three liners where Mie-Gruneisen EOS based on the shock Hugoniot was used (Section 4.5.3, page 110). The density of the collapsed liner material is directly related to the liner compressibility and the pressure generated from the explosive load. Distributions of density, compressibility and velocity over the entire jet length are depicted in Figure 8-12 for the copper jet. This figure shows that jet density decrease from slug to tip along the jet. Besides, the density contours also shows a radial density distribution on the circular cross-section of the jet (i.e. the density on the tip premises of the jet is 0.6% larger than that at its centreline). Figure 8-13 shows the velocity and the density histories of the copper jet recorded at the fixed gauge point. The distributions of jet density and velocity along the jet axis for the copper liner at a given time are shown in Figure 8-14. Both Figure 8-13 and Figure 8-14 demonstrate the increase of density reduction with the corresponding jet velocity.

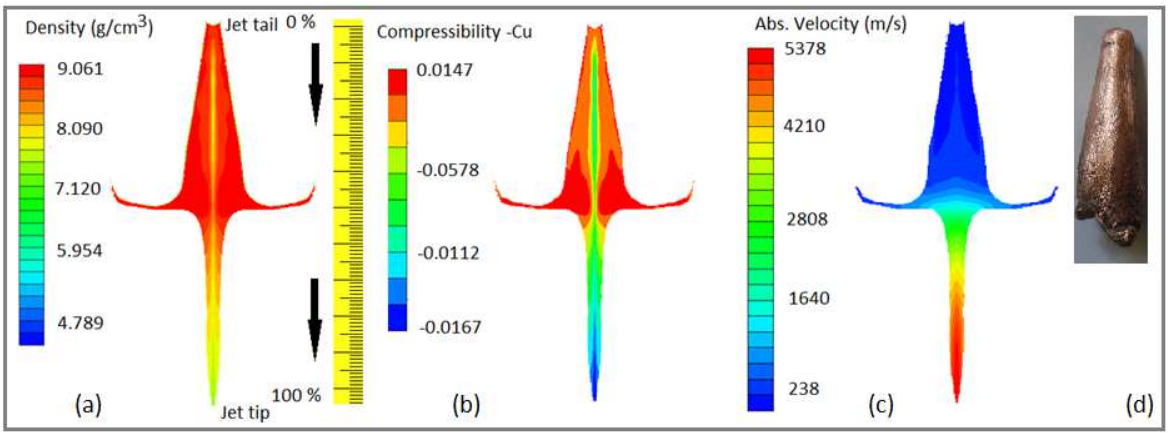

Figure 8-12 (a): Density, (b): compressibility and (c): velocity of the copper jet just before the jet tip impacts the target; (d): a picture of the recovered copper slug.

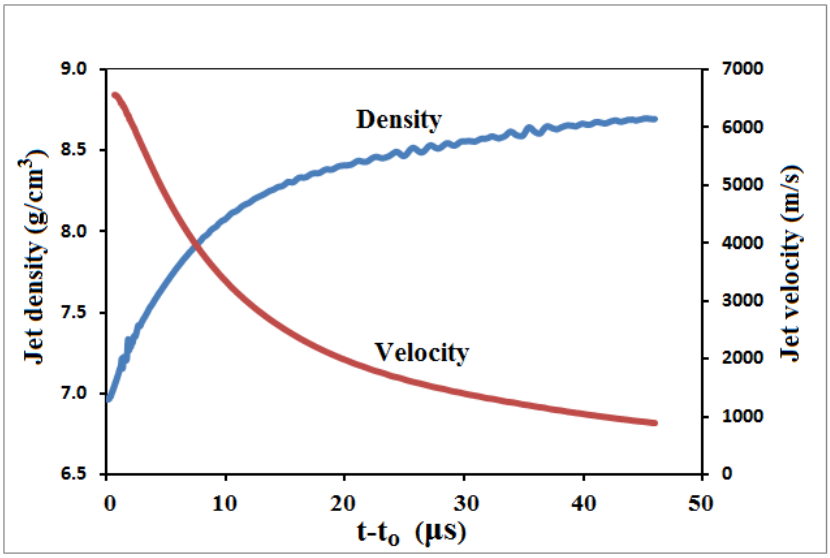

Figure 8-13 Jet velocity and density histories recorded at a fixed gauge point.

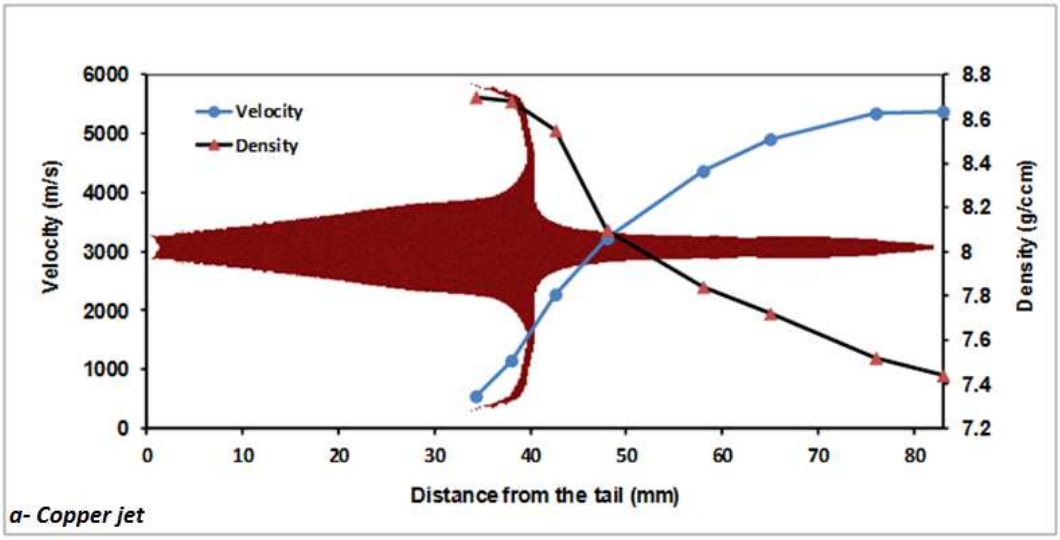

Figure 8-14 Jet density and velocity distributions along the jet axis for copper liner.

8.5.3 The penetration depth calculations

The projected effective jet lengths for the three shaped charge perforators with different liners were calculated by the back projection of the relation between time and effective jet length from the moment when the jet reaches the first steel layer. An example of the relation between time and effective jet length established by the data obtained from Autodyn jetting analysis is shown in Figure 8-15. However, this value cannot be used directly with Eq.(8-18) because the effective jet length has to be modified taking account of the thicknesses of the laminated steel and water layers.

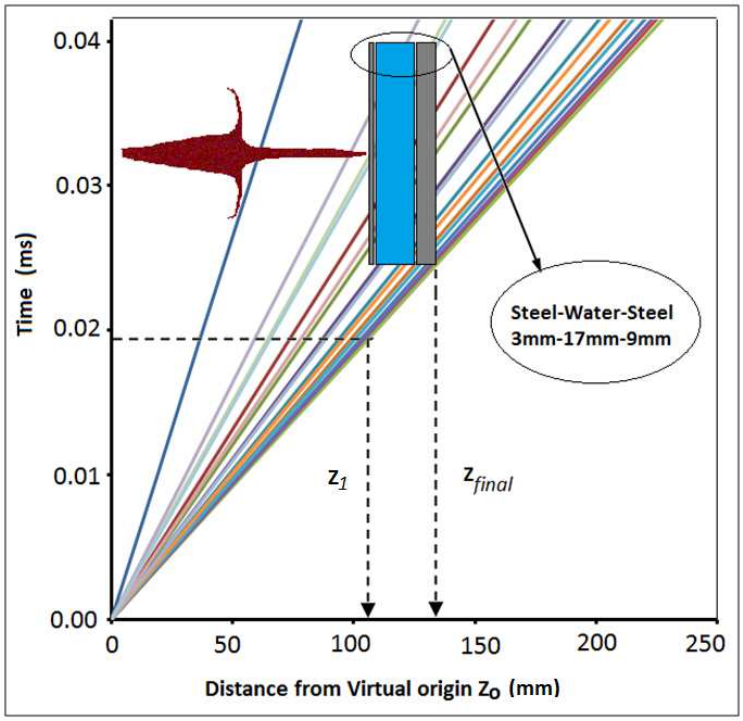

Figure 8-15 The fan plot of the copper jet showing the original and the modified effective jet length due to the presence of the laminated test layers.

The correction of the jet tip velocity is based on the uniform density formula Eq.(8-12). The exit jet tip velocity perforating a finite thickness target [103] is given by

$$V_{jex} = V_{jin}\left(\frac{Z_i}{Z_i+T_i}\right)^{\gamma_i}, \qquad 8\text{-}20$$

where V_{jex} and V_{jin} are the exit and the input jet tip velocities, respectively; Z_i is the effective jet length at the front of the target surface, T_i is the target thickness and i refers to the number of the target layer to be perforated.

However, Eq.(8-20) is not suitable for the penetration formula, Eq.(8-18), where non-uniform density effect is considered. Thus Eq. (8-20) was modified based on Eq.(8-18) to determine the exit jet velocity with considering the density reduction effect,

$$V_{jex} = \frac{bV_{jin}}{(a+b)\left(\frac{Z_i+T_i}{Z_i}\right)^{b\gamma_i}-a}. \qquad 8\text{-}21$$

Eq.(8-21) together with Eq.(8-18) can be used to predict the penetration depth of a continuous shaped charge jet into a multi-layered target when the non-uniform density distribution of the jet is considered. The values of the exit jet tip velocity and the relevant effective jet length for the test layers are presented in Table 8-5 while Table 8-6 gives the

penetration depth calculated using various methods including the modified virtual origin model [Eq.(8-18)] in Section 8.2 and the penetration reduction due to the density gradient and reduction.

Table 8-5 The effective jet length and the jet exit velocities of the three test layers.

Property	Zirconium	Copper	Powder
V_{tip} (m/s)	6075	5476	5320
V_{cutoff} (m/s)	1620	1610	1747
Z_o (cm)	11.5	10.7	12.2
Solid jet density ρ_j (g/cm^3)	6.51	8.93	11
Target density ρ_T (g/cm^3)	2.75	2.75	2.75
$\gamma = \sqrt{\rho_t/\rho_j}$	0.65	0.55	0.50
Vp_1 (m/s); Eq.(8-21)	5891.8	5324.2	5198.9
Vp_2 (m/s); Eq.(8-21)	5564.5	5053.7	4979.3
Vp_3 (m/s); Eq.(8-21)	5153.9	4714.4	4698.1
Vp_3 (m/s); Eq.(8-20)	5219.5	4769.7	4762.1
Z_{final} (cm)	14.4	13.6	15.1

Vp_1, Vp_2 and Vp_3 are the exit jet velocities as it perforate the steel, the water and the steel layers of the API laminated target layers, respectively.

The calculated penetration depths and the reduction percentages in penetration due to the density gradient along the jet length indicate that the reduction term has considerable influence on the predicted penetration depth of a shaped charge jet. Data in Table 8-6 are presented in Figure 8-16. It clearly shows that the modified virtual origin model largely improve the predictions of penetration depth by virtual origin model for all three liners.

Table 8-6 Comparison among experimental result, numerical simulation and the virtual origin model predictions for the penetration of jets with three different liners.

Liner	V_j (m/s) Eq. (8-20)	V_c (m/s)	a Value	Penetration depth (cm)				Difference Between Eqns. (8-12) and (8-18)	
				VO Eq. (8-12)	Mod.VO Eq. (8-18)	Exp.	Sim.	(cm)	(%)
Zirconium	5153.9	1620	0.077	72.73	63.57	68.0	59.0	9.2	12.5
Copper	4714.4	1610	0.089	82.67	72.04	64.0	65.0	10.6	12.8
Powder	4698.1	1747	0.049	97.10	78.18	80.0	75.0	18.9	19.4

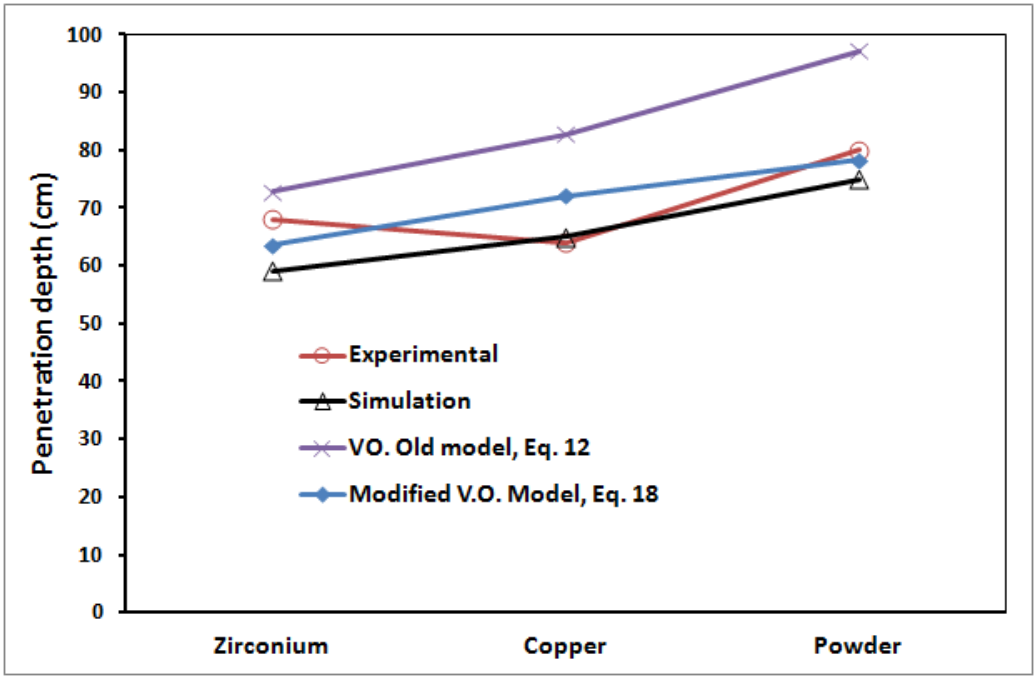

Figure 8-16 Comparison among experimental result, numerical simulation and the virtual origin model predictions for the penetration of jets with three different liners.

8.6 Summary

The density reduction of a shaped charge jet is developed during the jet formation, which has been shown experimentally and numerically in this chapter. This leads to the non-uniform distribution of the jet density and the original virtual origin penetration model is incapable of dealing with penetration of jet with non-uniform density distribution. A correlation between jet density reduction and jet velocity is proposed in this chapter, based on which an analytical solution of the modified virtual origin model is obtained. The validity of the modified virtual origin model is demonstrated by its largely improved predictions in comparison with experimental and numerical results.

CHAPTER.9 ZIRCONIUM SHAPED CHARGE JET BREAKUP TIME

9.1 Introduction:

The velocity gradient of a shaped charge jet causes the stretching of the jet after it has been formed. This leads to the axial breakup of the jet into small fragments, which can significantly decrease its penetration capability. Thus, it is necessary to predict the breakup time and the characteristics of the jet fragments.

Three approaches including hydrocode simulations, one-dimensional models and empirical formulae have been employed to predict the jet breakup time. These approaches have been summarised in Ref. [67] and discussed in Ref. [85]. Among these three approaches, the semi-empirical formula presented by Hirsch [4-5] has demonstrated its reliability and efficiency for the prediction of the breakup time of a shaped charge jet. Hirsch [5] estimated the breakup time t_b of a jet element according to:

$$t_b = \frac{2r}{\mathrm{V_{PL}}} \tag{9-1}$$

where r is the initial radius of the jet element when the jet forms, which can be measured from flash x-ray or estimated from:

$$r = \sqrt{2RT_L}\sin\left(\frac{\beta}{2}\right) \tag{9-2}$$

in which R is the initial inner radius of the liner element and β is the elemental collapse angle of the liner element calculated from jetting analysis (Pugh-Eichelberger-Rostoker model [50]). V_{PL} is a characteristic plastic velocity representing the average velocity difference between the neighbouring jet segments [5]. The physical meaning of the proposed breakup time formula in Ref.[5] is the same as the breakup time of a one-dimensional homogeneous ductile metal that undergoes a very high strain-rate deformation.

The reciprocal of V_{PL} (i.e. 1/ V_{PL}) represents the specific breakup time of a certain liner material [5]. Experimentally, V_{PL} can be measured using multiple flash x-ray units, where the position, the length, the radius and the velocity of each jet segment are determined, based on which the velocity difference between each pair of neighbouring jet segments can

be determined. In addition to the determination of breakup time, V_{PL} can also be used to calculate the total number of jet fragments (n) according to Hirsch [4]:

$$n = \frac{V_{tip} - V_{rear}}{V_{PL}} \qquad 9\text{-}3$$

where V_{tip} and V_{rear} are the jet tip and the rear velocities, respectively.

In the first part of this chapter, the parameters in Johnson-Cook (J-C) constitutive equation for the zirconium material will be calculated based on the data obtained from the tensile testing of zirconium specimens at different strain-rates and different temperatures. The second part includes the calculations of the V_{PL} for some zirconium liners based on J-C constitutive equation. The calculated V_{PL} values are implemented in a simple breakup time formula as a function of the scaled liner thickness to the charge diameter and the jet radius. The V_{PL} is calculated for shaped charge with conical zirconium liners of an apex angle of 46^o and an outer diameter of 36mm with different liner wall thickness values of 0.7, 1, 1.3, 1.7, 2, 2.3, 2.7, 3, 3.3, 3.7 and 4mm. The used explosive is HMX with a loading density of 1.891g/cm^3 and a total mass of 30.75gm. All the shaped charge jet output data were calculated using Autodyn jetting analysis, in which the elemental jet velocity and axial distances were used to calculate the jet strain-rate that was used to calculate V_{PL} using the Johnson-Cook constitutive equation.

9.2 Determination of V_{PL}

Various methods have been suggested by researchers for the calculation of V_{PL} in order to estimate the shaped charge breakup times for different liners [163].

Haugstad [86] presented a method to determine V_{PL} based on dimensional analysis of the parameters governing the jet breakup time model. The model consists of a rod of length L_o clamped at one end and moving with velocity V_o at the other end. Assuming a constant density ρ_o and constant flow stress σ_o and according to the π-theorem, only one non-dimensional number exists, i.e.

$$\psi\left(\left(\frac{\sigma_o}{\rho_o}\right)^{0.5}\left(\frac{1}{\lambda_o \eta_o}\right)\right) = Const. \qquad 9\text{-}4$$

where η_o is the strain-rate that can be calculated by $\eta_o = V_o/L_o$, $\lambda_o = \pi r_o$ is the perturbation wave length that causes the initial necking [164], r_o is the initial radius of the jet element. Thus,

$$V_{PL} = \lambda_o \eta_o = a\sqrt{\frac{\sigma_o}{\rho_o}} \qquad 9\text{-}5$$

where a=0.87 is a constant determined numerically using HEMP code [86]. Therefore, the average velocity difference between two neighbouring successive fragments, V_{PL}, is

$$V_{PL} = 0.87\sqrt{\frac{\sigma_o}{\rho}}. \qquad 9\text{-}6$$

Pfeffer [163] obtained a similar relation for V_{PL} using 2-D numerical hydrocode, i.e.

$$V_{PL} = 0.95\sqrt{\frac{\sigma_o}{\rho}}\ . \qquad 9\text{-}7$$

According to Hirsch [4], the velocity difference between the broken fragments in a copper jet is

$$V_{PL} = \sqrt{\frac{\sigma_y}{\rho}} \qquad 9\text{-}8$$

where σ_y is the dynamic yield stress of the copper material.

An alternative method to calculate V_{PL} was presented by Walters and Summers [163], where they used Kolsky's plastic velocity model to calculate the velocity difference between the particulated copper jet fragments uing different dynamic constitutive equations, which were validated against previous field measurements. The advantage of the Kolsky model is that V_{PL} is completely determined by the given constitutive equation. In addition, the V_{PL} values obtained from Kolsky model with different constitutive equations (i.e. Johnson-Cook, the modified Johnson-Cook and the Zerilli-Armstrong (Z-A) equations) are very close to the measured V_{PL} values for copper jets. Moreover, these constitutive equations contain the effect of temperature, strain-rate and grain size, which have direct effects on V_{PL} values, and hence, the breakup time. Therefore, the approach based on Kolsky model will be implemented in this study for zirconium liner using Johnson-Cook constitutive model (J-C).

Kolsky model [165] considers the equation of the plastic deformation along a wire during the wire drawing fabrication process. The plastic velocity is defined as the velocity, at which the wire would break [165]. Based on the relationships between engineering stress (strain) and true stress (strain), Walters and Summers [163] obtained the average velocity difference between two neighboring fragments, i.e.

$$V_{PL} = \frac{1}{\sqrt{\rho}}\int_0^{\varepsilon_{eN}} \sqrt{\frac{d\sigma_e}{d\varepsilon_e}}\ d\varepsilon_e\ = \frac{1}{\sqrt{\rho}}\int_0^{\varepsilon_N} \sqrt{\frac{d\sigma}{d\varepsilon} - \sigma}\ d\varepsilon \qquad 9\text{-}9$$

where ε_N is the true necking strain, σ is the true plastic stress, ε is the true strain and ρ is the initial liner density; subscript 'e' refers to engineering terms.

9.3 Calculation of the J-C constitutive equation parameters for zirconium

The Johnson-Cook constitutive equation (J-C) has been established in 1983 to study the effects of strain, strain-rate and temperature on the flow stresses for some metals and alloys [121]. The tensile test specimens of zirconium rods were machined from a cylinder of 6mm diameter and 20mm length. The strain-rates that were applied to the samples were 8×10^{-5}, 1.6×10^{-3} and 1100 s^{-1}, while the temperatures that were tested were 300 and 400K. The data published by Ramachandran et al. [166] for the zirconium material were combined with above measurements to determine the J-C parameters for zirconium. These combined experimental data extend the extrapolation ranges of temperature and strain-rate, which, however, was found to have a minor effect on the flow stresses at relatively low temperatures [166].

The temperature of 400K was chosen as the upper limit of the elevated temperature test because this temperature rise due to the severe plastic work was predicted from the Autodyn jet formation model for the zirconium liner driven by HMX explosive. The temperature calculation will be discussed in details in Section 9.4.

The general form of the J-C constitutive equation is:

$$\sigma = (A + B\varepsilon^n)(1 + Cln\dot{\varepsilon}^*)(1 - T_H^m) \qquad 9\text{-}10$$

where σ is the dynamic flow stress, ε is the effective plastic strain, A is the yield strength, B is the hardening constant, n is the hardening exponent, C is the strain-rate constant and m is the thermal exponent constant. $\dot{\varepsilon}^*$ is the normalized effective plastic strain-rate (i.e. the applied true strain-rate divided by the reference strain-rate). T_H is the homologous temperature that can be calculated by:

$$T_H = \frac{T - T_{room}}{T_{melt} - T_{room}} \qquad 9\text{-}11$$

where T_{room} is the room temperature and T_{melt} is the melting temperature of the material.

The J-C constants are calculated using the experimental data in this study together with the data reported in [166]. The general deduced J-C equation for the zirconium material is:

$$\sigma\,(MPa) = (170 + 450\varepsilon^{0.6})\left(1 + 0.01ln\frac{\dot{\varepsilon}}{\dot{\varepsilon}_o}\right)(1 - T_H^{0.5}) \qquad 9\text{-}12$$

where $\dot{\varepsilon}$ is the true dynamic strain-rate and can be calculated by:

$$\dot{\varepsilon} = \dot{\varepsilon}_e e^{-\varepsilon}, \qquad 9\text{-}13$$

in which $\dot{\varepsilon}_e$ is the engineering strain-rate and $\dot{\varepsilon}_o$ is the reference true initial strain-rate corresponding to $\dot{\varepsilon}_{eo}$=8×10^{-5} s^{-1} and can be calculated by:

$$\dot{\varepsilon}_o = 8\times10^{-5}e^{-\varepsilon}\,. \qquad 9\text{-}14$$

Thus $\frac{\dot{\varepsilon}}{\dot{\varepsilon}_{eo}} = \frac{\dot{\varepsilon}_e}{8\times10^{-5}}$, and Eq. (9-12) can be expressed as

$$\sigma\,(MPa) = (170 + 450\varepsilon^{0.6})\left(1 + 0.01ln\frac{\dot{\varepsilon}_e}{8\times10^{-5}}\right)(1 - T_H^{0.5})\,. \qquad 9\text{-}15$$

Eq. (9-15) is used to calculate the plastic stress-strain curves for the three test specimens as depicted in Figure 9-1 with their measured curves. It can be concluded that the presented J-C constitutive equation can reasonably predict the plastic behavior of the zirconium material up to the true strain of 0.40. The flow stresses calculated using J-C Eq. (9-15) are quite similar to those calculated by Ref. [166], apart from the grain size effect that is included only in Z-A model.

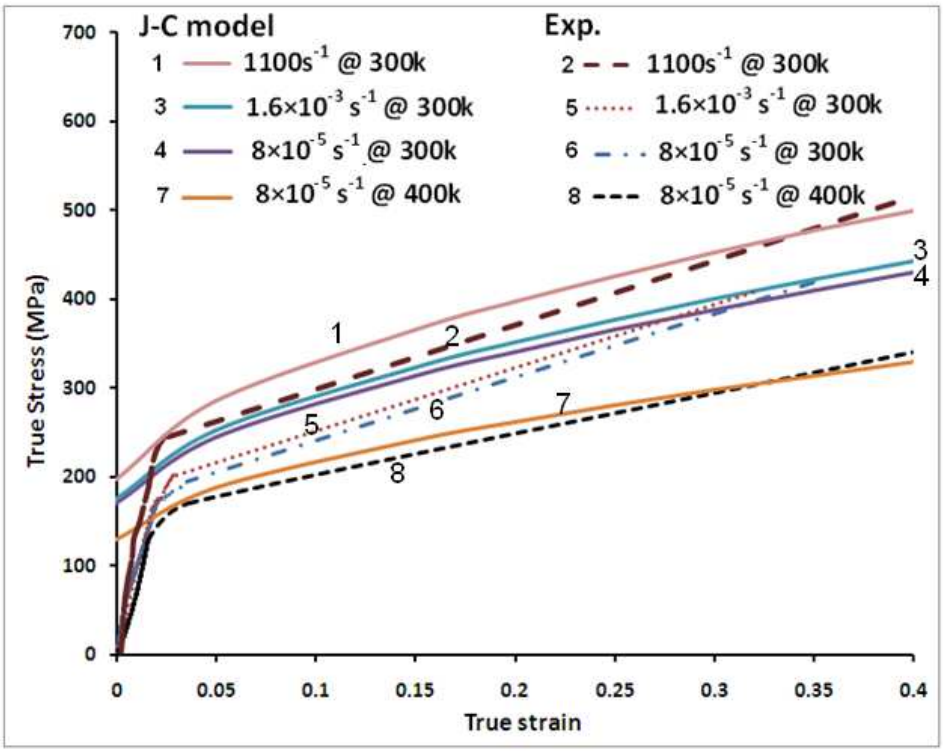

Figure 9-1 The measured and the calculated stress-strain curves for the four zirconium test specimens.

9.4 The jet temperature estimation

Von Holle and Trimble [167] measured the temperatures of shaped charge copper jets with Composition B explosive charges. The charge diameter was 81.3mm. The jet temperatures were measured at travelling distance of eight times this diameter. The measured average temperature was 432^{o}C with a standard deviation of 76 ^{o}C. Racah [14] investigated analytically the three different mechanisms of the liner heating when the liner collapsed to form a jet and when this jet is stretched. The first mechanism is the liner heating by the detonation wave as it grazes the liner. The calculated temperature for this mechanism is 30K for the copper liner. The second mechanism is the liner heating during the liner collapse process while the third one is the jet heating during its elongation. In order to find the zirconium jet temperature, Autodyn was used in this study to simulate shaped charge jet formation, in which the Mei-Gruneisen thermodynamic model based on shock equation of state was employed. Since the first mechanism only causes a small increase of temperature, it focuses on the jet heating due to severe plastic work of the jet rather than the heat transfer from the detonated explosive products to the jet material [164]. To validate and verify the hydrocode results for the jet temperature calculations, the shaped charge BRL-81.3 [168] was modelled using the jet formation simulation algorithm, during which the jet temperature was recorded at different times. It was assumed that the plastic deformation is continuous and smooth along the jet until its breakage, while the total jet heating due to these mechanisms was considered. The jet temperature was found to vary in the hoop direction along the crossection area of the jet. However, the absolute value of 780 K (i.e 482^{o}C+25^{o}C) is observed to be common along the jet profile, while the experimental measurement showed a temperature increase of 428^{o}C (i.e. 701K) using Composition B explosive. This means that the zirconium jet temperature can be reasonably predicted using hydrocode.

The OWP shaped charges with zirconium liners of different thicknesses were modelled in the same way and their jets were allowed to elongate up to 3 times its diameter. The jet temperatures were investigated over the entire jet length. From the produced jet temperature contours depicted in Figure 9-2 for the zirconium liner with thickness of 1.7mm, it can concluded that the temperature is not constant over the extended zirconium jet and its slug, but ranges between 425K and 402K at the rear and the tip of the jet, respectively. The jet elements were found to have the same temperature gradient when the jet is allowed to elongate to a distance of seven times the charge diameter. This means that the jet temperature can be assumed to be approximately constant from the time of jet

collapse on the liner axis to the moment when the jet breaks up. Walters and Summers [163] assumed an isothermal deformation of copper shaped charge jets in a similar attempt to calculate the V_{PL} for copper jet. The assumption gave very accurate results of V_{PL} using different constitutive equations when compared with the experimentally measured values for a range of shaped charges. Thus, it is reasonable to assume a homogeneous distribution of jet temperature and an isothermal process during the jet stretching.

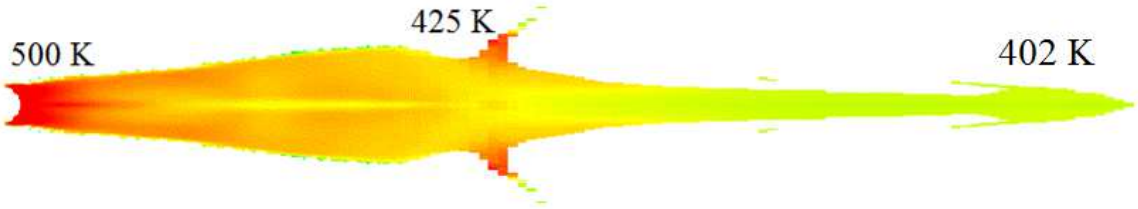

Figure 9-2 The zirconium jet temperature contours at the moment of jet formation for the zirconium liner with a wall thickness of 1.7mm.

9.5 Results

9.5.1 Calculations of the necking strain and V_{PL} using J-C constitutive equation

The J-C constitutive equation is used to calculate V_{PL} using the true stress and strain in Eq.(9-12). Assuming that velocity variables of both the jet tip and its slug remain unchanged during the stretching process, the engineering strain-rate will be independent of strain, and therefore $d\dot{\varepsilon}_e/d\varepsilon_e$ equals zero. Besides, it has been shown that the jet stretching deformation process is isothermal (i.e. $\frac{dT_H^m}{d\varepsilon} = 0$). Therefore, differentiation of J-C Eq. (9-10) gives:

$$\frac{d\sigma}{d\varepsilon} = (Bn\varepsilon^{n-1})\left(1 + Cln\frac{\dot{\varepsilon}_e}{\dot{\varepsilon}_{eo}}\right)(1 - T_H^m). \qquad 9\text{-}16$$

Since $\frac{\dot{\varepsilon}}{\dot{\varepsilon}_{eo}} = \frac{\dot{\varepsilon}_e}{8\times10^{-5}}$, thus

$$\frac{d\sigma}{d\varepsilon} = (Bn\varepsilon_P^{n-1})\left(1 + Cln\frac{\dot{\varepsilon}_e}{8\times10^{-5}}\right)(1 - T_H^m). \qquad 9\text{-}17$$

Applying the stability condition in order to calculate the necking strain (ε_N), i.e. $\frac{d\sigma}{d\varepsilon} = \sigma$, which leads to

$$(Bn\varepsilon_N^{n-1})\left(1+Cln\frac{\dot{\varepsilon}_e}{\dot{\varepsilon}_{eo}}\right)(1-T_H^m)=(A+B\varepsilon_N^n)\left(1+Cln\frac{\dot{\varepsilon}_e}{\dot{\varepsilon}_{eo}}\right)(1-T_H^m) \quad 9\text{-}18$$

or $$(Bn\varepsilon_N^{n-1})=(A+B\varepsilon_N^n) \quad 9\text{-}19$$

according to Eqns.(9-10) and (9-17).

The solution of this equation gives the values of the maximum necking strain ε_N, at which the V_{PL} will be estimated. Substitute the values of the J-C constants into Eq. (9-19), we have $0.6\varepsilon_N^{-0.4}-\varepsilon_N^{0.6}=0.378$.

The necking strain is ε_N=0.351, which is independent of strain-rate and temperature of the jet. The velocity difference between the jet fragments can be calculated using Eq.(9-9) based on true stress and true strain

$$\frac{d\sigma}{d\varepsilon}-\sigma=\left((Bn\varepsilon_P^{n-1})-(A+B\varepsilon^n)\right)\left(1+Cln\frac{\dot{\varepsilon}_e}{\dot{\varepsilon}_{eo}}\right)(1-T_H^m)\,; \quad 9\text{-}20$$

$$V_{PL}=\frac{1}{\sqrt{\rho}}\int_0^{\varepsilon_N}\sqrt{\left((Bn\varepsilon^{n-1})-(A+B\varepsilon^n)\right)\left(1+Cln\frac{\dot{\varepsilon}_e}{\dot{\varepsilon}_{eo}}\right)(1-T_H^m)}\ \mathrm{d}\varepsilon\,; \quad 9\text{-}21$$

$$V_{PL}=\sqrt{\frac{B(1-T_H^m)\left(1+Cln\frac{\dot{\varepsilon}_e}{\dot{\varepsilon}_{eo}}\right)}{\rho}}\int_0^{0.351}\sqrt{(n\varepsilon^{n-1})-\left(\varepsilon^n+\frac{A}{B}\right)}\ \mathrm{d}\varepsilon\,. \quad 9\text{-}22$$

The integration is done using the area under the curve over the strain range from 0 to 0.351. The area was found to be 0.265.

Substituting the values of the J-C parameters, the velocity difference between two neghibouring zirconium fragments is calculated by

$$V_{PL}=0.265\sqrt{\frac{450\times10^6\left(1-T_H^{0.5}\right)\left(1+0.01ln\frac{\dot{\varepsilon}_e}{8\times10^{-5}}\right)}{6500}} \quad 9\text{-}23$$

Table 9-1 lists the shaped charge parameters related to the jet breakup using the output data from the jetting analysis. The engineering strain rate $\dot{\varepsilon}_e$ can be calculated as follow:

$$\dot{\varepsilon}_e=\frac{V_{tip}-V_{rear}}{L_{jet}}, \quad 9\text{-}24$$

where L_{jet} is the jet length; V_{tip} and V_{rear} are the jet tip and slug velocities, respectively.

The calculated V_{PL} values and the number of fragments are also listed in Table 9-1. The melting temperature of the zirconium material is 1852^{o}C [169], while the reference temperature was taken to be 300K.

Table 9-1 Shaped charge parameters related to the jet breakup for the studied zirconium liners with different liner wall thicknesses

T_L (mm)	0.7	1	1.3	1.7	2	2.3	2.7	3	3.3	3.7	4
CD (mm)	36	36	36	36	36	36	36	36	36	36	36
T_L/CD	0.019	0.027	0.036	0.047	0.055	0.063	0.075	0.083	0.091	0.102	0.111
V_{tip} (m/s)	7307	6879	6634	6262	5928	5647	5352	5131	4905	4661	4496
V_{slug} (m/s)	4872	2721	1477	1338	1239	1155	1073	1226	441	414	395
Initial jet length L_{jet} (mm)	44.0	61.8	67.1	56.4	45.2	41.5	35.0	32.4	29.8	28.7	26.9
Liner Mass (g)	9.89	15.8	20.9	26.9	31.4	35.6	40.5	44.2	47.6	52.2	54.9
Jet mass (g)	2.01	3.57	4.69	5.49	6.09	6.63	7.32	7.17	9.31	9.88	9.93
Jet KE (kJ)	47.2	53.4	52.2	49.1	46.7	44.3	40.7	38.3	34.5	31.5	29.3
Jet temp. (K)	450	430	416	402	390	380	365	355	347	340	330
V_{PL} (m/s)	64.6	65.5	66.2	66.9	67.6	68.2	69.1	69.7	70.3	70.8	71.7
1/ V_{PL} (μs/mm)	15.5	15.3	15.1	14.9	14.8	14.7	14.5	14.3	14.2	14.1	13.9
No. of fragments	38	63	78	73	69	66	62	56	63	60	57

Note: T_L is the liner thickness and CD is the charge diameter.

The calculated velocity difference between the zirconium jet fragments is compared with that of the copper material measured by Hirsh [5], as shown in Figure 9-3. It shows that, at a certain value of T_L/CD, the zirconium material has lower V_{PL} values, which means that the zirconium jet has a longer time of elongation before its breakup. Therefore the zirconium liner showed a remarkable increase in its ductility when compared with copper liner. Two experimental measurements of the velocity difference between the zirconium jet fragments (V_{PL}) were 64.3 and 74.9m/s, respectively, according to Bourne et al.[13], which are close to the calculated values as shown in Figure 9-3. Bourne et al experiments to measure the V_{PL} values were carried out using 2 x-ray radiography pictures at two times in the range of 1000μs and about 50 μs apart.

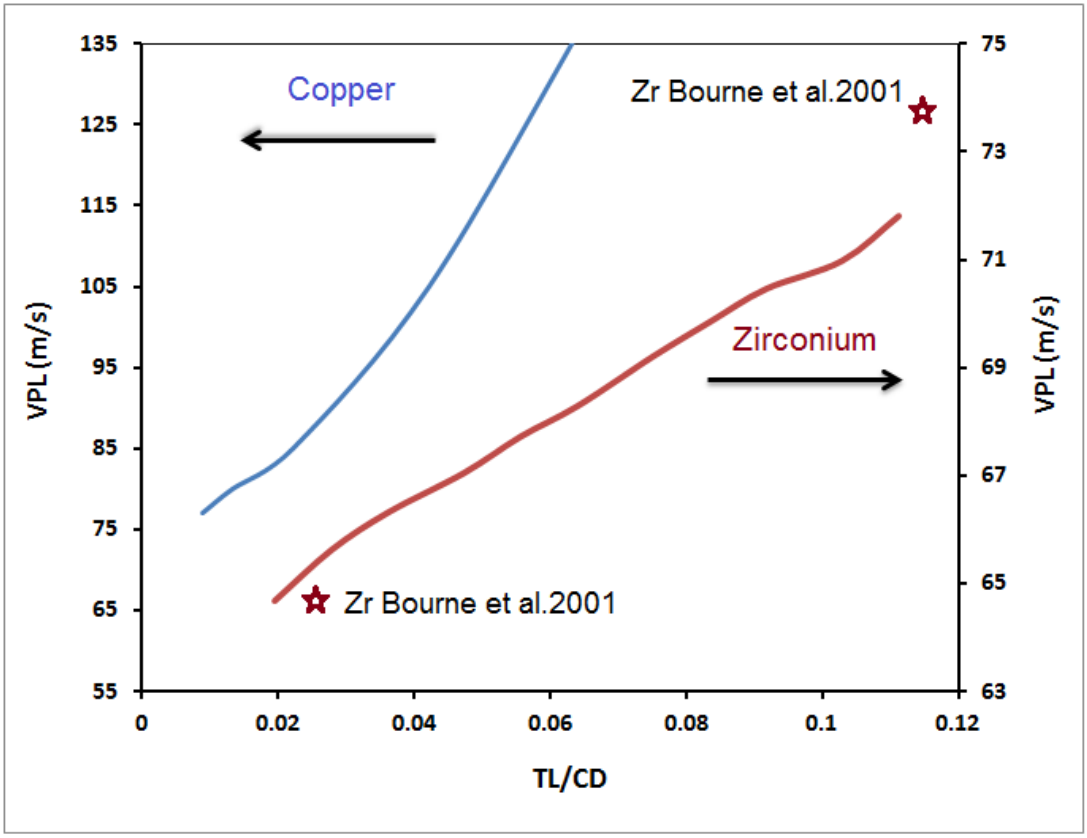

Figure 9-3 The velocity difference between the jet fragments for different T_L/CD values for both copper and zirconium jets.

Since the specific breakup time is considered as a characteristic property for a given shaped charge with a certain liner thickness, the obtained V_{PL} values and the scaled (T_L/CD) values are correlated as depicted in Figure 9-4 for zirconium material with copper material as a baseline. The relation for zirconium is almost linear and can be described by

$$\frac{1}{V_{PL}} = 15.71 - 16.169\left(\frac{T_L}{C_D}\right). \qquad 9\text{-}25$$

which is a similar to that proposed by Hirsch [5] for the copper material, which is

$$\frac{1}{V_{PL}} = 13.886 - 101.149\left(\frac{T_L}{C_D}\right). \qquad 9\text{-}26$$

Eqns. (9-25) and (9-26) have the same linear form, but the slope of Eq. (9-25) is much smaller than that of Eq. (9-26). Therefore, for a given value of T_L/CD, zirconium can achieve higher ductility than copper, which agrees with the experimental observations in Bourne et al. [13].

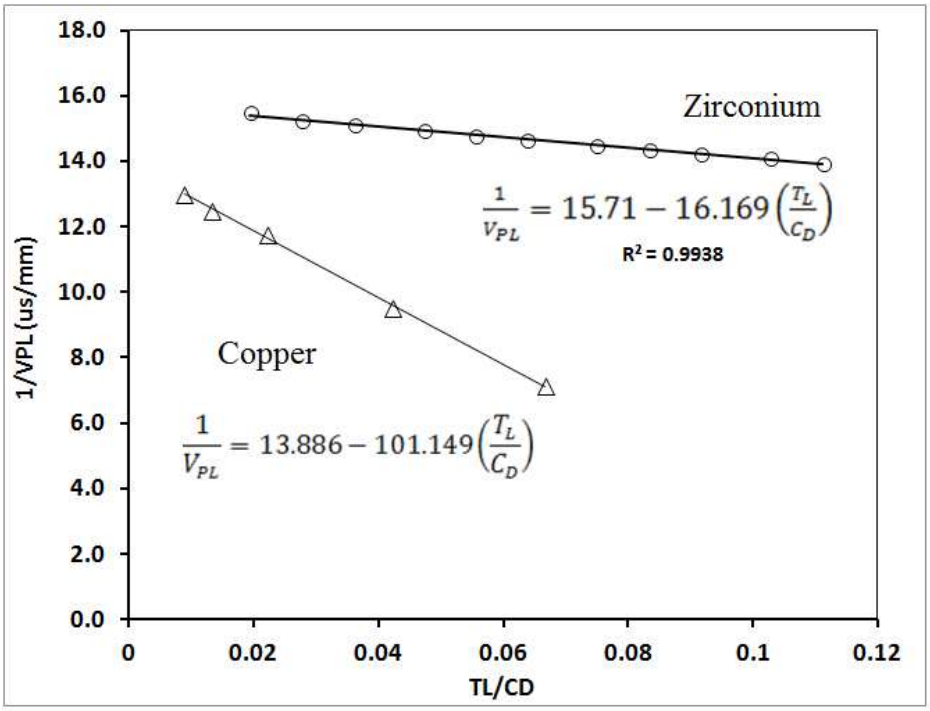

Figure 9-4 The specific breakup time ($1/V_{PL}$) as a function of the scaled value (T_L/CD) for zirconium and copper [5].

The importance of Eq.(9-25) is that it gives a direct method to estimate the specific elemental breakup time if T_L and CD are known for a zirconium shaped charge. The reciprocal of V_{PL} (i.e. $1/V_{PL}$) represents the liner specific breakup time per 1mm of jet length (i.e. μs/mm) and can be used directly to calculate the breakup time of a shaped charge jet according to Eq.(9-1), i.e.

$$t_b = 2r\left(15.71 - 16.169\left(\frac{T_L}{C_D}\right)\right) \qquad 9\text{-}27$$

where the initial jet element radius r can be measured from flash x-ray or calculated using Eq.(9-2), in which the collapse angle β is obtained from the jetting analysis. If $1/V_{PL}$ is in μs/mm and the radius r is in mm, then the breakup time will be in μs. The calculated jet tip radii and their breakup times for the four OWPs are shown in Table 9-2. This table shows the clear difference among the four liners in their jet tip radius and their breakup times although they have the same charge design except the liner thickness. Generally the higher the jet velocity of the liner element, the lower the breakup time of this element.

Table 9-2 The jet tip radius and jet breakup time for zirconium OWPs.

T_L (mm)	1	1.3	1.7	2
V_{tip} (m/s)	7879	7634	7262	6928
Jet tip radius (mm)	1.135	1.25	1.765	1.84
Breakup time (μs)	34.5	38.15	52.59	54.5

9.6 Summary

- The J-C constitutive equation constants are determined for the zirconium material and used to estimate the characteristic V_{PL} for some zirconium OWPs.

- The specific breakup time of the liner material, which is the reciprocal of the velocity difference between the particulated jet fragments, is calculated for zirconium shaped charge liners and found to be in the range of 64.6 to 71.7 m/s for the liner wall thickness ranges between 0.7 and 4mm, respectively.

- The breakup time of zirconium shaped charges is presented, by which the breakup time can simply be calculated by the jet radius and the scaled T_L/CD values.

CHAPTER.10 CONCLUSIONS AND RECOMMENDATIONS FOR FUTURE STUDIES

10.1 Introduction

This research covers a wide range of parametric studies based on Autodyn hydrocode and experiments for a range of OWPs with different liner materials and different shapes in order to investigate the characteristics of the produced jets and their penetration capabilities.

10.2 Conclusions

The following findings have been observed:

- The jetting analysis validation showed that the difference between the measured tip velocity and the numerical simulation is only 1.34%, while the difference between the measured and the calculated penetration depth was only 1.6%, which means that Autodyn can be used effectively in the jetting analysis and jet penetration.
- The produced jet tip velocity of an OWP has nearly the same value as the detonation velocity of the used explosive and is about 2.5 times the Gurney velocity of the explosive.
- The optimum design of a shaped charge with liner thickness of 1.5mm, cone apex angle of 56^{o} and total RDX mass of 26g can achieve 100cm depth of penetration into 35MPa concrete.
- Behind 20mm water stand-off distance, the penetration depth of OWP begins to decrease dramatically due to water resistance and jet erosion.
- Increasing the OWP steel charge casing from 1 to 8mm can increase the jet tip velocity by 800m/s.
- A simple empeical relation was presented to estimate the Gurney velocity of an explosive material in terms of its C-J pressure and its impulse. The maximum difference between the Gurney velocity calculated by this relation and that found in the survey for a range of explosive materials was 5.48%.
- Allison-Vitalli formula (i.e. VO model) of jet penetration depth is modified to include the target strength effect using Johnson's damage number and the confinement pressure effect using the Drucker-Prager model. The penetration reduction correction terms due to the consideration of concrete strength were found

to be 0.14 and 0.29 for the concrete targets with unconfined compressive strength of 26 and 55 MPa, respectively.

- The critical collapse angle as a function of flow velocity was calculated numerically and analytically for the zirconium liner material to determine the coherency of shaped charge jet. Four zirconium OWP liners with different shapes were studied and found to produce coherent jets. The bi-conical liner exhibited the largest penetration depth into target, which is 22% greater than that of the baseline conical zirconium liner.
- It was demonstrated that jet density reduction should be considered in the study of jet penetration. A modified VO penetration model based on non-uniform jet density is presented in this research, where the penetration reduction due to the jet density reduction was found to be 12.5, 12.8 and 19.4% for the zirconium, copper and copper-tungsten jets, respectively.
- The characteristic V_{PL} for some zirconium OWPs with different liner wall thicknesses ranging between 0.7 and 4mm, respectively, was calculated. It was found to be in the range of 64.6 to 71.7 m/s for the liner wall thickness ranges between 0.7 and 4mm, respectively. The V_{PL} was found to increase linearly with the increase in the liner wall thickness. For a given value of scaled liner thickness to the charge diameter (T_L/C_D), zirconium can achieve higher ductility than copper.
- A simple breakup time relation for zirconium OWPs is presented based on the characteristic V_{PL}, and the jet radius.

10.3 Future work

The following future research studies may be pursued:

- The proposed modified VO model has ignored target compressibility. Further study should be performed to assess whether the target compressibility during the jet penetration has a significant effect on the jet penetration.
- The homogeneity of the powder liner density may be largely improved using alternative pressing methods (e.g. cold/hot isostatic pressing), which is very important for the formation of a high quality jet.
- Other manufacturing processes could be further improved. For example, spinning techniques could be used to replace the current deep drawing method. Automatic filling and testing facilities may be used to replace the current manual filling, pressing and detonating procedures to reduce the variation and uncertainty.

- Jet density reduction and non-uniform distribution should be further investigated using more accurate instantaneous jet density measurement and numerical tools.
- Dynamic behavior of zirconium in a wider range of temperature and strain-rate should be tested to increase the accuracy and reliability of the zirconium J-C model.
- The zirconium jet temperature was estimated numerically. Reliable measurements of jet temperature are needed to validate the hydrocode.

REFERENCES

[1] L. Zernow, The density deficit in stretching shaped charge jets. *International Journal of Impact Engineering*, **1997**. *20***,** 6–10, p. 849-859.

[2] F. E. Allison and R. Vitali, *A New method of computing penetration variables for shaped charge jets*, Ballistic Research Laboratory Report No. 1184, **1963.**

[3] G. R. Cowan and A. H. Holtzman, Flow configurations in colliding plates: explosive bonding, *Journal of Applied Physics*, **1963**. *34*, 4, p. 928-939.

[4] E. Hirsch, A Formula for the shaped charge jet breakup-time. *Propellants, Explosives, Pyrotechnics*, **1979**. *4*, 5, p. 89-94.

[5] E. Hirsch, Scaling of the shaped charge jet breakup time. *Propellants, Explosives, Pyrotechnics*, **2006**. *31*, 3, p. 230-233.

[6] W. P. Walters and J. Zukas, *Fundamentals of shaped charge*. Wiley Interscience Publication, New York, **1989**.

[7] A. Schwartz, M. Kumar, and D. Lassila, Analysis of intergranular impurity concentration and the effects on the ductility of copper-shaped charge jets. *Journal of Metallurgical and Materials Transactions A*, **2004**. *35***,** 9, p. 2567-2573.

[8] E. Tamer, The factors affecting the performance of explosive reactive Armours. **2004**, *Master of Science Thesis*, Military Technical College: Cairo, Egypt.

[9] C. E. Joachim, *Rapid runway cutting with shaped charges*, Technical Report No. ADP001712, **1983**.

[10] N. J. Schoeneberg, Generation of transient antennas using cylindrical-shaped charges. Master Thesis, Texas Tech. University. **2003.**

[11] W. H. Lee, Oil well perforator design using 2D Eulerian code. *International Journal of Impact Engineering*, **2002**. *27*, 5, p. 535-559.

[12] S. L. Renfre, Liner and improved shaped charge especially for use in a well pipe perforating gun. Patent. US No. 5,509,356, **1996.**

[13] B. Bourne, K. G. Cowan, J. P. Curtis, Shaped charge warheads containing low melt energy metal liners, *Proceedings of the 19th International Symposium on Ballistics*. Switzerland**, 2001.**

[14] E. Racah, Shaped charge jet heating, *Propellants, Explosives, Pyrotechnics*, **1988**. *13*, p. 178-182.

[15] Z. Bogdan and W. Zenon, Formation of jets by shaped charges with metal powder liners, *Propellants, Explosives, Pyrotechnics*, **2008,** *33*, 6, p. 482-487.

[16] L. A. Glenn, J. B. Chase, J. Barker, D. J. Leidel, Experiments in support of pressure enhanced penetration with shaped charge perforators. *18th International Symposium & Exhibition on Ballistics*, San Antonio, TX, **1999**.

[17] D. Davinson and D. Pratt, A hydrocode-designed well perforator with exceptional performance, *17th International Symposium on Ballistics*. **1998**. Midrand, South Africa, p.1-9.

[18] M. Held, Determination of the material quality of copper shaped charge liners. *Propellants, Explosives, Pyrotechnics*, **1985**. *10*, 5, p. 125-128.

[19] W. P. Walters and D. R. Scheffler. A Method to increase the tip velocity of a shaped charge jet. *23rd International Symposium on Ballistics,* **2007**. Tarragona, Spain, p. 135-144.

[20] M. Held, Hydrodynamic theory of shaped charge jet penetration. *Journal of Explosives and Propellants.* Taiwan, **1991**. *7*.

[21] E. Tamer and L. Q.M., Parametric analysis of the penetration performance of shaped charges used as oil well perforators, *41st International. ICT-Conference*. **2010**, Karlsruhe, Germany.

[22] M. H. Keshavarz and S. Abolfazl, The simplest method for calculating energy output and Gurney velocity of explosives, *Journal of Hazardous materials,* **2006**, *131*, 1-3, p.1-5.

[23] T. Urbanski, M. Jureki and S. Laverton, Chemistry and Technology of Explosives. Vol. 1. Pergamon Press Oxford, UK, **1964**.

[24] D. J. Leidel and J. P. Lawson, *High performance powder metal mixtures for shaped charge liners*. **2001**, US Patent No. US7,811,354,B2.

[25] H. Elwany, *The use of polymer bonded explosives in improved linear shaped charge designs*, PhD Thesis, Cranfield University, U.K. **1994.**

[26] P.R.C. Green. *Ammunition for the Land Battle*. UK: BRASSEY'S, 4th Edition. Vol. 4. **1990**.

[27] P. Y. Chanteret and A. Lichtenberger, About varying shaped charge liner thickness. *17th International symposium on ballistics*. **1998**, Midrand, South Africa.

[28] M. Defourneaux, *Theorie hydrodynamique des charges creuses.* Mememorial d'Artillerie Francaise, **1970**. *44*, 2.

[29] J. Brown, P. J. Edwards and P. R. Lee, Studies of shaped charges with built-in asymmetries. Part II: Modelling. *Propellants, Explosives, Pyrotechnics*, **1996**. *21*, 2, p. 59-63.

[30] M. Moyses, Penetration by shaped charge jets with varying off-axis velocity distributions. *17th International Symposium on Ballistics*, **1998**. Midrand, South Africa.

[31] M. Held, Liners for shaped charges, *Journal of Battlefield Technology*, **2001,** *4*, 3, p. 1.

[32] W. Guo, S. K. Li, F. C. Wang and W. M. Wang, Dynamic recrystallization of tungsten in a shaped charge liner. Scripta Materialia, **2009**. *60*, 5, p. 329-332.

[33] T. F. Wang, and H. R. Zhu, Copper-Tungsten shaped charge liner and its jet. *Propellants, Explosives, Pyrotechnics*, **1996**. *21*, 4, p. 193-195.

[34] B. Bourne, P. Jones and K. G. Cowan, Grain crystallographic texture effects on the performance of shaped charges. *International Symposium on Ballistics*, **1993**. Quebec, Canada.

[35] V. Y. Gertsman, M. Hoffmann, H. Gleiter and R. Birringer, The study of grain size dependence of yield stress of copper for a wide grain size range. Acta Metallurgica et Materialia, **1994**. *42*, 10, p. 3539-3544.

[36] M. Meyers, U. Andrade, and A. Chokshi, The effect of grain size on the high-strain, high-strain-rate behavior of copper. *Metallurgical and Materials Transactions A*, **1995**. *26*, 11, p. 2881-2893.

[37] S. Fujiwara and K. Abiko, Ductility of ultra high purity copper, *Journal de physique* **1995**. *5*, (Colloque C7), p. 111.

[38] F. J. Zerilli and R. W. Armstrong, Constitutive relations for the plastic deformation of metals. *American Institute of Physics, API Conference proceeding*, **1994**, *309*, p. 989-992.

[39] J. P. Curtis, A Breakup model for shaped charge jets. *16th International Symposium on Ballistics.* **1996**. San Francisco.

[40] W. H. Tian, A. L. Fan, H. Y. Gao, J. Luo and Z. Wang, Comparison of microstructures in electroformed copper liners of shaped charges before and after plastic deformation at different strain-rates. *Materials Science and Engineering* A, **2003**. *350*, (1-2), p. 160-167.

[41] L. Lu, S. X. Li, and K. Lu, An abnormal strain-rate effect on tensile behavior in nanocrystalline copper. Scripta Materialia, **2001**. *45*, 10, p. 1163-1169.

[42] J. W. Reese and A. Hetz, *Coated metal particles to enhance oil field shaped charge performance*. **2001**, US Patent No. US 2002/0178962 A1.

[43] Y. Liu and Z. Shen, Numerical simulation on formation and penetration target of powder metal shaped charge jet, *International Conference on Computer Application and System Modelling (ICCASM)*, **2010**, 9, p. 518-521.

[44] W. P. Walters, P. Peregino, R. Summers and D. Leidel, *A Study of jets from un-sintered powder metal lined non-precision small calibre shaped charge*, Army Research Lab. Report No. ARL-TR-2391, **2001.**

[45] E. Bakker, K. Veeken, L. Behrmann, P. Milton, G. Shirton, A. Salsman and I. Walton, *The new dynamics in underbalanced perforating*. Oilfield Review, *15*, 4, **2003**.

[46] B. Grove, J. Heiland and I. Walton, Geologic materials' response to shaped charge penetration. *International Journal of Impact Engineering*, **2008**. *35*, 12, p. 1563-1566.

[47] C. Ö. Karacan, and P.M. Halleck, Comparison of shaped-charge perforating induced formation damage to gas- and liquid-saturated sandstone samples. *Journal of Petroleum Science and Engineering*, **2003**. *40*, 1-2, p. 61-75.

[48] Y. Luo, and Z. Shen, Study on orientation fracture blasting with shaped charge in rock. *Journal of University of Science and Technology Beijing, Mineral, Metallurgy and Material*, **2006**. *13*, 3, p. 193-198.

[49] G. Birkhoff, D. P. MacDougall, E. M. Pugh, and G. Taylor, Explosives with lined cavities, *Journal of Applied Physics*, **1948,** *19*, 6, p. 563-582.

[50] E. M. Pugh, R.J. Eichelberger and N. Rostoker, Theory of jet formation by charges with lined conical cavities, *Journal of Applied Physics*, **1952**. *23*, 5, p. 532-536.

[51] S. K. Godunov, A. A. Deribas and V. I. Mali, Influence of material viscosity on the jet formation process during collisions of metal plates. *Combustion, Explosion and Shock Waves*, **1975**. *11*, 1, p. 1-13.

[52] W. P. Walters, *Influence of material viscosity on the theory of shaped-charge jet formation*. Memorandum Report No. ARBRL-MR-02941, **1979**.

[53] E. Hirsch, A simple representation of the Pugh, Eichelberger, and Rostoker solution to the shaped charge jet formation problem," *Journal of Applied Physics*, **1979**. *50*, p. 4667-4670.

[54] G. X. Liu, The simplified model for predicting shaped charge jet parameters, *Propellants, Explosives, Pyrotechnics*, **1995**. *20*, 5, p. 279-282.

[55] E. F. Allison and R. Vitalli, *An application of the jet-formation theory to a 105mm shaped charge*. BRL Technical Report No. MD AD0277458, **1962**.

[56] R. J. Eichelberger, Re-examination of the nonsteady theory of jet formation by lined cavity charges. *Journal of Applied Physics*, **1955**. *26*, 4, p. 398-402.

[57] J. Carleone, P. C. Chou and C. A. Tanzio, One-dimensional computer code to model shaped charge liner collapse, jet formation and jet properties. **1975**, Dyna East corporation.

[58] G. Randers-Pehrson, An improved equation for calculating fragment projection angle. *International Symposium on Ballistics*. **1976**. Daytona Beach, FL.

[59] L. Behrmann and N. Birnabum, *Calculation of shaped charge jets using Engineering approximations and finite difference computer codes*. Technical Report No. AFATL-TR-73-160, **1973**.

[60] J. Carleone, Mechanics of shaped charges, M. Baltimore, Editor. **1987**, Computational Mechanics Associates.

[61] R. Gurney, *The initial velocities of fragments from Bombs, shell and grenades*. Aberdeen Proving Ground, Ballistic Research Lab. Report No. Md. BRL-405, **1943**.

[62] L. H. Thomas, Theory of the explosion of cased charges of simple shape. **1944**.

[63] T. Sterne, *A Note on the initial velocities of fragments from warheads*. Technical Report No. BRL-648, September, **1947**.

[64] P. Y. Chanteret, An analytical model for metal acceleration by grazing detonation. *7th International Symposium on Ballistics.* **1983**. Hague, Netherlands.

[65] J. E. Kennedy, *Gurney energy of explosives: estimation of the velocity and impulse imparted to driven metal*, Technical Report No. SC-RR-70-790. **1970**.

[66] G. E. Jones, J. E. Kennedy, and L.D. Bertholf, Ballistics calculations of R.W. Gurney. *American Journal of Physics*, **1980**. *48*: p. 264-269.

[67] P. C. Chou and W.J. Flis, Recent developments in shaped charge technology. *Propellants, Explosives, Pyrotechnics*, **1986**. *11*, 4, p. 99-114.

[68] G. E. Duvall and J. O. Erkman and C. M. Ablow, Explosive acceleration of projectiles. *Israel Journal of Technology*, **1969,** *7*, *6*, p. 469.

[69] L. A. Shushko, B. I. Shekhter and S. L. Krys'kov, Bending of a metal strip by a sliding detonation wave. *Combustion, Explosion, and Shock Waves*, **1975**. *11*, 2, p. 229-236.

[70] E. Hirsch, Improved Gurney formulas for exploding cylinders and spheres using "Hard Core" Approximation. *Propellants, Explosives, Pyrotechnics*, **1986**. *11*, 3, p. 81-84.

[71] P. C. Chou, Improved formulas for velocity, acceleration, and projection angle of explosively driven liners. *Propellants, Explosives, Pyrotechnics*, **1983**. *8*, 6, p. 175-183.

[72] A. Koch, N. Arnold, and M. Estermann, A simple relation between the detonation velocity of an explosive and its Gurney energy. *Propellants, Explosives, Pyrotechnics*, **2002**. *27*, 6, p. 365-368.

[73] I. G. Henry, *The Gurney formula and related approximations for the high-explosive deployment of fragments.* Report No. PUB-189, Aerospace Group, Hughes Aircraft Corporation, California, **1967**.

[74] M. Held, Plate velocities for asymmetric sandwiches. *Propellants, Explosives, Pyrotechnics*, **1997**. *22***,** 4, p. 218-220.

[75] A. Deribas, Physics of explosive work hardening and welding, N. Nauka, Editor. **1972**.

[76] H. R. Kleinhanss, Experimentelle untersuchungen zum kol- iapsprozeb bei hohlladungen. *Proceedings of The 3rd International Symposium on Military Applications*. **1971**. FRG.

[77] V. F. Lobanov, Numerical simulation of flow during compression of cylindrical samples by a glancing detonation wave. *Journal of Applied Mechanics and Technical Physics*, **1975**. *16*, 5, p. 795-798.

[78] Y. A. Gordopolov, A. N. Dremin and A. N. Mikhailov, Experimental determination of the dependence of the wavelength on the angle of collision in the process of the

explosive welding of metals. *Combustion, Explosion, and Shock Waves*, **1976**. *12*, 4, p. 545-549.

[79] A. Deribas and I. Zakharenko, Surface effects with oblique collisions between metallic plates. *Combustion, Explosion, and Shock Waves*, **1974**. *10***,** 3, p. 358-367.

[80] D. P. Bauer and S. J. Bless, *Strain-rate effects on ultimate strain of copper*. Technical Report No. AFML-TR-79-4021, **1979.**

[81] P. C. Chou and Carleone, *Calculation of shaped charge jet strain, radius and breakup time*. Technical Report No. BRL-CR-246, **1975**.

[82] J. M. Walsh, R. G. Shreffler and F. J. Willig, Limiting conditions for jet formation in high velocity collisions, *Journal of Applied Physics*, **1953**. *24*, 3, p. 349-359.

[83] P. C. Chou, J. Carleone and R. R. Karpp, Criteria for jet formation from impinging shells and plates, *Journal of Applied Physics*, **1976**. *47*, 7, p. 2975-2981.

[84] A. Cowan, Hydrocode and analytical code modeling of the effect of liner material grain size on shaped charge jet breakup parameters. *17th International Symposium on Ballistics*. **1998**. Midrand, South Africa.

[85] E. Hennequin, Modelling of the shaped charge jet breakup. *Propellants, Explosives, Pyrotechnics*, **1996**. *21*, 4, p. 181-185.

[86] B. Haugstad, On the breakup of shaped charge jets. *Propellants, Explosives, Pyrotechnics*, **1983**. *8*, 4, p. 119-120.

[87] G. Pfeffer, Determination par simulations numtriques de L'etat et des lois de fragmentation des jets de charges Creusses " *5th International Symposium on Ballistics*, **1980**. Toulouse, France.

[88] P. C. Chou and J. Carleone, A One dimensional theory to predict the strain and radius of shaped charge jets. *Proceeding of the first International Symposium on Ballistics*. **1974**. Orlando, FL.

[89] P. C. Chou and J. Carleone, Breakup of shaped charge jet. *2nd International Symposium on Ballistics*. **1976**. Daytona Beach, USA.

[90] R. Karpp and J. Simon, *An estimate of the strength of a copper shaped charge jet and the effect of strength on the breakup of a stretching jet*. US Army Ballistic Research Lab., BRL Report, **1976**.

[91] C. Miller, A New approach to the numerical analysis of shaped charge jets. *Proceedings of the 6th International Symposium on Ballistics*. **1981**. Orlando, FL.

[92] C. Miller, Generation of necks in an elongated shaped charge jet. *Proceedings of The BRL Symposium on Ballistics, ADPA*. **1982**.

[93] J. Carleone and P. C. Chou, *Shaped charge jet stability and penetration calculations*. Technical Report No. ADA050117, **1977**.

[94] J. M. Walsh, Plastic instability and particulation in stretching metal jets. *Journal of Applied Physics*, **1984**. *56*, 7, p. 1997-2006.

[95] J. E. Backofen, The use of analytical computer models in shaped charge design. *Propellants, Explosives, Pyrotechnics*, **1993**. *18***,** 5, p. 247-254.

[96] D. C. Pack and W. M. Evans, Penetration by high-velocity (Munroe) jets: I, *Proccedings of the Physical Society,* London, **1950**. B64, p. 298.

[97] R. Eichelberger, Experimental test of the theory of penetration by metallic jets. *Journal of Applied Physics*, **1956**. *27***,** 1, p. 63-68.

[98] E. M. Pugh, *A Theory of target penetration of jets*, National Defense Research Committee Armour and Ordnance Report No. A-274 (OSRD No. 3752), **1944.**

[99] O. A. Klamer, *Shaped charge scaling*. Technical Memorandum No. AD0600273, **1964**, Dover, NG, USA.

[100] G. R. Abrahamson and J. N. Goodier, Penetration by shaped charge jets of nonuniform velocity. *Journal of Applied Physics*, **1963**. *34*, 1, p. 195-199.

[101] R. Dipersio, J. Simon, B. Merendino, Penetration of shaped-charge jets into metallic targets. Ballistic Research Laboratory Memorandum Report No. 1296. **1965**.

[102] W. Schwartz, Modified SDM model for the calculation of shaped charge hole profiles. *Propellants, Explosives, Pyrotechnics*, **1994**. *19*, 4, p. 192-201.

[103] W. P. Walters, W. J. Flis, P. C. Chou, A survey of shaped-charge jet penetration models, *International Journal of Impact Engineering,* **1988,** *7*, 8, p. 307-325.

[104] V. P. Alekseevskii, Penetration of a rod into a target at high velocity. *Combustion, Explosion, and Shock Waves*, **1966**. *2*, 2, p. 63-66.

[105] N. S. Sanasaryan, Penetration of a cumulative jet into a barrier. *Fluid Dynamics*, **1975**. *10***,** 6, p. 997.

[106] D. R. Christman and J. W. Gehring, Analysis of high-velocity projectile penetration mechanics, *Journal of Applied Physics*, **1966**. *37*, 4, p. 1579.

[107] J. R. Doyle and R. L. Buchholz, Design, development, fabrication and testing program to demonstrate feasibility of the mass focus fragmentation warhead. **1973**.

[108] A. Tate, A theory for the deceleration of long rods after impact, *Journal of the Mechanics and Physics of Solids*, **1967**. 15, p. 387-399.

[109] A. Tate, Further results in the theory of long rod penetration. *Journal of the Mechanics and Physics of Solids*, **1969**. *17*, 3, p. 141-150.

[110] A. Tate, Long rod penetration models-Part I. A flow field model for high speed long rod penetration. *International Journal of Mechanical Sciences*, **1986**. *28*, 8, p. 535-548.

[111] M. Held and A. A. Kozhushko, Radial crater growing process in different materials with shaped charge jets. *Propellants, Explosives, Pyrotechnics*, **1999**. *24*, 6, p. 339-342.

[112] A. Tate, Long rod penetration models-Part II. Extensions to the hydrodynamic theory of penetration. *International Journal of Mechanical Sciences*, **1986**. *28*, 9 p. 599-612.

[113] D. A. Matuska, A model for high velocity penetrating. Proc. of ARO Workshop on Computational Aspects of Penetration Mechanics. **1982**. Aberdeen Proving Ground MD.

[114] M. Held, N. S. Huang, D. Jiang and C. Chang, Determination of the crater radius as a function of time of a shaped charge jet that penetrates water. *Propellants, Explosives, Pyrotechnics*, **1996**. *21*, 2, p. 64-69.

[115] M.S. Cowler, Autodyn jetting Analysis tutorial, **2001.**

[116] S. Malcolm, *Autodyn theory manual*, R. 3.0, Editor. **1997**, Century Dynamics: USA.

[117] V. S. Berg and D. S. Preece, Shaped charge induced concrete damage predictions using RHT constitutive modeling, *Journal of International Society of Explosives Engineers*, **2004,** *2*. p.261-272.

[118] G. Baudin and R. Serradeill, Review of Jones-Wilkins-Lee equation of state. *New Models and Hydrocodes for Shock Wave Processes in Condensed Matter, Paris*, France, Edited by Laurent Soulard; EPJ Web of Conferences, **2010**, *10*, p. 21.

[119] E. L. Lee, H. C. Hornig and J. W. Kury, *Adiabatic expansion of high explosive detonation products*, California University, Livermore. Lawrence Radiation Lab Report No. UCRL-50422, **1968.**

[120] C. M. Tarver, W. C. Tao and C. G. Lee, Sideways plate push test for detonating solid explosives, *Propellants, Explosives, Pyrotechnics*, **1996**. *21*, 5, p. 238-246.

[121] G. R. Johnson and W. H. Cook, A Constitutive model and data for metals subjected to large strains, high strain-rates and high temperatures. *Proceedings of the 7th Int. Symposium on Ballistics*. Netherlands, **1983.** p. 541-547.

[122] W. Herrmann, Constitutive equation for the dynamic compaction of ductile porous materials, *Journal of Applied Physics*, **1969**, *40*, 6, p. 2490-2499.

[123] N. Heider and S. Hiermaier, Numerical simulation of the performance of tandem warheads, *19th International Symposium of Ballistics*, Interlaken, Switzerland, **2001**, p.1493.

[124] W. Riedel, K. Thoma, S. Hiermaier and E. Schmolinske, Penetration of reinforced concrete by beta-b-500. numerical analysis using a new macroscopic concrete model for hydrocodes, *9th International Symposium on the Interaction of the Effects of Munitions with Structures*, **1999**. p. 1.

[125] Z. Tu and Y. Lu, Evaluation of typical concrete material models used in hydrocodes for high dynamic response simulations. *International Journal of Impact Engineering*, **2009**. *36*, 1, p. 132-146.

[126] J. Leppänen, Concrete structures subjected to fragment impacts, PhD thesis, Chalmers University of Technology, Göteborg, Sweden, **2004**, p. 40.

[127] C. J. Hayhurst, R. A. Clegg, I. H. Livingstone and N. J. Francis, The application of SPH techniques in Autodyn 2-D to ballistic impact problems, *16th International Symposium on Ballistics*, San Fransisco, USA, **1996**.

[128] J. Brookes and W. Yang, *Target for testing perforating system*, **2001**. US Patent No. US6,238,595 B1.

[129] R. A. Clegg, C. J. Hayhurst and I. Robertson, Development and application of a Rankine plasticity model for improved prediction of tensile cracking in ceramic and concrete materials under impact, *14th DYMAT Technical Meeting*. **2002**: Sevilla, Spain.

[130] B. Adel, Numerical approach in predicting the penetration of limestone target by an ogive-nosed projectile using Autodyn 3-D, *12th International Colloquium on Structural and Geotechnical Engineering* (ICSGE), **2007**, Egypt.

[131] B. Lusk, W. Schonberg, J. Baird, R. Woodley and W. Noll, *Using coupled Eulerian and Lagrangian grids to model explosive Interactions with buildings*. Technical report No. ADA481951, **2006**.

[132] J. Leppänen, Concrete subjected to projectile and fragment impacts: Modelling of crack softening and strain-rate dependency in tension. *International Journal of Impact Engineering*, **2006**. *32*, 11, p. 1828-1841.

[133] Marinko Ugrčić, Dušan Ugrčić, *FEM techniques in shaped charge simulation*, Scientific Technical Report Review,*Vol. LVIX*, No.1, **2009**, p. 26-34.

[134] J. E. Backofen, Air cratering by eroding shaped charge jets. *23rd International Symposium on Ballsitics*. **2007**. Spain. p. 689-696.

[135] D. Hasenberg, *Consequences of coaxial jet penetration performance and shaped charge design criteria*, Technical Report No. NPS-PH-10-001, **2010.**

[136] J. Curtis, F. Smith and A. White, The formation and stretching of bi-material shaped charge jets. *American Institute of Physics Conference proceedings*, **2011,** *1426*. p.116-119.

[137] M. H. Keshavarz, Prediction method for specific impulse used as performance quantity for *explosives. Propellants, Explosives, Pyrotechnics*, **2008**. *33*, 5, p. 360-364.

[138] D. R. Hardesty and J. E. Kennedy, Thermochemical estimation of explosive energy output. *Combustion and Flame Journal*, **1977**. *28*, p. 45-59.

[139] M. G. Vigil, *Optimized conical shaped charge design using the SCAP code*, Sandia National Laboratories Report No. SAND88-1790. **1988**.

[140] J. A. Zukas and W. Walters, Explosive effects and applications. **1997**, Springer.

[141] W. Johnson, *Impact strength of materials*. London, Edward Arnold, **1972**, p. 303.

[142] Q.M. Li, Johnson's damage number in impact dynamics, *International Journal of Impact Engineering*, **2011**. *38*, 5, p. 273-274.

[143] API, *Evaluation of well perforators, recommended practice RP 43*, American Petroleum Institute (API), January, **1991.**

[144] API, *Recommended practice 19B for evaluation of well perforators*, First Edition, **2001**

[145] Book of ASTM standard**,** ASTM C 192/C 192M-02 Standard practice for making and curing concrete test specimens in the laboratory, **2002,** 04, 02. p.2.

[146] Q.M. Li and H. Meng, About the dynamic strength enhancement of concrete-like materials in a split Hopkinson pressure bar test. *International Journal of Solids and Structures*, **2003**. *40*, 2, p. 343-360.

[147] A. N. Mikhailov and A. N. Dremin, *Flight speed of a plate propelled by products from a sliding detonation.* Combustion, Explosion, and Shock Waves, **1974**. *10*, *6*, p. 787-792.

[148] J. T. Harrison, *Improved analytical shaped charge code: Basc,* Technical Report No. ARBRL-TR-02300, **1981**.

[149] J. D. Walker, Incoherence of shaped charge jets, *American Institute of Physics Conference. Proceeding*, **1994**, *309,* p. 1869-1872.

[150] M. Held, Diagnostic of superfast jets with 25 km/s tip velocities, *Propellants, Explosives, Pyrotechnics*, **1998**. *23,* 5, p. 229-236.

[151] R. H. Nielsen, G. Wilfing, ULLMANN'S Encyclopedia of industrial chemistry, Zirconium and Zirconium Compounds, **2002**, Wiley-VCH Verlag GmbH & Co. KGAa, Vol. 39, p. 753.

[152] Zirconium-Machining, http://www.espimetals.com/index.php/technical-data/337-zirconium-machining, accessed on **1/10/ 2012.**

[153] M. C. Chick and L. A. Learmonth, *Determination of shock initiation and detonation characteristics of PE4 in proof test geometries*, Defence science and technology Organisation Materials research Laboratories, Report No. MRL-R-979, **1986.**

[154] R. K. Whartona, S. A. Formby and R. Merrifield, Airblast TNT equivalence for a range of commercial blasting explosives, *Journal of Hazardous Materials*, **2000,** *79*, 1–2, p. 31-39.

[155] W. L. Porter, B. Satterwhite, Evaluation of well perforator performance, *Journal of Petrolleum Technology*, **1976**. *28*, 12, p. 1466-1472.

[156] A. R. Kiwan and H. Wisniewski, *Theory and computations of collapse and jet velocities of metallic shaped charge liners*, Ballistic Research Labs Aberdeen Proving Ground MD, Report No. AD0907161. **1972**.

[157] F. E. Allison and G. M. Bryan, Cratering by a train of hypervelocity fragments. *Proceedings of the 2nd Hypervelocity Impact Effects Symposium.* **1957**.

[158] F. Jamet, Measurements of densities in shaped charge jets and detonation waves, *American Society for Non-Destructive Testing*, **1976**.

[159] K. D. Werneyer and F. J. Mostert, Analytical model predicting the penetration behaviour of a jet with a time-varying density profile, *21st International Symposium on Ballistics*, **2004,** South Africa, p. 390-397.

[160] F. M. Milton, D. W. Klaus and F. J. Mostert, An analytical penetration model for jets with varying mass density profiles, *22nd International symposium on Ballistics*, **2005**,Canada. p. 622-629.

[161] B. Grove and I. Walton, Shaped charge jet velocity and density profiles, *23rd International Symposium on Ballistics*, **2007,** Spain. p.103-110.

[162] AccuPyc-II-1340-Pycnometer, http://www.micromeritics.com/Product-Showcase/AccuPyc-II-1340.aspx, accessed on **1/10/2012.**

[163] W. P. Walters and R. L. Summers, *The velocity difference between particulated shaped charge jet particles for face-centered-cubic liner materials*, Army Research Lab Aberdeen Proving Ground MD Report No. ADA257348, **1992**.

[164] K. Cowan and B. Bourne. Further analytical modelling of shaped charge jet breakup phenomena. *19th International Symposium on Ballistics,* Switzerland, **2001**, p. 803-810.

[165] H. Kolsky, *Stress waves in solids*, Dover Phoenix Editions, **1963**.

[166] V. Ramachandran, A.T. Santhanam and R. E. Reed-Hill, Dislocation-solute interactions and mechanical behaviour of zirconium and titanium. *Indian Journal Technol*ogy, *11*, 10, p. 485-492.

[167] W. Von Holle and J. Trimble, Temperature measurement of shocked copper plates and shaped charge jets by two color ir radiometry, *Journal of Applied Physics*, **1976**, *47*, p. 2391-2394.

[168] C. L. Aseltine, *Analytical predictions of the effect of warhead asymmetries on shaped charge jets*. Technical Report No. ARBRL-TR-02214, **1980.**

[169] Matweb, http:/www.matweb.com/search/Datasheet.aspx?MatGuid=6e8936bad994f13bfb29923cc1506a9&ckck=1, accessed on **1/10/2012.**

APPENDICES

Appendix A: The numerical calculation of the critical angles β_c at different V_2

The analytical model used to calculate the critical collapse angles at different flow velocities is obtained on the basis of the momentum balance according to:

$$\tan^2\beta = \frac{P\left[\rho_o V_2^2\left(\frac{\mu}{\mu+1}\right)-P\right]}{(\rho_o V_2^2-P)^2} \quad \text{(A1)}$$

where P is the pressure, ρ_o is the initial liner density, μ is the compressibility (i.e. $\mu=\rho/\rho_o-1$).
The critical angles can be determined for a given impinging velocity V_2 from the condition $d\beta/d\mu = 0$. Thus, for $\beta=\beta_c$,

$$\frac{\mathrm{dP}}{\mathrm{d}\mu} = \frac{P[P-\rho_o V_2^2]}{(\mu+1)[\mu\rho_o V_2^2-P(\mu+2)]} \quad \text{(A2)}$$

So, EOS of the liner material is used with Eq. (A2) to calculate the critical angles β_c at different values of V_2. Shock EOS take the form of:

$$P = \frac{\rho C_0^2 \mu(\mu+1)}{(1-(S-1)\mu)^2} \quad \text{(A3)}$$

where C_o is the sound speed of the liner material and S is the slope of the shock speed-particle velocity line. For the zirconium material, S=1.018.
From Eq. (A3),

$$\frac{dP}{d\mu} = \frac{(1-(S-1)\mu)\rho C_0^2\left(\left(1-(S-1)\right)(2\mu+1)+2(\mu^2+\mu)(S-1)\right.}{(1-(S-1)\mu)^4} \quad \text{(A4)}$$

For simplicity, assume S≈1, therefore Eq. (A4) becomes:

$$\frac{dP}{d\mu} = \rho C_o^2(2\mu+1) \quad \text{(A5)}$$

Equating Eqs. (A2), (A5), and solving for the critical compressibility (i.e. μ_c). The obtained values for μ_c were substituted into EOS, Eq. (A3) to get the corresponding critical pressure; P_c. The Values of μ_c and P_c are used with Eq. (A1) to get β_c.

$$\frac{P[P-\rho_o V_2^2]}{(\mu+1)[\mu\rho_o V_2^2-P(\mu+2)]} = \rho C_0^2(2\mu+1) \ . \quad \text{(A6)}$$

Thus,

$$P^2 - (C_0^2(\mu+2)(2\mu+1)(\mu+1) - V_2^2)\rho P - (\rho C_0^2(2\mu+1)(\mu+1)(\mu\rho V_2^2)) = 0 \quad \text{(A7)}$$

$$P_c = \frac{\left(C_0^2(\mu+2)(2\mu+1)(\mu+1)-V_2^2\right)\rho \mp \sqrt{(C_0^2(\mu+2)(2\mu+1)(\mu+1)-V_2^2)\,\rho)^2+4(\rho C_0^2(2\mu+1)(\mu+1)\left(\mu\rho V_2^2\right))}}{2}. \quad \text{(A8)}$$

Let Y=μ+1 and Z= 2μ+1

$$P_c = \frac{\left(C_0^2YZ(Y+1)-V_2^2\right)\rho \mp \sqrt{(C_0^2YZ(Y+1)-V_2^2)\,)^2\rho^2+4(\rho^2C_0^2YZ\mu V_2^2)}}{2}. \quad \text{(A9)}$$

From EOS, s=1

$$P_c = \rho C_0^2\mu Y = \frac{\left(C_0^2YZ(Y+1)-V_2^2\right)\rho \mp \sqrt{(C_0^2YZ(Y+1)-V_2^2)^2\rho^2+4(\rho^2C_0^2YZ\mu V_2^2)}}{2} \quad \text{(A10)}$$

$$C_0^2\mu Y = \frac{\left(C_0^2YZ(Y+1)-V_2^2\right) \mp \sqrt{(C_0^2YZ(Y+1)-V_2^2\,)^2+4(C_0^2YZ\mu V_2^2)}}{2}, \quad \text{(A11)}$$

$$2C_0^2\mu Y - C_0^2YZ(Y+1) + V_2^2 = \mp\sqrt{(C_0^2YZ(Y+1) - V_2^2)^2 + 4(C_0^2YZ\mu V_2^2),} \quad \text{(A12)}$$

$$(2C_0^2\mu Y - C_0^2YZ(Y+1) + V_2^2)^2 = (C_0^2YZ(Y+1) - V_2^2)^2 + 4(C_0^2YZ\mu V_2^2), \quad \text{(A13)}$$

$$4C_0^4\mu^2Y^2 + 4C_0^2\mu Y(-C_0^2YZ(Y+1) + V_2^2) = 4(C_0^2YZ\mu V_2^2)\,, \quad \text{(A14)}$$

$$C_0^2\mu\,Y\; -C_0^2YZ(Y+1) + V_2^2 \;=\; ZV_2^2. \quad \text{(A15)}$$

Substitute the values of Y and Z,

$$\mu\,Y\; - YZ(Y+1) + \frac{V_2^2}{C_0^2} \;=\; Z\frac{V_2^2}{C_0^2}\;, \quad \text{(A16)}$$

$$\mu\,(\mu+1)\; - (\mu+1)(2\mu+1)(\mu+2) - (2\mu+1)\frac{V_2^2}{C_0^2} \;=\; -\frac{V_2^2}{C_0^2}, \quad \text{(A17)}$$

$$2\mu^3 + 6\mu^2 + \left(7 + 2\left(\frac{V_2}{C_0}\right)^2\right)\mu + 1 = 0\;, \quad \text{(A18)}$$

For the Zirconium material, ρ=6510 g/cm^3 and K=98.5G Pa.

Calculating the critical pressure P_c and the critical compressibility μ_c, the critical collapse angle is estimated from Eq. (A1) at different flow velocities V_2.

Appendix B: Proof of Inequality Eq.(8-6)

According to Eq.(8-5),

$$\frac{dP(t)}{dt} = V_j(t) + t\frac{dV_j(t)}{dt}. \tag{B1}$$

For uniform density distribution, Eq.(B1) together with Eqs.(8-9) and (8-10) lead to

$$\frac{dP(t)}{dt} = \mathrm{V_o}\left(\frac{t_o}{\mathrm{t}}\right)^{\frac{\gamma}{\gamma+1}} + t\frac{d}{dt}\left(\mathrm{V_o}\left(\frac{t_o}{\mathrm{t}}\right)^{\frac{\gamma}{\gamma+1}}\right) = \mathrm{V_o}\left(\frac{t_o}{\mathrm{t}}\right)^{\frac{\gamma}{\gamma+1}} + t\left(\frac{-\gamma}{\gamma+1}\right)\mathrm{V_o}(t_o)^{\frac{\gamma}{\gamma+1}}(t)^{\frac{-\gamma}{\gamma+1}-1}. \tag{B2}$$

Therefore, the inequality Eq.(8-6) is equivalent to $\mathrm{V_o}\left(\frac{t_o}{\mathrm{t}}\right)^{\frac{\gamma}{\gamma+1}} \geq \left(\frac{\gamma}{\gamma+1}\right)\mathrm{V_o}\left(\frac{t_o}{\mathrm{t}}\right)^{\frac{\gamma}{\gamma+1}}$ or $1 \geq \left(\frac{\gamma}{\gamma+1}\right)$, which is automatically satisfied.

For non-uniform density distribution, the velocity is determined by Eq.(8-16), which can be rewritten as

$$\left(\frac{V_0}{V_j}\right)^{b\gamma_0}\left(b\left(\frac{V_0}{V_j}\right) + a\right) = (a+b)\left(\frac{t}{t_0}\right)^{b\gamma_0}. \tag{B3}$$

For the shaped charge liners studied in this paper, a≅0.1, b≅1 and $V_o > V_j$, thus $b\left(\frac{V_0}{V_j}\right) + a \approx b\left(\frac{V_0}{V_j}\right)$ and $a + b \approx b$ with a maximum error less than 10%. Therefore, Eq.(B3) can be approximated by:

$$\left(\frac{V_0}{V_j}\right)^{b\gamma_0+1} \cong \left(\frac{t}{t_0}\right)^{b\gamma_0}. \tag{B4}$$

The inequality Eq.(8-6) can be proved easily by Eqs.(8-5), (8-14) and (B4) using the same procedure for uniform density distribution situation, which will not be presented here. Meanwhile, we also calculated the time histories of $V_j(t)$ and $\frac{dV_j(t)}{dt}$ numerically. Based on Eq.(B1), it has been shown that inequality Eq.(8-6) can be satisfied for the studied cases in Chapter 8.

Appendix C: Derivation of Eq. (8-18)

Assuming the hydrodynamic theory and starting from Eq. (8-8) for non-uniform density jet,

$$\int_{V^o}^{V(t)} \frac{-dV}{\mathrm{V_j}(t)} - \frac{1}{\gamma_o}\int_{V^o}^{V(t)} \frac{dV}{\mathrm{V_j}(t)\left(\frac{\mathrm{a}}{\mathrm{V_j^o}}\mathrm{V_j(t)+b}\right)} = \int_{t_o}^{t} \frac{dt}{t} \tag{C1}$$

$$\ln\left(\frac{V_j^o}{V(t)}\right) - \frac{1}{\gamma_o}\int_{V^o}^{V(t)} \frac{dV}{\mathrm{V_j}(t)\left(\frac{\mathrm{a}}{\mathrm{V_j^o}}\mathrm{V_j(t)+b}\right)} = \ln\left(\frac{t}{t_o}\right) \tag{C2}$$

$$t = t_o\left(\frac{\mathrm{V_j^o}}{\mathrm{V_j}}\right)^{\frac{b\gamma_O+1}{b\gamma_O}}\left[\frac{\left(\frac{\mathrm{a}}{\mathrm{V_j^o}}\mathrm{V_j+b}\right)}{\left(\frac{\mathrm{a}}{\mathrm{V_j^o}}\mathrm{V_j^o+b}\right)}\right]^{\frac{1}{b\gamma_O}} \tag{C3}$$

The total penetration will be achieved within time duration of t and V_c; the cutoff element velocity or the velocity of the last penetrating element. Thus, Eq. (C3) will be.

$$\mathrm{t} = t_o\left(\frac{\mathrm{V_j^o}}{V_c}\right)^{\frac{b\gamma_O+1}{b\gamma_O}}\left[\frac{\gamma_{Cutoff}}{\gamma_{tip}}\right]^{\frac{1}{b\gamma_O}} \tag{C4}$$

where γ_{cutoff} is the square root of the ratio of the target to the jet densities at the cutoff element, while γ_{tip} is the square root of the ratio of the target to the jet densities at the tip of the jet. When $\gamma_{cutoff}= \gamma_{tip=} \gamma_{o,}$ and b=1, this equation reduces to the constant density equation. The second term can be defined as the density reduction term.

From Eq.(C4), the impact velocity of the jet is determined by an algebraic equation of

$$b\left(\frac{V_0}{V_j}\right)^{b\gamma_0+1} + a\left(\frac{V_0}{V_j}\right)^{b\gamma_0} = (a+b)\left(\frac{t}{t_0}\right)^{b\gamma_0}. \tag{C5}$$

Eq.(C5) reduces to Eq.(8-9) for constant jet density when a=0 and b=1.

This equation also reduces to the constant density equation when $\gamma_{cutoff} = \gamma_{tip}$=constant and b=1.

To calculate the penetration of jet with non-uniform density distribution, the derived definitions of the total penetration time and the jet velocity at this time are used in the penetration equation (i.e. Eq. (8-5)).

$$\mathrm{P(t)} = Z_o\left(\left(\frac{\mathrm{V_j^o}}{\mathrm{V_{jc}}}\right)^{\frac{1}{b\gamma_O}} \quad \left(\frac{\gamma_{Cutoff}}{\gamma_{tip}}\right)^{\frac{1}{b\gamma_O}} - 1\right) \tag{C6}$$

Appendix D: The detailed drawing of a conical liner OWP Preliminary Design

D-1: OFHC Copper Liner

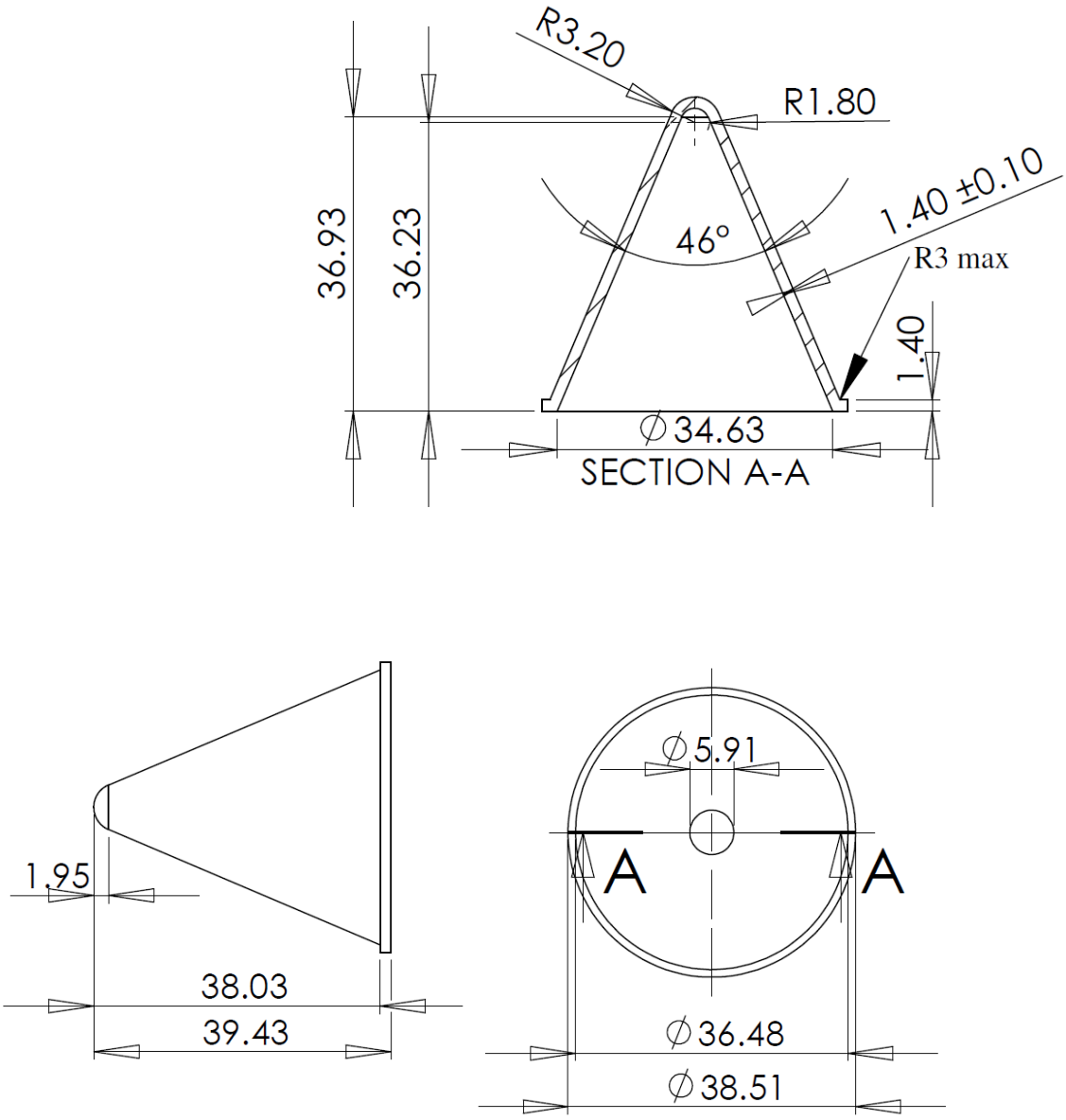

Units in mm

D-2: Steel casing

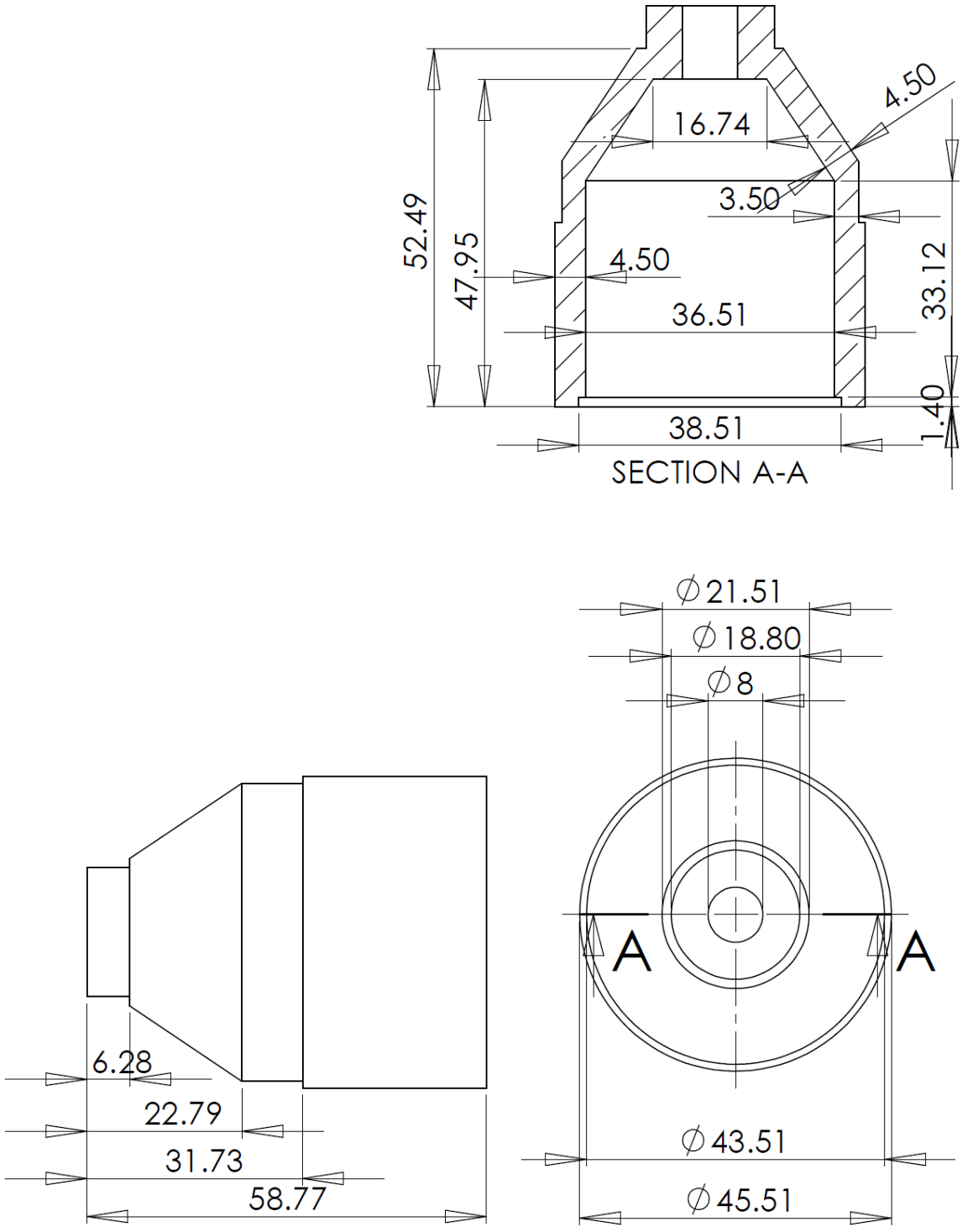

Units in mm

D-3: PE4 Explosive charge

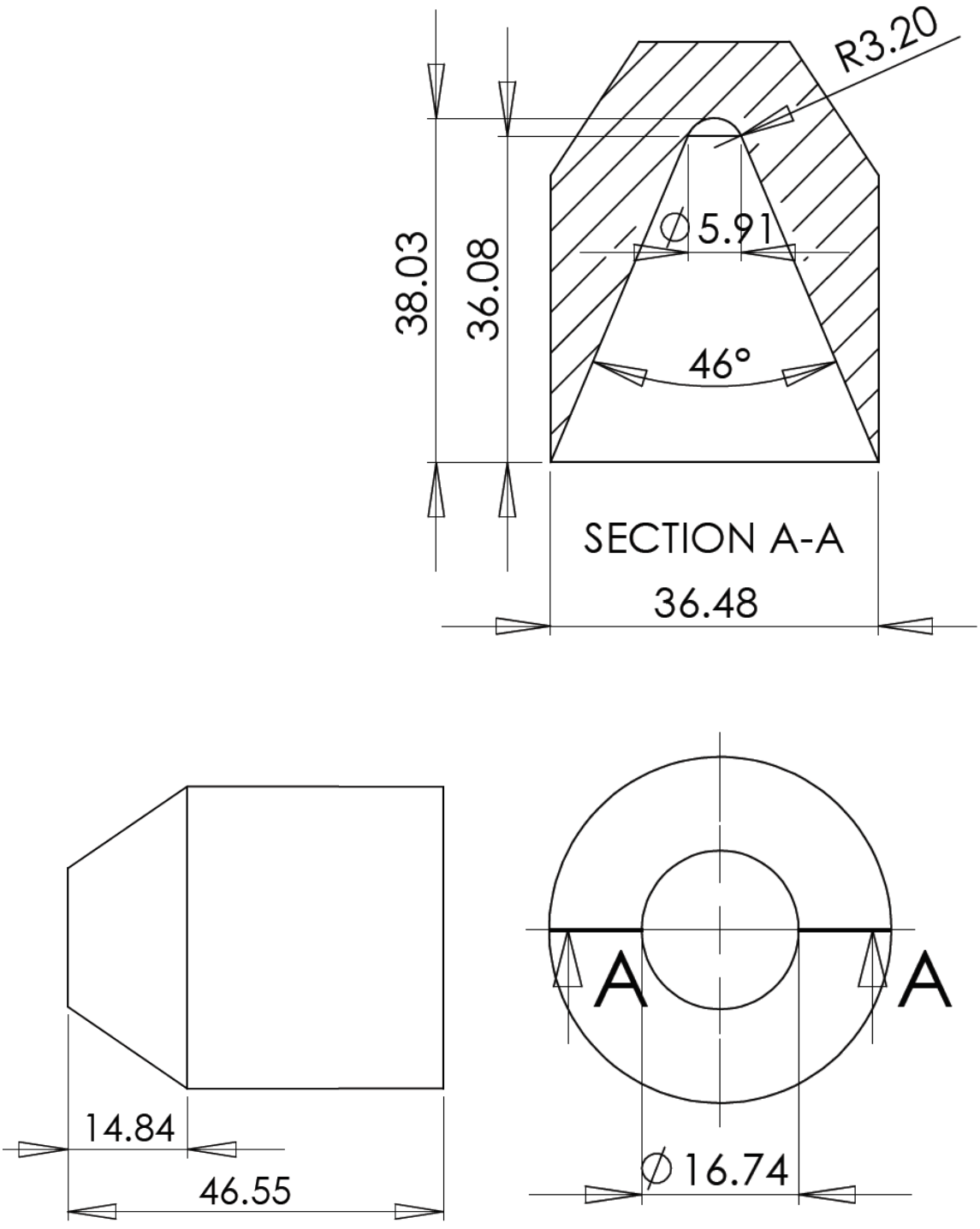

Units in mm.

(This page is intentionally left blank)